New Experimental Data for a Re-Calibration of the Fe-Ti Oxide Thermo-Oxybarometers.

INAUGURAL-DISSERTATION
zur
Erlangung der Doktorwürde
der
Naturwissenschaftlich-Mathematischen Gesamtfakultät
der Ruprecht-Karls-Universität
Heidelberg

vorgelegt von
Diplom-Mineralogin Ursula Sauerzapf
aus Heidelberg

New Experimental Data for a Re-Calibration of the Fe-Ti Oxide Thermo-Oxybarometers.

Gutachter:
Prof. Dr. Dominique Lattard
Hochschuldozentin Dr. Agnes Kontny

Tag der mündlichen Prüfung: 29.05.2006

Contents

Abstract

Despite their modest modal abundances, the Fe-Ti oxide minerals are important accessory minerals in igneous rocks. They are major carriers of rock magnetism and petrologic indicators of temperature and redox conditions during the magmatic stage (Buddington & Lindsley, 1964).

The titanomagnetite-ilmenite$_{ss}$ (Tmt-Ilm$_{ss}$) thermo-oxybarometer has been widely used to retrieve information on redox states in the Earth's mantle, processes in magma chambers, the crystallisation conditions of lunar or martian basalts, redox conditions during metamorphic evolution, or fluid-rock interactions.

However, the current thermodynamic formulations of the Tmt-Ilm$_{ss}$ thermo-oxybarometer (Andersen & Lindsley, 1988; Ghiorso & Sack, 1991) fail to reproduce experimental results, in particular at the high temperatures that are relevant for basaltic assemblages. This is shown in chapter 1 (section 1.3) by applying the formulations to experimental literature data. The shortcomings of the existing models are partly due to the limited T-fO_2-range of experiments used for the original calibrations. Further, the effect of small contents of Mg, Al, etc. typical for natural Tmt and Ilm$_{ss}$ was only partly evaluated, and the non-stoichiometry of the phases (in particular Tmt) was not considered at all.

To support a revised version of the Tmt-Ilm$_{ss}$ thermo-oxybarometer we have synthesised Tmt+Ilm$_{ss}$ assemblages in the systems Fe-Ti-O, Fe-Ti-Mg-O, Fe-Ti-Al-O and Fe-Ti-Mg-Al-O at 1 bar, $1000-1300\,^{\circ}C$ and under a large range of fO_2 (ΔNNO-5 to +5, fO_2 controlled by gas mixtures or solid-state buffers, see chapter 2 for experimental details). A large data set has also been provided for Ilm$_{ss}$ coexisting with pseudobrookite$_{ss}$ (Psb$_{ss}$). This forms the basis for an experimental calibration of a thermodynamic Ilm$_{ss}$-Psb$_{ss}$ (thermo-)oxybarometer model. The latter can be used to estimate oxygen fugacity in oxidised terrestrial igneous rocks, moderately reduced assemblages in mantle xenoliths, or strongly reduced lunar assemblages.

The textures of the synthetic samples have been used to evaluate whether equilibrium could be attained or at least closely approached in the run products. Indeed, the synthetic run products essentially consist of polycrystalline, equi-granular aggre-

gates, with idiomorphic, homogenous and evenly distributed grains ($10-50\,\mu m$). This suggests that the run products reflect or are close to an equilibrium state.

However, in many samples we have observed concentric variations in Ti/(Ti+Fe). Their formation is strongly related to the starting material and is probably driven by the redox processes that occur during the experiment (chapter 3). Synthesis products prepared from $Fe_2O_3 + TiO_2$ mixtures usually show an increase of Ti/(Ti+Fe) towards the sample pellet surface. As a result, single-phase samples develop a concentric phase inhomogeneity, while binary assemblages show variations of phase abundances, typically the formation of a Ti-rich monomineralic rim. In contrast, synthesis products prepared from $Fe^{\circ} + TiO_2$ mixtures have Fe-rich rims at the sample pellet surface. Nevertheless, local equilibrium is achieved in each of the sample regions.

At the outer max. $100\,\mu m$ of the sample pellets, samples that have been exposed to oxidising conditions during the quench process display oxy-exsolution features in the sense of Buddington & Lindsley (1964), which may form within <5 seconds. Oxy-exsolution does not affect the phase compositions in the central sample region but involves an increase of the sample bulk oxygen content.

For the re-calibration of the Fe-Ti thermo-oxybarometer, the data base on Tmt coexisting with Ilm_{ss} used to calibrate the models of Andersen & Lindsley (1988) and Ghiorso & Sack (1991) has now been extended towards higher temperatures (i.e. $1000-1300\,^{\circ}C$) and to a larger range of oxygen fugacities. The compositions of coexisting Fe-Ti oxide phases in the system Fe-Ti-O have been determined by EMP as a function of T and fO_2 (chapter 4).

The experimental data derived within this study has been compared to the existing thermo-oxybarometer models by Andersen & Lindsley (1988, QUILF) and Ghiorso & Sack (1991). The transition within the ilmenite-hematite solid solution series (from the long-range ordered $R\bar{3}$ to the long-range disordered $R\bar{3}c$ structure) causes an abrupt change of the slope of the experimentally determined isotherms, which gets increasingly pronounced with decreasing temperature. Andersen & Lindsley (1988) did not account for this transition, and consequently their model isotherms do not show the related sharp bend. Ghiorso & Sack (1991) in contrast did account for the Ilm-Hem transition, however their model heavily relies on old experimental data involving sample compositions that were not controlled by microanalytical methods.

Synthetic Tmt compositions are generally Ti-richer than predicted from the models. At high fO_2, this is probably related to errors in the standard state properties used for the Tmt endmembers. At low fO_2 and high T, the strong discrepancies be-

tween synthetic Tmt data and the models are presumably due to non-stoichiometric (i.e. cation vacant) Tmt.

Tmt non-stoichiometry has been investigated in the system Fe-Ti-O at $1100-1300\,^{\circ}C$ for Tmt in assemblages in which maximum (Tmt+Ilm_{ss}) versus minimum (Tmt+Wus, Tmt+Fe°) vacancy concentration is expected (chapter 5).

Three methods have been used to detect and quantify the vacancy concentrations: (1) Because cation deficiency involves a decrease of the Tmt cell dimensions at constant Ti/(Ti+Fe) ratio, lattice parameters have been determined by Rietveld analysis. (2) At constant Ti/(Ti+Fe), cation vacancies are associated with higher $Fe^{3+}/\Sigma Fe$ values. The latter have been determined by electron energy-loss spectroscopy on selected samples. (3) Annealing of a non-stoichiometric high-T Tmt at lower temperatures (e.g. $950\,^{\circ}C$) under oxygen-conserving conditions induces vacancy relaxation. This comes along with compositional changes in the phases, which result in the formation of Ilm_{ss} exsolution lamellae and rims in Tmt, i.e. an increase in the Ilm_{ss} proportion.

The results of the three different approaches indicate that Tmt in coexistence with Ilm_{ss} has only low vacancy concentration or is very close to stoichiometry at $X_{Usp}<0.7$ at all investigated temperatures. At $X_{Usp}>0.7$, the vacancy concentration increases with increasing X_{Usp} and T to about 2 cat% for $1300\,^{\circ}C$ at X_{Usp} close to 1. At $T\leq 1100\,^{\circ}C$, i.e. at temperatures relevant for crystallisation conditions of basic rocks, Tmt is close to stoichiometry for all compositions. However, as the revised version of the Tmt-Ilm_{ss} thermo-oxybarometer also will involve high-T calibration data, it is important to account for Tmt non-stoichiometry in its solid solution models.

To approach natural compositions, Tmt+Ilm_{ss} assemblages have also been produced in the system Fe-Ti-Mg-Al-O (chapter 6). For a comparison to the simple system Fe-Ti-O, the Mg-Al bearing Fe-Ti oxide compositions have been projected onto the Ilm-Hem and Mag-Usp binaries. X'_{Usp} and X'_{Ilm} of Mg-Al bearing phases are in reasonable agreement with the simple system Fe-Ti-O data. Therefore, the experimental isotherms determined for the system Fe-Ti-O can in principle also be applied to Mg-Al bearing samples. This provides a new, preliminary and graphical version of the Tmt-Ilm_{ss} thermo-oxybarometer, which has been tested on experimental data by Toplis & Carroll (1995). Compared to the T-fO_2 estimates derived with the previous models, the new, graphical thermo-oxybarometer brings significant improvements, especially in the temperature estimates.

Kurzfassung

Trotz ihrer geringen modalen Häufigkeiten sind die Fe-Ti-Oxid-Minerale wichtige akzessorische Minerale in magmatischen Gesteinen: Sie sind die Hauptträger des Gesteinsmagnetismus und petrologische Indikatoren für die Temperatur und die Redoxbedingungen während der magmatischen Phase.

Das Titanomagnetit-Ilmenit (Tmt-Ilm_{ss}) Thermo-Oxybarometer ist viel verwendet worden, um Informationen über den Redoxzustand des Erdmantels, Prozesse in Magmenkammern, die Kristallisationsbedingungen von Basalten des Mondes und des Mars, Redoxbedingungen während der magmatischen Entwicklung, oder Fluid-Gestein-Wechselwirkungen zu erhalten.

Insbesondere bei den hohen Temperaturen, die für basaltische Paragenesen relevant sind, gelingt es den gegenwärtigen thermodynamischen Formulierungen der Tmt-Ilm_{ss} Thermo-Oxybarometer jedoch nicht, experimentelle Ergebnisse zu reproduzieren. In Kapitel 1 (Abschnitt 1.3) ist dies durch Anwendung der Formulierungen auf experimentelle Daten aus der Literatur gezeigt. Die Schwächen der bestehenden Modelle beruhen zum Teil auf dem eingeschränkten T-fO_2-Bereich der für die ursprünglichen Kalibrierungen verwendeten Experimente. Außerdem wurde der Effekt von niedrigen Gehalten an Mg, Al, etc., die für natürlichen Tmt und Ilm_{ss} typisch sind, nur teilweise berücksichtigt, und die Unstöchiometrie der Phasen (besonders Tmt) wurde überhaupt nicht betrachtet.

Um zu einer revidierten Fassung des Tmt-Ilm_{ss} Thermo-Oxybarometers beizutragen haben wir Tmt+Ilm_{ss} Proben in den Systemen Fe-Ti-O, Fe-Ti-Mg-O, Fe-Ti-Al-O und Fe-Ti-Mg-Al-O bei 1 bar, $1000-1300\,^{\circ}C$ und in einem großen Sauerstofffugazitätsbereich synthetisiert (ΔNNO-5 bis +5, eingestellt mit Hilfe von Gasmischungen oder Festkörperpuffern, siehe Kapitel 2). Ein umfangreicher Datensatz wurde auch für Ilm_{ss} und koexistierenden Pseudobrookit$_{ss}$ (Psb_{ss}) erzeugt. Dieser Datensatz bildet die Grundlage für eine experimentelle Kalibrierung eines thermodynamischen Ilm_{ss}-Psb_{ss} (Thermo-)Oxybarometer-Modells. Letzteres kann zur Abschätzung der Sauerstofffugazität in oxidierten, terrestrischen magmatischen Gesteinen, mäßig reduzierten Paragenesen in Mantel-Xenolithen oder stark reduzierten Mondparagenesen verwendet werden.

Anhand der Texturen der synthetischen Proben wurde beurteilt, ob ein Gleichgewichtszustand erreicht wurde. Tatsächlich bestehen die Proben im Wesentlichen aus polykristallinen, gleichkörnigen Aggregaten mit idiomorphen, homogenen und gleichmäßig verteilten Körnern ($10-50\,\mu m$). Das legt nahe, dass die Syntheseprodukte einen Gleichgewichtszustand widerspiegeln oder ihm zumindest nahe kommen.

In vielen Proben haben wir jedoch konzentrische Variationen des Ti/(Ti+Fe) Verhältnisses beobachtet (Kapitel 3). Ihre Bildung ist abhängig von dem verwendeten Ausgangsmaterial und wird wahrscheinlich durch die während des Experiments ablaufenden Redoxprozesse gesteuert. Syntheseprodukte aus Fe_2O_3+TiO_2-Mischungen zeigen normalerweise einen Anstieg von Ti/(Ti+Fe) hin zur Oberfläche der Probenpille. Aufgrund dessen entwickeln einphasige Proben eine konzentrische Phaseninhomogenität, während zweiphasige Proben Variationen der Phasenhäufigkeiten aufweisen, typischerweise die Bildung eines Ti-reichen monomineralischen Saumes. Im Gegensatz dazu zeigen Syntheseprodukte aus Fe°+TiO_2-Mischungen Fe-reiche Säume an der Pillenoberfläche. Dennoch wurde in jedem der Probenbereiche ein lokales Gleichgewicht erreicht.

Proben, die während des Abschreckvorgangs oxidierenden Bedingungen ausgesetzt waren, zeigen im Bereich der äußeren $100\,\mu m$ der Probenpille Oxidationsentmischungen im Sinne von Buddington & Lindsley (1964). Diese können sich innerhalb von weniger als 5 Sekunden bilden. Die Oxidation wirkt sich nicht auf die Phasenzusammensetzungen in der inneren Probenregion aus, geht aber mit einer Vergrößerung des Gesamt-Sauerstoffgehaltes der Probe einher.

Für eine Rekalibrierung des Fe-Ti-Thermo-Oxybarometers wurde der für Tmt+Ilm_{ss} bestehende Datensatz, der für die Kalibrierung der Modelle von Andersen & Lindsley (1988) und Ghiorso & Sack (1991) verwendet worden war, hin zu höheren Temperaturen und auf einen breiteren Sauerstofffugaziätsbereich erweitert. Die Zusammensetzungen der koexistierenden Fe-Ti-Oxid-Phasen im System Fe-Ti-O wurden mit Hilfe der Elektronenstrahlmikrosonde als Funktion von T und fO_2 bestimmt (Kapitel 4).

Die experimentellen Daten, die im Rahmen dieser Arbeit erzeugt wurden, wurden mit den existierenden Thermo-Oxybarometer Modellen von Andersen & Lindsley (1988, QUILF) und Ghiorso & Sack (1991) verglichen. Die Phasenumwandlung innerhalb der Ilmenit-Hematit Mischkristallreihe (von der geordneten $R\bar{3}$ zur ungeordneten $R\bar{3}c$ Struktur) verursacht eine abrupte Änderung in der Steigung der experimentell bestimmten Isothermen, die mit sinkender Temperatur zunehmend ausgeprägter wird. Andersen & Lindsley (1988) haben dieser Umwandlung nicht

Rechnung getragen, weshalb ihre Modell-Isothermen keinen entsprechenden Knick zeigen. Ghiorso & Sack (1991) berücksichtigen zwar die Umwandlung, allerdings beruht ihr Modell entscheidend auf älteren experimentellen Daten, zu denen Probenzusammensetzungen gehören, die nicht mit mikroanalytischen Methoden geprüft wurden.

Synthetische Tmt-Zusammensetzungen sind im Allgemeinen Ti-reicher als von den Modellen berechnet. Bei hohem fO_2 steht dies wahrscheinlich in Zusammenhang mit Fehlern in den verwendeten Werten für die thermodynamischen Eigenschaften der Tmt Endglieder. Bei niedrigem fO_2 und hohem T beruhen die starken Abweichungen zwischen synthetischem Tmt und den Modellen vermutlich auf unstöchiometrischem Tmt, also Tmt mit Kationenmangel.

Die Unstöchiometrie von Tmt wurde im System Fe-Ti-O bei 1100 °C bis 1300 °C untersucht. Tmt wurde in unterschiedlichen Paragenesen synthetisiert, für die maximale (Tmt+Ilm_{ss}) bzw. minimale (Tmt+Wus, Tmt+Fe) Leerstellenkonzentration erwartet wird (Kapitel 5).

Um die Leerstellen nachzuweisen und zu quantifizieren wurden drei Methoden angewendet: (1) Da der Einbau von Leerstellen bei konstantem Ti/(Ti+Fe) Verhältnis zu einer Verringerung der Größe der Einheitszelle führt, wurden die Gitterparameter mit Hilfe der Rietveld-Analyse bestimmt. (2) Bei konstantem Ti/(Ti+Fe) sind Kationenleerstellen mit höheren $Fe^{3+}/\Sigma Fe$-Werten verknüpft. Letztere wurden für ausgewählte Proben mittels Elektronen-Energieverlust-Spektroskopie bestimmt. (3) Tempern eines unstöchiometrischen Titanomagnetits bei niedrigeren Temperaturen (950 °C) unter Sauerstoffabschluss führt zur Ausheilung der Leerstellen. Dies geht mit Änderungen der Phasenzusammensetzungen einher, was wiederum zu Bildung von Ilm_{ss}-Entmischungslamellen und -Säumen in Tmt, also zu einer Vergrößerung des Ilm_{ss} Anteils, führt.

Die Ergebnisse der drei Methoden weisen darauf hin, dass mit Ilm_{ss} koexistierender Tmt für $X_{Usp}<0.7$ bei allen untersuchten Temperaturen nur niedrige Leerstellenkonzentrationen hat oder nahe an der stöchiometrischen Zusammensetzung ist. Für X_{Usp} steigt die Leerstellenkonzentration mit zunehmendem Ti-Gehalt und zunehmender Temperatur auf etwa 2 Kationenprozent für 1300 °C und X_{Usp} nahe 1. Für $T\leq 1100$ °C, also bei Temperaturen die für die Kristallisationsbedingungen basaltischer Gesteine relevant sind, ist Tmt bei allen Zusammensetzungen nahezu stöchiometrisch. Da die revidierte Fassung des Tmt-Ilm_{ss} Thermo-Oxybarometers auch Hochtemperatur-Kalibrierungsdaten mit einbeziehen wird, ist es wichtig, in den enthaltenen Mischungsmodellen der Tmt-Unstöchiometrie Rechnung zu tragen.

Um sich natürlichen Zusammensetzungen anzunähern, wurden auch im System Fe-Ti-Mg-Al-O Tmt-Ilm_{ss} Proben hergestellt (Kapitel 6). Für einen Vergleich zum System Fe-Ti-O wurden die Mg-Al-haltigen Fe-Ti-Oxid-Zusammensetzungen in die binären Systeme Ilm-Hem und Mag-Usp projiziert. X'_{Usp} und X'_{Ilm} der Mg-Al haltigen Phasen stimmen im Wesentlichen mit den Daten im System Fe-Ti-O überein. Daher können die für das einfache System Fe-Ti-O bestimmten Isothermen prinzipiell auch auf Mg-Al-haltige Proben angewendet werden. Dies liefert eine neue, vorläufige und graphische Version des Thermo-Oxybarometers, die an experimentellen Daten von Toplis & Carroll (1995) getestet wurde. Verglichen mit den T-fO_2-Abschätzungen der vorherigen Modelle bringt das neue, graphische Thermo-Oxybarometer insbesondere in den Temperaturabschätzungen eine signifikante Verbesserung.

1 Introduction

1.1 A short presentation of Fe-Ti oxide minerals and their significance

The iron-titanium (Fe-Ti) oxide minerals are of great significance for petrology. Though they generally occur in accessory abundances, they are ubiquitous in both metamorphic and igneous rocks of the Earth's crust, in the Earth's mantle as well as in lunar and martian basalts and meteorites.

Fe-Ti oxides incorporate iron as both ferrous and ferric ions, which makes them sensible redox indicators. The distribution of Fe^{2+}, Fe^{3+} and Ti between coexisting Fe-Ti oxides (e.g. between titanomagnetite and ilmenite$_{ss}$, or ilmenite$_{ss}$ and pseudobrookite$_{ss}$) is a function of temperature (T) and oxygen fugacity (fO_2). Consequently, coexisting Fe-Ti oxides can yield thermo-barometric information (e.g. Buddington & Lindsley, 1964). Further, Fe-Ti oxides are the major carriers of rock magnetism.

The Fe-Ti oxides have been studied extensively since the early 20th century under different points of view, for example to answer crystallographic and crystal chemical, petrologic or geomagnetic questions (e.g. Verwey, 1939; Néel, 1948; Chevallier *et al.*, 1955; Ramdohr, 1955; Akimoto, 1962; Taylor, 1964; Buddington & Lindsley, 1964; O'Reilly, 1984; Wechsler *et al.*, 1984; Dunlop & Özdemir, 1997).

Among the phases in the system Fe-Ti-O, three Fe-Ti oxide solid solution series are of special interest for natural rocks and within this study (Fig. 1.1). These are the cubic titanomagnetite (Tmt), the rhombohedral ilmenite-hematite (Ilm$_{ss}$), and the orthorhombic $Fe_2TiO_5 - FeTi_2O_5$ (Psb$_{ss}$) solid solution series (Table 1.1, for all abbreviations also see appendix, Table A.1).

Magnetic properties of Fe-Ti oxide phases Despite their low modal abundances, Fe-Ti oxides (e.g. Tmt, Ilm$_{ss}$, see Table 1.1) are the major carriers of rock magnetism (O'Reilly, 1984; Banerjee, 1991; Dunlop & Özdemir, 1997). The magnetic order of these phases depends on temperature and composition.

The Curie temperature (T_C) marks the transition from a paramagnetic (at high T) to a ferrimagnetic state. In magnetite it occurs at 575 to 585 °C (Hunt *et al.*, 1995, and references therein). The Curie temperature of Tmt decreases with increasing Ti-content (transition temperature of Usp: −153 °C).

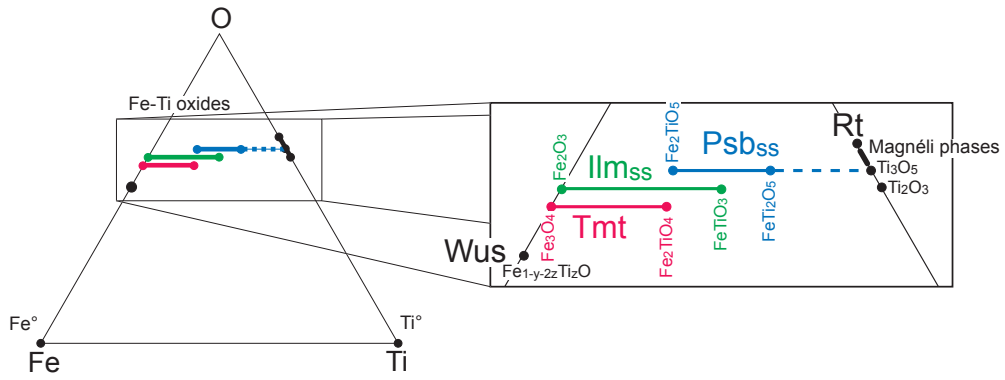

Fig. 1.1 Phases occurring in the system Fe-Ti-O, schematically presented in the Fe-Ti-O triangle. Phases occurring are metallic iron (Fe°) and titanium (Ti°), iron oxide phases (wüstite (Wus), magnetite, hematite), titanium oxide phases (rutile (Rt) and the Magnéli phases (Ti_nO_{2n-1}, $4 \leqslant n \leqslant 9$), anosovite ($Ti_3O_5$), and Ti_2O_3), and mixed iron-titanium oxide phases. The latter are Tmt, Ilm_{ss}, and Psb_{ss} (Table 1.1).

Table 1.1 Fe-Ti oxide solid solution series

general name	**abbr.**	**solid solution endmembers**	**formula**
titanomagnetite	Tmt	magnetite Fe_3O_4 - ulvöspinel Fe_2TiO_4	$(Fe_{1-x}Ti_x)_3O_4$[a]
$ilmenite_{ss}$	Ilm_{ss}	hematite Fe_2O_3 - ilmenite $FeTiO_3$	$(Fe_{1-x}Ti_x)_2O_3$[a]
$pseudobrookite_{ss}$	Psb_{ss}	pseudobrookite Fe_2TiO_5 - $FeTi_2O_5$[b]	$(Fe_{1-x}Ti_x)_3O_5$[a]

a) x is Ti/(Ti+Fe) in the phase
b) "ferropseudobrookite", name discredited by IMA Commission on New Minerals and Mineral Names (CNMMN)

The Curie temperature of titanomagnetite can be used to estimate its composition (e.g. Akimoto *et al.*, 1958; Kontny *et al.*, 2003). This is especially useful when Tmt grains cannot be analysed by the electron microprobe (e.g. due to small grain size, dendritic grains or fine intergrowths with another phase).

The permanent magnetism of minerals allows a study of the Earth's ancient magnetic field (i.e. palaeomagnetism). Magnetic minerals are "microscopic fossile 'compasses'", also providing information on plate motions (from Dunlop & Özdemir, 1997).

The Tmt-Ilm_{ss} thermo-oxybarometer The Tmt-Ilm_{ss} oxide thermo-oxybarometer can be used to derive temperature and oxygen fugacity that prevailed during crystallisation or re-equilibration of a Tmt-Ilm_{ss} assemblage. It is an important tool to retrieve information, for example on fluid movement in and redox states

of the Earth's mantle, processes in magma chambers or crystallisation conditions of lunar and martian basalts (e.g. Carmichael, 1967; Frost, 1991; Frost & Lindsley, 1991; Ghiorso & Sack, 1991; Haggerty, 1991b; Harlov, 1992; Evans & Scaillet, 1997; Scaillet & Evans, 1999; Herd *et al.*, 2001, 2002; Xirouchakis *et al.*, 2002; Devine *et al.*, 2003).

In 1964, Buddington & Lindsley introduced the original version of the Fe-Ti oxide thermo-oxybarometer and presented a graphical solution. During the following years, a lot of further development has been carried out by several authors (e.g. Lindsley & Podpora, 1983; Andersen & Lindsley, 1988, see section 1.3).

At present, there are two broadly used thermodynamic formulations of the thermo-oxybarometer: These are (I) the formulation which is incorporated in the QUILF package (Andersen & Lindsley, 1988; Lindsley & Frost, 1992; Frost & Lindsley, 1992; Andersen *et al.*, 1993) and (II) the model supplied by Ghiorso & Sack (1991).

These formulations have yielded a wealth of reasonable thermo-barometric estimates on different volcanic suites (e.g. Ghiorso & Sack, 1991; Frost & Lindsley, 1992). However, their application does not always give satisfactory results (both regarding temperature and oxygen fugacity estimation), as is seen for example by comparison to experimental data (see section 1.3). Therefore a further development of the Fe-Ti oxide thermo-oxybarometer model is necessary.

The shortcomings of the thermo-oxybarometer models result from combined effects of weaknesses concerning the underlying data and models (see sections 1.2 and 1.3 for more details). In a future version of the Tmt-Ilm_{ss} thermo-oxybarometer, these points will have to be accounted for. For this purpose, experimental data is required in several respects: The existing calibration data set lacks data for temperatures above 1000 °C, and also for oxygen fugacities significantly above or below the FMQ (fayalite-magnetite-quartz) buffer equilibrium. Additional experimental data at these conditions are required and are provided by the present thesis. Further, experimental investigation of the effect of minor elements like Mg, Mn and Al is supplied in order to contribute to an improvement of Fe-Ti oxide solid solution models.

The Ilm_{ss}-Psb_{ss} thermo-oxybarometer Not only the Tmt-Ilm_{ss} assemblage but also the Ilm_{ss}-Psb_{ss} assemblage can be used to estimate temperature and especially oxygen fugacity. The Ilm_{ss}-Psb_{ss} (thermo-)oxybarometer can be applied for example in oxidised terrestrial igneous rocks (Frost & Lindsley, 1991; Haggerty, 1991a), moderately reduced assemblages in mantle xenoliths (Haggerty, 1991b) or strongly reduced lunar assemblages (e.g. El Goresy *et al.*, 1974; El Goresy & Woermann,

1977). A preliminary calibration of the Ilm_{ss}-Psb_{ss} thermo-oxybarometer (based on thermodynamic data) has been provided by Anovitz *et al.* (1985), but the experimental data needed for a more comprehensive calibration are still missing. It is one aim of this study to close this gap and supply the required data.

This thesis provides experimental data on Fe-Ti distribution between coexisting Fe-Ti oxides (both Tmt+Ilm_{ss} and Ilm_{ss}+Psb_{ss}) in the system Fe-Ti$\pm$Mg$\pm$Al-O at 1000 °C to 1300 °C and a large range of oxygen fugacities (5 magnitudes below to 5 magnitudes above the Ni-NiO buffer equilibrium).

For this purpose, synthesis and re-equilibration experiments have been carried out at atmospheric pressure and under subsolidus conditions to produce binary Fe-Ti oxide assemblages (Ilm_{ss}+Psb_{ss}, Tmt+Ilm_{ss}). X-ray diffraction analysis has been used to characterise the synthesised phases. The samples have been investigated with a scanning electron microscope (SEM) to examine phase distribution and textures. Phase compositions have been determined by electron microprobe (EMP) analysis.

The results of synthesis and re-equilibration experiments during this study suggest that part of the shortcomings of the thermo-oxybarometer formulations - at low fO_2 and high T - are due to cation-deficient Tmt. Therefore it is desirable to include Tmt non-stoichiometry in the Tmt-Ilm_{ss} thermo-oxybarometer formulation. For this purpose a data set on Tmt non-stoichiometry as a function of oxygen fugacity, temperature and composition is required. Within this thesis different approaches to quantify Tmt non-stoichiometry are used (e.g. determination of $Fe^{3+}/\sum Fe$ by electron energy-loss spectroscopy, lattice parameter determination).

By supplying extensive experimental data on Fe-Ti distribution between Fe-Ti oxides and by providing data on the effect of minor elements and on non-stoichiometry, this thesis intends to pave the way for improved versions of the Fe-Ti oxide (thermo-)oxybarometer formulations. Regarding the Tmt-Ilm_{ss} thermo-oxybarometer, a further development of the thermodynamic modelling by Mark S. Ghiorso (Seattle) under incorporation of new experimental data (this thesis, Lattard *et al.*, 2005; Evans *et al.*, in press; Harrison *et al.*, 2000, and others) is in progress.

1.2 State of the art: crystalline phases in the system Fe-Ti-O

1.2.1 A general introduction to relevant Fe-Ti oxide phases: chemistry, structure and stability

In natural rocks, Fe-Ti oxides are generally present as accessory minerals and coexist with silicate phases. The Fe-Ti oxide assemblage that occurs in a rock, and the compositions of involved oxide phases are related to temperature and oxygen fugacity prevailing during rock formation or re-equilibration.

While natural systems are complex (involving a number of minor elements like Mg, Al, Mn, Cr, Nb etc.), the simple system Fe-Ti-O offers a valid simplification for phase relations and compositions of Fe-Ti oxide phases in natural rocks. Therefore, the experimental investigations within the present thesis will focus on the simple system Fe-Ti-O and also consider the systems Fe-Ti-Mg-O, Fe-Ti-Al-O, and Fe-Ti-Mg-Al-O.

In nature, titanomagnetite and ilmenite$_{ss}$ are the most common Fe-Ti oxides. Dependent on temperature, oxygen fugacity and bulk chemistry, they may coexist with each other or with Psb$_{ss}$, rutile, wüstite, or metallic iron in binary and ternary assemblages (cf. Fig. 1.2a). The system Fe-Ti-O further includes anosovite (Ti_3O_5), Ti_2O_3, the Magnéli phases (Ti_nO_{2n-1}, $4 \leqslant n \leqslant 9$), and metallic titanium (see section 1.1, Fig. 1.1). At temperatures $< 300\,^{\circ}C$ titanomaghemite (Tmh, a cation-deficient spinel phase) forms as a low-temperature oxidation product of titanomagnetite.

Exchange reactions along Fe-Ti oxide solid solution series All three Fe-Ti oxide solid solution series - titanomagnetite, ilmenite$_{ss}$ and pseudobrookite$_{ss}$ - are governed by the "ilmenite substitution" $2Fe^{3+} \leftrightarrow Fe^{2+} + Ti^{4+}$. Additionally, in the orthorhombic Psb$_{ss}$ series the exchange reaction $2Ti^{3+} \leftrightarrow Fe^{2+} + Ti^{4+}$ occurs at high T and low fO_2 towards the Ti endmember Ti_3O_5. Both exchange reactions influence the cationic ratio Ti/(Ti+Fe) in the concerning minerals, whereas the oxygen content (i.e. cation/oxygen ratio) remains constant.

Non-stoichiometry in Fe-Ti oxide phases A variation in the cation/oxygen ratio (i.e. non-stoichiometry) of a phase (e.g. Tmt) produces a broadening of the single-phase field towards the oxygen apex (cation deficiency) or the Fe-Ti base of the triangle (cation excess), as is schematised in Fig. 1.2b. This results in a definite but limited phase width at any given cationic ratio.

A cation-deficient Fe-Ti oxide phase has a higher oxygen content compared to its stoichiometric analogue. At given cationic ratio Ti/(Ti+Fe) the cation-deficient phase occurs at higher oxygen fugacity than a stoichiometric or cation excess phase.

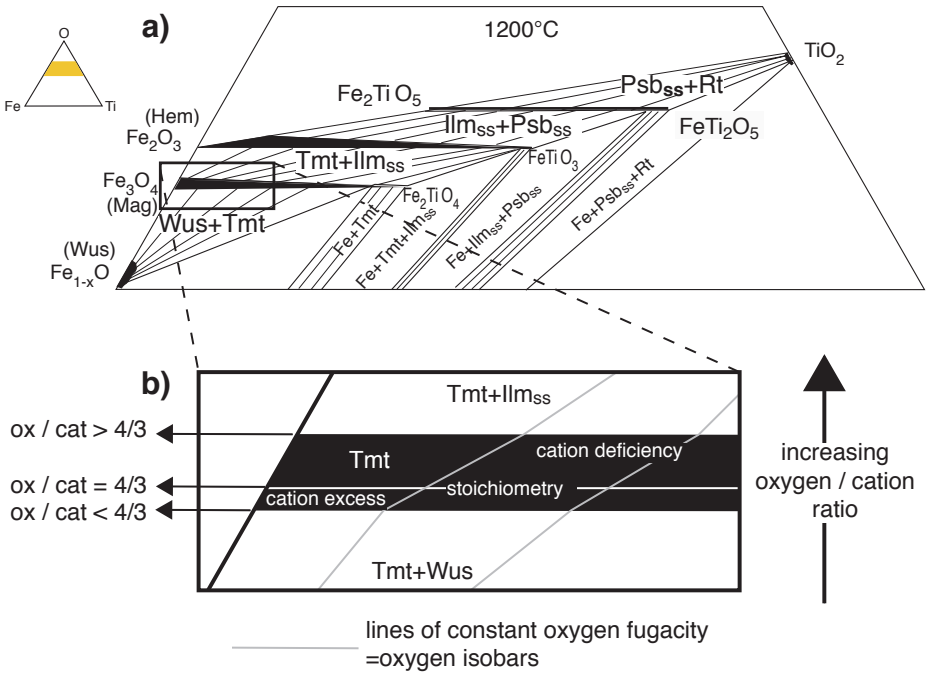

Fig. 1.2 a) Schematic phase relations in the Fe-Ti-O system at 1200 °C and 1 bar illustrated in the Fe-Ti-O triangle (modified after Grey *et al.*, 1974; Grey & Merritt, 1981). Phase relations at very low fO_2 have been omitted (cf. Grey & Merritt, 1981). b) Schematic illustration of non-stoichiometry in Tmt in the system Fe-Ti-O, enlargement near Tmt single-phase field. Height of the Tmt phase field is exaggerated and is assumed to be constant over the Tmt solid solution series.

From a crystallographic point of view, a variation in oxygen content of a phase at given cationic ratio (Ti/(Ti+Fe)) can be achieved by cation or anion interstitials, or cation or anion vacancies. However, anion defects (i.e. oxygen defects) are not relevant to Fe-Ti oxides (for Tmt: Dieckmann, 1982; Aragón & McCallister, 1982).

For the formation of cation vacancies and cation interstitials, several exchange reactions are conceivable (equations 1.1, 1.2, 1.3, 1.4, M denotes a cation on a regularly occupied site, I denotes an interstitial ion, □ represents a cation vacancy). Tmt non-stoichiometry will be treated in more detail in section 1.2.3, pages 13 et sqq.

$$2Fe^{2+} \leftrightarrow Ti^{4+} + \square \tag{1.1}$$

$$3Fe^{2+} \leftrightarrow 2Fe^{3+} + \square \tag{1.2}$$

$$Ti_M^{4+} \leftrightarrow Fe_M^{2+} + Fe_I^{2+} \tag{1.3}$$

$$2Fe_M^{3+} \leftrightarrow 2Fe_M^{2+} + Fe_I^{2+} \tag{1.4}$$

Phase relations in dependence of temperature and oxygen fugacity Phase relations and compositions in the system Fe-Ti-O are a function of temperature (T), oxygen fugacity (fO_2), pressure (P) and bulk composition (X). This study is restricted to atmospheric pressure. Triangular plots generally refer to one fixed temperature.

According to the Gibbs phase rule, in a ternary system such as the system Fe-Ti-O, three phases of fixed composition coexist in a divariant equilibrium (variables: P, T). At given temperature and pressure, the oxygen fugacity of a ternary assemblage is fixed. In binary parageneses (e.g. Tmt-Ilm_{ss} and Ilm_{ss}-Psb_{ss}) the number of components is reduced. Binary assemblages are stable over a wide range of fO_2-P-X conditions (Fig. 1.2a).

At a given pressure, temperature and oxygen fugacity (i.e. along one oxygen isobar, Fig. 1.3), the phase assemblage is determined by the cationic ratio Ti/(Ti+Fe). With increasing Ti/(Ti+Fe), increasingly oxygen rich assemblages occur under identical T-fO_2 conditions.

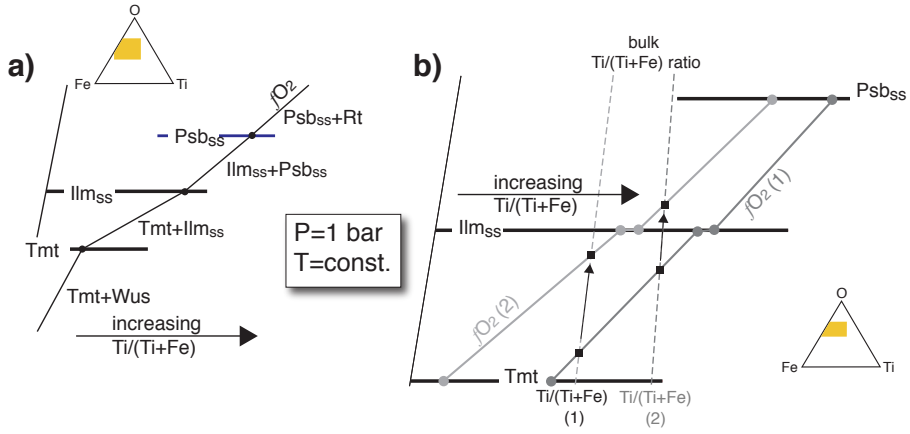

Fig. 1.3 a) Exemplary plot of an oxygen isobar within the triangle Fe-Ti-O crossing several different phase fields. b) Compositions of coexisting Fe-Ti oxides (circles) connected by two oxyisobars (grey diagonal lines, $fO_2(1)<fO_2(2)$), schematically illustrated in the triangle Fe-Ti-O. At given cationic ratio (dashed lines) an oxidation results in a shift of sample bulk (squares) towards the oxygen apex (arrows). Horizontal lines represent the Fe-Ti oxide solid solution series (Tmt, Ilm_{ss}, Psb_{ss}).

At a given cationic ratio Ti/(Ti+Fe) the oxygen content of the sample bulk increases with increasing oxygen fugacity. Within one two-phase field, this is accomplished by a shift of phase proportions and a shift of phase compositions towards higher Fe-contents (Fig. 1.3b). Larger changes in oxygen fugacities result in increasingly oxygen-rich assemblages with increasing fO_2 (Fig. 1.3b).

Within a two-phase field, the compositions of both participating phases (Fe-Ti oxide solid solutions) shift towards the Fe-rich endmembers with increasing oxygen fugacity (Fig. 1.3, Fig. 1.4a). This comes along with an oxidation of Fe^{2+} to Fe^{3+} and (for a given cationic ratio Ti/(Ti+Fe)) involves an increase of the proportion of the more oxidised phase (e.g. Ilm_{ss} in a Tmt+Ilm_{ss} sample).

The distribution of Fe and Ti between coexisting Fe-Ti oxides gets more random with increasing temperature. Therefore, the conodes between coexisting Fe-Ti oxides in the Fe-Ti-O triangle become steeper with increasing temperature (Fig. 1.4b).

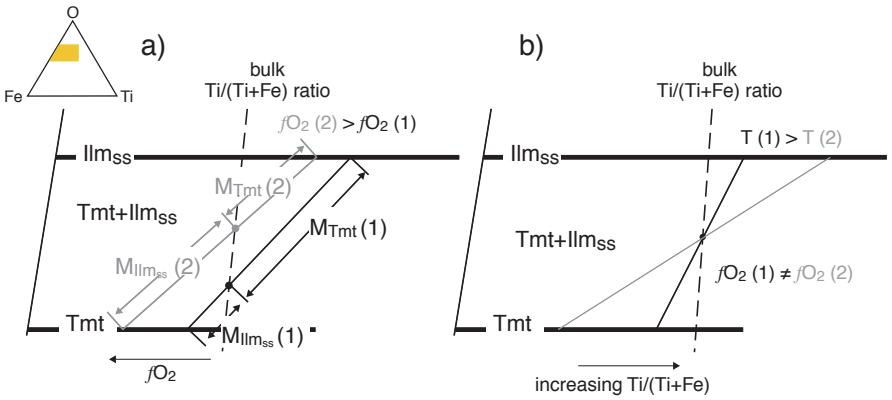

Fig. 1.4 Effect of a) oxidation and b) temperature change on binary Fe-Ti oxide assemblage of fixed bulk cationic ratio Ti/(Ti+Fe), schematised in the Fe-Ti-O triangle. a) Shown are two exemplary conodes for two different oxygen fugacities ($fO_2(2)$ (grey conode) > $fO_2(1)$ (black conode)). M (e.g. $M_{Tmt}(2)$, $M_{Tmt}(1)$) is the modal proportion of the phase within the assemblage. (b): Bulk Ti/(Ti+Fe) *and* oxygen content are constant. Shown are conodes for two different temperatures. Note that *sample bulk* is constant, not *oxygen fugacity*.

To understand the behaviour and properties of Fe-Ti oxide phases, knowledge of their crystal structure and stability is required. In this chapter, a short description of the phases relevant for this study will be provided. The phases will be treated in order of increasing oxygen content.

1.2.2 Wüstite

Wüstite (Wus, $Fe_{1-y-2z}Ti_zO$) has the NaCl structure. Ideally, if the composition was stoichiometric (Fe_1O_1), Fe^{2+} ions would occupy all of the octahedral sites within a cubic close packed arrangement of oxygens, leaving the tetrahedral sites unoccupied. However, wüstite is apparently always non-stoichiometric (Lindsley, 1991) with Fe^{3+} substituting for part of the Fe^{2+} on octahedral sites (reaction 1.5) or filling ideally unoccupied tetrahedral sites (reaction 1.6). For charge balancing reasons, this involves the formation of cation vacant octahedral sites.

$$3Fe^{2+}_{oct} \leftrightarrow 2Fe^{3+}_{oct} + \square_{oct} \tag{1.5}$$

$$3Fe^{2+}_{oct} + 2\square_{tet} \leftrightarrow 2Fe^{3+}_{tet} + 3\square_{oct} \tag{1.6}$$

Although wüstite is generally considered to be a Fe oxide rather than a Fe-Ti oxide, limited amounts of Ti (about 8.5 mol% TiO_2 at 1300 °C, Simons & Woermann, 1978) can be incorporated into the wüstite structure at high temperatures, according to reaction 1.7. However, Ti-"rich" wüstite cannot be quenched to room temperature (Simons & Woermann, 1978; Senderov *et al.*, 1993; Sauerzapf *et al.*, 2005).

$$2Fe^{2+} \leftrightarrow Ti^{4+} + \square \tag{1.7}$$

1.2.3 Titanomagnetite

The term titanomagnetite (general formula $(Fe_{1\text{-}x}Ti_x)_3O_4$ for *stoichiometric* Tmt) refers to the *cubic spinel solid solution series* between magnetite (Fe_3O_4, Mag) and ulvöspinel (Fe_2TiO_4, Usp). Both endmembers and all intermediate compositions are inverse spinels (Waychunas, 1991).

Spinel has the general formula AB_2O_4. The spinel structure is based on a cubic close packing of oxygens with A and B cations of different valence state occupying one eighth of the tetrahedral sites and half of the octahedral sites (e.g. Lindsley, 1976; Fleet, 1981, 1982; O'Neill & Navrotsky, 1983, 1984, see Fig. 1.5). In *normal spinels*, B cations occupy octahedral sites and A cations the tetrahedral sites, i.e. the formula can be written as $(A)[B]_2O_4$ (): tetrahedral sites, []: octahedral sites). In *inverse spinels*, half of the B cations occupy tetrahedral sites. The A ions as well as the other half of the B ions are distributed randomly on the octahedral sites: $(B)[AB]O_4$.

Consequently, in the inverse spinel mineral magnetite $(Fe^{3+})[Fe^{2+}Fe^{3+}]O_4$, Fe^{3+} occupies the tetrahedral sites, and Fe^{2+} and Fe^{3+} are situated on the edge-sharing octahedral sites. Electron hopping between Fe^{2+} and Fe^{3+} on octahedral sites results in the high electrical conductivity of magnetite at $T > 120\,K$. At $T < 120\,K$

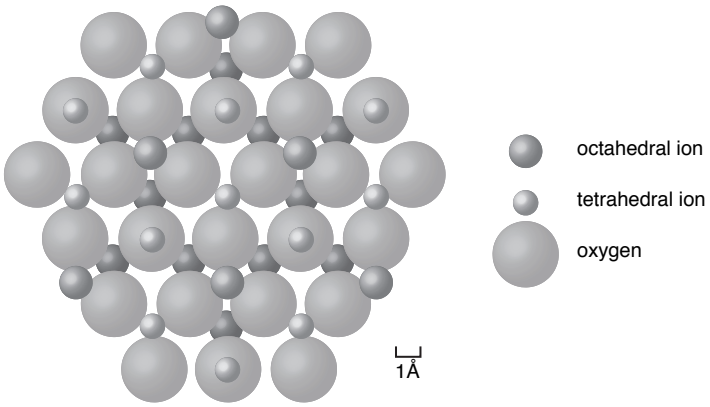

Fig. 1.5 Schematic illustration of the spinel structure projected onto the (111) plane after Klein & Hurlbut (1993). The circles represent octahedral, tetrahedral and oxygen ions. Shown is one cubic close packed oxygen layer and the cation layers on either side of it.

(Verwey temperature of magnetite) electron hopping is inhibited and Fe^{2+} and Fe^{3+} are ordered within the octahedral sites resulting in a decrease in symmetry (from cubic to monoclinic) and electrical conductivity (e.g. Verwey, 1939; Zuo *et al.*, 1990).

Ulvöspinel $(Fe^{2+})[Fe^{2+}Ti^{4+}]O_4$ is also an inverse spinel. Fe^{2+} occupies the tetrahedral sites and Fe^{2+} and Ti^{4+} are randomly distributed over octahedral sites. Only few studies have reported significant amounts of Ti^{4+} on tetrahedral sites (e.g. Forster & Hall, 1965; Gorter, 1957), while other author did not find any evidence for tetrahedral Ti^{4+} (Stephenson, 1969; O'Reilly & Banerjee, 1965; Ishikawa *et al.*, 1964, reported by Bleil, 1976). It is now general consensus that Ti^{4+} is restricted to octahedral sites (e.g. Trestman-Matts *et al.*, 1983).

Titanomagnetite miscibility gap At temperatures $>800\,^{\circ}C$ (i.e. temperatures relevant for experiments reported in the following chapters) the titanomagnetite solid solution is continuous between magnetite and ulvöspinel. At T below about $600\,^{\circ}C$ to $800\,^{\circ}C$ however, there is a miscibility gap (e.g. Vincent *et al.*, 1957; Lindsley, 1981; Price, 1981, Fig. 1.6). The solvus has been examined experimentally by Vincent *et al.* (1957); Lindsley (1981); Price (1981) and calculated by Trestman-Matts *et al.* (1983) and O'Neill & Navrotsky (1984). Vincent *et al.* (1957) reported an asymmetric solvus. The results of Lindsley (1981) are in general agreement with the previous work by Vincent *et al.* (1957). The low consolute temperature reported by Price (1981) is most probably due to small amounts of Mg in the natural samples he used (see Lindsley, 1981). Except for O'Neill & Navrotsky (1984), all authors sug-

gest a consolute temperature of <600 °C. O'Neill & Navrotsky (1984) in contrast have calculated solvi that reach up to about 760 °C.

While Trestman-Matts *et al.* (1983) obtain a solvus that shifts towards Fe_2TiO_4 with decreasing temperature, the solvus after O'Neill & Navrotsky (1984) shifts towards Fe_3O_4. Trestman-Matts *et al.* (1983) state that "at the present time the precise shape of the solvus has not been established" (also referring to the then unpublished but prepared paper by O'Neill & Navrotsky (1984)). Quenching from temperatures above the consolute temperature is rapid enough to conserve a homogeneous titanomagnetite (Lindsley, 1981).

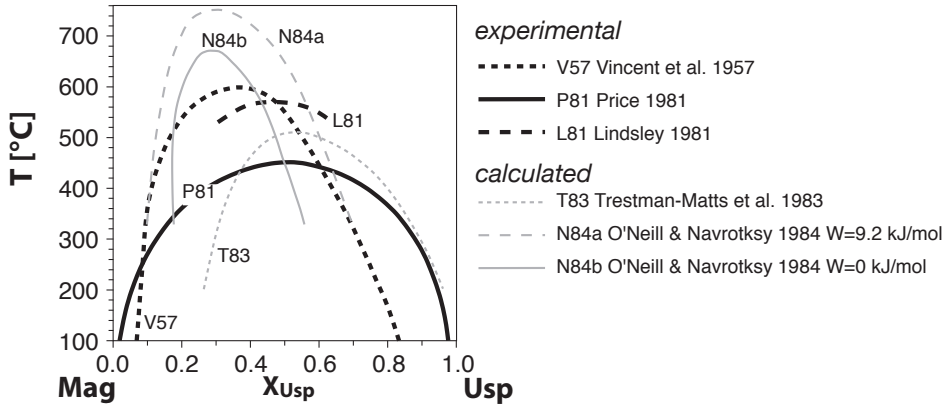

Fig. 1.6 Solvus within the titanomagnetite solid solution series according to Lindsley (1981), Price (1981) and Vincent *et al.* (1957) (black lines, experimental data), and Trestman-Matts *et al.* (1983) and O'Neill & Navrotsky (1984) (grey lines, calculated).

Titanomagnetite cation distribution models If it is assumed that Ti is fixed to the octahedral sites of the spinel structure along the Tmt solid solution series, a change in Tmt cation distribution involves only an electron transfer between the tetrahedral and octahedral sites. While the equilibrium cation distribution is temperature dependent (in-situ measurements by Trestman-Matts *et al.*, 1983), it cannot be quenched to room temperature (O'Neill & Navrotsky, 1984; Jensen & Shive, 1973).

This is in agreement with X-ray and neutron diffraction, as well as magnetic measurements on *quenched* Tmt annealed at different temperatures, which detected no difference in cation distribution for different synthesis or annealing temperatures (e.g. O'Donovan & O'Reilly, 1980; Wechsler *et al.*, 1981, 1984). However, earlier work on the basis of saturation magnetization measurements (Stephenson,

1969; Bleil, 1971, 1976) suggested that the cation distribution depended on synthesis temperature and that it is preserved during quenching. These studies may have been complicated by imperfect control of Tmt stoichiometry (O'Neill & Navrotsky, 1984).

Trestman-Matts *et al.* (1983) suggest that - though "true high temperature distributions are most likely not quenchable" - "the rate of cooling through the range 300 °C to room temperature ... could play a significant role in what distribution is retained". The results of Stephenson (1969), Bleil (1971) and Bleil (1976) may thus also be explained by different quench rates.

For the cation distribution between octahedral and tetrahedral sites along the stoichiometric titanomagnetite solid solution join ($(Fe_{1-x}Ti_x)_3O_4$, x=Ti/(Ti+Fe)) several models have been proposed (e.g. Akimoto, 1954; Néel, 1955; Chevallier *et al.*, 1955; O'Reilly & Banerjee, 1965; Trestman-Matts *et al.*, 1983; O'Neill & Navrotsky, 1984). The older models by Akimoto (1954); Néel (1955); Chevallier *et al.* (1955) and O'Reilly & Banerjee (1965) did not account for a temperature-dependence of the cation distribution.

1) The **Akimoto (1954) model** (Fig. 1.7a) results from application of the substitution reaction $Fe^{3+}_{tet}Fe^{3+}_{oct} \leftrightarrow Fe^{2+}_{tet}Ti^{4+}_{oct}$. Both octahedral and tetrahedral sites are involved in this exchange over the complete compositional (i.e. X_{Usp}) range.

2) The **Néel (1955) - Chevallier *et al.* (1955) model** (Fig. 1.7b) accounts for the tetrahedral site preference of Fe^{3+} and octahedral site preference of Fe^{2+}. At X_{Usp}<0.5 Fe^{2+} substitutes for octahedral Fe^{3+} until the latter is used up (at X_{Usp}=0.5). This means that at $X_{Usp} < 0.5$ the tetrahedral sites are not involved in the exchange reaction, which can be described as $2Fe^{3+}_{oct} \leftrightarrow Fe^{2+}_{oct}Ti^{4+}_{oct}$. At $X_{Usp} > 0.5$ however, simultaneous exchange of Fe^{2+} vs. Fe^{3+} on tetrahedral sites and Ti^{4+} vs. Fe^{2+} on octahedral sites results in an overall exchange reaction $2Fe^{3+}_{tet}Fe^{2+}_{oct} \leftrightarrow 2Fe^{2+}_{tet}Ti^{4+}_{oct}$, i.e. a global $2Fe^{3+} \leftrightarrow Fe^{2+}Ti^{4+}$.

3) The **O'Reilly & Banerjee (1965) model** (Fig. 1.7c) is a combination of the former models, being identical to the Néel (1955) - Chevallier *et al.* (1955) model at $X_{Usp} \leq 0.2$ and $X_{Usp} \geq 0.8$, and following the Akimoto (1954) model for intermediate compositions. According to this model, the cation distribution along Tmt deviates from linear behaviour at $X_{Usp} = 0.2$ and $X_{Usp} = 0.8$. Such deviations have also been observed in investigations of lattice parameter and saturation moment as a function of X_{Usp} (cf. Lindsley, 1976, and references therein).

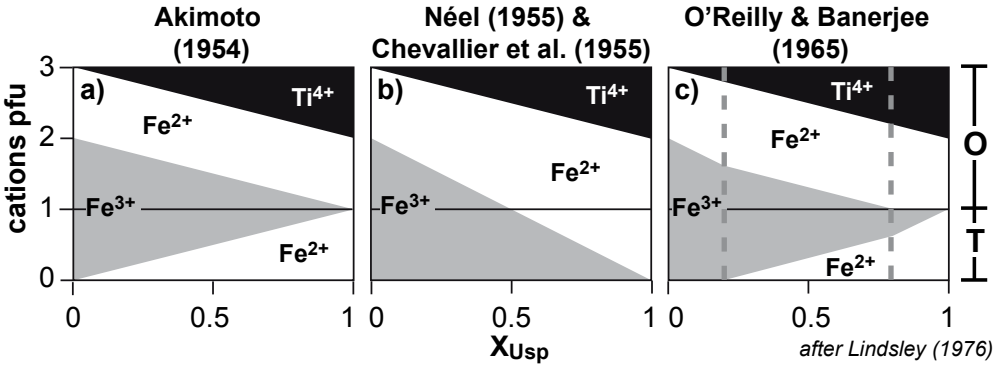

Fig. 1.7 Distribution of Ti^{4+} (black), Fe^{2+} (white) and Fe^{3+} (grey) (as cations pfu) on octahedral (O) and tetrahedral (T) sites of spinel along the titanomagnetite solid solution join according to the models by a) Akimoto (1954), b) Néel (1955) and Chevallier *et al.* (1955) and c) O'Reilly & Banerjee (1965). The horizontal line at 1 cation pfu separates octahedral from tetrahedral sites. The dashed grey lines in (c) mark X_{Usp}=0.2 and X_{Usp}=0.8.

4) Based on thermoelectric coefficient measurements **Trestman-Matts *et al.* (1983)** and Wu & Mason (1981, for Mag) derived a cation distribution of Tmt, which is dependent on synthesis temperature (Fig. 1.8). According to this approach, the cation distribution basically matches the Néel (1955) - Chevallier *et al.* (1955) model at T=0 K, the O'Reilly & Banerjee (1965) model at room temperature, and the Akimoto (1954) model at about 300 °C. In contrast to the three previous models, the Trestman-Matts *et al.* (1983) model assumes some ferrous iron on tetrahedral sites also for the magnetite endmember. The amount of tetrahedral Fe^{2+} increases with increasing temperature. The temperature dependence of the amount of tetrahedral Fe^{3+} decreases with increasing temperature and ulvöspinel content (Fig. 1.9).

High-temperature titanomagnetite non-stoichiometry As described on page 5 the composition of Tmt can deviate from stoichiometric oxygen/cation ratio (i.e. from 4/3). Previous studies (Dieckmann, 1982; Aragón & McCallister, 1982) suggest that in non-stoichiometric Tmt the oxygen lattice remains intact, and that cation vacancies or interstitials are responsible for a decreased or increased cation/oxygen ratio, respectively. Cation vacancies are presumed on octahedral sites of the Tmt structure (Wechsler *et al.*, 1984). The highest cat/O ratio of Tmt is expected for Tmt coexisting with a Ti-O-poorer phase, thus with Wus or metallic Fe°. The lowest cat/O ratio is expected for Tmt in coexistence with a Ti-/O-richer phase, i.e. Tmt+Ilm_{ss} (cf. Fig. 1.2b). Stoichiometric Tmt is expected within the Tmt single-

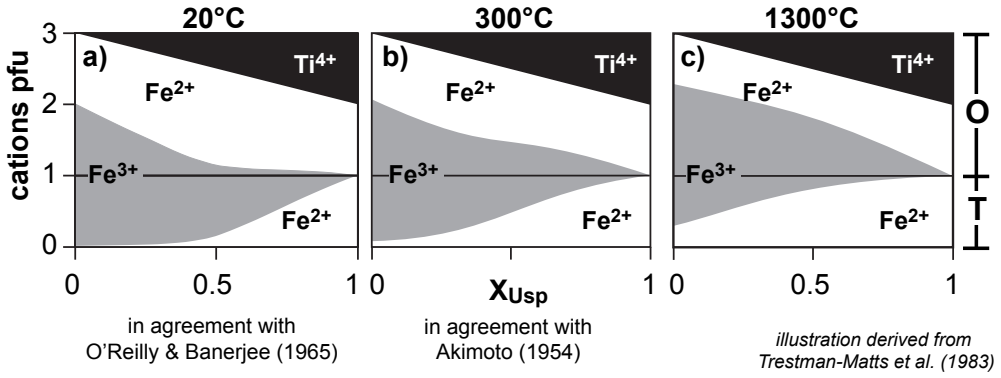

Fig. 1.8 Distribution of Ti^{4+} (black), Fe^{2+} (white) and Fe^{3+} (grey) (as cations pfu) on octahedral (O) and tetrahedral (T) sites of spinel along the titanomagnetite solid solution join according to the model by Trestman-Matts *et al.* (1983) at 20 °C, 300 °C, and 1300 °C. The horizontal line at 1 cation pfu separates octahedral from tetrahedral sites.

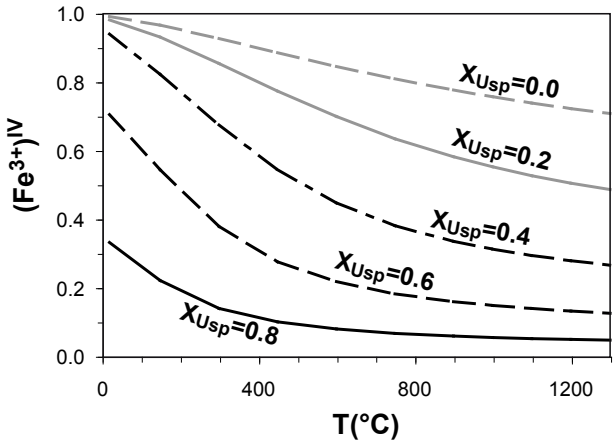

Fig. 1.9 The temperature dependence of Fe^{3+} in tetrahedral sites for different X_{Usp} after Trestman-Matts *et al.* (1983). $(Fe^{3+})^{IV}$ is equal to ordering parameter b according to Trestman-Matts *et al.* (1983), equation 1.10.

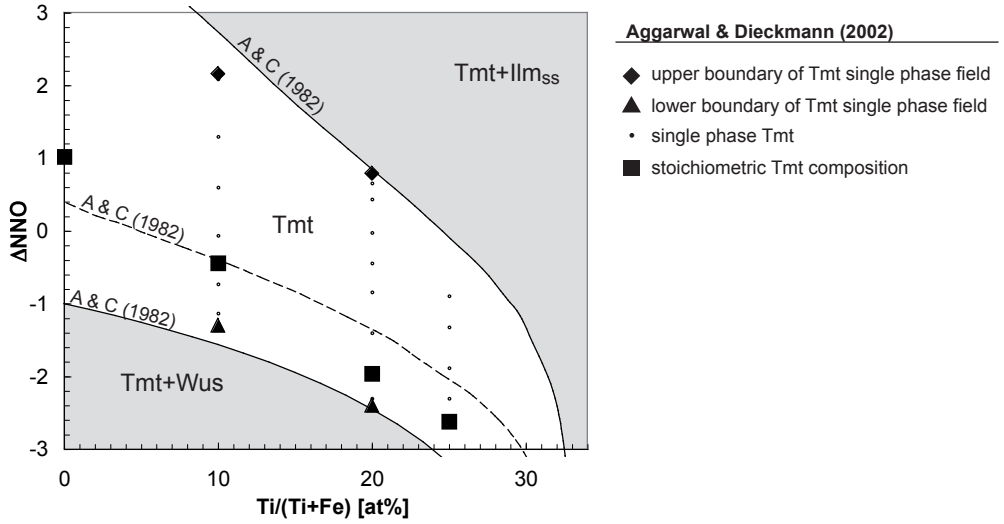

Fig. 1.10 Single-phase field of Tmt (white), and Tmt+Ilm$_{ss}$ and Tmt+Wus two-phase fields (grey), in a plot of oxygen fugacity (expressed as ΔNNO) versus composition (cationic ratio Ti/(Ti+Fe)). Solid lines are boundaries of the Tmt field after Aragón & McCallister (1982), dashed line marks the composition of stoichiometric Tmt after Aragón & McCallister (1982). Symbols correspond to data after Aggarwal & Dieckmann (2002) for single-phase Tmt (small circles), stoichiometric Tmt compositions (squares), the upper fO_2 boundary of Tmt (rhombs), and the lower fO_2 boundary of Tmt (triangles).

phase field (Fig. 1.10). High-T non-stoichiometry of titanomagnetite is expected to be limited to few cat% (Dieckmann, 1982; Senderov *et al.*, 1993; Lattard, 1995).

The formula of non-stoichiometric Tmt can be given as $(Fe_{1-x}Ti_x)_{(3-\delta)}O_4$ (x=Ti/(Ti+Fe)). The parameter δ is used to quantify Tmt non-stoichiometry. δ is the number of cation vacancies ($\delta > 0$: $(Fe_{1-x}Ti_x)_{(3-\delta)}\square_\delta O_4$) or cation interstitials ($\delta < 0$) per formula unit.

To generate Tmt non-stoichiometry (a deviation from stoichiometric cat/O-ratio), basically the following two exchange reactions are conceivable:

$$3Fe^{2+} \leftrightarrow 2Fe^{3+} + \square \tag{1.8}$$

$$2Fe^{2+} \leftrightarrow Ti^{4+} + \square \tag{1.9}$$

More exchange reactions can be put up, but are mathematically linear combinations of reactions 1.8 and 1.9.

In literature, each of the exchange reactions has been held to be exclusively responsible for vacancy formation (reaction 1.8: Aggarwal & Dieckmann, 2002; Aragón & McCallister, 1982; reaction 1.9: Senderov *et al.*, 1993; Lattard, 1995).

It is conceivable that reaction 1.8 could be prevailing at magnetite-rich (i.e. Fe^{3+}-rich) compositions, while reaction 1.9 could preponderate at high X_{Usp} (i.e. high Ti-contents).

Accounting for composition along the solid solution join, cation distribution and non-stoichiometry, Tmt formula can be given as

$$(Fe^{3+}_{b}Fe^{2+}_{1-b})[Fe^{3+}_{(2-2x)+2v(3+x)-b}Fe^{2+}_{(b+x)-v(9+x)}Ti^{4+}_{x(1-v)}\square_{3v}]O^{2-}_{4} \qquad (1.10)$$

where () and [] denote tetrahedral and octahedral sites respectively, b is the number of Fe^{3+} ions on tetrahedral sites, here x is X_{Usp}, v is the vacancy concentration (3v=δ) and $\square$ represents a cation vacancy (Wanamaker & Moskowitz, 1994).

Literature on titanomagnetite non-stoichiometry Several previous papers have investigated Tmt non-stoichiometry theoretically (Aragón & McCallister, 1982) and also experimentally (Dieckmann, 1982; Aggarwal & Dieckmann, 2002; Senderov *et al.*, 1993; Lattard, 1995) (Fig. 1.11). However, at T$<$ 1300 °C and intermediate Tmt composition, data is only provided by the study of Aggarwal & Dieckmann (2002).

For pure magnetite, according to Dieckmann (1982) δ_{max} decreases with decreasing temperature (δ_{max} is the maximum value of δ possible for Tmt with given Ti/(Ti+Fe) at given T and P; δ_{max} corresponds to Tmt in coexistence with ilmenite$_{ss}$). This was confirmed for titanomagnetite solid solution by Aggarwal & Dieckmann (2002), who additionally described a trend of decreasing δ_{max} with increasing X_{Usp}. In contrast, Senderov *et al.* (1993) report only low vacancy concentrations at low X_{Usp}, but higher δ at high X_{Usp}.

Aggarwal & Dieckmann (2002) have investigated Tmt non-stoichiometry by in-situ thermo-gravimetry (at selected T and fO_2). They did not provide details on the equilibration times required and did not examine the samples after the thermo-gravimetric measurements. The phase boundary of single-phase titanomagnetite towards high fO_2 (boundary between single-phase Tmt and two-phase Tmt+Ilm$_{ss}$ field) reported by Aggarwal & Dieckmann (2002) is in contrast to that arising from the experiments presented in the following chapters and reported in Lattard *et al.* (2005). As Aggarwal & Dieckmann (2002) did not check for phase purity, it is conceivable that at high fO_2 their alleged single-phase Tmt sample contains small amounts of ilmenite$_{ss}$.

In contrast, Senderov *et al.* (1993) worked on *quenched* samples. There are inconsistencies between single-phase Tmt and Tmt(+Ilm$_{ss}$) data regarding the cation

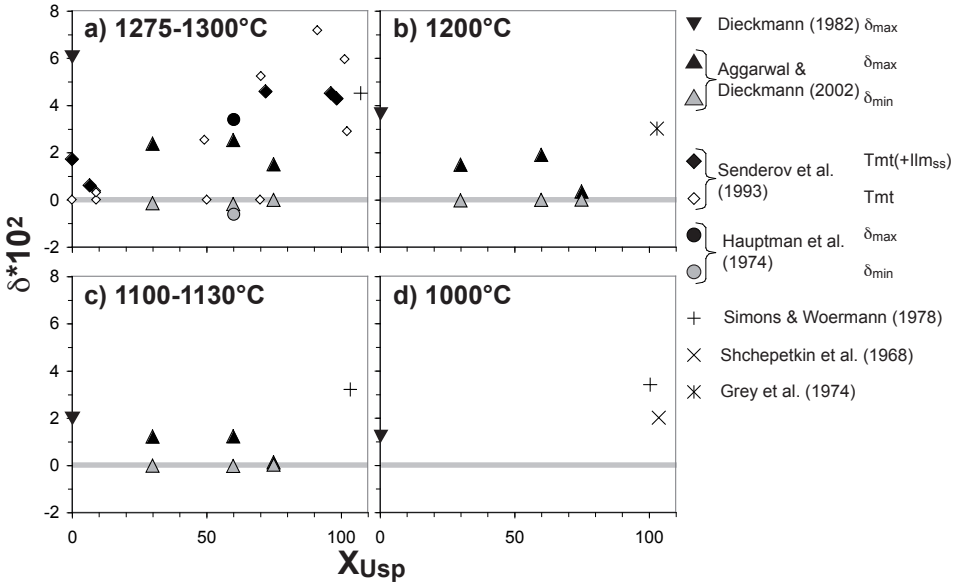

Fig. 1.11 δ versus Tmt composition (X_{Usp}) for a) $1275-1300\,^{\circ}$C, b) $1200\,^{\circ}$C, c) $1100-1130\,^{\circ}$C, and d) $1000\,^{\circ}$C. Different symbols represent different authors. Black filled symbols and crosses indicate Tmt with maximum vacancy concentration (δ_{max}). Grey symbols represent Tmt with minimum δ. Single-phase Tmt by Senderov *et al.* (1993) is represented by small open symbols. The grey horizontal lines in each diagram mark stoichiometric Tmt composition (δ=0).

vacancy concentration. They used relative electron microprobe oxygen analyses, which according to Aggarwal & Dieckmann (2002) might not be a good tool to quantitatively estimate the amount of non-stoichiometry. Nevertheless, EMP oxygen analyses from Senderov *et al.* (1993) are in general agreement with observations from lattice parameter determination. Further, the results by Hauptman (1974), which were obtained by thermo-gravimetric investigations on quenched samples, basically support the values for δ obtained by Senderov *et al.* (1993) (Fig. 1.11). However, at intermediate compositions, only few data points (single-phase Tmt) are available. These suggest increasing non-stoichiometry with increasing X_{Usp}, though the exact shape of this trend can hardly be derived.

A possible explanation for the inconsistencies between in-situ studies (Aggarwal & Dieckmann, 2002; Dieckmann, 1982) and investigations on quenched samples (Senderov *et al.*, 1993; Hauptman, 1974) may be that point defects at iron-rich compositions - formed by exchange reaction $3Fe^{2+} \leftrightarrow 2Fe^{3+} + \square$ - might not be quenchable, whereas those due to exchange reaction $2Fe^{2+} \leftrightarrow Ti^{4+} + \square$ might be. However, this would make us expect higher vacancy concentrations according to Aggarwal & Dieckmann (2002) compared to Senderov *et al.* (1993) and Hauptman (1974), which is not the case. This contradiction is not fully understood and cannot be resolved without further experimental work.

Lattice parameters of titanomagnetite Lattice parameters of titanomagnetites (and their low-T oxidation products titanomaghemites, see below) have been examined by several authors (e.g. Akimoto *et al.*, 1958; Banerjee *et al.*, 1967; Nishitani & Kono, 1983; Wechsler *et al.*, 1984; Readman & O'Reilly, 1972; Senderov *et al.*, 1993). Within the stoichiometric titanomagnetite solid solution $Fe_3O_4 - Fe_2TiO_4$ a non-linear trend of increasing a_0 with increasing X_{Usp} is observed (Wechsler *et al.*, 1984; Senderov *et al.*, 1993) (Fig. 1.12).

For titanomagnetite at 1300 °C, Senderov *et al.* (1993) report a range of cell dimensions at constant Ti/(Ti+Fe) for Tmt equilibrated at different oxygen fugacities. They attribute these variations in lattice parameter to different stages of non-stoichiometry (i.e. cation vacancies or interstitials, Fig. 1.12). The (possible) influence of cation distribution and the *distribution* of lattice defects (vacancies or interstitials) on the cell dimensions also has to be considered.

1.2.4 Titanomaghemite

At low temperatures (T$<$ 300 °C) oxidation of titanomagnetite produces titanomaghemite (Tmh), which is a strongly cation-deficient spinel (e.g. Readman & O'Reilly, 1970; O'Donovan & O'Reilly, 1978). Above $\sim 300 - 350$ °C

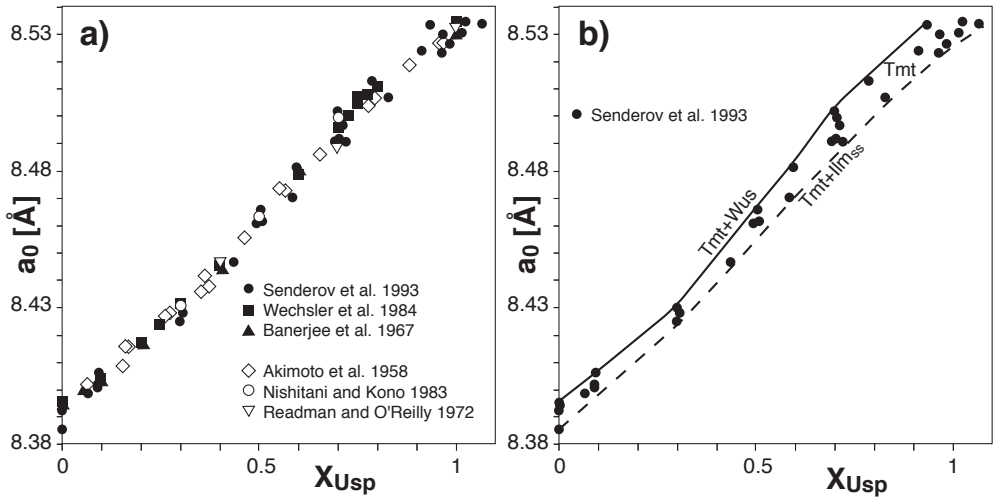

Fig. 1.12 Tmt lattice parameter a_0 versus X_{Usp}. a) Filled symbols represent studies on Tmt, empty symbols represent non-oxidized or precursor Tmt from studies on Tmt oxidation. Note the range of a_0 at given X_{Usp}. b) Data by Senderov *et al.* (1993) and derived a_0-X_{Usp} trend for Tmt in coexistence with Ilm_{ss} (dashed line) and Tmt coexisting with Wus (solid line).

titanomaghemite becomes unstable in favour of a stoichiometric Fe-richer Tmt coexisting with Ilm_{ss} (e.g Ozima & Larson, 1970). Tmh is not stable at the temperatures relevant for the present study (i.e. 950 - 1300 °C), but it is an important Fe-Ti oxide phase in natural rocks, which has been extensively described in literature and examined especially regarding its magnetic moment and lattice parameter (e.g. O'Reilly & Banerjee, 1967; Sanver & O'Reilly, 1970; Readman & O'Reilly, 1971, 1972; Rahman & Parry, 1978). For this thesis the extensively studied Tmh can serve as an example for a cation-deficient cubic Fe-Ti oxide phase and be compared to high-T non-stoichiometric Tmt.

(Titano-)maghemitisation can be continuous towards Fe_2O_3 (Maghemite: $\gamma - Fe_2O_3$, spinel type structure) and cover all compositions within the quadrilateral $Fe_3O_4 - Fe_2TiO_4 - Fe_2TiO_5 - Fe_2O_3$ (Readman & O'Reilly, 1971, Fig. 1.13). Consequently, titanomaghemites can be isochemical to members of the hematite-ilmenite solid solution series (e.g. Fe_2O_3) or to pseudobrookite (Psb, Fe_2TiO_5), but they display a spinel structure (Lindsley, 1976) and incorporate high concentrations of cation vacancies (theoretically up to 11 cat% ($\delta * 10^2 = 33$) for Fe_2O_3: $Fe_{8/3}\square_{1/3}O_4$, and 20 cat% ($\delta * 10^2 = 60$) for Fe_2TiO_4: $Fe_{8/5}Ti_{4/5}\square_{3/5}O_4$). Cation vacancies are essentially situated on the octahedral sites of the spinel lattice (Waychunas, 1991, and references therein). Nevertheless low concentrations of tetrahe-

dral vacancies have also been reported (Schmidbauer, 1987; Collyer *et al.*, 1988; Allan *et al.*, 1989, cited in Harrison & Putnis 1996).

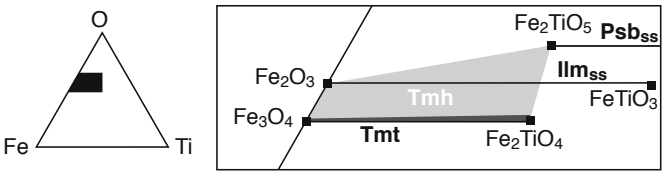

Fig. 1.13 Possible compositional range for titanomaghemite (Tmh, light grey) according to Readman & O'Reilly (1971), and for high-T titanomagnetite (Tmt, dark grey) roughly following both Senderov *et al.* (1993) and Aggarwal & Dieckmann (2002), illustrated in the Fe-Ti-O triangle. Thin horizontal lines represent Tmt, Ilm_{ss} and Psb_{ss} solid solution series, squares mark endmember compositions.

1.2.5 Ilmenite$_{ss}$

The solid solution between the *rhombohedral oxides* hematite (Fe_2O_3, Hem) and ilmenite ($FeTiO_3$, Ilm) is here referred to as ilmenite$_{ss}$ (Ilm_{ss}). Hematite has a trigonal (rhombohedral) structure analogous to the corundum structure: Based on hexagonal closed packing of oxygens, trivalent cations (i.e. Fe^{3+} in Hem) occupy 2/3 of the octahedral sites, forming layers perpendicular to the c-axis in which coordination octahedra form connected six-fold rings. In ilmenite, layers filled with Fe^{2+} and Ti^{4+}, respectively, alternate along the c-axis.

The solid solution along the Ilm_{ss} join is driven by the exchange reaction $2Fe^{3+} \leftrightarrow Fe^{2+}Ti^{4+}$. At Fe^{3+}-rich compositions, Ilm_{ss} has the hematite structure and the substituted amounts of Fe^{2+} and Ti^{4+} are distributed randomly over the cation layers. At high Ti contents, Fe^{2+} and Ti^{4+} are ordered on alternating layers in accordance with the ilmenite structure (Fig. 1.14a). At intermediate compositions, there is a second order transition between the long-range disordered hematite ($R\bar{3}c$) and the ordered ilmenite ($R\bar{3}$) structure (Fig. 1.14b). The composition at which this transition occurs (after Harrison *et al.*, 2000) is shifted towards increasing Ti-content with increasing temperature.

At T$<$800 °C there is a solvus between ilmenite and hematite (Fig. 1.14b). Previous experimental studies (e.g. Lattard, 1995; Senderov *et al.*, 1993, and many others) do not report exsolution during quenching as a result of this miscibility gap.

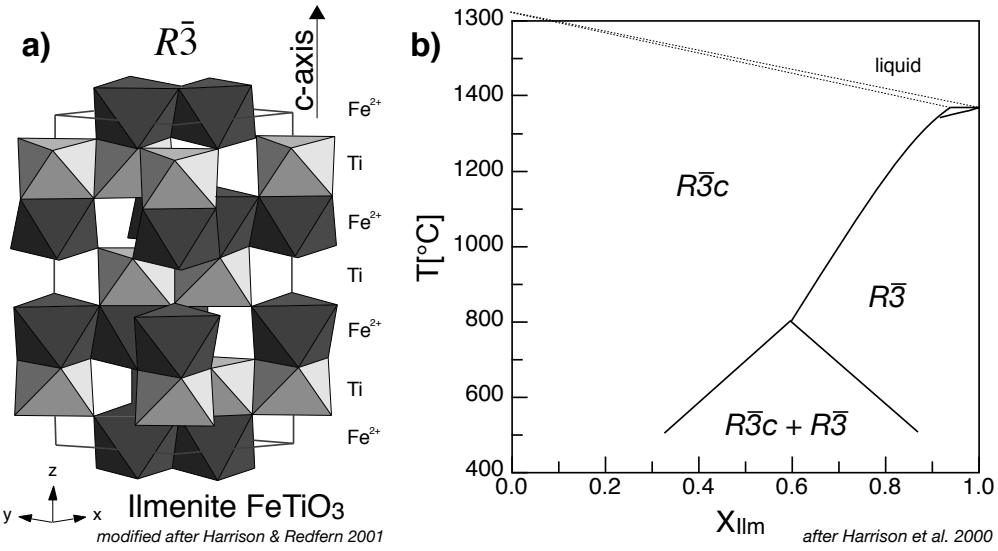

Fig. 1.14 a) Schematic illustration of the ilmenite structure: TiO6 (light grey) and FeO6 (dark grey) octahedra are arranged in alternating layers perpendicular to the c-axis (modified after Harrison & Redfern, 2001). b) Calculated phase diagram for the system $Fe_2O_3 - FeTiO_3$, after Harrison *et al.* (2000). Note that the composition of the phase transition between the long-range ordered $R\bar{3}$ structure and the disordered $R\bar{3}c$ structure shifts towards increasingly Ti-rich compositions with increasing T. At T<800 °C there is a miscibility gap within the solid solution series.

1.2.6 Pseudobrookite$_{ss}$

The *orthorhombic series* (pseudobrookite$_{ss}$, Psb$_{ss}$) covers solid solution between the ferric endmember $Fe_2^{3+}Ti^{4+}O_5$ (pseudobrookite, Psb), the ferrous endmember $Fe^{2+}Ti_2^{4+}O_5$ (former name ferropseudobrookite) and also the Ti endmember $Ti_2^{3+}Ti^{4+}O_5$ (anosovite) (at T>1300 °C Grey & Ward, 1973; Ender *et al.*, 1980; Grey & Merritt, 1981). Between the ferrous and the ferric endmember the solid solution is governed by the ilmenite exchange reaction (see page 5), between the ferric endmember and anosovite by the substitution $Fe^{2+}Ti^{4+} \leftrightarrow 2Ti^{3+}$.

Between Fe_2TiO_5 (Psb) and $FeTi_2O_5$ the solid solution is continuous at T>1140 °C (see Fig. 1.15). At 1140 ± 10 °C $FeTi_2O_5$ decomposes to ilmenite + rutile (Haggerty & Lindsley, 1969). At temperatures between 1140 °C and 1066 °C, Psb$_{ss}$ displays two miscibility gaps (Grey & Merritt, 1981, see Fig. 1.15), one between Fe^{3+}-rich Psb$_{ss}$ and $Fe^{2+}Ti_2O_5$, and a second one between $Fe^{2+}Ti_2O_5$ and Ti_3O_5. The intermediate composition is slightly richer in Ti compared to $FeTi_2O_5$ and disappears at 1066 °C. This leaves one single gap between Ti_3O_5 and about $Fe_{0.8}^{2+}Fe_{0.4}^{3+}Ti_{1.8}^{4+}O_5$.

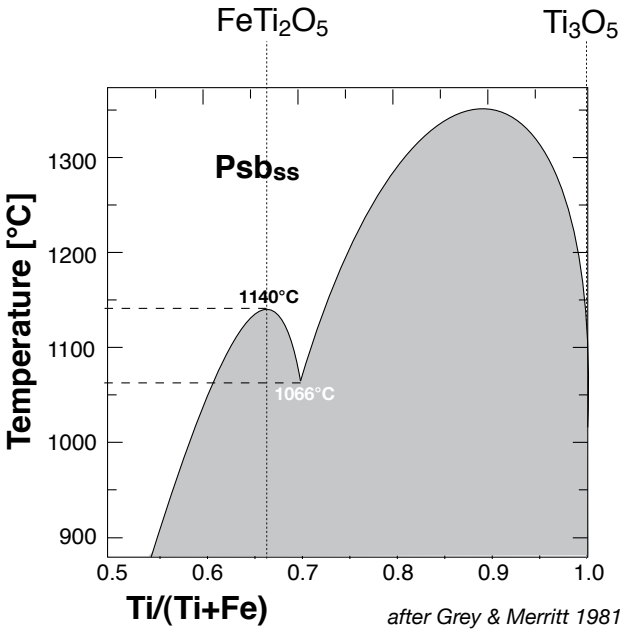

Fig. 1.15 Solvi within the orthorhombic pseudobrookite$_{ss}$ solid solution series (modified after Grey & Merritt, 1981). The shaded area represents the miscibility gap.

With decreasing temperature this single gap broadens towards the Fe-richer composition, and the Fe_2TiO_5 endmember finally breaks down to hematite + rutile at $585 \pm 10\,^{\circ}C$ (e.g. Haggerty & Lindsley, 1969; Grey *et al.*, 1974; Merritt & Turnbull, 1974; Simons & Woermann, 1978; Grey & Merritt, 1981).

1.3 Thermo-oxybarometry

The petrologic significance of Fe-Ti oxides was established by Buddington & Lindsley in their classical study in 1964. These authors first showed that the composition of coexisting Tmt and Ilm_{ss} can potentially be used to estimate temperature and oxygen fugacity (fO_2) during formation or subsequent re-equilibration of a Fe-Ti oxide paragenesis.

Principles of Fe-Ti oxide thermo-oxybarometry The equilibrium between Tmt and coexisting Ilm_{ss} can be described by equations 1.11 and 1.12.

$$FeTiO_3(Ilm) + Fe_3O_4(Mag) \rightarrow Fe_2O_3(Hem) + Fe_2TiO_4(Usp) \quad (1.11)$$

$$4Fe_2^{3+}Fe^{2+}O_4(Mag) + O_2 \rightarrow 6Fe_2^{3+}O_3(Hem) \quad (1.12)$$

The exchange reaction $2Fe^{3+} \leftrightarrow Fe^{2+}Ti^{4+}$ that governs the exchange along the Fe-Ti oxide solid solution entails that with increasing Ti-Fe^{2+} content the $Fe^{3+}/\Sigma Fe$ value in both Fe-Ti oxides decreases. $Ilmenite_{ss}$ is oxygen-richer (oxygen/cation=3/2=1.5) compared to titanomagnetite (oxygen/cation=4/3$\approx$ 1.3). For Ilm_{ss} and Tmt of the same cationic ratio, $ilmenite_{ss}$ has a higher $Fe^{3+}/\Sigma Fe$. Further, the distribution of Fe and Ti between coexisting Fe-Ti oxides depends on temperature. Towards higher temperature, the distribution gets more and more random between the phases. In the triangle Fe-Ti-O this is expressed by increasingly steepened Fe-Ti oxide conodes with increasing temperature. This can be described by equation 1.11.

The Tmt-Ilm_{ss} thermo-oxybarometer: previous versions The Buddington & Lindsley (1964) (Fig. 1.16) thermo-oxybarometer was one of the first thermo-oxybarometers established in geo-sciences and also became one of the most commonly used. The publication of Buddington & Lindsley (1964) provides an empirical calibration based on experimental Fe-Ti-O data by Lindsley (1962, 1963, hydrothermal buffer technique, experiments at $\sim$500 to 1000 °C). Since this calibration data set was restricted to a relatively narrow range of oxygen fugacities (corresponding to NNO, FMQ, WM, and MnO-Mn_3O_4, for abbreviations see appendix A.1), temperatures below 1000 °C, and the pure system Fe-Ti-O, further calibration data has been collected during the following years:

- The fO_2-T range of the experimental database in the system Fe-Ti-O has been enlarged, e.g. towards high temperatures and low oxygen fugacities (e.g.

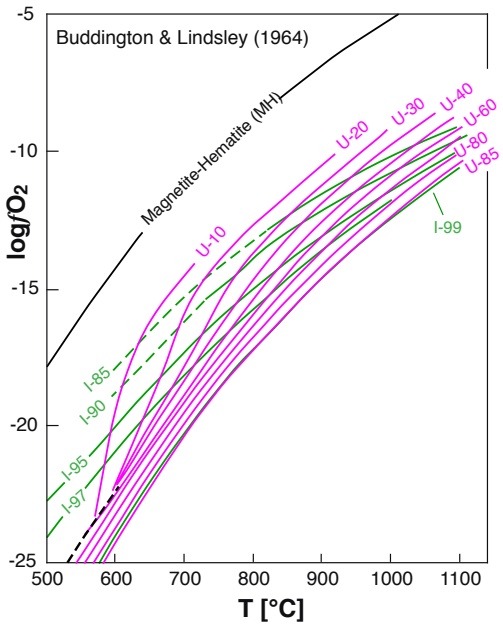

Fig. 1.16 Graphical version of the Fe-Ti oxide thermo-oxybarometer after Lindsley (1963); Buddington & Lindsley (1964), presented in a diagram of oxygen fugacity (as logfO_2) vs. temperature. Pink lines are titanomagnetite isopleths, the labels denote the ulvöspinel content (e.g. U-10: 10% Usp component in titanomagnetite). Green lines indicate ilmenite$_{ss}$ isopleths (e.g. I-97: 97% Ilm component). T and fO_2 of coexisting Tmt and Ilm$_{ss}$ are defined by the intersecting point of the corresponding isopleths. Also shown is the curve for the magnetite-hematite (MH) solid-state buffer equilibrium. Black dashed line marks the structural transition within the ilmenite-hematite solid solution.

Hammond *et al.*, 1982; Simons & Woermann, 1978, 1000 – 1300 °C, IQF: iron-quartz-fayalite solid-state buffer equilibrium).

- The experimental data was extended to Mn- or Mg-bearing compositions (e.g. Pickney & Lindsley, 1976; Andersen *et al.*, 1991).

In order to bring up thermodynamically based formulations of the thermo-oxybarometer, solid solution models for the cubic and rhombohedral series have been developed (Rumble, 1970; Powell & Powell, 1977; Andersen & Lindsley, 1988; Andersen *et al.*, 1991; Ghiorso & Sack, 1991; Andersen *et al.*, 1993). Currently, two thermodynamic formulations of the Tmt-Ilm$_{ss}$ thermo-oxybarometer are in use and have been broadly applied during the last years:

(I) the model incorporated in the QUILF software package (QUILF-model) (Andersen & Lindsley, 1988; Andersen *et al.*, 1993)

(II) the Ghiorso & Sack (1991) formulation.

The QUILF model Andersen *et al.* (1993) have presented a computer program called QUILF and state that "program QUILF assesses equilibria among Ti-magnetite, ilmenite, augite, pigeonite, orthopyroxene, olivine, and quartz (or sub-assemblages thereof). Oxide and silicate equilibria are related through the QUIlF equilibrium" (equations 1.13, 1.14: QUIlF reaction).

$$SiO_2 + 2Fe_2TiO_4 \leftrightarrow 2FeTiO_3 + Fe_2SiO_4 \tag{1.13}$$

$$\text{quartz} + \text{ulvöspinel} \leftrightarrow \text{ilmenite} + \text{fayalite} \tag{1.14}$$

They continue that "depending on the assemblage, QUILF can provide information on temperature, pressure, oxygen fugacity and the activities of SiO_2, TiO_2, and Fe°". The QUIlF reaction involves only the Tmt and Ilm_{ss} endmembers Ilm and Usp, respectively. The addition of Fe_3O_4 and Fe_2O_3 components allows the estimation of temperature and oxygen fugacity based on oxide phase relations.

The QUILF model (Fig. 1.17) is based on the solid solution models by Andersen & Lindsley (1988) for Fe-Ti oxides (titanomagnetite and $ilmenite_{ss}$) and Andersen *et al.* (1991) for Fe-Mg-Ti oxides and olivine, as well as on a solid solution model for coexisting pyroxenes and olivines plus quartz (Davidson & Lindsley, 1989).

The solid solution models by Andersen & Lindsley (1988) and Andersen *et al.* (1991) consider only Ilm_{ss} with high X_{Ilm}, which are expected to crystallise in the $R\bar{3}$ space group. The authors do not account for the structural transition within the ilmenite-hematite solid solution series. Ilm_{ss} is treated as an asymmetric Margules solution.

For the spinels, two solid solution models based on different cation distribution have been derived. One is based on the cation distribution by Akimoto (1954). Further, a "site mixing model" has been put up based on the cation distribution given in the papers by Wu & Mason (1981) and Trestman-Matts *et al.* (1983). Wu & Mason (1981) and Trestman-Matts *et al.* (1983) have proposed cation distributions, which are significantly different from the Akimoto (1954) model at temperatures relevant for the Fe-Ti oxide thermo-oxybarometer (i.e. $\gg 300\,°C$).

Both models work equally well to explain the macroscopic properties of Tmt in equilibrium with Ilm_{ss}, so the simpler Akimoto (1954) based model was incorporated in the QUILF model. Andersen & Lindsley (1988) and Andersen *et al.* (1991) also consider the effect of Mg and Mn on Fe-Ti oxides.

The Ghiorso & Sack (1991) model Ghiorso & Sack (1991) provided a thermo-oxybarometric formulation of the equilibrium between coexisting Tmt and Ilm_{ss},

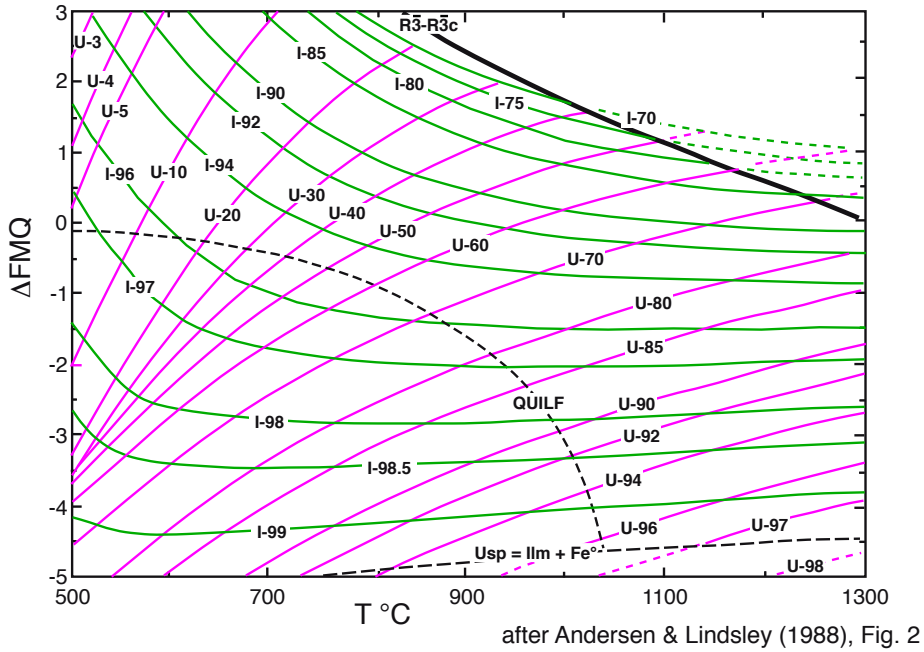

Fig. 1.17 Graphical illustration of the thermodynamic Fe-Ti oxide thermo-oxybarometer formulation based on Andersen & Lindsley (1988), presented in a diagram of oxygen fugacity (as logfO_2) vs. temperature. Pink lines are titanomagnetite isopleths, with labels denoting the ulvöspinel contents (e.g. U-10: 10% Usp component in titanomagnetite). Green lines indicate ilmenite$_{ss}$ isopleths (e.g. I-98: 98% Ilm component). Dashed black lines mark the QUIlF (quartz-ulvöspinel-ilmenite-fayalite) equilibrium, and the reaction Usp↔Ilm+Fe°. The solid black line on the upper right of the diagram marks the structural transition within the ilmenite-hematite solid solution.

which is internally consistent with thermodynamic models for olivine and pyroxene solid solutions (Sack & Ghiorso, 1989) and the end-member thermodynamic data base by Berman (1988) and Berman & Brown (1985). The model by Ghiorso & Sack (1991, Fig. 1.18) incorporates the solid solution models by Sack & Ghiorso (1991a,b) (Fe-Mg-titanomagnetite-aluminate spinels, chromian spinels) and Ghiorso (1990) (rhombohedral oxides: hematite-ilmenite-geikielite solid solution) and is also available as software version.

Comparison of the QUILF and Ghiorso & Sack (1991) models A comparative illustration of both the QUILF model (Andersen & Lindsley, 1988; Andersen *et al.*, 1993) and the model after Ghiorso & Sack (1991) (grey lines) in a Roozeboom diagram (Fig. 1.19) reveals the significant differences between the models. The Ghiorso & Sack (1991) model clearly shows a sharp bend in each of the isotherms,

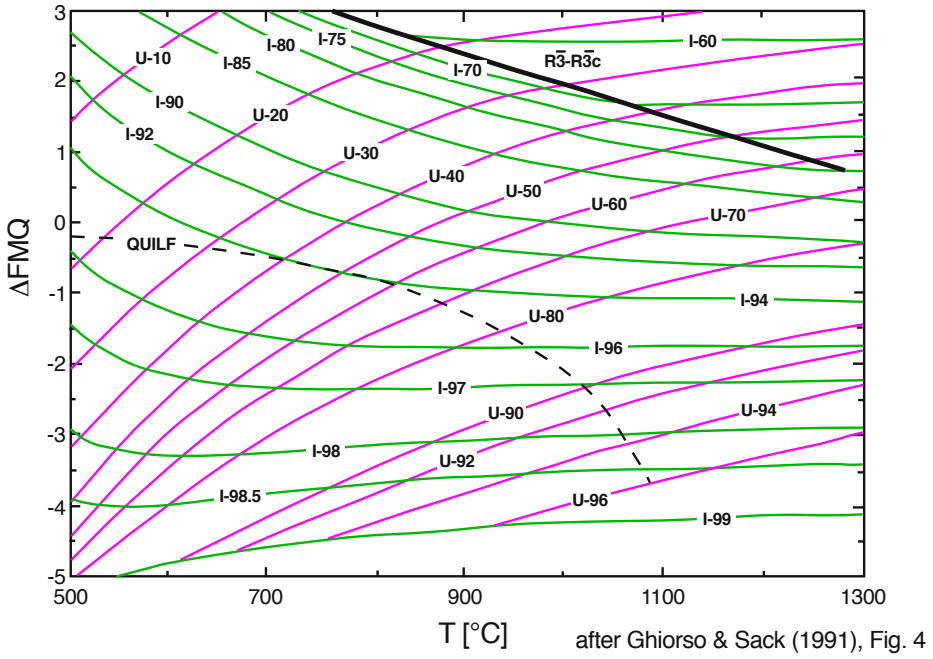

Fig. 1.18 Graphical illustration of the thermodynamic Fe-Ti oxide thermo-oxybarometer formulation by Ghiorso & Sack (1991), presented in a diagram of oxygen fugacity (as logfO_2) vs. temperature. Pink lines are titanomagnetite isopleths, labels denote the ulvöspinel contents (e.g. U-10: 10% Usp component in titanomagnetite). Green lines indicate ilmenite$_{ss}$ isopleths (e.g. I-98: 98% Ilm component). Dashed back line marks the QUIlF equilibrium. Solid black line indicates the transition between the R$\bar{3}$ and R$\bar{3}$c structures in Ilm$_{ss}$.

which is related to the structural transition within the ilmenite-hematite solid solution series. The isotherms after the QUILF model however, do not show such kink. Especially at X_{Ilm}<0.6 the QUILF isotherms are significantly wider spaced and are shifted towards higher X_{Usp} compared to the Ghiorso & Sack (1991) isotherms.

Application of the thermo-oxybarometer formulations Both formulations are the product of sophisticated thermodynamic treatments, based on sound experimental data and crystal chemical considerations. Their application has yielded a wealth of reasonable thermo-barometric estimates.

Numerous publications have used the T-fO_2 estimates derived from application of the above formulations to gain information on oxidation states in the Earth mantle and crust (focussing for example on generation of basic magmas, processes in magma chambers, fractionation paths or fluid movements in the mantle, oxidation states of and processes in igneous or metamorphic rocks), and on martian and lunar

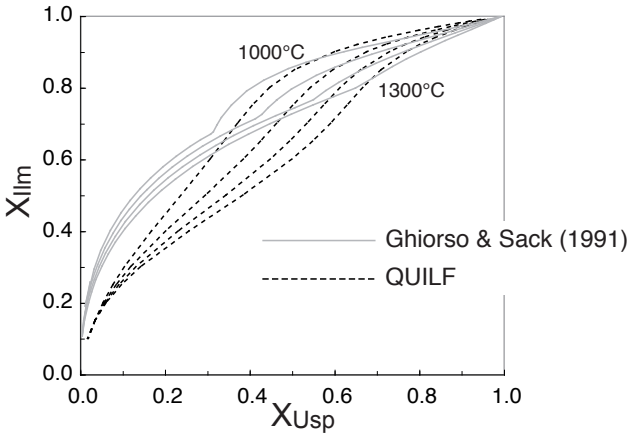

Fig. 1.19 Comparison of the QUILF model (dashed lines, Andersen & Lindsley, 1988; Andersen *et al.*, 1993) and the model after Ghiorso & Sack (1991) (grey lines) in a Roozeboom diagram of X_{Ilm} versus X_{Usp}. The lines represent $1000-1300\,^{\circ}C$ isotherms with increasing temperature from left to right.

basalts (e.g. Evans & Scaillet, 1997; Scaillet & Evans, 1999; Harlov, 2000; Herd *et al.*, 2001; Harlov, 1992; Herd *et al.*, 2002; Xirouchakis *et al.*, 2002; Devine *et al.*, 2003) .

A comparison of results with the QUILF model and the Ghiorso & Sack (1991) model from intermediate to silicic rocks shows that the Ghiorso & Sack (1991) estimates spread over a significantly larger temperature interval compared to the Andersen & Lindsley (1988) estimates (Fig. 1.20). Application of the thermo-oxybarometer formulations to experimental data (e.g. Scaillet & Evans, 1999; Toplis & Carroll, 1995, see below) shows that the thermo-oxybarometric results are not always satisfactory: Scaillet & Evans (1999) have carried out hydrothermal crystallisation experiments at 760 to 900 °C under controlled oxygen fugacity (NNO to NNO+2.7, controlled by a Shaw membrane). In their experiments they used a glass produced from a natural dacite sample from Mt Pinatubo. Annealing at constant temperature induces crystallisation of multi-phase assemblages (e.g. plagioclase+hornblende+biotite+Fe-Ti oxides). Applied to the Tmt+Ilm_{ss} bearing run products of Scaillet & Evans (1999), both models yield temperatures and also oxygen fugacities that generally are significantly overestimated (Ghiorso & Sack 1991: ΔT up to 300 °C; $\Delta \log fO_2$ up to >1; QUILF: ΔT up to about 100 °C, $\Delta \log fO_2$ up to ~ 1; $\Delta T = T_{calculated} - T_{experimental}$, $\Delta \log fO_2 = \Delta NNO_{calculated} - \Delta NNO_{experimental}$; Fig. 1.21).

At higher temperatures experimental data by Toplis & Carroll (1995) is available

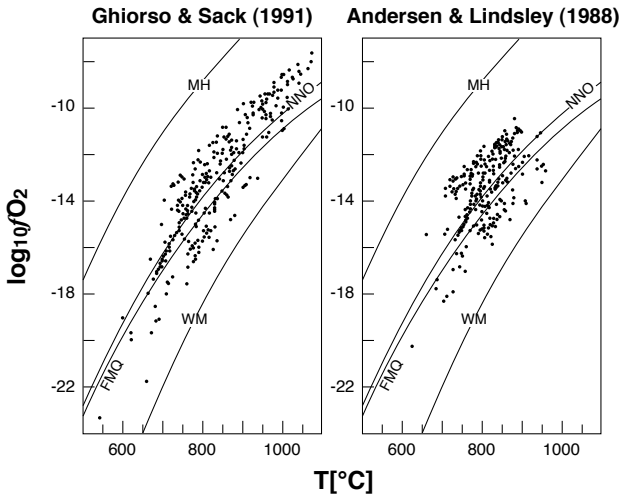

Fig. 1.20 Comparison of values of temperature and oxygen fugacity calculated from the compositions of coexisting Tmt and Ilm_{ss} reported from a wide variety of intermediate to silicic rocks (table 1 by Ghiorso & Sack (1991)), derived with the model by Ghiorso & Sack (1991, left) and according to Andersen & Lindsley (1988, right). After Fig. 9 of Ghiorso & Sack (1991).

for comparison. Toplis & Carroll (1995) have carried out crystallisation experiments on a ferrobasaltic composition at 1 bar, 1050 to 1100 °C and ΔNNO -1.6 to +0.3. Comparison between experimental data and T-fO_2 estimates reveals significant discrepancies in temperature - especially pronounced for the QUILF model - and also oxygen fugacity (both models: ΔT up to -150 °C, ΔlogfO_2 up to ± 1; Fig. 1.21).

Both the study of Scaillet & Evans (1999) and that of Toplis & Carroll (1995) have been conducted on natural compositions. This could suggest that the observed deviations between experiment and calculation are related to the presence of minor concentrations of elements like Mg, Al and Mn in the phases. However, discrepancies are also observed when applying the models to simple system Fe-Ti-O data, for example the 1300 °C subsolidus synthesis experiments (at 1 bar) by Senderov *et al.* (1993, Fig. 1.21). Divergences between experimental data and thermo-oxybarometric estimates in both T and fO_2 are pronounced, reaching up to ΔT=-400 °C and ΔlogfO_2=-4.

Reasons for unsatisfactory T-fO_2 estimates As stated in section 1.1, the shortcomings of the existent thermo-oxybarometer have several reasons, which are:

a) the calibration data set, which covers only a limited T-fO_2 range,

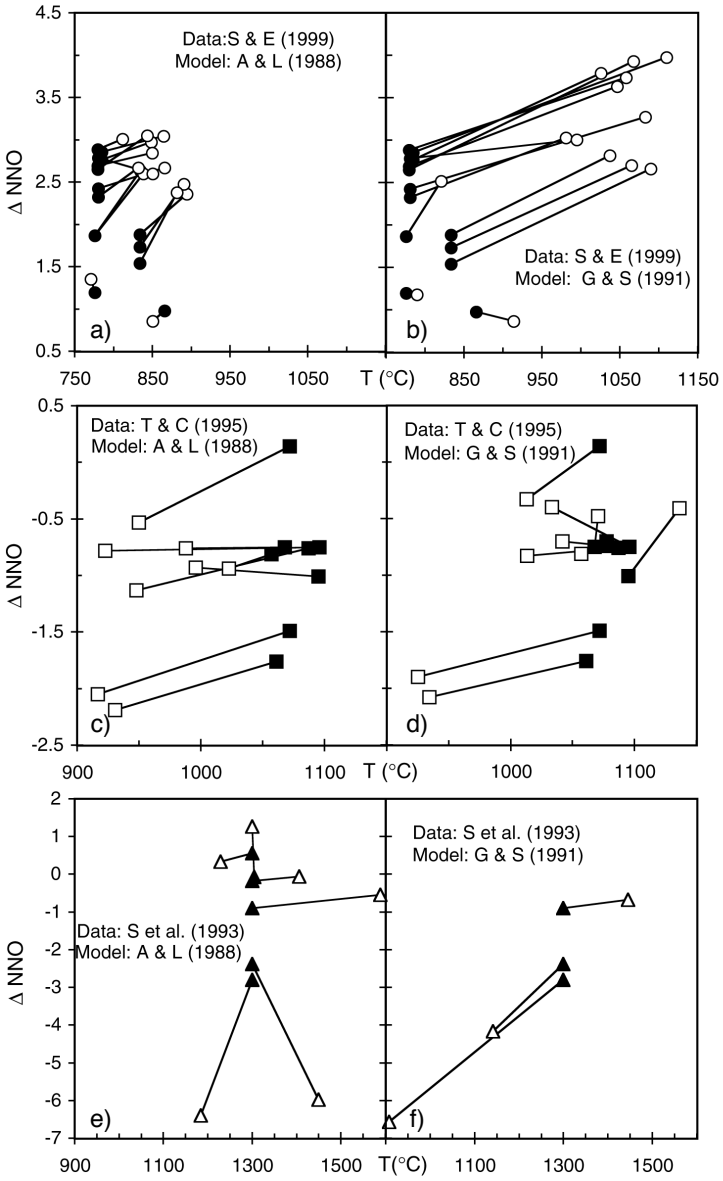

Fig. 1.21 Comparison of experimental and estimated T and fO_2 for Tmt-Ilm_{ss} parageneses: experimental data by a) and b) Scaillet & Evans (1999), c) and d) Toplis & Carroll (1995), e) and f) Senderov *et al.* (1993). Filled symbols represent experimental values, empty symbols represent estimates derived from the QUILF software (diagrams on the left) and the Ghiorso & Sack (1991) model (right). ΔNNO=logfO_2(sample)-logfO_2(buffer). The logfO_2 values for the NNO buffer are from O'Neill & Pownceby (1993a).

b) the incorporated solution models for both Tmt and Ilm_{ss} and their ability to account correctly for minor contents of elements like Mg, Mn, Al, etc.,

c) the thermodynamic data (e.g. heat capacity) applied for endmember components,

d) consideration of cation order/disorder and structural transitions within the solid solution series as a function of temperature and composition, and

e) missing comprehension of non-stoichiometry, especially concerning Tmt.

One major factor - and the one this study is mainly intended to deal with - is the limited experimental data set that has been available for calibration. Fig. 1.22 provides a summary of the data available for calibration of the QUILF model (Andersen & Lindsley, 1988; Andersen *et al.*, 1993) and the thermo-oxybarometer model by Ghiorso & Sack (1991). It is apparent that data are missing for temperatures above $1000\,^{\circ}$C and oxygen fugacities outside FMQ $\pm$ 1.

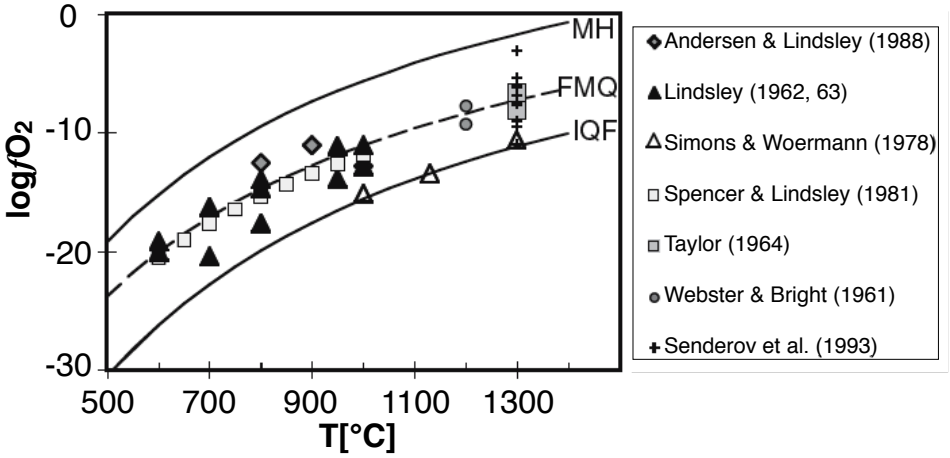

Fig. 1.22 T-fO_2 range of the experimental data available for calibration of the QUILF model (Andersen *et al.*, 1993; Andersen & Lindsley, 1988) and the thermo-oxybarometer formulation by Ghiorso & Sack (1991). The data by Senderov *et al.* (1993, crosses) has *not* been used for calibration.

The experimental calibration data used in the Andersen & Lindsley (1988) model concentrate essentially on the Ti-rich side of the Ilm-Hem solid solution series, and the model does not consider the structural transition within this series. In this respect it has to be pointed out that Lindsley & Frost (1992) and Andersen & Lindsley (1988) have cautioned the users of their formulation (Andersen *et al.*, 1993) to beware of applications outside the calibration range ($800-1000\,^{\circ}$C, FMQ -1.7

to +2.2) and especially at high oxygen fugacity (exceeding two magnitudes above the fayalite-magnetite-quartz equilibrium). Further, both thermodynamic models (QUILF Andersen & Lindsley, 1988; Ghiorso & Sack, 1991) do not account for any non-stoichiometry potentially present in Tmt or Ilm_{ss}.

The Ilm_{ss}-Psb_{ss} (thermo-)oxybarometer The paragenesis Ilm_{ss}-Psb_{ss}, which compared to the assemblage Tmt+Ilm_{ss} is stable at higher bulk Ti-contents for a given oxygen fugacity, or at higher oxygen fugacity for given bulk (Ti/(Ti+Fe)), also has potential to estimate oxygen fugacity and - in principle - temperature. The paragenesis in particular occurs in Ti-rich rocks, for example of the Moon or Mars. Analogous equations as for the Tmt-Ilm_{ss} thermo-oxybarometer can be put up for $ilmenite_{ss}$ coexisting with $pseudobrookite_{ss}$ (equations 1.11, 1.12).

Anovitz *et al.* (1985) provided a preliminary version of the Ilm_{ss}-Psb_{ss} oxybarometer, based on calorimetric and phase equilibrium data. While the compositions of both phases strongly depend on oxygen fugacity, the $pseudobrookite_{ss}$ composition is practically independent of temperature (Fig. 1.23). $Ilmenite_{ss}$ composition is dependent on T only at restricted ranges of oxygen fugacity. Consequently, the paragenesis Ilm_{ss}-Psb_{ss} has to be considered as an oxygen barometer rather than a true *thermo*-oxybarometer.

For the development of a thermodynamic formulation calibration data is required.

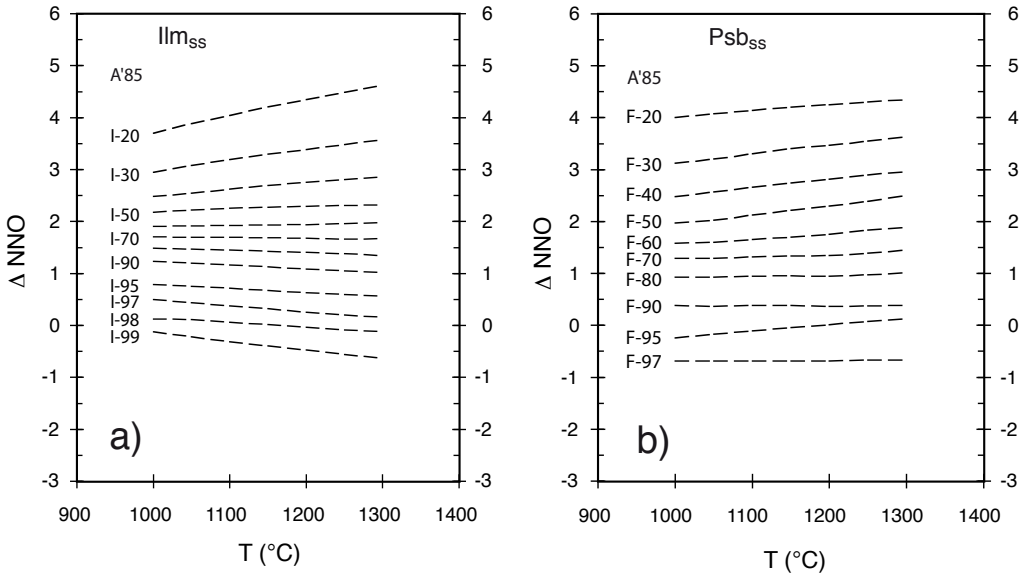

Fig. 1.23 Isopleths (dashed lines) of the compositions of coexisting a) Ilm_{ss} (e.g. I-20 corresponds to 20 mol% $FeTiO_3$) and b) Psb_{ss} (e.g. F-60 corresponds to 60 mol% $FeTi_2O_5$) as a function of temperature (T) and oxygen fugacity (ΔNNO), after Anovitz *et al.* (1985).

1.4 Aims of the present study

It has been shown in section 1.3 that the current Fe-Ti thermo-oxybarometer formulations yield unsatisfactory results and need further development. It has been presented that this failure has several reasons, one major being the limited range in T and fO_2 of calibration data. Additional data on equilibrium composition of coexisting Tmt+Ilm_{ss}, and Ilm_{ss}+Psb_{ss} is needed, especially at high temperatures (T$\geqslant$ 1000 °C) and both high and low oxygen fugacities (higher than FMQ+1 or lower than FMQ-1) .

Such experimental data is required for the simple system Fe-Ti-O, but the effect of minor elements (e.g. Mg, Al, Mn) has to be considered as well.

Current formulations do not account for non-stoichiometry. However, a comprehensive experimental study that confirms this approximation or supplies data to enable a incorporation of non-stoichiometry is lacking. This thesis intents to detect and quantify Tmt non-stoichiometry as a function of T and composition (i.e. Ti/(Ti+Fe)).

It is the aim of this study to contribute to a re-calibration of the Fe-Ti oxide thermo-oxybarometer by providing

- equilibrium compositions of Fe-Ti oxides (i.e. mainly Tmt, Ilm_{ss}, Psb_{ss}) at T and fO_2 complementary to the existing data set,
  - in the system Fe-Ti-O, generally coexisting in binary assemblages, and
  - of Mg and/or Al bearing Fe-Ti oxides, generally coexisting in binary, but also in ternary assemblages,
- new qualitative and quantitative data on Tmt non-stoichiometry (cation vacancies).

2 Experimental and analytical methods

2.1 General approach

Within the present study, different types of experiments have been carried out, which are described in the following. Fig. 2.1 presents a flow chart of preparation and accomplishment of experiments, and subsequent analysis.

- *Equilibration experiments:*
  - Synthesis runs were performed at 1 bar at temperatures from 1000 °C to 1300 °C under controlled oxygen fugacity in the range ΔNNO=-5 to +5 (i.e. conditions complementary to the existing calibration data) to produce binary Fe-Ti oxide assemblages (Fe°+Tmt, Wus+Tmt, Tmt+Ilm_{ss}, Ilm_{ss}+Psb_{ss}, Psb_{ss}+Rt) as well as some single-phase samples or ternary assemblages.
  - Some re-equilibration experiments have been carried out at the same T-fO_2 conditions as the synthesis experiments. The purpose was to confirm that the synthesis run products indeed reflected or at least closely approached equilibrium. The starting materials were fragments of synthesis run products.
- *Annealing experiments:*
  - At the high temperatures that prevailed during synthesis or re-equilibration experiments ($\geq$ 1000 °C), Tmt in coexistence with Ilm_{ss} is supposed to be non-stoichiometric (cation-deficient). Annealing at 950 °C is intended to cause vacancy relaxation in the originally non-stoichiometric Tmt leading to the formation of stoichiometric Tmt plus coexisting Ilm_{ss}.

Run durations varied from 18 hours at 1300 °C up to 357 h (i.e. 15 days) at 1000 °C (both synthesis and re-equilibration experiments), and 7 to 33 days for annealing experiments at 950 °C.

Polished sections of all quenched run products were examined with a scanning electron microscope (SEM) to check the phase assemblages and textures. X-ray

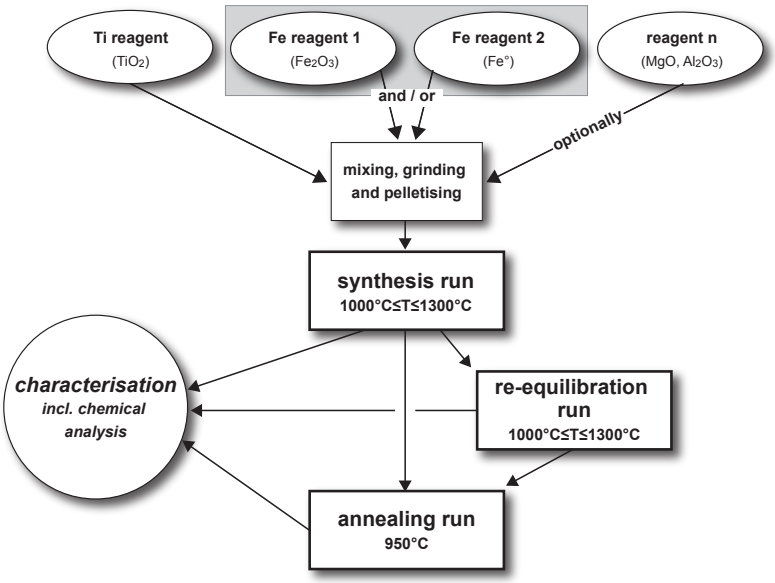

Fig. 2.1 Flow chart of preparation and types of experiments, and characterisation of run products.

diffraction was applied for phase determination especially on high-T synthesis products. Lattice parameters were determined for selected samples (both high-T and annealed). Phase compositions were obtained from electron microprobe (EMP) analyses for Ti, Fe, Mg and Al. Oxygen was not analysed. EMP analyses of high-T run products and of annealed samples, in combination with the relative amounts of coexisting phases (i.e. modal proportions) were used to estimate high-T non-stoichiometry (see chapter 5). Modal phase proportions were derived from image analysis or Rietveld analysis, or were calculated from analytical data (phase compositions from EMP) and the cationic ratio of the starting material (known from sample preparation, weighing). Further, $Fe^{3+}/\Sigma Fe$ was determined on chosen samples by electron energy-loss spectroscopy (EELS). Combined with EMP results, this allows the calculation of Tmt non-stoichiometry.

2.2 High-temperature experiments

2.2.1 Preparation of starting mixtures

For the preparation of starting mixtures for synthesis experiments we used dried TiO_2 (anatase, 99.9%, Aldrich Chemical Comp. Inc.) as Ti-bearing component.

For Fe, we chose dried Fe^{3+}-oxide (Fe_2O_3, 99.9%, Alpha Products) or dried and reduced (under H_2, 500 °C) metallic iron (99+%, Heraeus).

In binary mixtures of Fe_2O_3 and TiO_2, or Fe° and TiO_2 any given Ti/(Ti+Fe) cationic ratio can be adjusted (see Fig. 2.2). The bulk oxygen content however, arises from the selected cationic ratio. Most synthesis experiments have been carried out using $Fe_2O_3 - TiO_2$ mixtures. $Fe^\circ - TiO_2$ starting mixtures have only been applied in very few cases. By using a starting mixture of the three components $TiO_2 + Fe_2O_3 + Fe^\circ$ a specific oxygen content of the sample can be adjusted for a selected cationic ratio Ti/(Ti+Fe) (within the shaded area in Fig. 2.2c).

To approach natural Fe-Ti oxide compositions small amounts of MgO (99.5%, Ventron) and/or γ-Al_2O_3 (purest, Merck) have been added to some starting materials (for starting mixtures see appendix A.2, table A.3).

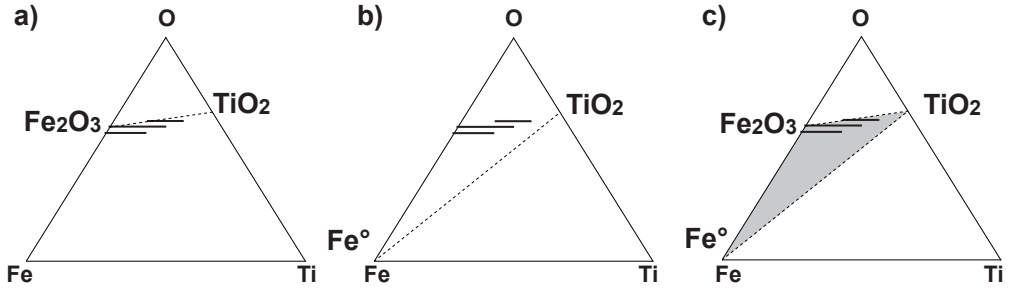

Fig. 2.2 Binary mixtures of a) $Fe_2O_3 + TiO_2$ or b) $Fe^\circ + TiO_2$ have bulk compositions along the connecting lines between the constituents. c) $Fe_2O_3 + Fe^\circ + TiO_2$ mixtures can be used to adjust any bulk composition within the shaded triangle. Black horizontal lines represent (from bottom to top) Tmt, Ilm_{ss} and Psb_{ss} solid solutions (for orientation).

Pre-heating of reagents at $800 - 1000\,^\circ$C prior to preparation of the starting mixtures has been done for several starting mixtures to avoid weighing errors originating from water- or OH-bearing reagents. It has turned out however that this procedure results in grain coarsening. Careful subsequent grinding could not entirely reverse this effect. The coarsened grain size affects the texture and phase distribution in the run product by inducing the formation of large monomineralic aggregates rather than homogenous phase distribution. The majority of the synthesis samples have been produced from starting materials that have not been pre-treated.

Reagents (TiO_2, Fe_2O_3, Fe°, MgO, Al_2O_3) were mixed and subsequently ground in an agate mortar under acetone. 200-300 mg were pressed into pellets of about 5 mm in diameter and 2-5 mm height. The high temperature runs have been interrupted once for some experiments in the system Fe-Ti-O equilibrated at T$\leq$ 1200 °C, and for most Mg and Al bearing samples. The runs were continued (at

identical T and fO_2) after grinding the sample to a powder (in an agate mortar under acetone) and producing a new pellet.

Fragments of selected synthesis products have been further used as starting material for re-equilibration or annealing experiments.

2.2.2 High-temperature techniques

All high-temperature experiments (synthesis, re-equilibration and annealing) were conducted in vertical quench furnaces, with a hot zone ($\pm 0.5\,^{\circ}C$) of approximately 3 cm in length. The furnace tube has an inner diameter of about 4 cm. A radial temperature gradient was not detected. The temperature was measured before and after the runs with a type S ($Pt - Pt_{90}Rh_{10}$) thermocouple calibrated against the melting points of silver (960.8 °C) and gold (1064.4 °C). The temperature was controlled within $\pm 0.2\,^{\circ}C$ by commercial controllers. Samples were attached to a ceramic rod and positioned within the hot zone of the furnace.

The furnaces were equipped with a gas mixing apparatus. High-purity CO ($CO > 99.97$ vol%) and CO_2 ($CO_2 > 99.995$ vol%) gases were mixed with electronic valves (Millipore) in appropriate ratios to adjust the desired oxygen fugacities. For a given CO/CO_2 ratio, the resulting oxygen fugacity depends on temperature. Deines *et al.* (1974) give a comprehensive list to determine the CO/CO_2 ratio that is required to adjust a desired fO_2 value at given temperature. However, this list assumes pure gases, while the used gases do contain certain (albeit small) amounts of impurities.

The CO/CO_2 gas mixtures flow from the bottom to the top of the furnace tube at a rate of $200\,cm^3/min$. When using CO-rich gas mixtures the air was flushed out of the furnace with CO_2 before adding CO to avoid small explosions (reaction of CO with oxygen in air at high T). At temperatures of 1000 °C to 1300 °C, the use of CO/CO_2 gas mixtures allows to set up oxygen fugacities in the range between about NNO-6 and +5 (and also lower fO_2 for extremely CO rich mixtures and pure CO). The specific accessible oxygen fugacities are dependent on the synthesis temperature.

The oxygen fugacity was measured after the experiments with an yttria-stabilised zirconia sensor (SIRO2). The oxygen concentration gradient between the CO/CO_2 gas mixture at a given temperature and the reference gas (air) inside the sensor tube produces an electromotive force (e.m.f.), which is a measure of the oxygen fugacity. $\log fO_2$ can be calculated from the electromotive force by equation 2.1 (Nernst relationship, Huebner, 1975, 0.68 is value for air, i.e. reference) and translated into ΔNNO according to equation 2.2 (after O'Neill & Pownceby, 1993a).

$$\log fO_2 = \left(\frac{e.m.f.\,[\mathrm{mV}]}{T\,[K]} * 20.16 \right) - 0.68 \tag{2.1}$$

$$\Delta NNO = \log fO_2 - \frac{-478967 + 248.518T - 9.7961T \ln T}{RT \ln 10} \tag{2.2}$$

The fO_2 sensor was tested at 1300 °C against the Ni-NiO (NNO) and wüstite-magnetite (WM) equilibria. The fO_2 value bracketed for the first equilibrium matches well that of O'Neill & Pownceby (1993a). The experimental results for the WM equilibrium point to a value 0.2 to 0.25 higher than that of O'Neill (1988), but match better the values retrieved from the equation of Darken & Gurry (1945, reported by Huebner, 1971).

In fact, the WM buffer measurements of O'Neill (1988) were only performed at temperatures between 600 and 1000 °C and - given the large non-stoichiometry of wüstite in equilibrium with magnetite especially at high temperatures - it is doubtful whether the equation provided by this author can be adequately extrapolated to 1300 °C.

In gas mixtures with CO $>$ 1 vol%, the fO_2 values retrieved from the e.m.f. measurements are in general slightly higher (less than 0.2 log unit difference) than those listed in the tables of Deines *et al.* (1974). With decreasing CO content and temperature, the discrepancy between the two sets of values dramatically increases. At 1100 °C, for instance, the measured fO_2 value for pure CO_2 is 1.2 log unit higher than the value calculated by Deines *et al.* (1974). This is probably due to the presence of O_2 as impurity in the CO_2 used (N_2 and $O_2 <$ 25 vol pm, according to the supplier). Kress & Carmichael (1988) also noted differences between observed and predicted fO_2 values that strongly increased with increasing CO_2 proportion in the gas.

Repeated long-time e.m.f. measurements have shown that gas mixtures with CO contents higher than 1 vol% need less than 20 minutes to establish stable fO_2 values. At lower CO contents, however, up to one hour is necessary to attain the desired fO_2 value and fluctuations can still occur thereafter. On the whole, we estimate the accuracy of the experimental fO_2 values to about $\pm$0.2 log unit at moderate to low oxygen fugacities (ΔNNO $<$ +1; CO $>$ 1 vol%), but up to about $\pm$0.5 log unit at high fO_2.

2.2.3 Synthesis experiments

The control of oxygen fugacity during synthesis experiments has been achieved by two different approaches, i.e. by CO/CO_2 gas mixtures and by solid-state buffers.

Gas mixture experiments In gas mixture experiments the adjustment of the oxygen content of the sample to the prevailing oxygen fugacity is achieved by exchange of oxygen between sample and surrounding gas, provided enough fresh gas is flowed around the sample. Considering the small volume of the sample pellets (about 40 to 100 mm^3) a flow rate of 200 cm^3/min has proven sufficient to ensure a good oxygen exchange.

To optimize the contact between sample and gas, the sample pellets were placed on a grid of platinum wire (which is attached to a ceramic rod, Fig. 2.3). As sample and metal only share a very small surface and no melt ever occurs in the samples, negligible Fe-loss to the wire but maximum contact of sample with gas mixture can be achieved. Up to six pellets can be put in the furnace at once, distributed on two different levels of platinum grid with a distance of approximately 1 cm from one grid to the other.

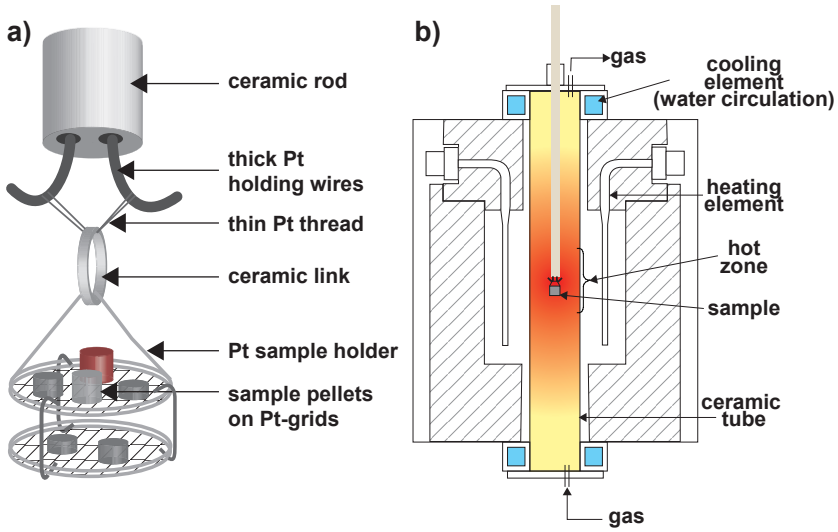

Fig. 2.3 Mounting for gas mixture experiments. a) Mounting of the sample pellet holder to a ceramic rod. b) Assembly of the gas mixing furnace and position of the sample in the furnace.

Both for $Fe_2O_3 + TiO_2$ and $Fe^\circ - TiO_2$ mixtures, the oxygen content of the starting material is strongly different from the desired bulk composition of the synthesis assemblage. Therefore, drastic changes in the total oxygen content of the sample pellet (by exchange with gas) occur during synthesis. In some cases, ternary $Fe^\circ - Fe_2O_3 - TiO_2$ mixtures have also been used, but the simpler binary mixtures were generally preferred.

At the beginning of the gas mixture experiments, the samples were positioned in

air in the constant temperature zone of the furnace. Then, the furnace was closed and the gas flow was turned on. To terminate the experiments, samples were drop quenched within the furnace or in some cases pulled out and dipped into water.

Solid-state buffer experiments In solid-state buffer experiments, oxygen is exchanged between the sample and a solid-state oxygen buffer to adjust the bulk oxygen content of the sample. Chemical equilibria that control oxygen fugacity are called oxygen buffers. Such chemical reactions involve components with different valence states of one element (Eugster, 1957; Eugster & Wones, 1962). To prepare a solid-state buffer pellet, the chemical components participating in such a reaction (e.g. nickel and nickeloxide) were mixed in appropriate proportions and pressed to a pellet (or into an adequate crucible). To fix oxygen fugacity, during the experiment a solid-state buffer pellet has to retain all components that are participating in the buffer reaction.

A solid-state buffer pellet has only a limited capacity to accept or donate oxygen. For this reason, the oxygen content of the starting material has to be close to that of the synthesis assemblage. This can be achieved by using ternary oxide mixtures ($Fe_2O_3 + Fe^{\circ} + TiO_2$).

Sample and buffer pellet were enclosed together in an evacuated silica glass ampoule ($\varnothing = 5 - 7\,\text{mm}$). The pellets were separated by a short (3 - 10 mm) silica glass rod to avoid contamination of the sample by the buffer material. Another rod was inserted to minimize the internal volume of the ampoule. Prior to sealing, the silica glass tube was evacuated with a rotary vane pump to a vacuum in the order of 10^2 mbar. Special care was taken not to oxidise the samples during the sealing procedure.

Previous experimental studies using the silica-glass tubes technique have shown no discernable oxidation related to either leakage of the ampoule or insufficient vacuum within the ampoule (Lattard & Partzsch, 2001).

Ampoules were attached to a ceramic rod and positioned in the hot zone of the furnace. At the end of the experiments, the silica-glass ampoules were pulled out of the furnace and quenched into water, a procedure that lasted less than one minute.

2.2.4 Re-equilibration experiments

The difference between re-equilibration experiments and synthesis experiments is the different starting material. We used assemblages of synthetic Fe-Ti oxides for re-equilibration experiments, compared to reagent mixtures for synthesis experiments. The experimental techniques, however, are identical to those of gas mixing and solid-state buffer synthesis experiments. During a re-equilibration experiment,

phase assemblages and phase compositions of the starting materials are expected to adjust to the new fO_2-T conditions.

2.2.5 Annealing experiments

For annealing experiments, fragments of high-T run products (30-100 mg) were sealed in evacuated silica ampoules ($\varnothing = 3-4$ mm) following the procedure described for solid-state buffer experiments in section 2.2.3. However, in contrast to solid-state buffer experiments, *no* solid-state buffer pellet was added. The purpose of sealing the samples in evacuated silica glass ampoules was to keep the bulk composition of the synthesis product fixed (including oxygen, not fO_2) during 950 °C annealing.

2.2.6 Quenching procedures

Drop quench In most cases the run products (pellets) of gas mixing runs were drop-quenched into water at the bottom of the furnace. Sample and sample holder were attached to a ceramic rod by using a Pt wire ($0.100-0.125$ mm diameter, see Fig. 2.3). The Pt wire was molten electrically or ripped mechanically (by turning or pulling the holding wires, compare Fig. 2.3) at the end of the experiment.

"External quench" Sometimes (e.g. when the holder was sticking to the attachment and no drop-quench was possible) the samples had to be pulled out of the furnace (i.e. exposed to air) and quenched into water outside the furnace. Usually, this procedure took less than one minute ($5-60$ s).

In rare cases, the CO gas was turned off few minutes before the furnace was opened. Afterwards, the sample was pulled out of the furnace and quenched into water. In these rare cases the complete procedure could last up to five minutes. During this time, the sample was subjected to oxidizing conditions at high T (first pure CO_2 gas, then air).

Quenching of SiO_2 glass ampoules Silica-glass ampoules of both synthesis and annealing runs were pulled out of the furnace and quenched into water. Pulling out and dipping into water took <10 seconds, but it has to be considered that sample pellets enclosed in ampoules cool slower than pellets that are directly quenched into water. Furthermore, the cooling rate of annealing ampoules ($\varnothing = 3-4$ mm) is expected to be slightly higher than of synthesis ampoules ($\varnothing = 5-7$ mm). No effect of the different quenching rates could be detected in the run products.

In contrast to synthesis pellets from gas mixing experiments, which are exposed to air during pulling out of the furnace, the sample in a silica ampoule remains in the atmosphere inside the ampoule while temperature decreases.

2.3 Characterisation and analysis of the run products

2.3.1 Optical examination (eye, binocular)

After the runs, both pellets and ampoules were checked for distinctive features. During the experiment, pellets from gas mixing runs lose their original reddish (due to Fe_2O_3) or grey (due to Fe°) colour and become dark grey to anthracite and generally have a weak lustre. Sometimes, different lustre points to differences in phase distribution or grain size in portions of the sample. A light, weakly lucent surface indicates the presence of metallic iron.

Ampoules were checked for cracks or fractures and dimming of the SiO_2 glass. Cracks were observed very rarely and in these cases are assumed to have formed during quenching. As cracks may potentially also point to a leaky ampoule, the concerning samples have been discarded.

The inner wall surface of some *synthesis ampoules* was milky and sometimes brownish dimmed, especially close to the sample or buffer pellets. Observations revealed a very thin reaction film covering the silica glass. The tube wall remains unchanged in most of its thickness. The ampoule is thus considered to be leak proof. Si-contamination of sample or buffer was *not* observed.

In rare cases, *annealing ampoules* displayed slightly dimmed tube walls. This was observed exclusively in very few ampoules that contained samples equilibrated at very low fO_2 prior to annealing. The dimming is probably due to the formation of metallic Fe° that easily evaporates into the gaseous phase and partly condensates at the SiO_2 glass.

2.3.2 X-ray powder diffraction

Qualitative phase determination The phases present in the run products were identified by X-ray powder diffraction at room temperature. This was done regularly for synthesis run products. Due to the limited amount of material available, only selected re-equilibration run products and annealing run products were chosen for X-ray analysis. X-ray diffraction measurements in the range $2\Theta = 10 - 80^\circ$ have been carried out with a Philips PW 3710-BASIS powder diffractometer, using CuKα radiation (40 kV, 30 mA) and a secondary monochromator. Samples were

powdered and prepared on a flat glass holder. Phases were identified by means of the JCPDS-ICDD database (PCPDFWIN, version 1.30, 1997).

Determination of lattice parameters Lattice parameters were determined by using the Philips PW 3710-BASIS powder diffractometer, as described above. X-ray diffraction patterns in the range $2\Theta = 10 - 110^\circ$ were acquired at room temperature. Counting rates were $0.01^\circ 2\Theta/$ sec, with counting times of two seconds per step and a step size of $0.02^\circ 2\Theta$. Samples were prepared on a flat glass holder from $7 - 20$ mg sample material, which was ground and mixed with a Si standard powder (mixing ratio: weight proportion Si/sample = 1/2).

Rietveld analysis using the GSAS® software package after Larsen & von Dreele (2000) was applied to determine a_0. The refinement procedure involved fitting of lattice parameters, atom position coordinates, isotropic thermal parameter and site occupancy multiplier for each phase. The background was fitted by a Chebyshev polynomial, with 10 to 15 (usually 12) background parameters. The Gaussian and Lorenzian components of the peaks were refined separately for each phase to fit the profile shapes. Further, refinement accounted for 2Θ zero offset, profile asymmetry, specimen displacement and transparency. Intensities were fitted by a quantitative phase analysis and refinement of preferred orientation of silicon (111).

2.3.3 Scanning electron microscopy

Scanning electron microscopy was used to observe and document the textures and phase assemblages visible in embedded, polished and carbon-coated sample fragments, and sometimes also to investigate the surface topography (e.g. crystal shapes and sizes) of the sample pellet surface. This has been performed with a LEO 440 scanning electron microscope (SEM), equipped with a tungsten cathode, and generally operated at an accelerating voltage of 15 kV and a filament current of $2.5 - 2.8$ A at a working distance of $12 - 20$ mm.

Textures and phase assemblages of the samples have been examined on polished sections of all quenched run products by using the BSE (back scattered electron) detector and a sample current of about $1 - 10$ nA. The intensity of detected Back Scattered Electrons (BSE) is dependent on the atomic numbers of the elements in the examined material, and thus gives information on the composition of the observed phases. As we deal with Fe-Ti oxides, a lighter colour in the BSE picture generally refers to a higher concentration of Fe (atomic numbers: Fe: 26, Ti: 22, O: 8). Magnesium (Mg, atomic number: 12) and aluminium (Al, atomic number: 13), which could complicate this relation, are usually present in small amounts only.

To investigate pellet surface features (on small uncoated sample fragments), the SE (secondary electrons) detector has been used. Sample current has been adjusted to about $500 - 1000\,\mathrm{pA}$.

2.3.4 Electron microprobe (EMP) analysis

To determine the cationic composition of phases in all examined samples, electron microprobe analysis was carried out on polished, carbon-coated sections of the sample fragments. Up to six samples were embedded together in separate drillings within one sample holder (diameter of sample holder: 1 inch).

The phases were analysed for Fe, Ti, Mg and Al with a Cameca electron microprobe (SX-51) operated at an acceleration voltage of 15 kV and a beam current of 20 nA. Counting times were 20 s on peak and 10 s on background. The standards used were synthetic hematite (for Fe), rutile (for Ti), periclase (for Mg) and gahnite (for Al). The raw data were corrected with the "PAP" software (Pouchou & Pichoir, 1985). To avoid possible instrumental drift, the standardisation was checked at least every two hours. If the measurements could not be reproduced within less than 1%, the standardisation was repeated.

Repeated analyses on unzoned grains show that the precision of the analyses is excellent (1σ standard deviations for the Ti/(Ti+Fe) values $\leq 0.5\,\%$ relative). Duplicate or triplicate series of analyses on about 15 samples yielded comparable Ti/(Ti+Fe) per cent values within $\pm 0.2\,\mathrm{at\%}$ (Fig. 2.4).

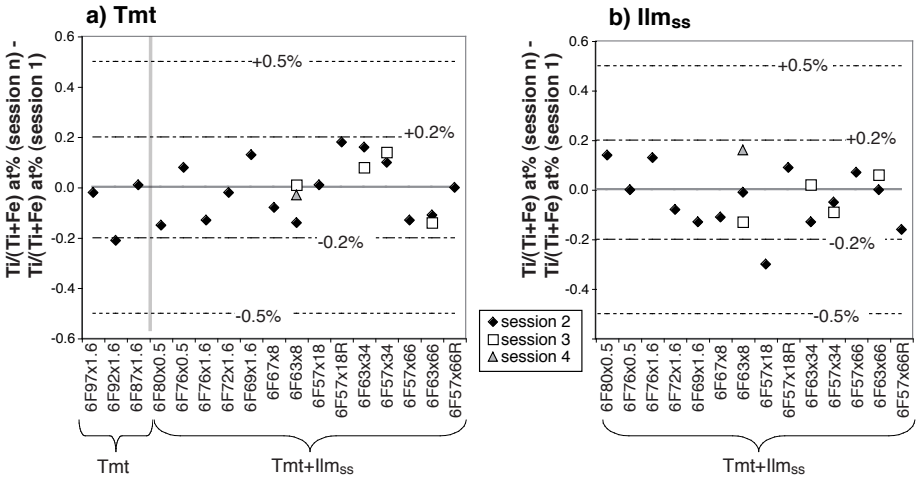

Fig. 2.4 Deviation in Ti/(Ti+Fe) at% between repeated EMP analyses on a) Tmt and b) Ilm$_{ss}$. Note that identical symbols do not refer to the same EMP session, but to the second, third or fourth session for each sample.

Investigators that are using electron microprobe analysis to gain exact analyses of Fe-Ti oxides have long discussed that the use of hematite and rutile as standard materials, especially for ilmenite$_{ss}$ analyses, might result in an overestimation of Ti and an underestimation of Fe. This is supported by analyses of well-known materials by other scientists at facilities outside the Mineralogisches Institut Heidelberg (e.g. Bernard Evans, Seattle, personal comm.). It is conceivable that this systematic error may be avoided by using ilmenite$_{ss}$ and/or titanomagnetite of well-known composition as calibration standards.

In contrast, measurements at the SX51 in Heidelberg gave numerous hints that neither overestimation of Ti nor underestimation of Fe occurred (in Heidelberg), when using hematite and rutile calibration standards. In many single-phase samples, the cationic ratio of the starting mixture could be reproduced by EMP analysis (e.g. Table 2.1, samples produced within the thesis of Ralf Engelmann, Heidelberg). Further, comparative analyses have been performed by D.H. Lindsley at

Table 2.1 Composition of single-phase Tmt from EMP analysis, compared to Ti/(Ti+Fe) ratio of sample bulk from starting mixture

name	Ti/(Ti+Fe) [at%]		
	bulk	EMP	
		mean	σ
6F69x81	31.00	30.94	(20)
6F68x81	32.00	31.95	(11)
6F67x81	33.00	32.95	(11)

Stony Brook, using a natural ilmenite calibration standard. The analyses on two Ti-rich Tmt-Ilm$_{ss}$ run products from this thesis yielded only slightly higher Ti/(Ti+Fe) at% (difference $\leqslant 0.5$ at%) than those given in this thesis. Thus, this confirms the Heidelberg analysis results.

Summarised, these observations indicate that the possible overestimation of Ti and underestimation of Fe by the electron microprobe may in some way be associated with the microprobe used (e.g. correction software...) rather than with the calibration standards.

Regarding the analyses carried out within the present thesis at the Cameca SX-51 microprobe in Heidelberg, using hematite and rutile as standards, it is safe to estimate the accuracy for all compositions at ± 0.005 for the Ti/(Ti+Fe) values, i.e. $\pm 0.5\%$ for the per cent values. However, repeated analyses on a single-phase, very homogeneous synthetic ilmenite sample suggest that the MgO content of the sample

is probably underestimated by up to 5 % relative (for a MgO content of about 2 wt%, Table 2.2).

Table 2.2 EMP analysis [wt%] for Ilm_{ss} of single-phase sample 6IT60M2x1.5a, compared to wt% calculated from starting mixture assuming Ilm_{ss} oxygen content (i.e. two cations and three oxygens pfu) and calculating all iron as FeO.

wt%	EMP[1]		calculated	EMP/calculated
	mean	σ		
$Fe_{tot}O$	54.38	0.33	54.83	0.992
TiO_2	40.35	0.24	40.65	0.993
MgO	2.00	0.03	2.07	0.966
Σ	96.78	0.39	97.55	0.992
Ti/(Ti+Fe)	40.02	0.21	40.00	1.001

1) 27.02.2004, n=10

2.3.5 Electron energy-loss spectroscopy

Tmt non-stoichiometry δ can be calculated from $Fe^{3+}/\Sigma Fe$, when the cationic ratio Ti/(Ti+Fe) of the sample is known (from EMP analysis). Thus, we applied electron energy-loss spectroscopy (EELS) to determine $Fe^{3+}/\Sigma Fe$ and derive δ.

Fe $L_{2,3}$-ELNES (energy-loss near-edge structure) spectra were collected with a Gatan DigiPEELS 766 parallel electron spectrometer attached to a Philips CM 12 transmission electron microscope. The measurements were carried out at the Technische Universität Darmstadt in cooperation with Peter van Aken.

For sample preparation, three different methods have been used:

1) Small sample fragments were crushed between glass plates to produce small and thin wedge-shaped fragments.

2) The sample was cut out of a thin section by using an ultra sonic driller and then thinned to perforation by Ar ion-beam bombardment.

3) Thin foils were cut of the sample with a focussed ion beam (FIB). Samples were mounted on a standard TEM grid. The FIB foil has a constant thickness of < 100 nm.

For more details on the technique we refer to chapter 5, section 5.5.

3 Textures of synthetic sub-solidus Fe-Ti oxide assemblages in the system Fe-Ti±Al±Mg-O

3.1 Introduction

Micro-textures of both natural and synthetic Fe-Ti oxide minerals have long caught the interest of outstanding scientists. Fe-Ti oxide textures give insight into (micro-) processes which occur in Fe-Ti oxide minerals, and which are driven by changes in redox conditions or temperature (e.g. Buddington & Lindsley, 1964; Haggerty, 1991a; Price, 1980, 1982). However, interpretation of the textural observations is not unique. This is shown by the prominent discussion in the 1960s between D.H. Lindsley, A.F. Buddington and P. Ramdohr: Trellis ilmenite exsolution in titanomagnetite had been interpreted by Ramdohr (e.g. 1955) to originate from unmixing of extensive solid solution between $FeTiO_3$ and Fe_2TiO_4 (e.g. Vincent *et al.*, 1957). Finally, it was the experimental work of Donald H. Lindsley, which showed that this texture was due to oxidation (Buddington & Lindsley, 1964).

Textures in natural Fe-Ti oxide samples (e.g. zoning, trellis and sandwich lamellae etc.) have been widely described in Paul Ramdohr's pioneer books "Lehrbuch der Erzmikroskopie" (Schneiderhöhn & Ramdohr, 1931) and "Die Erzminerale und ihre Verwachsungen" (Ramdohr, 1955). An overview is also given in S.E. Haggerty's Mini-Atlas (Haggerty, 1991a).

Within this study, Fe-Ti oxide textures have been taken into account to decide whether equilibrium could be attained or at least closely approached during high-T synthesis or re-equilibration experiments. The experiments yielded mostly binary, but also single-phase or ternary polycrystalline assemblages. A random distribution of equigranular crystals over the sample, and chemical homogeneity of the crystals and of a phase over the sample pellet point towards equilibrium. Only few of the investigated samples display clear evidence for dis-equilibrium, mainly chemical inhomogeneity (section 3.6) of crystals. However, investigation of the samples has revealed some special textural features:

- Especially binary samples produced from $Fe_2O_3 + TiO_2$ mixtures often display monomineralic rims (see section 3.4) at the surface of a sample pellet. These concentric features are frequent in our samples, but to our knowledge have only been reported once in literature by Senderov *et al.* (1993). These

authors suggested that the monomineralic rims at the surface of their synthetic Fe-Ti oxide sample pellets formed during quenching. However, they give neither a comprehensive description nor an explanation for the formation of the texture. Despite the rare report, to our knowledge such features seem not to be an uncommon phenomenon in solid-state Fe-Ti oxide synthesis experiments (Lindsley, pers. comm.). Concentric textures and inhomgeneities are also observed in single-phase samples and in samples produced from $Fe^{\circ} + TiO_2$ mixtures.

- Exsolution textures have been observed, which have already been described in literature for both synthetic and natural samples (e.g. Buddington & Lindsley, 1964; Lattard, 1995). According to their origin, exsolution textures can be divided into
  - oxy-exsolution textures in the sense of Buddington & Lindsley (1964), forming as a result of oxidation (observed in externally quenched high-T samples, see section 3.5), and
  - exsolution textures that are related to vacancy relaxation (Lattard, 1995) at constant bulk composition (observed in annealed samples, will be discussed in chapter 5).

This chapter gives an overview of the textures encountered in synthetic high-T Fe-Ti assemblages produced within this thesis and tries to relate these textures to the processes occurring during the experiments. Understanding the observed textures is essential for the further use and interpretation (chapters 4, 5, 6) of the data derived from our run products.

The focus is on synthesis runs, which were all performed at subsolidus conditions. In some cases, re-equilibration run products are considered for comparison.

3.2 General remarks on experimental conditions and procedures

The aim of the synthesis experiments was to produce mainly binary, but also ternary and single-phase Fe-Ti oxide assemblages. Synthesis runs were performed at subsolidus conditions using starting mixtures with different bulk cationic ratio Ti/(Ti+Fe), at 1000 °C to 1300 °C, 1 bar and oxygen fugacities ranging from NNO-5 to NNO+5. Oxygen fugacity has been controlled by using CO/CO_2 gas mixtures, or by solid-state buffers (only for $T \leq 1100$ °C) which were enclosed together with the sample in an evacuated SiO_2 glass ampoule (see chapter 2 for experimental details).

In the Fe-Ti-O system three different combinations of the reagents Fe_2O_3, Fe° and TiO_2 were used for the starting mixtures (see also chapter 2):

a) $Fe_2O_3 + TiO_2$,

b) $Fe^\circ + TiO_2$, and

c) $Fe_2O_3 + Fe^\circ + TiO_2$.

For few type a) starting mixtures, the reagents were separately pre-annealed at $800 - 1000\,^\circ C$ before mixing. For experiments in the systems Fe-Ti-Mg-O, Fe-Ti-Al-O and Fe-Ti-Mg-A-O, small amounts of MgO and/or Al_2O_3 were added to starting mixtures, which were generally of type a) but also of type c).

Cylindrical pellets with a diameter of about 5 mm and about 2 to 5 mm in height were prepared from the starting mixtures. To facilitate the attainment of equilibrium, especially runs with Mg or Al bearing samples were interrupted once (after 1-2 days). The run was continued (at identical T and fO_2) after grinding the sample to a powder and producing a new pellet. This has also been accomplished for some samples in the system Fe-Ti-O at $T < 1200\,^\circ C$.

Further, short-time experiments with run durations of 1, 4 and 24 hours have been carried out to investigate the development of textures during early stages of the experiment.

For more detailed information on experimental conditions and procedures, and analytical methods see chapter 2.

3.3 General description of common textural features

3.3.1 Crystal shapes, sizes and distribution

Synthesis run products (one, two, or rarely three coexisting Fe-Ti oxide phases: e.g. Tmt, Tmt+Ilm_{ss}, Tmt+Ilm_{ss}+Psb_{ss}; see Fig. 3.1) consist of polycrystalline, roughly equigranular aggregates, with grain sizes around $10 - 50\,\mu m$ (increasing grain size with increasing T). Mostly grains are roughly isometric and subhedral. In rare cases Psb_{ss} forms perfectly euhedral, isometric to oblong rhomboid crystals. The grains are randomly orientated over the whole sample and with respect to each other.

3.3.2 Porosity and cracks

Porosity usually amounts to about $10 - 20\,\%$ of the sample volume. The pores may be isometric or elongated (reaching up to some tens of μm) and generally do not

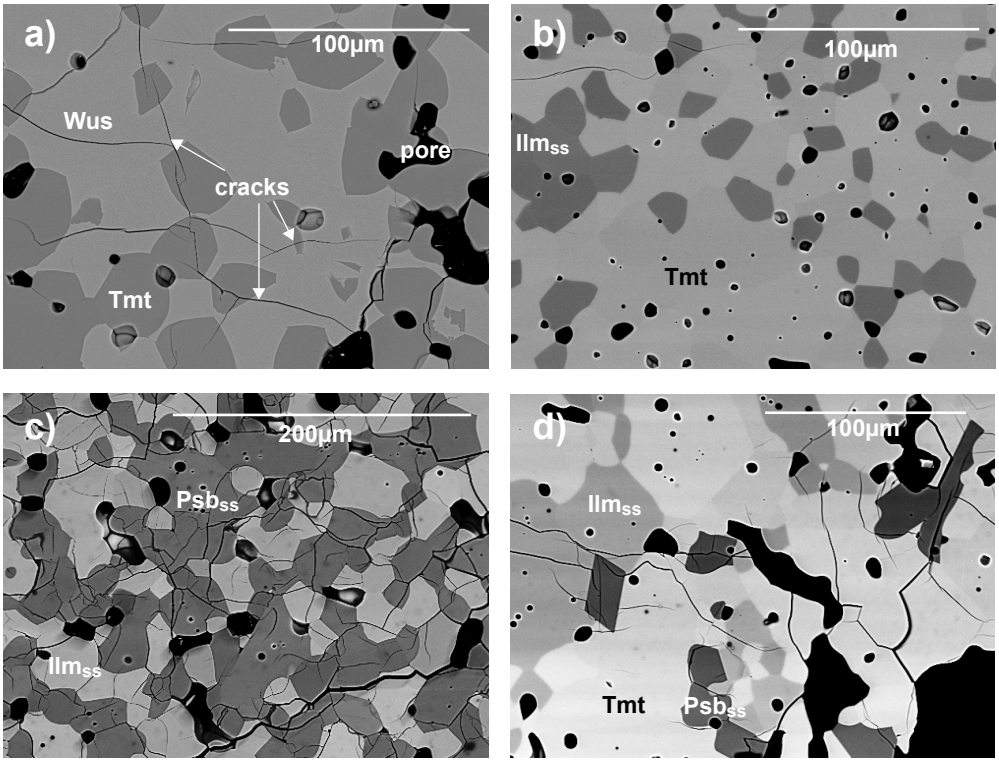

Fig. 3.1 BSE pictures of Fe-Ti oxide two-phase samples consisting of a) Tmt+Wus (6F83x66), b) Tmt+Ilm_{ss} (6F72x4.4), c) Ilm_{ss}+Psb_{ss} (6F47x7), and d) one three-phase sample Tmt+Ilm_{ss}+Psb_{ss} (6F59.5A5.5x66), all synthesised at 1300°C. All pictures show pores and cracks, as exemplarily marked in picture (a).

show a preferred orientation. Pores (about 10 to 30 µm in diameter) usually occur *between* mineral grains , but small ($\leq$ 10 µm), usually isometric pores can also occur *within* the grains.

Psb_{ss} often shows regular, prismatic voids within the Psb_{ss} grains ("negative crystals", Fig. 3.2), which are arranged in a preferred crystallographic orientation within the crystal. This orientation has not been determined. However, as the voids are usually arranged parallel to the long side of the Psb_{ss} grains, an orientation parallel to the crystallographic c-axis may be suggested. The "negative crystals" preferably occur in Psb_{ss} that was synthesised at intermediate to high fO_2.

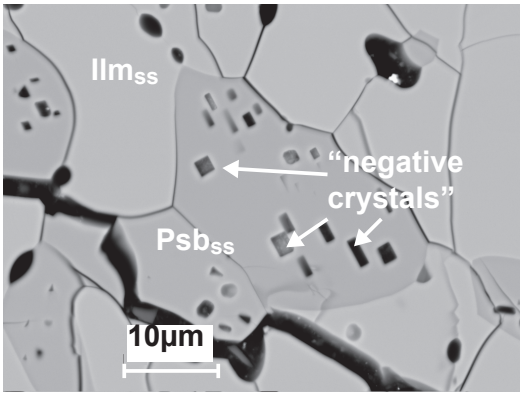

Fig. 3.2 Oriented, prismatic voids ("negative crystals") in Psb_{ss} crystals within a Ilm_{ss}-Psb_{ss} sample (3F57x0.4). The sample also displays pores and cracks (black).

Further, investigation of polished sections shows frequent cracks within the samples. These can be divided into two types.

- First, we observed relatively broad "primary" cracks, which clearly formed during synthesis, probably as a result of shrinking during very early stages of the experiment. They may extend deep into the pellet and - as far as they are open to the surrounding atmosphere - have to be treated as sample surface.
- Second, there are fine "secondary" fractures, which probably form during quenching or preparation of the section, thus *after* the high temperature treatment of the sample. They often cross single crystals. "Secondary" fractures can be seen very often in BSE pictures but have no significance for our investigations.

3.4 Formation of concentric textures - correlation to the starting material

3.4.1 General remarks

In most of the synthesis products, some kind of concentric feature has been observed.

Many samples display concentric variations in local bulk Ti/(Ti+Fe). The term local bulk describes the average Ti/(Ti+Fe) over the present phases in a small area of the sample (some tens of µm). Variations in local bulk chemistry do not have to represent variations in the overall sample bulk, i.e. a decrease in Ti/(Ti+Fe) within one sample region can be compensated by an increase in another.

In single-phase samples, a variation in local bulk across the sample corresponds to a variation in phase composition. In assemblages of two or more phases, a variation in local bulk can be achieved by a variation in the modal abundances of the phases, or a change of phase assemblage, e.g. the formation of a monomineralic rim.

SEM-investigation of one pellet fragment (not embedded, sample 5F44x2.8 synthesised at 1200 °C from $TiO_2 + Fe^{\circ}$-mixture) reveals an outer crust around an inner, highly porous sample region. The crust partly exfoliates from the pellet (see Fig. 3.3). Observations on cross sections of other samples (e.g. Fig. 3.11) indicate that the outer part of a monomineralic sample rim (both Fe- or Ti rich, see sections 3.4.3 and 3.4.4) may peel off the pellet in many cases. As the crust may be easily removed mechanically, it might often not have been conserved during preparation of the cross sections.

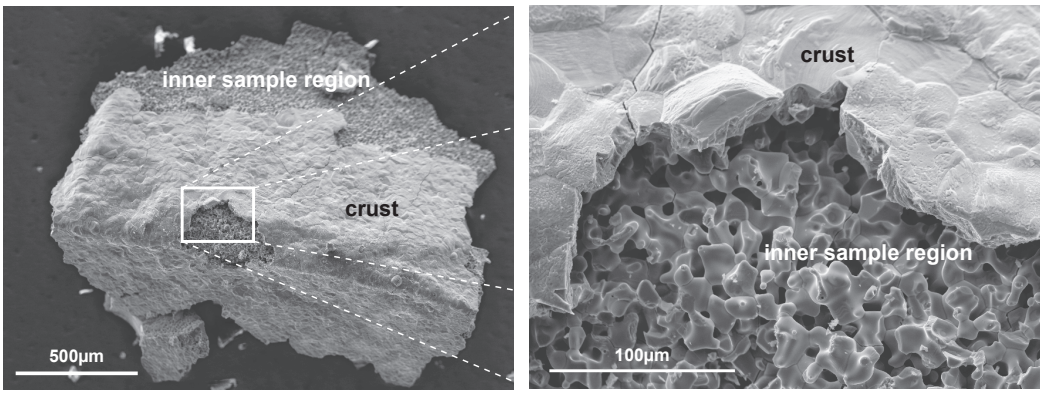

Fig. 3.3 SE pictures of a pellet fragment of synthesis sample 5F44x2.8: A dense outer crust around the highly porous inner pellet.

The observations from the present study reveal that concentric textures are essentially influenced by the type of the starting mixture ($Fe_2O_3 + TiO_2$, $Fe^\circ + TiO_2$, $Fe_2O_3 + Fe^\circ + TiO_2$) and the treatment of a sample (e.g. pre-annealing of the reagents, intermediate grinding etc.). Most samples have been produced from $Fe_2O_3 + TiO_2$ mixtures in gas-mixing experiments.

3.4.2 Experiments with $Fe_2O_3 + TiO_2$ starting mixtures from pre-annealed reagents

Samples (mainly Tmt+Ilm_{ss} assemblages) synthesised from mixtures of separately pre-annealed Fe_2O_3 and TiO_2 do not show a concentric inhomogeneity but display a coarser texture (Fig. 3.4) than those produced from un-heated reagents. Throughout the sample pellet monomineralic areas of both phases are observed, which usually are grain aggregates rather than single grains and reach up to $> 100\,\mu m$ in diameter. Compared to samples synthesised from unheated starting materials (see following section), porosity is increased concerning both absolute amount and pore size. Additionally to small pores within the monomineralic aggregates, extensive irregular voids can be observed between the monomineralic areas.

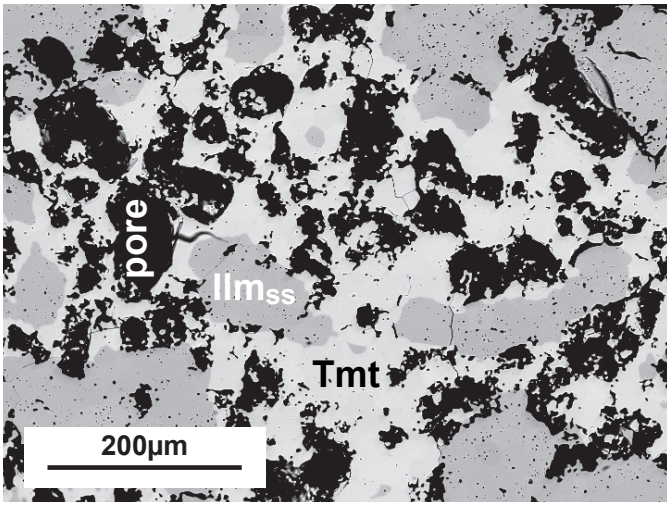

Fig. 3.4 BSE picture of a Tmt+Ilm_{ss} sample (5F60x83.5) synthesised at 1200 °C, NNO-4.6 from separately pre-annealed reagents ($Fe_2O_3 + TiO_2$).

3.4.3 Experiments with $Fe_2O_3 + TiO_2$ starting mixtures

Samples synthesised from $Fe_2O_3 + TiO_2$ mixtures typically display *increasing* local bulk Ti/(Ti+Fe) towards the sample surface.

Binary assemblages In samples which consist of binary assemblages Tmt+Ilm_{ss} or Ilm_{ss}+Psb_{ss}, the increasing local bulk Ti/(Ti+Fe) towards the sample surface is usually reflected in the formation of a Ti-rich monomineralic rim ($20-200\,\mu m$ in thickness). The rim consists of Ilm_{ss} or Psb_{ss}, respectively, and extends along the sample pellet surface and along "primary" cracks (Fig. 3.5, Fig. 3.6). Such samples make up the majority of the synthesis products investigated within this thesis.

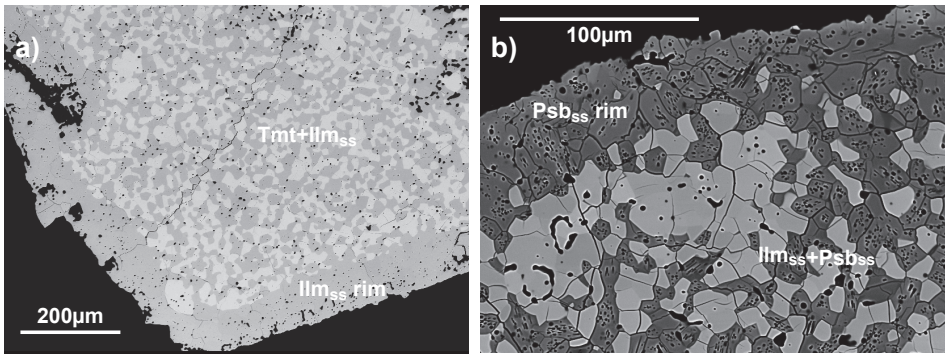

Fig. 3.5 Ti-rich rims around two-phase Fe-Ti oxide assemblages in samples synthesised from $TiO_2 + Fe_2O_3$ starting mixtures: a) monomineralic Ilm_{ss}-rim around a Tmt-Ilm_{ss} assemblage (5F69x1.25), b) monomineralic Psb_{ss}-rim around Ilm_{ss}-Psb_{ss} (3F57x0.4).

The phase composition in the rim is often slightly richer in Ti compared to that in the central two-phase region (Table 3.1). Some samples are zoned in Ti-content towards the sample surface (Fig. 3.7). As the monomineralic rims are usually thin, it is often hard or even impossible to carry out EMP linescans.

Few Tmt+Ilm_{ss} samples display a second, outermost thin Psb_{ss} rim surrounding the first monomineralic Ilm_{ss} rim (Fig. 3.8). EMP analyses of these rims show that Ti/(Ti+Fe) increases within the monomineralic Ilm_{ss} rim towards the outer Psb_{ss} rim. A chemical inhomogeneity within the Psb_{ss} rim ($20-60\,\mu m$) could not be observed. In the central two-phase region and along the monomineralic rims, the phase compositions are in agreement with *one* oxygen isobar at synthesis temperature. The compositions of directly adjoining Psb_{ss} and Ilm_{ss} grains (i.e. at direct contact between Ilm_{ss} rim and outer Psb_{ss} rim), and Tmt and Ilm_{ss} grains (i.e. in central

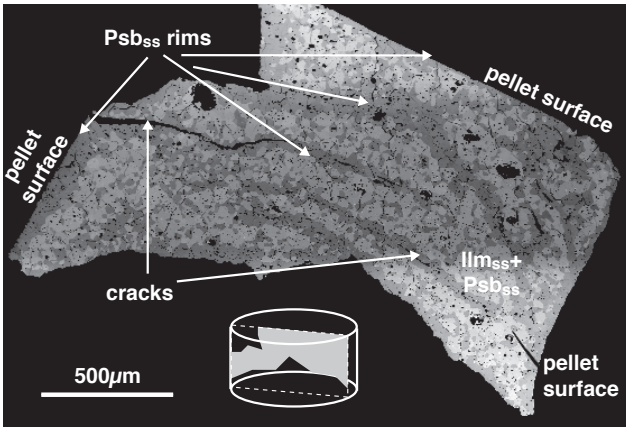

Fig. 3.6 BSE picture of a pellet fragment of sample 6F42x34. Around the central Ilm$_{ss}$+Psb$_{ss}$ assemblage, the sample displays monomineralic Psb$_{ss}$ rims at the pellet surface and along "primary" cracks, which extend from the pellet surface deep into the sample. Sketch illustrates the presumed position of the section within the sample pellet.

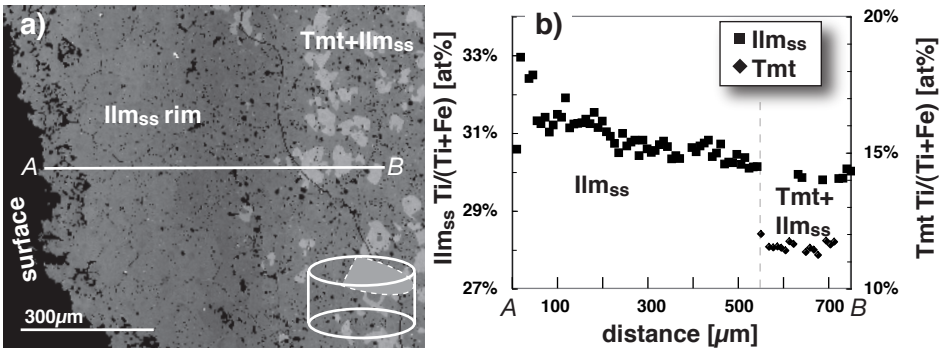

Fig. 3.7 a) BSE picture and b) EMP linescan of an Ilm$_{ss}$ rim around a central Tmt+Ilm$_{ss}$ assemblage (sample 5F72x0.5). The white line in (a) marks the position of the linescan shown in (b). The thickness of the rim is probably overstated due to a cutting effect. The sketch in (a) illustrates presumed position of the section within the pellet.

Table 3.1 Selected Tmt+Ilm_{ss} (upper part of the table) and Ilm_{ss}+Psb_{ss} (lower part) samples with monomineralic Ilm_{ss} and Psb_{ss} rims, respectively: Comparison between phase compositions in central sample region vs. rim.

run no	T[°C]	ΔNNO	center			rim		
			n	Ti/(Ti+Fe) [at%]		n	Ti/(Ti+Fe) [at%]	
				mean	(σ)		mean	(σ)
Tmt+Ilm_{ss} samples with monomineralic Ilm_{ss} rims: Ilm_{ss} compositions								
6F72x1.6	1303	0.7	10	36.21	(17)	5	36.76	(28)
6F63x34a	1301	-2.4	10	48.81	(20)	3	49.39	(26)
6F57x34a	1301	-2.4	10	48.89	(17)	3	49.42	(09)
5F76x0.5	1202	1.6	10	30.14	(18)	5	30.54	(21)
5F72x0.5	1202	1.6	10	30.12	(26)	5	31.21	(53)[2]
5F72x1.25	1200	0.7	10	36.34	(16)	3	37.92	(63)[2]
5F69x1.25[1]	1200	0.7	10	36.57	(20)	3	36.72	(14)
5F63x2.8[1]	1200	-0.1	10	40.20	(22)	3	40.27	(43)
5F63x33.5[1]	1201	-2.6	10	49.02	(26)	3	48.92	(14)
5F57x33.5	1201	-2.6	10	48.91	(12)	3	49.58	(19)
5F54.5x61.5[1]	1200	-3.6	10	49.50	(17)	3	49.83	(28)
5F54.5x83.5	1200	-4.6	10	50.20	(18)	3	50.86	(16)
3F63x30[1]	1100	-2.6	10	48.75	(34)	3	49.27	(50)[2]
Ilm_{ss}+Psb_{ss} samples with monomineralic Psb_{ss} rims: Psb_{ss} compositions								
F42(g)6[1]	1300	-0.9	10	62.55	(22)	5	62.68	(22)
6F42x34[1]	1300	-2.4	10	65.87	(14)	3	66.00	(09)
6F42x34a	1301	-2.4	10	65.64	(25)	3	66.22	(22)
5F50x1.25[1]	1200	0.7	10	56.42	(11)	3	56.42	(14)
5F47x2.8[1]	1200	-0.1	10	58.96	(22)	3	58.73	(16)
5F42x33.5	1201	-2.6	10	65.77	(14)	3	66.67	(34)
5F42x61.5	1200	-3.6	10	67.51	(21)	3	68.02	(14)
3F57x0.4[1]	1099	1.5	10	51.40	(30)	6	51.19	(35)
3F50x1.25	1101	0.5	10	57.54	(17)	3	57.85	(12)

[1]) rim and center agree within 1σ
[2]) zoned rim

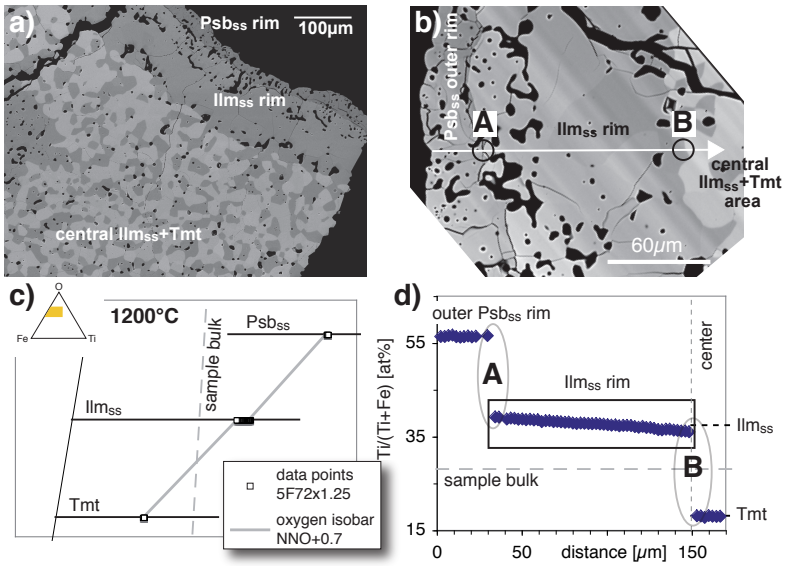

Fig. 3.8 a), b) BSE pictures of sample 5F72x1.25 displaying an outer monomineralic Psb_{ss} rim around an Ilm_{ss} rim, which surround the central Tmt+Ilm_{ss} assemblage. White arrow in (b) indicates position of EMP linescan shown in (c) and (d). c) Compositions of all phases (squares) along the EMP linescan are on one oxygen isobar (grey line, according to further experimental data, Table 3.2 and appendix A.3). d) Within the Ilm_{ss} rim the EMP linescan shows an increasing Ti-content towards sample surface. Analyses presented in Table 3.2 are from regions A and B.

sample region) comply with Ilm_{ss}+Psb_{ss} and Tmt+Ilm_{ss} composition in other synthesis samples (chapter 4) synthesised at comparable T-fO_2 conditions (Table 3.2).

In binary assemblages, a change in local bulk Ti/(Ti+Fe) usually translates into a change in modal phase abundances. In sample 5F69x2.8a (Fig. 3.9, Tmt+Ilm_{ss}), an Ilm_{ss} rim (about 100 µm in thickness) covers the pellet (A in Fig. 3.9). Towards the center of the pellet it is adjoined by a binary Tmt+Ilm_{ss} zone of high modal proportion of Tmt (about $200-300$ µm in thickness, B in Fig. 3.9). In the central Tmt+Ilm_{ss} assemblage (C in Fig. 3.9) the Tmt proportion is slightly lower than in the outer Tmt+Ilm_{ss} belt. The compositions of the phases are homogeneous over the whole binary zone (regardless of phase abundances, see Fig. 3.9).

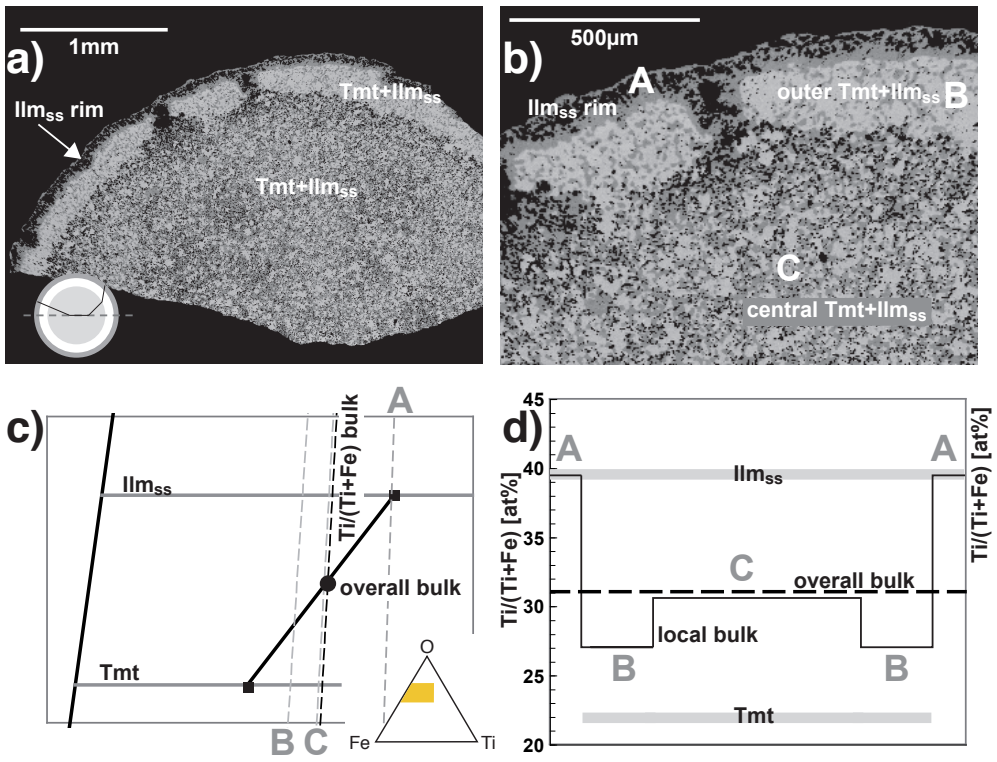

Fig. 3.9 a), b) BSE pictures of sample 5F69x2.8a, showing an Ilm_{ss} rim (A) and concentric variations in phase abundances in Tmt+Ilm_{ss} area (zones B, C). Sketch illustrates section through complete pellet and position of fragment. c) Phase compositions (black squares), sample bulk Ti/(Ti+Fe) (black dashed line) and local bulk compositions (grey dashed lines) schematically illustrated in the Fe-Ti-O triangle. d) Schematized illustration of phase compositions (grey bars) and variations in local bulk (black line) over the sample, for a profile through the pellet as sketched in picture (a) (dashed grey line in sketch).

Table 3.2 Compositions of adjoining Psb_{ss} and Ilm_{ss} crystals (bold, region A in Fig. 3.8d), and adjoining Ilm_{ss} and Tmt crystals (bold, B in Fig. 3.8) from EMP linescan along sample 5F72x1.25, as illustrated in Fig. 3.8. Comparison with Tmt and Ilm_{ss} composition of central grains in sample 5F72x1.25 (italic), and other samples synthesised at identical T and fO_2 (i.e. 1200 °C and NNO+0.7).

	sample	Tmt			Ilm_{ss}			Psb_{ss}		
		n	Ti/(Ti+Fe) [at%]		n	Ti/(Ti+Fe) [at%]		n	Ti/(Ti+Fe) [at%]	
			mean	(σ)		mean	(σ)		mean	(σ)
					Ilm_{ss}+Psb_{ss}					
A	**5F72x1.25**				**1**	**39.20**		**1**	**56.59**	
	5F50x1.25				10	39.10	(18)	10	56.42	(11)
					Tmt+Ilm_{ss}					
B	**5F72x1.25**	**1**	**18.13**		**1**	**36.06**				
	5F72x1.25	*10*	*18.03*	*(15)*	*10*	*36.34*	*(16)*			
	5F69x1.25	10	18.22	(10)	10	36.57	(20)			

Single-phase samples Single-phase samples - especially Tmt - are generally inhomogeneous in composition within the crystals and over the sample, showing an increase of Ti/(Ti+Fe) towards the pellet surface (Fig. 3.10). Compared to the sample bulk composition, the central sample region generally has a slightly lower Ti/(Ti+Fe) value. In some single-phase Tmt samples, we observed an intermediate increase in Ti/(Ti+Fe) (Fig. 3.11).

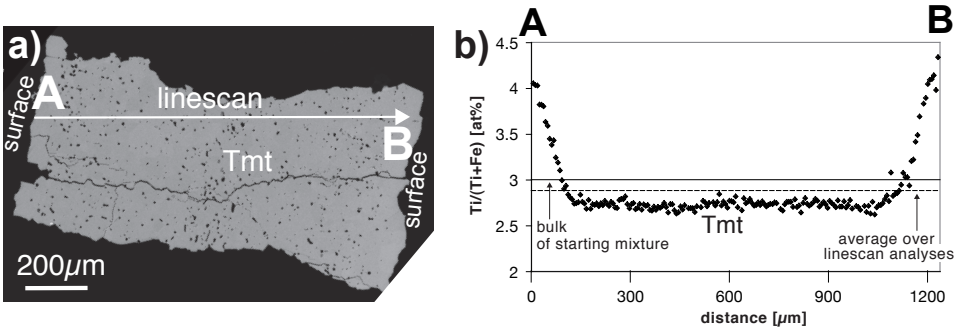

Fig. 3.10 a) BSE picture and b) EMP linescan over a single-phase Tmt sample (6F97x1.6): Ti content rises towards the sample surface. The central sample region is slightly depleted in Ti compared to the sample bulk composition. Note that the sample bulk composition of the starting mixture (solid horizontal line) and the averaged composition of all linescan analyses (dashed horizontal line) match within EMP uncertainites.

To summarise, a general trend of increasing local bulk Ti/(Ti+Fe) towards the sample surface and concentric variations in porosity have been observed in both two-phase and single-phase samples synthesised from $Fe_2O_3 + TiO_2$ mixtures.

Synthesis with intermediate grinding For some experiments, $Fe_2O_3 + TiO_2$ mixtures have been annealed at synthesis conditions for about half of the total run time (or less), then quenched and ground to a powder under acetone in an agate mortar. New pellets have been produced which have been re-run (chapter 2). Comparison of the sample after the first and second annealing reveals that the monomineralic rims which form during the first annealing have disappeared after grinding and the second annealing. According to our observations, the second annealing does not produce monomineralic rims (Fig. 3.12).

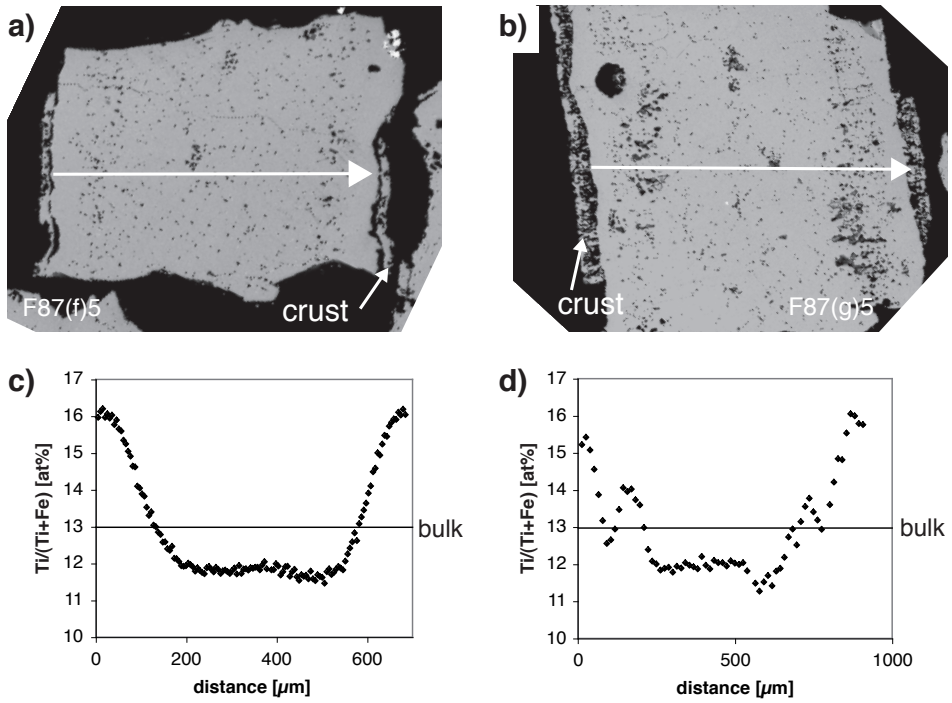

Fig. 3.11 a), b) BSE pictures of two single-phase Tmt samples (a) F87(f)5, NNO-0.7, b) F87(g)5 NNO-1.4, both 1200 °C). Arrows indicate positions of EMP linescans, which are illustrated in (c) and (d). Horizontal lines in (c) and (d) are the sample bulk compositions, which perfectly match the average of EMP analyses over the linescan.

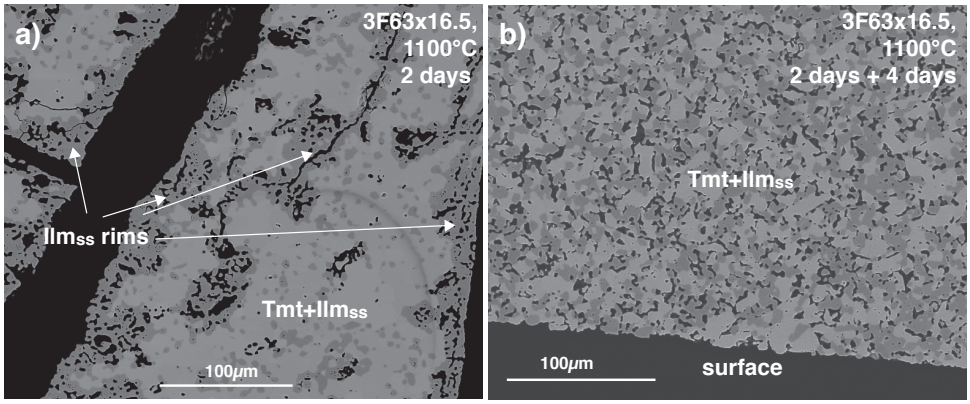

Fig. 3.12 Comparison of the texture in sample 6F63x16.5, a) after 2 days run time before intermediate grinding, and b) after intermediate grinding and additional 4 days run time. Note that monomineralic Ilm_{ss} rims can be observed in (a) but not in (b).

3.4.4 Experiments with $Fe^{\circ} + TiO_2$ starting mixtures

Samples synthesised from $Fe^{\circ} + TiO_2$ typically show a pronounced formation of concentric shells and a *decrease* of Ti/(Ti+Fe) towards the surface of the sample pellets.

Many Tmt+Ilm_{ss} samples synthesised from $Fe^{\circ} + TiO_2$ show a Tmt rim around a central area. The latter consists of single-phase Ilm_{ss} or of Ilm_{ss}+Tmt with only a low Tmt proportion (Fig. 3.13). This reflects a strong and abrupt change in Ti/(Ti+Fe) from the inner (often single-phase) area to the outer monomineralic rim. Single-phase core regions are usually inhomogeneous, with decreasing Ti/(Ti+Fe) towards the sample surface (5F65x2.8a, Fig. 3.13).

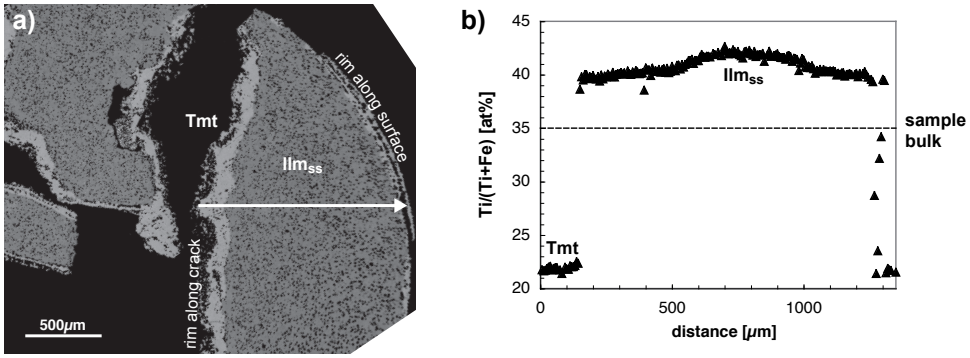

Fig. 3.13 a) BSE picture of sample 5F65x2.8a synthesised from Fe°+TiO_2 starting material. The sample displays a pronounced shell formation. A single-phase Ilm_{ss} core region (medium grey) is surrounded by Tmt rims (light grey), which surround the sample fragments and extend along the sample surface and along cracks. Sample displays pores and cracks (black). b) EMP profile along arrow marked in (a).

The product of one experiment, which was supposed to yield an Ilm_{ss}+Psb_{ss} assemblage consists of several concentric shells (Fig. 3.14). From surface to core these are a thin Tmt shell, a larger Ilm_{ss} rim, a broad Psb_{ss} shell and a central region with a Psb_{ss}+Rt assemblage. Boundaries between the shells are sharp. Within the single-phase shells Ti/(Ti+Fe) decreases towards the sample surface. Within the central two-phase region the phase compositions are homogenous. Compositions of all phases along the EMP linescan (Fig. 3.14b) are in agreement with compositions along one oxygen isobar (comparison to phase compositions according to chapter 4, see appendix A.3).

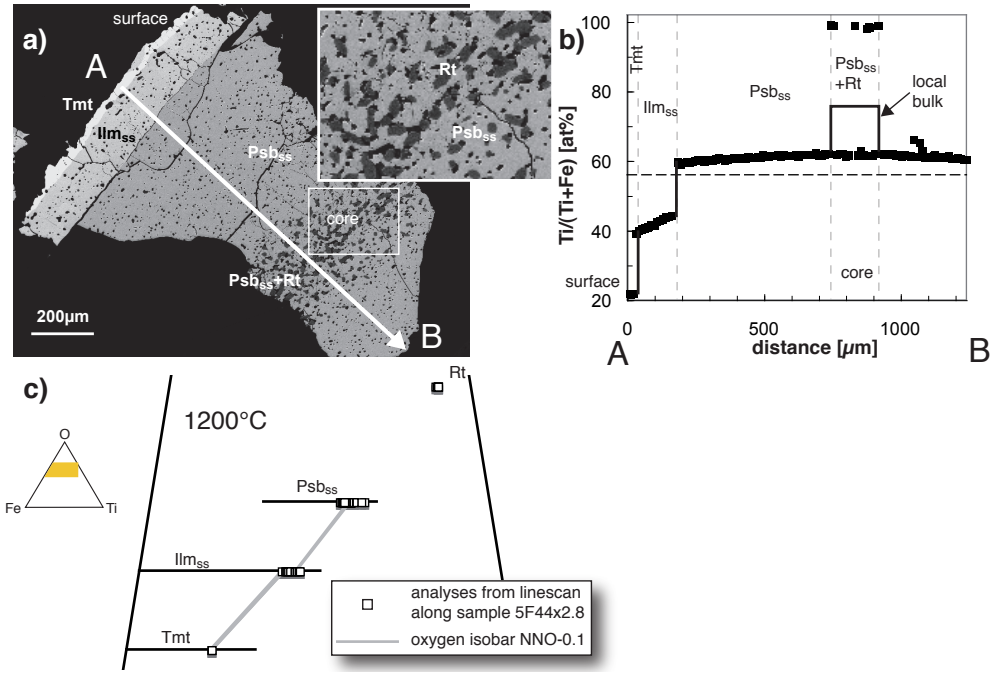

Fig. 3.14 a) BSE picture of sample 5F44x2.8 synthesised from Fe°+TiO_2 starting materials, revealing a pronounced shell formation. A central rutile-Psb_{ss} region (rutile: dark grey) is surrounded by a Psb_{ss} shell (grey), followed by an Ilm_{ss} (medium grey) and an outermost Tmt shell (light grey). Sample displays pores and cracks (black). b) EMP linescan as marked by arrow in (a). The local bulk composition is shown by a solid black line, which in single-phase shells coincides with the single data points (black squares) of the linescan. Dashed horizontal line is overall sample bulk. c) Phase compositions along EMP linescan (squares) in comparison with oxygen isobar for NNO-0.1, 1200°C (grey lines, see appendix A.3), illustrated in the Fe-Ti-O triangle.

3.4.5 Experiments with $Fe_2O_3 + Fe^\circ + TiO_2$ starting mixtures

Ternary $Fe^\circ + Fe_2O_3 + TiO_2$ mixtures have been used in solid-state buffer experiments and in some gas mixing experiments. No systematic difference in the texture produced by these two types of experiments could be observed.

In most samples produced from $Fe^\circ + Fe_2O_3 + TiO_2$ mixtures *no concentric texture* can be observed (Fig. 3.15). However, some samples do display thin monomineralic rims of an either Ti- or Fe-rich phase along the sample surface. In few cases, we observed even adjoining Ti- and Fe-rich rims around a central binary part (Fig. 3.16).

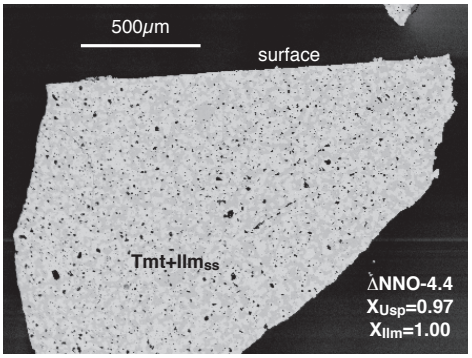

Fig. 3.15 BSE picture of sample 3IT60IW (Tmt+Ilm_{ss}), synthesised at 1100 °C in a silica ampoule together with an iron-wüstite buffer pellet. No monomineralic rims can be observed in the sample.

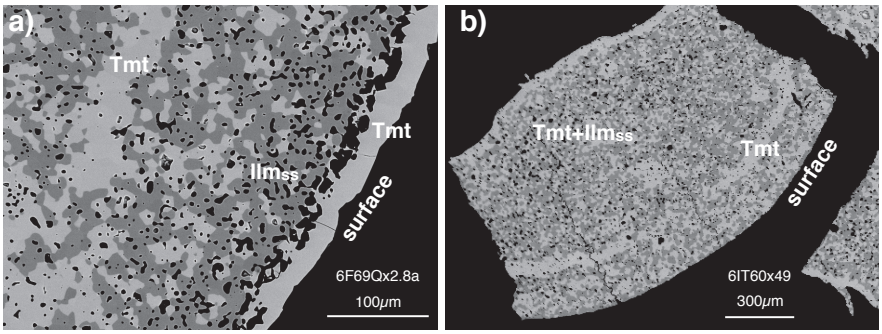

Fig. 3.16 BSE pictures of samples synthesised from ternary $Fe_2O_3 + Fe^\circ + TiO_2$ mixtures. a) Sample 6F69Qx2.8a displays a thin monomineralic Tmt rim (light grey) around an Ilm_{ss} rich - although not monomineralic - zone of the sample (dark grey). b) Sample 6IT60x49 shows monomineralic Tmt (light grey) zones parallel to the sample surface, but no outer monomineralic rim.

3.4.6 Time-dependent experiments

Time-dependent experiments have been carried out to investigate the temporal development of the observed textures, especially of concentric features. Samples with bulk Ti/(Ti+Fe)=0.47 and 0.67 have been prepared from $Fe_2O_3 + TiO_2$, $Fe^\circ + TiO_2$ and $Fe_2O_3 + Fe^\circ + TiO_2$ mixtures and annealed at 1300 °C and NNO-0.2 for 1, 4 and 20 hours.

For $Fe_2O_3 + TiO_2$ and $Fe^\circ + TiO_2$ mixtures, the results show that the concentric structure (Ti-rich rims for $Fe_2O_3 + TiO_2$ and Fe-rich rims for $Fe^\circ + TiO_2$) is already formed within the first hour of the experiments. No monomineralic rims are observed in run products from $Fe_2O_3 + Fe^\circ + TiO_2$ mixtures. This means that the textures that are observed in the equilibration runs (subsections 3.4.3 and 3.4.4) essentially form during less than one hour.

In the sample 6F047x3.8_1 (i.e. $Ti/(Ti + Fe) = 0.47$, prepared from $Fe^\circ + TiO_2$, run duration 1 hour) a (titano-)magnetite rim is formed around a thin Ilm_{ss} rim and a central Ilm_{ss}+Psb_{ss} assemblage. The (titano-)magnetite rim is strongly inhomogeneous. It is practically pure magnetite at the surface. Within the rim, there is a relatively sharp increase of Ti content (within about $50 - 70\,\mu m$ to Ti/(Ti+Fe)≈ 0.24). Ti/(Ti+Fe) further increases towards the border to the Ilm_{ss} rim to about 0.29 (Fig. 3.17). Run products of the same starting mixture, but annealed at the same T and fO_2 for 4 and 20 hours do also show outer Tmt rims. After 4 hours, the Tmt rim is still strongly inhomogeneous (17.7<Ti/(Ti+Fe) at%<23.4). However, an outer *magnetite* rim was not observed after 4 hours run duration.

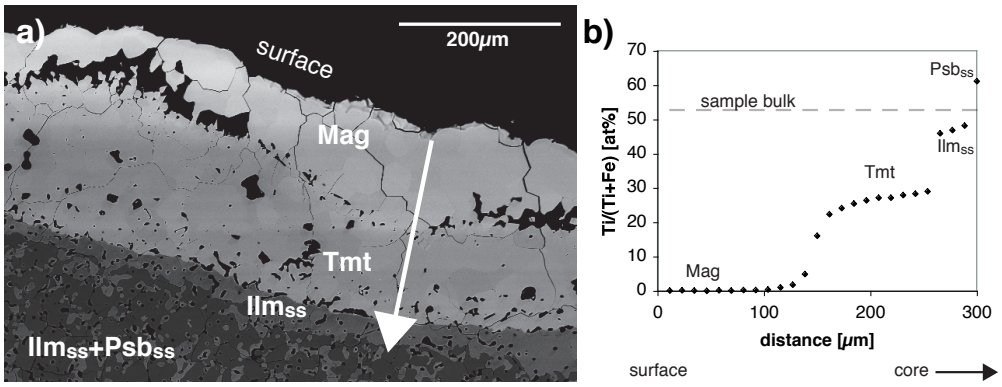

Fig. 3.17 a) BSE picture of sample 6F047x3.8_1, showing an outer (titano-)magnetite rim (light grey) and a thin Ilm_{ss} rim (medium grey) around central Ilm_{ss}+Psb_{ss}. b) EMP linescan across the monomineralic rims along the white arrow shown in picture (a).

3.4.7 Interpretation and conclusion

The presence (or absence) of concentric features (e.g. monomineralic rims, concentric phase inhomogeneity) strongly depends on the starting material.

- Run products synthesised from $Fe_2O_3 + TiO_2$ starting mixtures display Ti-rich rims. In single-phase products, Ti/(Ti+Fe) increases towards the pellet rim. Two-phase run products show Ti-rich *monomineralic* rims, i.e. Ilm_{ss} or Psb_{ss} rims around a Tmt+Ilm_{ss} or Ilm_{ss}+Psb_{ss} assemblage, respectively. The $Fe_2O_3 + TiO_2$ starting mixtures are strongly oxidised compared to the final synthesis product (i.e. compared to Tmt+Ilm_{ss} or Ilm_{ss}+Psb_{ss} assemblages). They have to be reduced during the experiment.
- Run products synthesised from $Fe^\circ + TiO_2$ starting mixtures display pronounced shell formation, with increasingly Fe-rich shells towards the sample surface. $Fe^\circ + TiO_2$ starting mixtures are strongly reduced compared to the final assemblages. They have to be oxidized during the experiment.
- Run products synthesised from $Fe^\circ + Fe_2O_3 + TiO_2$ starting mixtures in general do not show concentric textures. $Fe^\circ + Fe_2O_3 + TiO_2$ starting mixtures have an oxygen content close to the final assemblage. Only slight reduction or oxidation occurs during synthesis.

The fact that the monomineralic shells are arranged concentrically and also extend along cracks suggests that their formation is related to the surrounding gas phase. The strongly different textures observed for starting materials with different oxygen contents indicate that the oxygen gradient between sample pellet and surrounding gas may be the driving force for rim formation.

Run products with Fe-rich rims, produced from $Fe^\circ + TiO_2$ starting mixtures
The (titano-)magnetite rim observed in sample 6F047x3.8_1 (1300 °C, ΔNNO-0.2), after 1 hour run duration consists of pure magnetite at the surface. Before the synthesis run however, the sample consisted of a mixture of Fe° and TiO_2 with a homogeneous (at a scale of $5 - 10\,\mu m$) Ti/(Ti+Fe) ratio of 0.53. This reveals that element (i.e. Fe) migration has to be involved in the rim formation.

At the oxygen fugacity of the experiment, metallic iron is highly unstable. We suggest that for this reason, during early stages of the experiment Fe° migrates towards the sample surface, where it is oxidised to magnetite by reaction with the surrounding gas.

After run durations of four hours or more (time-dependent experiments of 4 or 20 hours, regular synthesis experiments with run durations $\geq$ 1 day), samples from

$Fe^{\circ} + TiO_2$ starting mixtures with similar Ti/(Ti+Fe) and equilibrated at similar oxygen fugacity compared to 6F047x3.8_1 (e.g. 5F44x2.8, 1200 °C, ΔNNO-0.1, run duration 68 hours, bulk Ti/(Ti+Fe)=0.56) also display monomineralic Tmt rims. Outer pure magnetite zones however have not been observed in these samples. The phase compositions of all occurring concentric shells in the "regular" synthesis experiments (i.e. in synthesis experiments with run durations $\geq$ 1 day) correspond to one oxygen isobar, reflecting the oxygen fugacity of the surrounding gas. This suggests that - after the initial and fast migration of Fe - titanium migrates more slowly towards the sample surface and reacts with magnetite under formation of a Tmt. Ti migration continues until all phase compositions throughout the sample are in agreement with the imposed oxygen fugacity (i.e. along one oxygen isobar).

The run products are inhomogeneous over the sample pellets, i.e. equilibrium has not been attained with respect to the bulk sample. However, on a local scale, the phase compositions are in equilibrium with the surrounding oxygen fugacity. A complete homogenisation of the sample would require element migration and decomposition of Fe-Ti oxide phases. Probably, the energetic difference to the equilibrium state is too small to induce this process.

Run products with Ti-rich rims, produced from $Fe_2O_3 + TiO_2$ starting mixtures

The reason for formation of Ti-rich monomineralic rims in samples synthesised from $Fe_2O_3 + TiO_2$ is not that evident. The formation of Ti-rich rims also has to involve element migration (e.g. Fig. 3.8). However, neither the migrating elements nor the direction of their migrations are clear.

As the starting material is oxidised compared to the surrounding gas, it could be assumed that Fe_2O_3 tends to migrate towards the sample surface where it can be reduced by reaction with the gas phase. In this case, we would expect the formation of Fe-rich rims at the sample surface, which has not been observed. Probably the oxygen gradient between sample and the surrounding surface is less pronounced than for $Fe^{\circ} + TiO_2$ starting materials, and thus no such Fe-migration occurs.

As one possible explanation for the formation of Ti-rich monomineralic rims, it may be suggested that the monomineralic rims form within the compositional field of the involved phases during reduction in early stages of the experiments (Fig. 3.18). Early during reduction the bulk composition of a sample with Ti/(Ti+Fe)>0.33 (Fig. 3.18, composition A) plots within the Psb_{ss} compositional field. This may result in an early formation of Psb_{ss} at the pellet surface, i.e. in direct contact with the gas mixture. However, this does not have to involve a migration of elements, whereas the formation of Ti-rich monomineralic rims does (see above). We suggest that in the course of the synthesis experiment, Ti migrates to-

wards the sample surface in order to adjust the compositions of the *existing* phases to the prevailing oxygen fugacity (i.e. to compositions along one oxygen isobar). This might be energetically more favourable than to decompose the phases (at constant Ti/(Ti+Fe)) to produce a stable paragenesis.

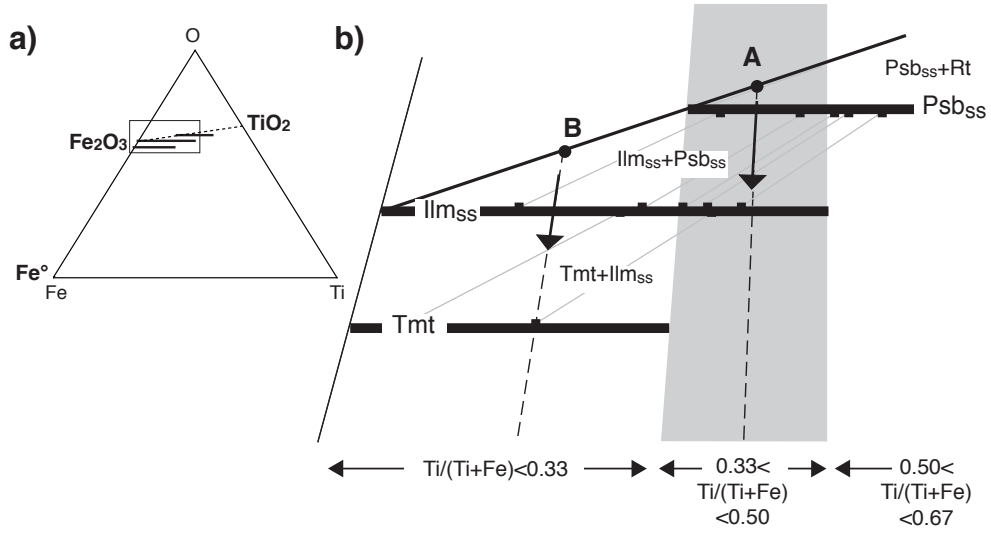

Fig. 3.18 Decrease of the oxygen content of samples from $Fe_2O_3 + TiO_2$ starting mixtures to the final assemblage, for exemplary mixtures A and B, illustrated in the triangle Fe-Ti-O. a) $Fe_2O_3 + TiO_2$ starting mixtures plot on the dashed line. b) The production of the final Tmt+Ilm_{ss} or Ilm_{ss}+Psb_{ss} assemblage (squares represent exemplary phase compositions according to chapter 4, connected by thin grey tie-lines) involves a decrease of the oxygen content (arrows) at constant cationic ratio Ti/(Ti+Fe) (dashed lines). Horizontal lines represent Tmt, Ilm_{ss} and Psb_{ss} solid solutions (from bottom to top).

However, it is not clear if and how the following phenomena can be explained by the above scenario.

- A sample with Ti/(Ti+Fe)<0.33 prepared from $Fe_2O_3 + TiO_2$ should not display a monomineralic Psb_{ss} rim, as the Ti/(Ti+Fe) of the starting mixture does not intersect the Psb_{ss} single-phase compositional field but lies within the binary Ilm_{ss}-Psb_{ss} field (starting composition B in Fig. 3.18). However, Psb_{ss} rims *have* been observed in such samples (e.g. sample 6F72x0.15).

- Experiments starting from pre-annealed $Fe_2O_3 + TiO_2$ mixtures do not produce a concentric texture although their oxygen content and consequently their reduction paths are identical to mixtures from untreated Fe_2O_3 and TiO_2

(of the same Ti/(Ti+Fe)). Probably, this is related to the coarser grain size of the starting material.

- Single-phase Tmt samples produced from $Fe_2O_3 + TiO_2$ mixtures do show an increase in Ti/(Ti+Fe) towards the sample surface, but no outer shell of another oxygen rich phase, which could have formed during the reduction path.

It has been suggested by D.H. Lindsley (person. comm.) that the monomineralic, Ti-rich rims (in samples synthesised from $Fe_2O_3 + TiO_2$ starting materials) result from Fe loss of the sample. Fe-depleted rims may be caused by a reaction of Fe with the surrounding gas (CO component), with the reaction product escaping into the gas phase. Further, Fe loss to the Pt holder during gas mixing runs is also possible, but due to the small, shared surface of Pt and sample should be of negligible extend. However, the formation of Fe-rich rims, which has been observed for $Fe^{\circ} + TiO_2$ starting mixtures cannot be explained by Fe loss.

Fe loss during the synthesis would result in an increased bulk Ti/(Ti+Fe). However, the averaged composition of all analyses of a linescan over a single-phase Tmt sample synthesised from $Fe_2O_3 + TiO_2$ (e.g. Fig. 3.10, Fig. 3.11) is generally in very good agreement with the bulk composition of the starting material. This suggests that no significant amount of Fe is lost to the gas. An increased Ti/(Ti+Fe) at the rim is compensated by a decreased Ti/(Ti+Fe) in inner sample regions.

Monomineralic rims as observed within the present study have also been observed by Senderov *et al.* (1993). These authors did not investigate these textures in detail and attributed them to quench phenomena. In the present study, we could clearly show that such rims are no quench phenomena, but form prior to quenching during early stages of the experiment.

3.5 Oxy-exsolution textures

3.5.1 SEM observations and EMP analysis

Near the sample surface as well as along cracks, products from gas mixing runs that have been quenched outside the furnace (external quenching, chapter 2) display thin exsolution lamellae and rims (thickness mostly $\ll 1\,\mu m$) of an oxygen- and titanium-richer phase (Ilm_{ss}, Psb_{ss}, or Rt) in grains of the host phase (Tmt, Ilm_{ss}, or Psb_{ss}, see Fig. 3.19). In contrast to internal quenching, external quenching

involves a drastic increase of fO_2 during the quench procedure (see chapter 2.2.6). Quenching inside the furnace does not produce exsolution features.

The quench exsolution features are restricted to the sample surface region, which is in direct contact with the surrounding gas. Usually, these features affect the outer max. $50-200\,\mu m$ of the sample. In a binary assemblage they can affect both coexisting phases (i.e. producing Ilm_{ss} lamellae in Tmt next to Psb_{ss} lamellae in Ilm_{ss}). They may extend beyond monomineralic rims or only affect their outer part. This confirms that quench exsolution features form *after* monomineralic rims.

Due to the different symmetries of the minerals Tmt, Ilm_{ss}, Psb_{ss}, and rutile, the quench exsolution features produced are different in their characteristics. Ilm_{ss} exsolutions in Tmt produce three sets of lamellae, which are beautifully orientated along (111) planes of the titanomagnetite (Fig. 3.19a). In contrast, Psb_{ss} exsolution lamellae in Ilm_{ss} are closer spaced and preferably aligned approximately perpendicular to the sample surface (Fig. 3.19b). Rutile exsolutions in Psb_{ss} have rarely been observed. Rutile forms fine, relatively short exsolution lamellae, which often have short oval swellings (Fig. 3.19c).

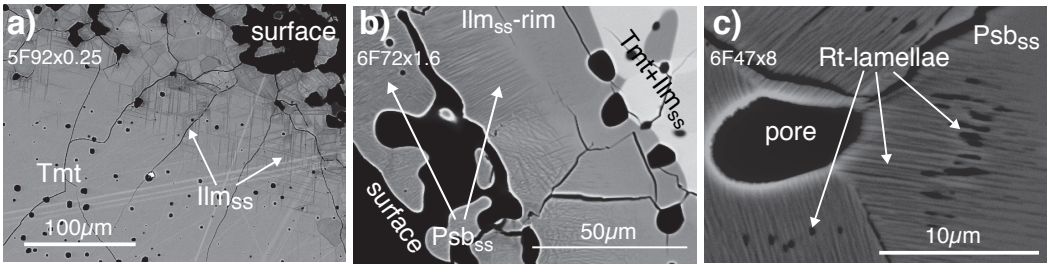

Fig. 3.19 Quench exsolution features at sample surfaces: a) Ilm_{ss} exsolution lamellae in Tmt, b) Psb_{ss} exsolution lamellae within a monomineralic Ilm_{ss} rim, and c) very fine rutile lamellae in Psb_{ss}.

The proportion of the sample volume, which is affected by the exsolution features, is about $2-10\,vol\%$. This volume was estimated by assuming typical thickness of the concerned region and typical diameter and height of the sample pellet. "Primary" cracks, which may extend into the sample pellet and probably have to be considered as sample surface, have been neglected. Indeed, the exsolved phases can be detected by X-ray diffraction provided they are not part of the equilibrium assemblage (i.e. in a Tmt+Ilm_{ss} sample Psb_{ss} exsolutions in Ilm_{ss} can be detected, whereas Ilm_{ss} exsolved from Tmt contributes to the main Ilm_{ss} peaks).

One peculiar run product is especially useful to document the chemical changes associated with external quenching (sample 6F67x7, Fig. 3.20). In this experiment, CO gas was turned off about $2-5$ minutes before quenching. Near the surface, the sample displays relatively thick, vermicular Psb_{ss} exsolutions, and an outermost thin

Ilm_{ss} rim. In the BSE picture, the Ilm_{ss} rim appears to be brighter than the Ilm_{ss} in contact to Tmt, which points to higher Fe-content in the rim. The exsolution features are big enough to enable EMP analyses (see Fig. 3.20). EMP analyses of the host phase have also been carried out. The compositions of Tmt and Ilm_{ss} in the central sample region (analyses from A in Fig. 3.20) are homogeneous and in agreement with phase compositions from other experiments carried out at the same temperature and comparable oxygen fugacity (oxy-isobar labelled -0.4 in Fig. 3.20, at 1300 °C). In contrast, Tmt and Ilm_{ss} compositions near the sample surface (analyses from B in Fig. 3.20) are richer in Fe, plotting nearly parallel to the NNO+0.7 oxy-isobar. The analyses from this region yield a significant range in Ti/(Ti+Fe) ratios for both Tmt and Ilm_{ss}. Analyses on Ilm_{ss} and neighboured Psb_{ss} from region C (inner rim, Fig. 3.20) are also inhomogeneous and plot nearly parallel to the NNO+1.4 oxy-isobar. The Ilm_{ss} from region D - i.e. the outermost Ilm_{ss} rim - is strongly inhomogeneous and very Fe-rich. This is in agreement with the bright colour in the BSE picture. The compositions of Ilm_{ss} and Psb_{ss} from D plot near the NNO+3.3 oxy-isobar, but are even shifted towards higher Fe-contents (especially for Ilm_{ss}) and describe a flatter slope.

3.5.2 Interpretation and conclusion

EMP analyses on sample 6F67x7 (Fig. 3.20) revealed that the compositions of the phases become successively Fe-richer towards the sample surface. Comparison with oxy-isobars derived from other synthesis experiments shows that this represents increasing oxygen fugacity. In fact, the described exsolution features only form in samples that have been exposed to air (and for 6F67x7 also to CO_2 prior to air), i.e. to higher oxygen fugacity. Thus, the quench exsolution features observed within this study are clearly due to oxidation of the sample and can be regarded as oxy-exsolution in the sense of Buddington & Lindsley (1964).

Oxy-exsolution features form within the time required for external quenching (i.e. *after* increase of the oxygen fugacity by turning the CO flow of and pulling the sample into air, and *before* cooling the pellet to room temperature in water). In some cases, external quenching took only less than 5 seconds.

Whereas oxy-exsolution features form in the very last seconds or minutes of an experiment, monomineralic rims form during very *early* stages. Surface oxy-exsolution and rim formation are thus two independent processes.

To our understanding, hardly any quenching procedure that involves a change in oxidation (i.e. removal of the sample from a furnace and the prevailing oxygen fugacity) can be rapid enough to completely avoid the formation of oxy-exsolution features. Quenching within a controlled atmosphere is thus mandatory. In samples

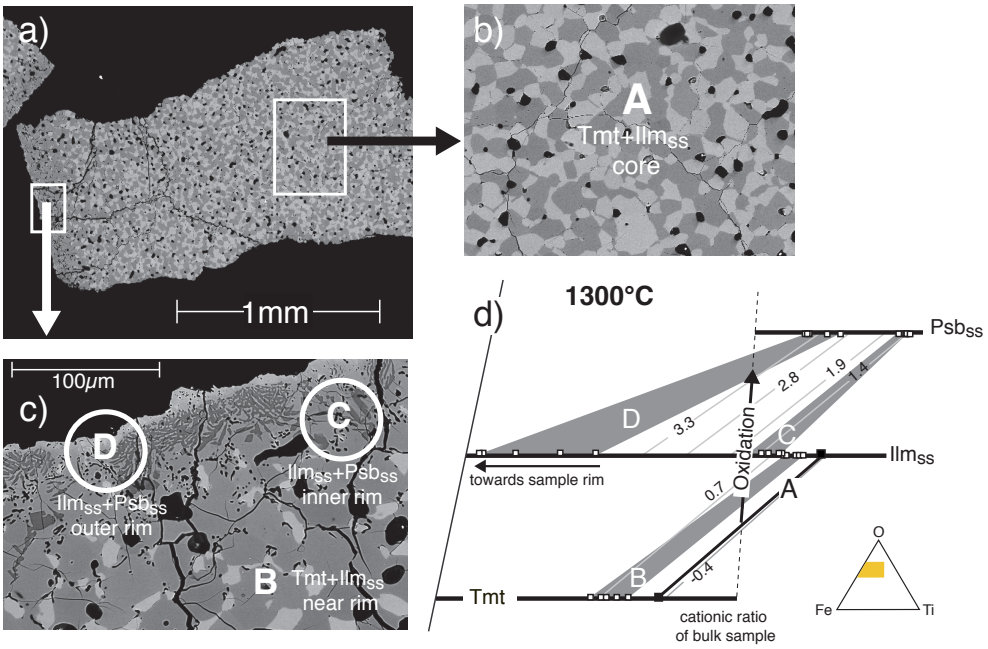

Fig. 3.20 a) BSE picture of externally quenched sample 6F67x7 and enlargements of b) central sample region and c) surface region. c) The surface region displays relatively large Psb_{ss} exsolution features. d) Analyses in different sample regions (from core to rim: A, B, C, D) plotted in the triangle Fe-Ti-O. Analyses in area A are represented by black filled squares, connected by a black tie-line. Grey areas connect the phase compositions (empty squares) measured within regions B, C and D. Light grey diagonal lines are oxy-isobars (numbers: ΔNNO) at 1300 °C derived within this study (see chapter 4 and appendix A.3).

that display oxy-exsolution features, the regions near the pellet surface have a higher oxygen content compared to the central sample region (cf. Fig. 3.20). This also affects the bulk sample oxygen content. Therefore, samples with oxy-exsolution features are not adequate for annealing experiments in closed system conditions (in sealed evacuated silica glass ampoules, chapter 2), because the actual bulk oxygen content of the annealed fragment might be higher than assumed from the phase compositions in the central sample region.

EMP analyses of sample 6F67x7 have also shown that the compositions in the central part of the sample are not affected by oxidation, even though for this sample the complete procedure of external quenching took extraordinarily long. This resulted in extremely thick oxy-exsolution features and an oxidised region, which extended unusually deep into the sample pellet. Tmt and Ilm_{ss} phase compositions

Table 3.3 Comparison of phase compositions in the central sample regions of samples equilibrated at NNO-0.08 and 1200 °C that display (upper part), resp. do not show (lower part) oxy-exsolution features. Note that the phase compositions of both groups are in good agreement. The lower Ti/(Ti+Fe) ratios for both phases in sample 6F69x2.8a cannot be explained but are not related to oxy-exsolution.

run no	ΔNNO	Tmt			Ilm_{ss}		
		n	Ti/(Ti+Fe) [at%]		n	Ti/(Ti+Fe) [at%]	
			mean	(σ)		mean	(σ)
samples with oxy-exsolution							
5F63x2.8	-0.08	10	22.01	(11)	10	40.20	(22)
5F69Qx2.8	-0.08	10	22.12	(13)	10	40.08	(12)
samples without oxy-exsolution							
5F69Qx2.8a	-0.08	10	22.10	(15)	10	40.03	(16)
5F69x2.8a	-0.08	10	21.66	(11)	11	39.42	(18)
5F63x2.8a	-0.08	10	22.27	(14)	10	40.21	(19)

obtained from the central regions of further samples *with* oxy-exsolution features agree with those from samples *without* oxy-exsolution features (see Table 3.3).

Thus, the central parts of the sample pellets can be considered to reflect the synthesis conditions (Table 3.3) and can be used to derive data on Fe-Ti distribution between Fe-Ti oxide phases for the re-calibration of the Fe-Ti thermo-oxybarometer (chapter 4).

3.6 Chemical inhomogeneities of phases in products of synthesis runs

Generally spoken, the chemical homogeneity (within the detection limit of the electron microprobe) of the phases in a sample improves with temperature and synthesis time.

While single-phase samples (especially Tmt samples) often show inhomogeneities of Ti/(Ti+Fe) over the sample pellet (Fig. 3.10, Fig. 3.11), samples consisting of binary (or ternary) assemblages usually display homogeneous phase compositions over the whole sample.

The presence of Mg and especially Al in a sample usually increases the run duration required to achieve a homogeneous sample. Run durations that proved sufficient for the simple system Fe-Ti-O (e.g. 24 h at 1300 °C), produced inhomogeneous samples under the presence of Mg and Al. In Mg- and Al-bearing systems intermediate grinding has turned out to be crucial. In the simple system Fe-Ti-O in-

termediate grinding was not necessary to produce homogeneous binary Fe-Ti oxide assemblages at T$\geq$ 1200 °C (and only rarely necessary at T<1200 °C).

Fe-Al spinel In some Al bearing products of synthesis runs (e.g. binary Tmt+Ilm$_{ss}$ assemblages), grains of a Fe-Al rich spinel phase (Table 3.4) have been observed (Fig. 3.21). The Fe-Al spinel consists of about $63-84$ mol% hercynite component, about $10-13$ mol% ulvöspinel component, and about $3-19$ mol% magnetite component (molefractions can be derived from cation p.f.u, given in Table 3.4).

Table 3.4 Selected EMP analyses of Fe-Al spinel grains in the systems Fe-Ti-Al-O and Fe-Ti-Al-Mg-O, given in wt% (upper part of the table) and cations per formula unit (lower part)

sample	5F59.5A5.5x33.5		6IP46M1A1x1.5		6F70M1A1x55	
n	3		2		4	
wt%	mean	(σ)	mean	(σ)	mean	(σ)
FeO	47.51	(35)	55.27	(07)	47.15	(48)
TiO_2	5.49	(09)	4.92	(55)	5.89	(28)
Al_2O_3	47.44	(33)	37.55	(92)	44.66	(76)
MgO	0.02	(02)	1.78	(21)	2.47	(04)
SiO_2	0.05	(03)	0.02	(00)	0.07	(02)
Σ	100.52	(10)	99.58	(21)	100.26	(14)
cations pfu	mean	(σ)	mean	(σ)	mean	(σ)
Fe^{3+}	0.071	(009)	0.399	(001)	0.159	(008)
Fe^{2+}	1.123	(001)	1.033	(003)	1.022	(008)
Ti^{4+}	0.124	(002)	0.115	(013)	0.133	(007)
Al^{3+}	1.681	(010)	1.371	(027)	1.576	(021)
Mg^{2+}	0.001	(001)	0.082	(010)	0.110	(002)

The Fe-Al spinel grains are generally surrounded by Tmt grains, which show increasing Al-content towards the Fe-Al spinel (Fig. 3.22, especially apparent in picture (c)). The boundary between Tmt and Fe-Al spinel is sharp. In part of the samples, the Fe-Al spinel grains and also the directly adjoining Tmt are highly porous. Some samples do not contain Fe-Al spinel, but show significant inhomogeneity in Tmt, especially regarding the Al-content.

In most samples, the occurrence of Fe-Al spinel grains is rare, and the related Al inhomogeneity is restricted to a small sample region. In some samples however, Fe-Al spinel is more frequent and Tmt is inhomogeneous in Al content throughout the sample. Such samples have been ground, pressed to a new pellet and re-run.

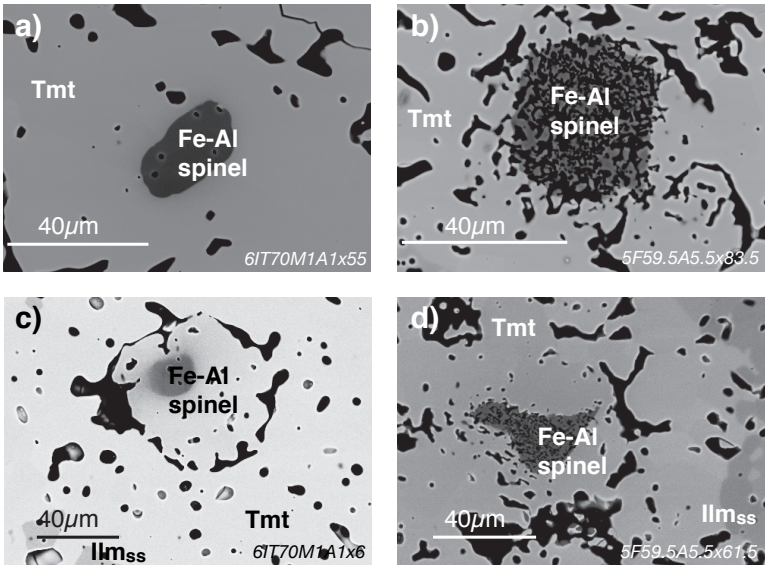

Fig. 3.21 BSE pictures of Fe-Al spinel grains (dark grey) within Tmt (light grey) in Tmt+Ilm_{ss} assemblages synthesised at 1300 °C (a, c) and 1200 °C (b, d). Not the differences in brightness of Tmt around Fe-Al spinel in picture (c).

Usually both Tmt inhomogeneity and the Fe-Al grains had disappeared after this second synthesis cycle.

The starting materials for Al-bearing samples consist of $Fe_2O_3 \pm Fe^{\circ} + TiO_2 + Al_2O_3 \pm MgO$. Thus, the Fe-Al spinel cannot be a relict of the starting material. Possibly Fe-Al spinel forms during early stages of the experiment. The formation may be triggered by an inhomogeneity in the element distribution (e.g. Al-rich areas), and requires the migration of elements (e.g. Fe).

3.7 Summary and conclusion

The synthesis and re-equilibration products produced within this study were used to derive data on the equilibrium distribution of Fe and Ti between Fe-Ti oxides (as a function of T and fO_2) to contribute to a re-calibration of the Fe-Ti thermo-oxybarometers. Further, they were investigated to derive information concerning Tmt non-stoichiometry. Therefore, it is important to evaluate if the observed textures do or do not reflect equilibrium and how these textures may affect further investigations and interpretations.

Concentric textures and inhomogeneities, and oxy-exsolution features represent

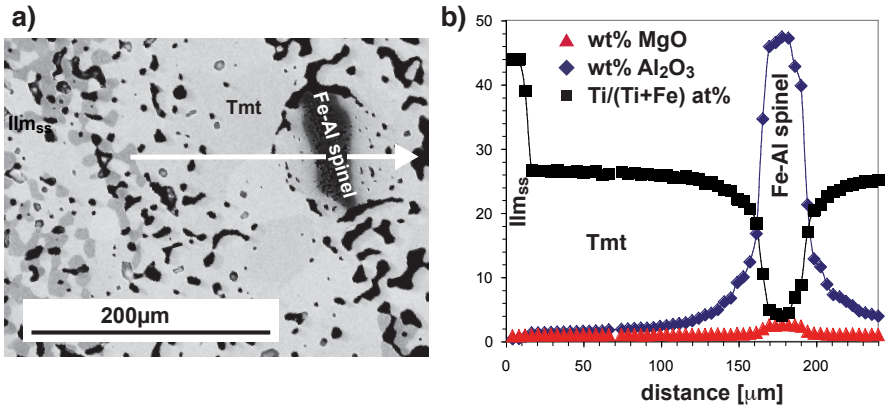

Fig. 3.22 a) BSE picture of a Fe-Al spinel grain (dark grey) included in Tmt (light grey) in a Tmt+Ilm$_{ss}$ sample (Ilm$_{ss}$: medium grey; 6IT70M1A1x6). The Fe-Al spinel shows fine pores (black). The arrow marks the position of the EMP line scan shown in picture (b). b) EMP line scan across Fe-Al spinel, along white arrow in picture (a). Tmt displays an increase in MgO, Al_2O_3 and a decrease in Ti/(Ti+Fe) towards the Fe-Al spinel grain.

variations in local bulk composition over the sample pellet. Phase compositions in the central sample regions reflect synthesis temperature and oxygen fugacity. Thus, they can be used to derive information on equilibrium Fe-Ti distribution between coexisting phases.

However, these textures and inhomogeneities have to be accounted when the bulk of a sample fragment is considered. They can influence measurements in which physical properties are derived from the bulk sample (e.g. magnetic, calorimetric and thermogravimetric measurements). This has to be considered for further investigations within this study.

This chapter has shown that synthetic single-phase samples (especially Tmt) very often display an increase of the Ti/(Ti+Fe) ratio towards the sample surface. This reveals that the production of homogeneous single-phase samples - especially Tmt - is difficult and requires special care. To our experience, the use of a ternary starting material $Fe^{\circ} + Fe_2O_3 + TiO_2$, and at least two annealing cycles with intermediate grinding are the most promising approaches. Quenching within the furnace atmosphere is absolutely required. To check the phase homogeneity and purity, careful examinations of the samples with SEM and EMP are strongly advisable.

In many existing studies, the synthetic Tmt was not carefully characterised regarding its chemical homogeneity. This especially holds for older studies, because

microanalytical devices (EMP, SEM) were not available. The risk therefore remains that such samples were inhomogeneous to some extent.

Concentric textures observed in many run products are expected to be common in synthetic Fe-Ti oxide samples (e.g. monomineralic rims: D.H. Lindsley, pers. comm.), although they have been rarely reported (e.g. Senderov *et al.*, 1993) and mostly misinterpreted.

Examination of the concentric textures has revealed that strong element migration over the sample is involved in the formation of - both Fe-rich and Ti-rich - monomineralic rims. The formation of the Fe-Al spinel phase also requires element migration. This has to be especially emphasised, as all experiments have been carried out at subsolidus conditions.

4 Phase relations and phase compositions in the system Fe-Ti-O: new experimental calibration data for the Fe-Ti oxide thermo-oxybarometers

4.1 Introduction

The Tmt-Ilm_{ss} thermo-oxybarometer (see section 1.3) is a powerful tool to retrieve information on oxygen fugacity and temperature that prevailed during formation and recrystallisation of crustal and mantle rocks of the Earth and of martian and lunar rocks.

As mentioned in chapter 1, section 1.3, thermodynamic formulations of the Tmt-Ilm_{ss} thermo-oxybarometer (Andersen & Lindsley, 1988; Andersen *et al.*, 1993; Ghiorso & Sack, 1991) are available and have been broadly used during the last years. However, these often yield unsatisfactory results. This can be shown by applying the formulations to experimental data and comparing T-fO_2 estimates and experimental T-fO_2 conditions (see section 1.3, Fig. 1.21). A major reason for the discrepancies between experimental and estimated values is the limited set of experimental data, which was available for the calibration of the thermo-oxybarometer models (see section 1.3, Fig. 1.22).

Consequently, there is a strong need for more data on the compositions of coexisting titanomagnetite and $ilmenite_{ss}$ in the Fe-Ti-O system as a function of temperature (in the range $1000-1300\,^{\circ}C$) and oxygen fugacity (in the range NNO-5 to +5). This is the main focus of the present chapter.

In addition, compositional data for the $ilmenite_{ss}$-$pseudobrookite_{ss}$ assemblage in the same fO_2-T range are presented. The latter paragenesis is another potential thermo-oxybarometer (chapter 1.3) for oxidised terrestrial igneous rocks (e.g. Frost & Lindsley, 1991), for some moderately reduced assemblages in mantle xenoliths (Haggerty, 1991b) and for strongly reduced lunar assemblages (e.g. El Goresy *et al.*, 1974; El Goresy & Woermann, 1977). Although a preliminary calibration of the Ilm_{ss}-Psb_{ss} thermo-oxybarometer has been proposed by Anovitz *et al.* (1985) on the basis of thermodynamic data, the experimental data needed to refine the model are still missing.

To round off the investigation, chemical data on further assemblages (single-phase Tmt or Ilm_{ss}, Ilm_{ss}+Rt) is provided.

4.2 General experimental approach

Experiments which aimed at yielding parageneses of Fe-Ti oxides with equilibrium compositions were performed at subsolidus conditions at 1 bar and temperatures between 1000 and 1300 °C under controlled oxygen fugacities in the range ΔNNO-5 to ΔNNO+5 (chapter 2). The great majority of the experiments were syntheses from Fe_2O_3+TiO_2 mixtures in gas-mixing furnaces. At 1000 and 1100 °C solid-state buffer experiments have also been carried out. To check whether equilibration was attained or at least closely approached in the synthesis runs, we performed parallel experiments with different bulk compositions under the same T-fO_2 conditions and also a few re-equilibration experiments (chapter 2, see also section 4.3.2).

Phase compositions were obtained from electron microprobe analyses for Ti and Fe. Oxygen was not analysed, which means that the analytical results presented in this chapter do not give any direct evidence about non-stoichiometry (cation vacancies or cation interstitials, see section 1.2).

4.3 Results

Most run products consist of two coexisting Fe-Ti oxide phases, mostly Tmt + Ilm_{ss} or Ilm_{ss} + Psb_{ss}. A few samples contain only one of the three Fe-Ti oxide phases. All run products consist of polycrystalline, roughly equigranular aggregates, with grain sizes around $10 - 50\,\mu m$.

In order to avoid the possible influence of oxy-exsolution features or monomineralic rims (chapter 3), all phase compositions reported in the following have been measured on crystals from the central part of the samples (at least 200 µm away from their surfaces or from cracks). For a more detailed description of textures encountered in synthetic Fe-Ti oxide assemblages see chapter 3.

4.3.1 Indications for the attainment of equilibrium

There are several good indications that the phase compositions reported in the following section reflect equilibrium conditions during the high temperature experiments.

(1) In the overwhelming majority of the two-phase run products, both phases are homogeneous within the crystals and over the whole *two-phase domain* of the sample. This is reflected by the low $1\,\sigma$ standard deviations for the Ti/(Ti+Fe) values of the corresponding phases, which are below 0.5 % in most samples (relative value for 10 to 12 single analyses; see appendix A.3 for σ values).

Higher 1σ which reflect slightly varying compositions in neighbouring crystals of the same phase, are registered only in very few two-phase products of runs at 1000 °C. In contrast, single-phase products from gas mixture runs tend to display compositional variations over the whole sample (see chapter 3).

(2) At given T-fO_2 conditions, the phase compositions in two-phase run products are independent of the bulk composition of the sample within the permitted Ti/(Ti+Fe) range, i.e. $Ti/(Ti+Fe)_{Tmt} < Ti/(Ti+Fe)_{bulk} < Ti/(Ti+Fe)_{Ilm_{ss}}$. Run products with different bulk Ti/(Ti+Fe) values have only different modal proportions (Fig. 4.1). This is clearly demonstrated by the results of the numerous experiments in which several samples with different bulk compositions were simultaneously synthesised under given T-fO_2 conditions. These results were also reproduced in further runs under identical T-fO_2 conditions. The phase compositions measured in all products from runs under the same T-fO_2 are generally identical within the 1σ standard deviations (see appendix A.3). In very few cases this is not satisfied, but phase compositions still agree within the analytical (EMP) uncertainties (± 0.005 for the values of Ti/(Ti+Fe) [at%]).

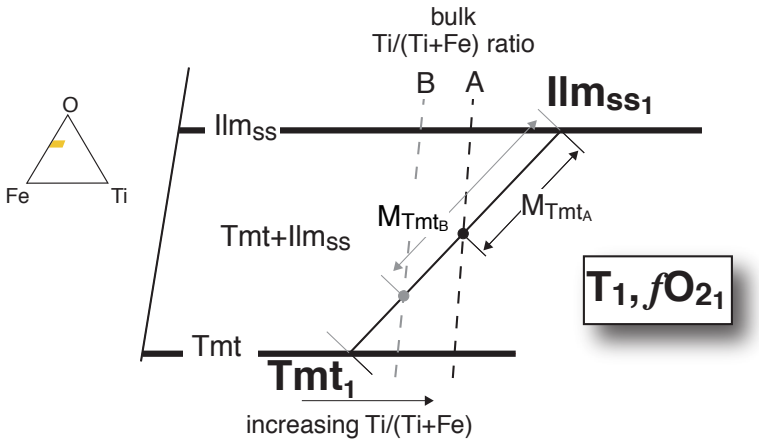

Fig. 4.1 Schematised phase compositions (Tmt_1, Ilm_{ss1}) and modal proportions (M_{Tmt_A}, M_{Tmt_B}) of two binary (here Tmt+Ilm_{ss}) samples of different bulk cationic ratio (A and B, represented by black and grey dashed lines), but equilibrated at identical T and fO_2 (T_1, fO_{2_1}), schematically illustrated in the triangle Fe-Ti-O.

(3) As will be detailed in section 4.3.2, the compositions of phases from re-equilibration runs at 1300 °C perfectly match those obtained from corresponding synthesis runs. For products of re-equilibration runs at 1100 °C, the phase compositions still match those of corresponding synthesis runs within the uncertainties (Ti/(Ti+Fe)±0.005, Table 4.1).

All these considerations support the view that equilibrium was attained or at least closely approached in our synthesis and re-equilibration runs and that the phase compositions from two-phase assemblages in the central part of the samples reliably represent the corresponding T-fO_2 conditions (see also chapter 3).

4.3.2 Re-equilibration experiments

In re-equilibration experiments fragments of pellets, which were produced during synthesis experiments, were exposed to new T-fO_2 conditions with the aim of obtaining an equilibrium paragenesis. In contrast to synthesis runs, pre-reacted Fe-Ti oxide phases are used as starting material. In some cases a new phase assemblage crystallised, otherwise the existing Fe-Ti oxide phases adjusted their compositions to the new conditions. The experimental conditions of both synthesis and subsequent re-equilibration experiments are listed in Table 4.2, the phase compositions of the re-equilibration run products in Table 4.3.

As already stated above, the compositions of phases from re-equilibration runs match those obtained from corresponding synthesis runs.

Fig. 4.2a illustrates a set of re-equilibration experiments in which three samples of different bulk composition originally synthesised at 1300 °C at two different fO_2 were simultaneously re-equilibrated *at the same temperature* at an intermediate oxygen fugacity. The phase compositions of the three re-equilibration products are in perfect agreement with each other and also with compositions of synthesis runs at identical - or at least very similar - T and fO_2. The final phase compositions have been **approached from both the Fe-rich side through reduction (samples 6F72x8R and 6F69x8R) and from the Ti-rich side through oxidation (6F63x8R)**. Thus a **true reversal experiment** could be completed.

Further re-equilibration experiments have been carried out (Fig. 4.2b and c), which involved a *change in temperature* (i.e. a rotation of the conode, cf. chapter 1.2) but not necessarily a significant change in the bulk oxygen content of the sample by reduction or oxidation. An increase in temperature causes an anti-clockwise rotation of the conode, producing a steeper tie-line (and vice versa for a temperature decrease). When no significant change of the sample oxygen content is involved, the phase compositions of coexisting Fe-Ti oxides are approached from *opposite*

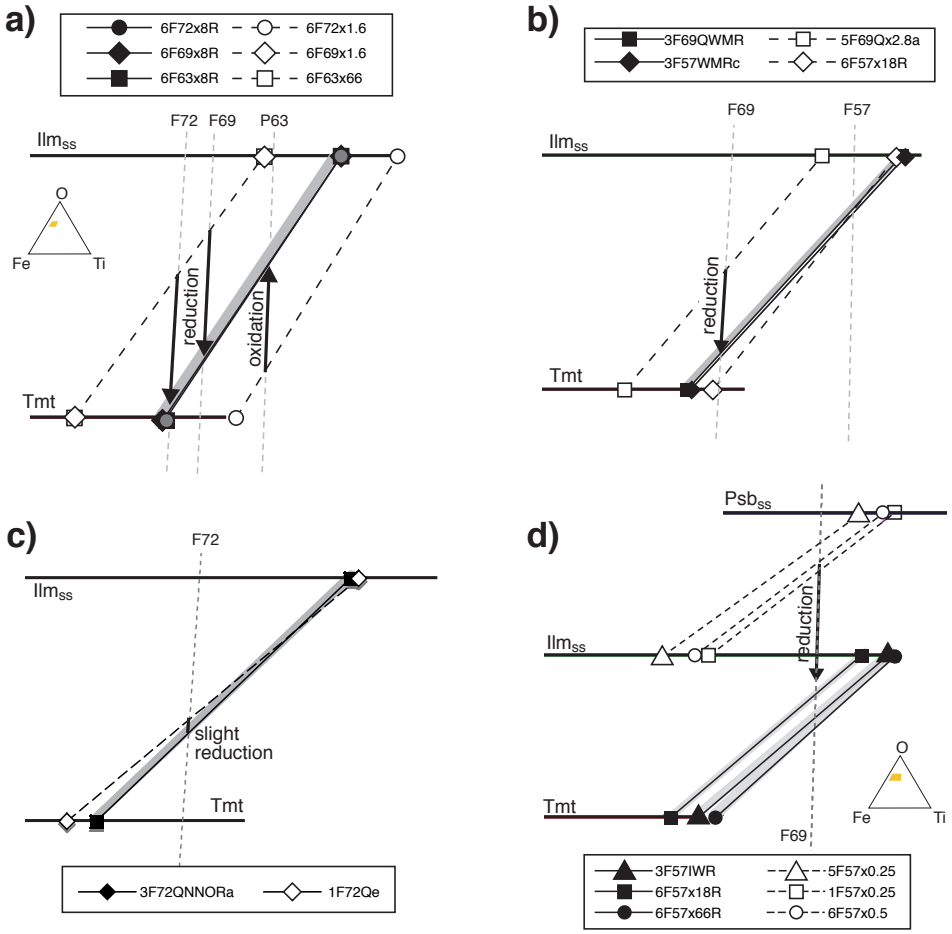

Fig. 4.2 Phase compositions of coexisting Tmt and Ilm_{ss} from products of re-equilibration runs (filled symbols, solid tie lines), compared with phase compositions and assemblage of the starting materials (open symbols, dashed tie lines), plotted in part of the Fe-Ti-O triangle. The thick grey lines represent Tmt+Ilm_{ss} tie-lines from synthesis experiments at T and fO_2 of the re-equilibration run. Thin dashed lines labelled F72, F69, P63 and F57 mark the cationic ratios of the bulk compositions (numbers refer to Fe/(Fe+Ti) ratios). Horizontal thick lines are for the Tmt, Ilm_{ss} and Psb_{ss} solid solutions. a) Re-equilibration runs at 1300 °C, carried out at identical temperature but different fO_2 than the synthesis runs. b) Re-equilibration at 1100 °C and fO_2 corresponding to the WM buffer. The starting materials were produced at higher temperature (1200 and 1300 °C). For re-equilibration experiment 3F57WMRc, synthesis and re-equilibration tie lines cross at the bulk cationic ratio of the sample, i.e. the sample oxygen content remained approximately constant during re-equilibration. c) Re-equilibration at 1100 °C and fO_2 corresponding to the NNO buffer. The starting material was originally synthesised at lower temperature (1000 °C). d) Re-equilibration at 1100 or 1300 °C of samples which were originally synthesised at different temperature and strongly higher fO_2. Re-equilibration involves a change of assemblage from Ilm_{ss}+Psb_{ss} to Tmt+Ilm_{ss}.

directions during re-equilibration, i.e. a temperature increase involves an approach of Tmt composition from the *Fe-rich* side and of Ilm_{ss} composition from the *Ti-rich* side (Fig. 4.2b, 6F57x18R), and vice versa for a temperature decrease (Fig. 4.2c). In the re-equilibration runs 3F69QWMR and 3F57WMRc (1100 °C, NNO-2.0; Fig. 4.2b), the Tmt composition could be bracketed by reduction and oxidation, i.e. approached from the Fe-rich (3F69QWMR) *and* the Ti-rich (3F57WMRc) side.

In cases where the re-equilibration conditions were strongly different from the synthesis conditions, re-equilibration causes a change of *phase assemblage*. Fig. 4.2d presents the phase compositions of three different re-equilibration runs and their preceding synthesis runs. In all three cases, Tmt+Ilm_{ss} assemblages are formed from Ilm_{ss}+Psb_{ss} assemblages. Re-equilibration temperature is higher, lower or identical to synthesis temperature, but in any case a re-equilibration involves a strong decrease of oxygen fugacity.

Fig. 4.2 shows that the result from re-equilibration experiments both at 1100 and 1300 °C are in good agreement with synthesis runs (black solid tie-lines from re-equilibration experiments coincide with light grey bars from synthesis experiments).

The phase compositions have been approached both from the Fe-rich and Ti-rich side, by reduction and oxidation and from higher and lower temperature. The equilibrium phases and phase compositions have been produced both by reaction of oxide mixtures to the Fe-Ti oxides (synthesis), and also by change of the phase compositions of existing Fe-Ti oxides (re-equilibration). This supports that equilibrium conditions were - at least - closely approached in both types of experiments.

Table 4.1 Comparison of phase compositions in products of synthesis runs (*italic*) and re-equilibration runs (regular, R at the end of sample name) at identical or at least very similar T and fO_2. Results are also listed in the tables in appendix A.3.

sample name	T [°C]	ΔNNO	Tmt			Ilm_{ss}		
				Ti/(Ti+Fe) [at%]			Ti/(Ti+Fe) [at%]	
			n	mean	(σ)	n	mean	(σ)
6F72x8R[1]	1300	-0.8	10	27.34	(17)	10	44.19	(16)
6F69x8R[1]	1300	-0.8	10	27.36	(12)	10	44.11	(15)
6F63x8R[1]	1300	-0.8	10	27.57	(11)	10	44.26	(18)
6F67x8[1]	*1300*	*-0.7*	*10*	*26.88*	*(12)*	*10*	*43.48*	*(17)*
6F63x8[1]	*1300*	*-0.7*	*10*	*27.01*	*(22)*	*10*	*43.75*	*(21)*
6F57x18R	1301	-1.6	10	30.41	(13)	10	47.58	(20)
6F57x18	*1301*	*-1.6*	*10*	*30.20*	*(13)*	*10*	*47.45*	*(25)*
6F57x66R	1299	-3.5	10	34.52	(26)	10	50.65	(17)
6F63x66	*1299*	*-3.5*	*11*	*34.31*	*(16)*	*8*	*50.17*	*(24)*
6F57x66	*1299*	*-3.5*	*10*	*34.39*	*(17)*	*10*	*50.40*	*(19)*
3F72QNNORa	1100	0.0	10	20.54	(19)	10	42.00	(20)
3F76Qe	*1098*	*0.0*	*10*	*20.22*	*(19)*	*10*	*41.76*	*(17)*
3F69Qe	*1098*	*0.0*	*10*	*20.14*	*(15)*	*10*	*41.76*	*(15)*
F69 (e) 3	*1100*	*0.0*	*10*	*19.99*	*(21)*	*10*	*41.85*	*(40)*
3F69QWMR	1100	-2.0	10	27.97	(13)	10	48.06	(14)
3F57WMRc	1100	-2.0	10	28.29	(12)	10	48.37	(09)
3IT60WMa	*1101*	*-2.0*	*10*	*27.81*	*(18)*	*10*	*48.08*	*(16)*
3F57IWR	1100	-4.4	10	32.94	(18)	10	50.16	(20)
3IT60IW	*1100*	*-4.4*	*10*	*32.46*	*(16)*	*10*	*49.78*	*(10)*
3F57K67IWa	*1101*	*-4.4*	*10*	*32.55*	*(13)*	*10*	*50.03*	*(23)*

1) Slightly higher Ti/(Ti+Fe) ratios in re-equilibration runs are in agreement with slightly lower fO_2 (cf. Fig. 4.3).

Table 4.2 Experimental conditions of re-equilibration runs and preceding synthesis runs

bulk	synthesis run						re-equilibration run					
Ti/(Ti+Fe)	no.	T [°C]	t [*h*]	oxygen fugacity		phases	name	T [°C]	t [*h*]	oxygen fugacity		phases
[*at%*]				buffer / CO %	ΔNNO					buffer / CO %	ΔNNO	
re-equilibration at 1300 °C												
28.0	6F72x1.6	1303	23	1.6	0.7	TI	6F72x8R	1300	26	8.00	-0.8	TI
31.0	6F69x1.6	1303	23	1.6	0.7	TI	6F69x8R	1300	26	8.00	-0.8	TI
37.0	6F63x66	1299	18	66.0	-3.5	TI	6F63x8R	1300	26	8.00	-0.8	TI
43.3	1F57x0.25	999	264	0.3	1.5	IP	6F57x18R	1301	24	18.00	-1.6	TI
43.3	6F57x0.5	1301	42	0.5	1.9	IP	6F57x66R	1299	18	66.00	-3.5	TI
re-equilibration at 1100 °C												
28.0	1F72Qe	999	192	NNO	0.0	TI	3F72QNNORa	1100	143	NNO	0.0	TI
31.0	5F69Qx2.8a	1200	>24	2.8	-0.1	TI	3F69QWMR	1100	217	WM	-2.0	TI
43.3	6F57x18R	1301	24	18.0	-1.6	TI	3F57WMRc	1100	143	WM	-2.0	TI
43.3	5F57x0.25	1201	99	0.3	2.3	IP	3F57IWR	1100	217	IW	-4.4	TI

TI: $Tmt+Ilm_{ss}$
IP: $Ilm_{ss}+Psb_{ss}$

Table 4.3 Phase compositions in products of synthesis runs and subsequent re-equilibration runs. See also tables in appendix A.3.

synthesis run								re-equilibration run					
name	phases	Ti/(Ti+Fe) [at%]						name	phases	Ti/(Ti+Fe) [at%]			
		Tmt		Ilm_{ss}		Psb_{ss}				Tmt		Ilm_{ss}	
		n[1]	X[2]	n	X	n	X			n	X	n	X
re-equilibration at 1300°C													
6F72x1.6	Tmt+Ilm_{ss}	10	18.6	10	36.2			6F72x8R	Tmt+Ilm_{ss}	10	27.3	10	44.2
6F69x1.6	Tmt+Ilm_{ss}	10	18.6	10	36.2			6F69x8R	Tmt+Ilm_{ss}	10	27.4	10	44.1
6F63x66	Tmt+Ilm_{ss}	11	34.3	8	50.2			6F63x8R	Tmt+Ilm_{ss}	10	27.6	10	44.3
1F57x0.25	Ilm_{ss}+Psb_{ss}			10	32.8	10	50.8	6F57x18R	Tmt+Ilm_{ss}	10	30.4	10	47.6
6F57x0.5	Ilm_{ss}+Psb_{ss}			12	31.4	13	49.6	6F57x66R	Tmt+Ilm_{ss}	10	34.5	10	50.7
re-equilibration at 1100°C													
1F72Qe	Tmt+Ilm_{ss}	13	18.0	9	42.8			3F72QNNORa	Tmt+Ilm_{ss}	10	20.5	10	42.0
5F69Qx2.8a	Tmt+Ilm_{ss}	10	22.1	10	40.0			3F69QWMR	Tmt+Ilm_{ss}	10	28.0	10	48.1
6F57x18R	Tmt+Ilm_{ss}	10	30.4	10	47.6			3F57WMRc	Tmt+Ilm_{ss}	10	28.3	10	48.4
5F57x0.25	Ilm_{ss}+Psb_{ss}			10	28.4	10	47.3	3F57IWR	Tmt+Ilm_{ss}	10	32.9	10	50.2

1) n is number of EMP analysis points
2) X is mean value of Ti/(Ti+Fe) [at%] according to EMP analysis

4.3.3 Phase boundaries and compositions

The chemical compositions of the Fe-Ti oxide phases in our synthesis and re-equilibration run products and the run conditions are listed in the appendix (appendix A.3). The Ti/(Ti+Fe) [at%] values for Tmt, Ilm_{ss} and Psb_{ss} are plotted in Fig. 4.3 versus ΔNNO at the four different run temperatures (1000, 1100, 1200 and 1300 °C). At all temperatures these diagrams show the continuous shifts of the phase boundaries of the Fe-Ti oxides towards the Ti side with decreasing oxygen fugacity. These shifts reflect the ilmenite substitution $2Fe^{3+} \leftrightarrow Fe^{2+}Ti^{4+}$.

According to previous studies (e.g. Webster & Bright, 1961; Taylor, 1964; Senderov *et al.*, 1993; Aggarwal & Dieckmann, 2002), Tmt with very variable compositions are stable over a wide range of oxygen fugacities at all temperatures. This is confirmed by this study's data (single-phase Tmt and Tmt+Ilm_{ss}), and further data by R. Engelmann (Heidelberg, Ph.D. thesis in preparation) also considering Tmt in coexistence with wüstite.

At 1300 °C and fO_2 corresponding to that of the wüstite-magnetite buffer (WM) for instance, the compositional range of Tmt extends from $\mathrm{Ti}/(\mathrm{Ti}+\mathrm{Fe}) = 0\,\mathrm{at}\%$ (pure magnetite) in coexistence with wüstite up to $\mathrm{Ti}/(\mathrm{Ti}+\mathrm{Fe}) = 27\,\mathrm{at}\%$ in coexistence with Ilm_{ss}, i.e. from X_{Usp}=0.0 to 0.8. At each temperature, single-phase Tmt is stable at a given composition over 3 to 5 $\log fO_2$ units.

The large phase field of Tmt is partly related to deviations from stoichiometry (e.g. Hauptman, 1974; Rahman & Parry, 1978; Dieckmann, 1982; Senderov *et al.*, 1993; Lattard, 1995; Aggarwal & Dieckmann, 2002). It must be stressed however that the degree of non-stoichiometry is not directly proportional to the range of oxygen fugacity under which Tmt is stable at any given composition and temperature (compare Fig. 4.3 to Fig. 4.4).

In contrast to titanomagnetite, the single-phase domain of ilmenite-hematite solid solution at given fO_2 is very restricted. At low fO_2, the Ti/(Ti+Fe) values for Ilm_{ss} in coexistence with Tmt are max. 2 % lower than those of Ilm_{ss} in equilibrium with Psb_{ss}. The Ilm_{ss} single-phase domain broadens with increasing fO_2. At 1200 °C and ΔNNO=+4.2 for instance, the boundary Ti/(Ti+Fe)-values for the rhombohedral oxide are about 7 % apart (Fig. 4.3).

At $T \geqslant 1200\,^{\circ}C$ and ΔNNO<-3, both Tmt and Ilm_{ss} are richer in Ti than their endmembers ulvöspinel and ilmenite, i.e. Fe_2TiO_4 and $FeTiO_3$ (Fig. 4.5). This is in agreement with the data of Simons & Woermann (1978) and Senderov *et al.* (1993), but in contradiction with those of Taylor (1964). In several run products the corresponding Ti-excess is significant, i.e. definitely outside the estimated uncertainties of $\pm 0.5\,\mathrm{at}\%$ for the Ti/(Ti+Fe) values.

Most probably, the Ti excess in both phases reflects non-stoichiometry, resulting

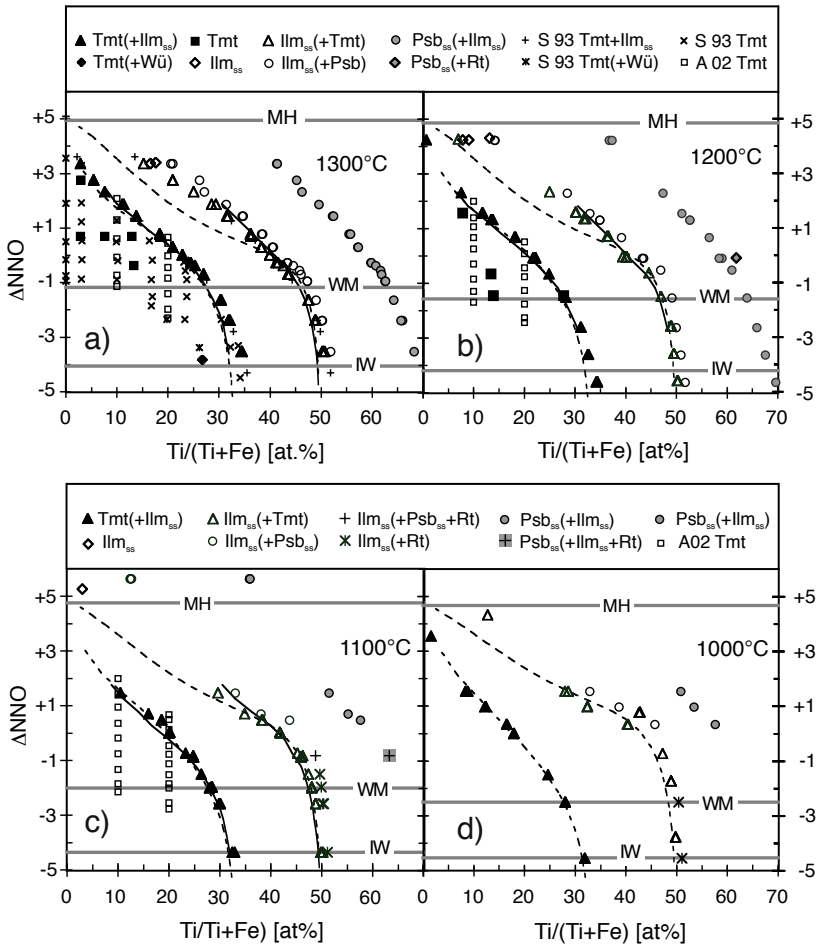

Fig. 4.3 Ti/(Ti+Fe) values [at%] of Tmt, Ilm_{ss}, and Psb_{ss} in run products as a function of temperature (a: 1300 °C, b: 1200 °C, c: 1100 °C, d: 1000 °C) and oxygen fugacity (ΔNNO). Triangles represent phase compositions of coexisting Tmt (black) and Ilm_{ss} (empty), circles represent coexisting Ilm_{ss} (empty) and Psb_{ss} (grey), both in two-phase run products of the present study. Most other symbols designate single-phase products from this study (Tmt: black squares, Ilm_{ss}: empty diamonds), or taken from Senderov *et al.* (1993, S93, single-phase Tmt and Tmt+Ilm_{ss}) or Aggarwal & Dieckmann (2002, A02). The curves represent the compositions of coexisting Tmt and Ilm_{ss} as calculated from the model of Ghiorso & Sack (1991) (solid curves), or from the QUILF software (dashed curves), using the model of Andersen & Lindsley (1988). Horizontal lines labelled MH, WM and IW mark oxygen fugacity that can be adjusted with the solid-state oxygen buffers at given temperature (see appendix A.1 for abbreviations).

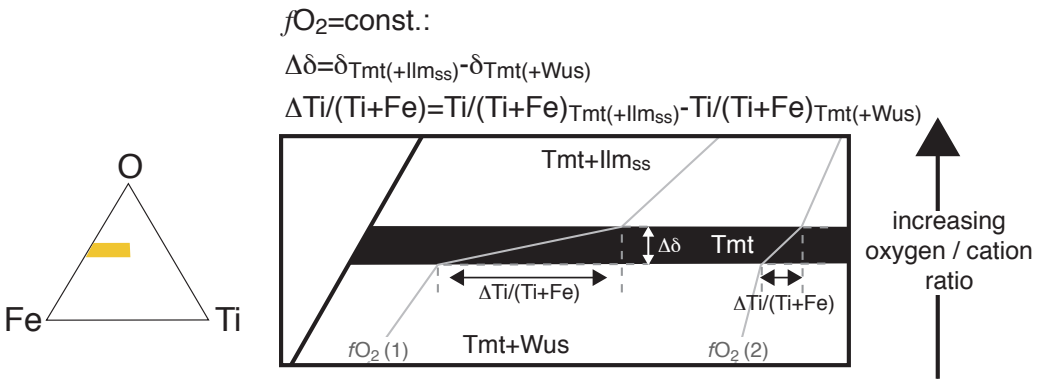

Fig. 4.4 Schematic representation of the compositional Tmt single-phase field (black wedge), illustrated in the triangle Fe-Ti-O. Assumed is constant non-stoichiometry over Tmt solid solution. Grey lines represent lines of constant oxygen fugacity (oxygen isobars), which cross the Tmt single-phase field at a flat angle at high Fe-contents (high fO_2: $fO_2(1)$) but at a steeper one at low Fe-contents (low fO_2: $fO_2(2)$).

from the substitution two Fe^{2+} against one Ti^{4+} and one cation vacancy ($2Fe^{2+} \leftrightarrow Ti^{4+} + \square$, Senderov *et al.*, 1993; Lattard, 1995), but in principle it may also be related to small Ti^{3+} contents (e.g. Grey *et al.*, 1974; Simons & Woermann, 1978). Non-stoichiometry will be considered in more detail in chapter 5.

A comparison of the titanomagnetite compositions (in Tmt+Ilm_{ss} assemblages) at $\Delta NNO < 2$ reveals a continuous shift towards the Fe-side with decreasing temperature, i.e. increasing Fe^{3+} content with decreasing temperature (Fig. 4.5a).

In case of the rhombohedral phase coexisting with titanomagnetite, the behaviour is more complex (Fig. 4.5b). The mineral compositions are hardly dependent on temperature, especially at low and at high fO_2. In the middle oxygen fugacity range the isotherms present inversion points and cross over at X_{Ilm} values which correspond to the transition between the ordered $R\bar{3}$ and the disordered $R\bar{3}c$ structure (Harrison *et al.*, 2000). This is exemplified in Fig. 4.5c for the 1300 °C and 1100 °C isotherms.

Fig. 4.5d shows the compositions of Ilm_{ss} coexisting with Psb_{ss} as a function of fO_2 and temperature. At $X_{Ilm} > 1$, Ilm_{ss}(+Psb_{ss}) synthesised at 1300 °C and given fO_2 is richer in Ti than Ilm_{ss}(+Psb_{ss}) synthesised at 1200 °C.

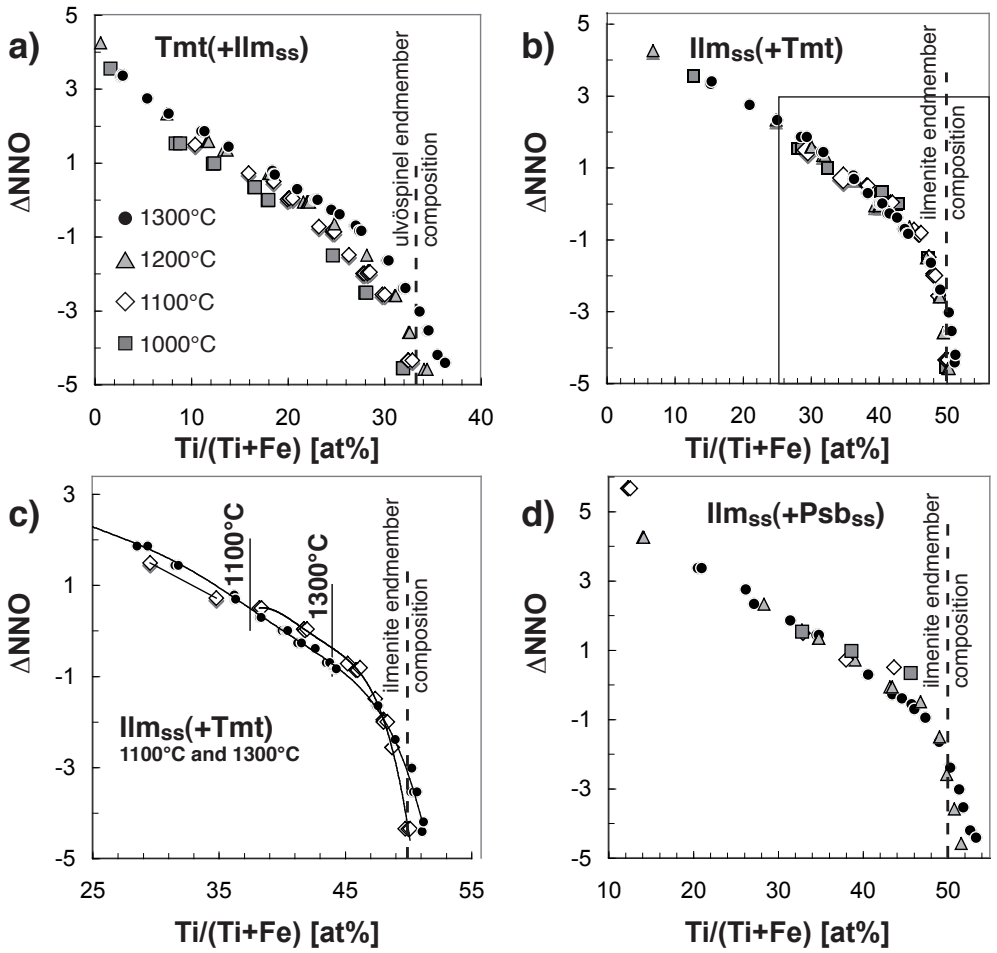

Fig. 4.5 Ti/(Ti+Fe) values [at%] of Tmt and Ilm_{ss} at 1000 °C (squares), 1100 °C (rhombs), 1200 °C (triangles) and 1300 °C (circles). The lines represent polynomial third order fits to the experimental data. The vertical dashed lines represent ulvöspinel and ilmenite endmember compositions. a) Tmt in coexistence with Ilm_{ss}. b) Ilm_{ss} in coexistence with Tmt. c) Enlargement of rectangular shown in picture (b). Ilm_{ss} in coexistence with Tmt at moderate to low oxygen fugacities, focus on 1100 °C and 1300 °C data. The solid vertical lines represent the compositions of Ilm_{ss} at which the transformation between the ordered ilmenite structure and the disordered hematite structure occurs at different temperatures (Harrison *et al.*, 2000). d) Ilm_{ss} in coexistence with Psb_{ss}.

4.4 Discussion

4.4.1 Comparison with previous experimental data on phase compositions and boundaries.

The compositions of coexisting Tmt and Ilm_{ss} retrieved from our experimental results at 1300 °C are in perfect agreement with those of Senderov *et al.* (1993) (Fig. 4.6).

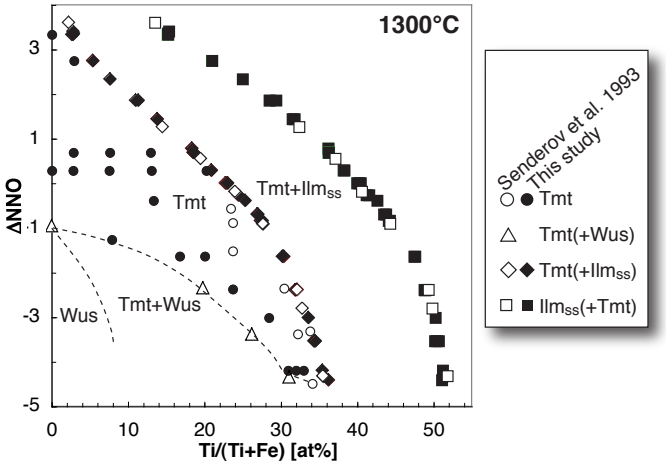

Fig. 4.6 Compositions of Tmt and Ilm_{ss} at 1300 °C retrieved in the present study (filled symbols) compared with the data of Senderov *et al.* (1993) (empty symbols). The dashed lines represent the boundaries of the binary Tmt-Wus phase field, based on unpublished experimental data by R. Engelmann (Heidelberg).

The extent of the single-phase domain of Tmt is in reasonable agreement with the data of Aggarwal & Dieckmann (2002) at 1300 °C. At 1200 °C and 1100 °C, and Ti/(Ti+Fe)=10 and 20 at% however, Aggarwal & Dieckmann (2002) report single-phase Tmt at higher oxygen fugacities than ours, i.e. single-phase Tmt within the Tmt+Ilm_{ss} phase field derived from this study's data (Fig. 4.7). At Ti/(Ti+Fe)=25at% Aggarwal & Dieckmann (2002) did not determine the upper (towards high fO_2) stability limit of Tmt.

Aggarwal & Dieckmann (2002) exclusively employed in-situ thermogravimetry and they state that on crossing the upper fO_2 stability limit of Tmt they record a large mass change due to the oxidation of Tmt to Ilm_{ss}.

Their samples were not quenched and not subsequently examined with microanalytical methods and it is not clear whether all these samples were really single-phase titanomagnetite in the reported in-situ conditions. The question especially arises for

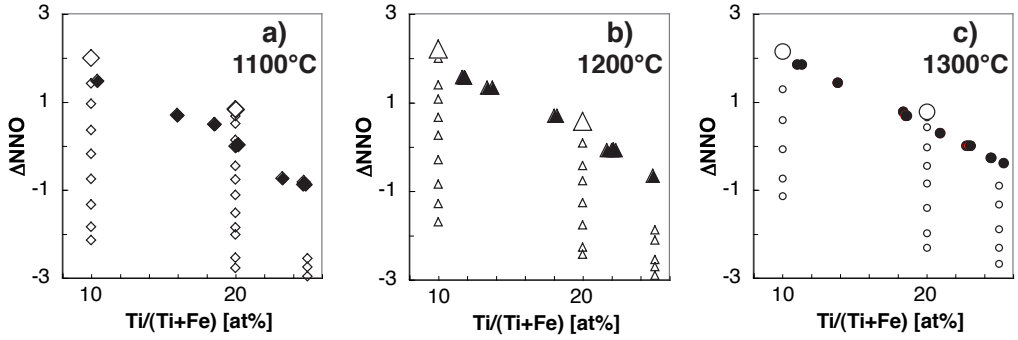

Fig. 4.7 Comparison of the compositions of Tmt retrieved from the present study (filled symbols) with those reported by Aggarwal & Dieckmann (2002) (empty symbols) at a) 1100 °C, b) 1200 °C, and c) 1300 °C. Small empty symbols represent single-phase Tmt, large empty symbols the upper fO_2-stability limit of Tmt, both according to Aggarwal & Dieckmann (2002).

the samples equilibrated at the highest oxygen fugacities, which may have contained small amounts of Ilm_{ss}. Because the disagreement between our results and those of Aggarwal & Dieckmann (2002) strongly increases with *decreasing* synthesis temperature, the most probable explanation is that the samples of Aggarwal & Dieckmann (2002) did not reach equilibrium during the thermogravimetric measurements, especially at 1100 and 1200 °C. Aggarwal & Dieckmann (2002) do not report the time spans allowed for re-equilibration during their measurements. For further comparison between this study and the data by Aggarwal & Dieckmann (2002) - especially concerning Tmt non-stoichiometry - see chapter 5.

4.4.2 Comparison with the thermodynamic thermo-oxybarometer formulations on the titanomagnetite-ilmenite$_{ss}$ assemblage

At first sight, the compositions of *titanomagnetite* in Tmt-Ilm_{ss} assemblages are in general agreement with those retrieved from the models of Andersen & Lindsley (1988) and Ghiorso & Sack (1991). A closer look at the data however, reveals significant discrepancies, which are especially pronounced at low fO_2 (Fig. 4.8). As already discussed in the preceding section, at low oxygen fugacities and high temperatures (1200 and 1300 °C) our synthetic titanomagnetites in equilibrium with Ilm_{ss} have especially high Ti concentrations, most probably in relation to cationic vacancies (Senderov *et al.*, 1993; Lattard, 1995). As the models do not account for vacancies, it is not surprising that they predict significantly lower Ti values.

Further, our synthetic titanomagnetites display higher Ti concentrations than those retrieved from the Ghiorso & Sack (1991) model at all temperatures also un-

der moderate to high oxygen fugacities (ΔNNO>-1). The latter differences might reflect errors in the standard state properties used for the ulvöspinel endmember.

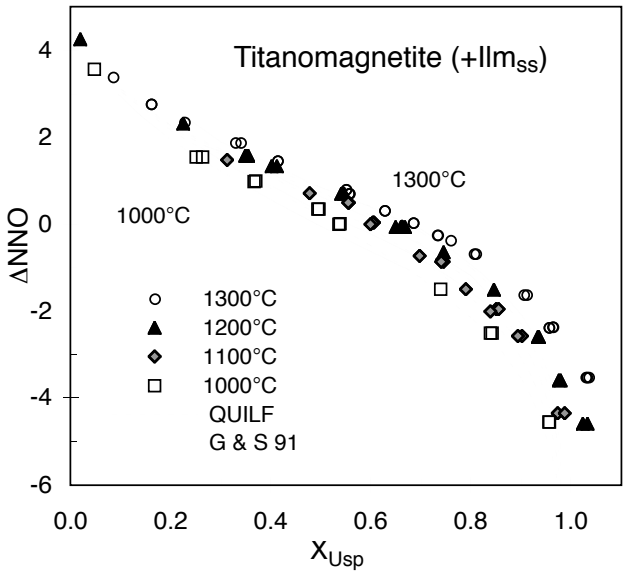

Fig. 4.8 Composition of titanomagnetite in equilibrium with Ilm_{ss} as a function of temperature and oxygen fugacity. Symbols represent experimental data from the present study, the curves are isotherms calculated with the model of Ghiorso & Sack (1991) (solid curves) and with the QUILF software (dashed curves).

As shown in Fig. 4.9 the variation of the *ilmenite$_{ss}$* composition as a function of T and fO_2 is quite different from that calculated with the QUILF software, which is based on the model of Andersen & Lindsley (1988), especially at high oxygen fugacities and low X_{Ilm}. Whereas our experimental data show practically no temperature dependence of Ilm_{ss} composition at ΔNNO>1, the isotherms of Andersen & Lindsley (1988) are shifted towards lower fugacities with increasing temperature. The strongest discrepancies between experimental and calculated values are at the highest temperatures (1300 and 1200 °C). In contrast the isotherms of Ghiorso & Sack (1991) point to higher fO_2 than our data at ΔNNO>1.

The differences in the two thermodynamic treatments of Ilm_{ss} are even more apparent in a Roozeboom plot. A Roozeboom plot of X_{Ilm} vs. X_{Usp} allows a simultaneous consideration of Ilm_{ss} and Tmt composition. Fig. 4.10 shows the composition of coexisting synthetic ilmenite$_{ss}$ and titanomagnetite, and polynomial curves fitted to the experimental data. Usually two third order polynomials were fitted to each

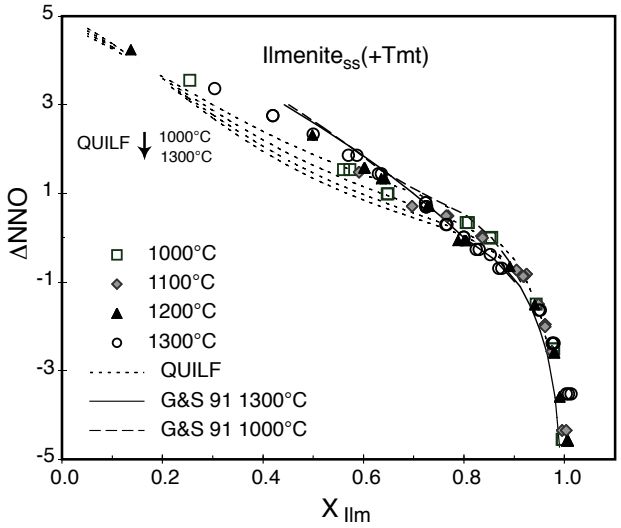

Fig. 4.9 Composition of Ilm$_{ss}$ in equilibrium with Tmt as a function of temperature and oxygen fugacity. Symbols represent experimental data from the present study, the curves are isotherms calculated with the model of Ghiorso & Sack (1991) (thick solid and dashed curves) and with the QUILF software (thin dotted curves).

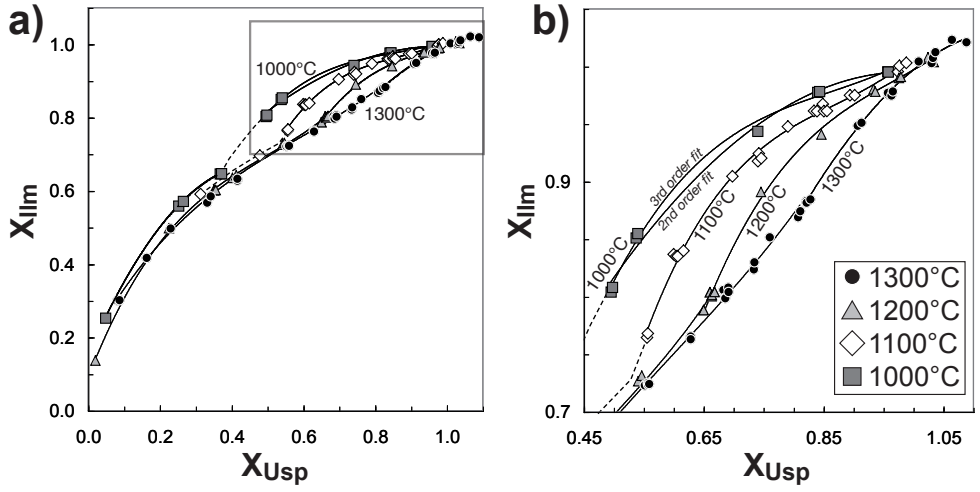

Fig. 4.10 a) Roozeboom plot of coexisting Ilm$_{ss}$ and Tmt from run products at different temperatures (symbols). Solid lines are third order polynomial fits to experimental data. For 1000 °C data a second order fit is drawn additionally. Dashed lines are graphic interpolations between the fit curves. b) Enlargement of the Ti-rich part of the diagram (rectangle in picture (a)).

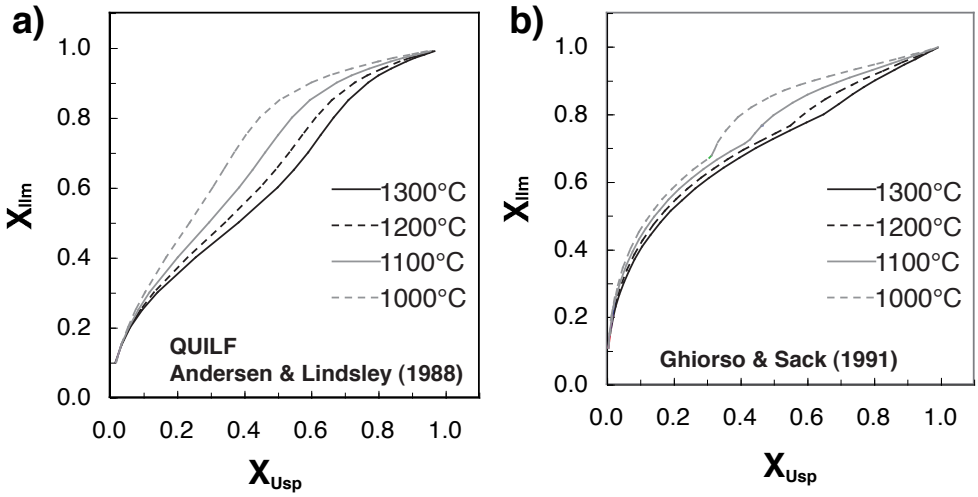

Fig. 4.11 Roozeboom plot of the isotherms derived from the models by a) Andersen & Lindsley (1988, QUILF) and b) Ghiorso & Sack (1991) from 1000 °C to 1300 °C.

temperature curve, one on the Fe-rich side ($R\bar{3}c$) and one on the Ti-rich side ($R\bar{3}$) of the transition within the ilmenite-hematite solid solution (Harrison *et al.*, 2000). To the 1000 °C data on the Ti-rich side ($R\bar{3}$) a second or a third order polynomial can be fitted almost equally well (third order fit: R^2=0.9968, second order fit: R^2=0.9937). The isotherms on the side of the long-range ordered $R\bar{3}$ structure are conspicuously bent and distinctly spread up. In contrast, the isotherms for the $R\bar{3}c$ structure are hardly distinguishable.

The isotherms derived from the QUILF model (Andersen & Lindsley, 1988) do not show the bend related to the structural change of Ilm_{ss} ($R\bar{3}$ to $R\bar{3}c$, Fig. 4.11a), which *is* accounted for by the isotherms of Ghiorso & Sack (1991, Fig. 4.11b) and which is also present in our experimental data (Fig. 4.10). Experimental and model isotherms are distinctly different over the whole compositional range (Fig. 4.12).

In fact, it is not fair to plot values retrieved from the model of Andersen & Lindsley (1988) at ΔNNO>1 although such values can be easily obtained by using the QUILF software (Andersen *et al.*, 1993). Andersen & Lindsley (1988) have based their solution model for Ilm_{ss} only on compositions close to $FeTiO_3$ and did not consider the effect of the $R\bar{3}$ to $R\bar{3}c$ transition on the solution properties of Ilm_{ss} (chapter 1.3). Consequently, they truncated their isopleth diagram at the $R\bar{3}$-$R\bar{3}c$ transition (cf. Figs. 2, 5 in Andersen & Lindsley, 1988) and cautioned the readers that "application ... to natural samples outside the range of the experimental calibration will lead to larger uncertainties". Lindsley & Frost (1992) did not rec-

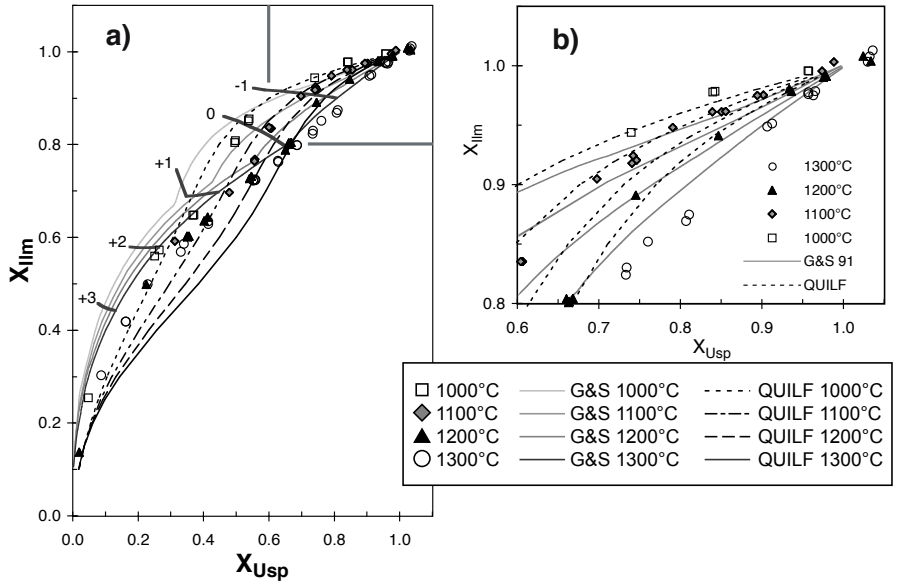

Fig. 4.12 a) Roozeboom plot of coexisting Ilm_{ss} and Tmt from run products at different temperatures (symbols) compared with the isotherms calculated with the models of Ghiorso & Sack (1991) (grey curves) and Andersen & Lindsley (1988) (QUILF, black curves). Also note the iso-ΔNNO curves (thick lines) from Ghiorso & Sack (1991). b) Enlargement of the upper right corner of picture (a).

ommend the use of the QUILF algorithms at high fO_2 conditions. For oxidised Fe-Ti oxide parageneses that contain hematite-rich Ilm_{ss} at T> 1000 °C the mis-application of their model leads to strong underestimates of the equilibration temperatures (Fig. 4.12). At somewhat lower temperatures (around 800 °C), which are more relevant to relatively oxidised volcanic rocks (e.g. Pinatubo Dacite, cf. Evans & Scaillet, 1997; Scaillet & Evans, 1999), the (mis-)use of the QUILF software yields to overestimated temperatures (chapter 1.3, Fig. 1.21).

In contrast, the model by Ghiorso & Sack (1991) *does* account for the $R\bar{3}$ to $R\bar{3}c$ transition, and consequently the model isotherms show a related bend (Fig. 4.11b). However this model relies heavily on experimental data obtained from sample compositions that could not be controlled with micro-analytical methods (e.g. Ishikawa, 1958). In fact, the model does not adequately reproduce the $ilmenite_{ss}$ compositions at ΔNNO>1 (Fig. 4.3, 4.9). At any given fO_2 and T in this fugacity range, X_{Ilm} is overestimated (Fig. 4.9) and this is the main reason for the fO_2 overestimates for the data relevant to the Pinatubo dacite (chapter 1.3, Fig. 1.21).

In any case, it is clear that unsatisfactory thermodynamic models for X_{Ilm} are mainly responsible for the wrong temperature estimates for oxidised Fe-Ti oxide parageneses from the models of both Andersen & Lindsley (1988) and Ghiorso & Sack (1991). For the temperatures investigated experimentally within this study (i.e. 1000 °C to 1300 °C) at ΔNNO>1 the modelled X_{Ilm} values are either too low (Andersen & Lindsley, 1988) or too high (Ghiorso & Sack, 1991), which translates into either too low or too high estimated temperatures (Figs. 4.9, 4.12).

In the case of moderately to highly reduced Tmt-Ilm_{ss} assemblages (ΔNNO<0) the most apparent discrepancy between experimental data and current models concerns the 1300 °C results, which plot to the right high X_{Usp} and high *temperature* side of the isotherms in the Roozeboom diagram (Fig. 4.12). The models produce temperature overestimates.

Further misestimates by using the Ilm_{ss}-Tmt thermo-oxybarometer arise from the minor element content in natural Fe-Ti oxides and the appropriate consideration in the thermodynamic formulations. The effect Mg and Al on Fe-Ti oxide phase relations and compositions will be treated in chapter 6.

4.4.3 Comparison with the thermodynamic model of Anovitz *et al.* (1985) on the ilmenite$_{ss}$ - pseudobrookite$_{ss}$ assemblage

Some of our results on the chemical compositions of coexisting ilmenite$_{ss}$ and pseudobrookite$_{ss}$ solid solutions are plotted together with isopleths calculated by Anovitz *et al.* (1985) using a model based on calorimetric and phase equilibrium data (Fig. 4.13). In accordance with Anovitz *et al.* (1985) our data show that the compositions of both phases strongly depend on the redox conditions. On the other hand, the pseudobrookite$_{ss}$ compositions are practically independent of temperature and the ilmenite$_{ss}$ isopleths display a temperature dependence only at low or at very high oxygen fugacities. Consequently, as already noted by Anovitz *et al.* (1985), the Ilm_{ss}-Psb_{ss} equilibrium is not well-suited for thermometric applications but has a good potential as an "oxy-barometer".

The best agreement between our data and those of Anovitz *et al.* (1985) is at 1000 °C and ΔNNO=1.5. At lower oxygen fugacities the model drastically overestimates fO_2 by as much as 2 log units for the most reduced conditions. At high fO_2 the model predicts too high fO_2 from the compositions of Psb_{ss}, but too low fO_2 from the composition of Ilm_{ss}.

One reason for the discrepancies between our data and the model of Anovitz *et al.* (1985) is clearly seen in the thermodynamic treatment of the ilmenite-hematite solid solution used by the latter authors. They chose the model of Spencer & Lindsley

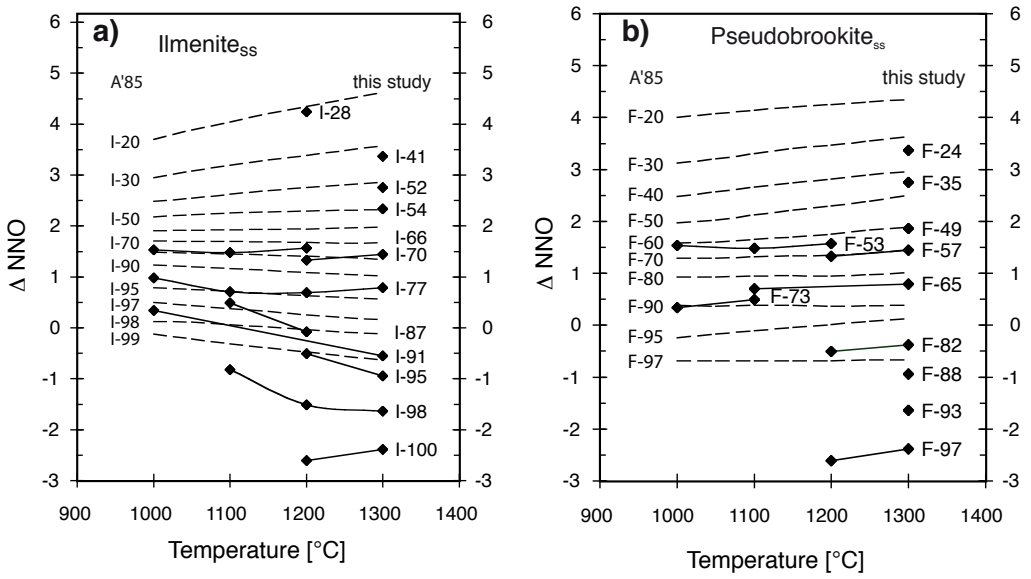

Fig. 4.13 Isopleths of the compositions of coexisting Ilm_{ss} and Psb_{ss}. a) Ilm_{ss} in equilibrium with Psb_{ss}. I - e.g. I-20 - represents the mol% of $FeTiO_3$ in Ilm_{ss}. b) Isopleths of the compositions of Psb_{ss} in equilibrium with Ilm_{ss}. F (e.g. F-20) represents the mol% of $FeTi_2O_5$ in Psb_{ss}. Black rhombs represent data from the present study with interpolated curves (solid lines). Dashed lines depict the data of Anovitz *et al.* (1985) (A'85).

(1981) which does not consider the effects of the $R\bar{3}$ to $R\bar{3}c$ transition and of non-stoichiometry.

Both pseudobrookite$_{ss}$ endmembers (Fe_2TiO_5 and $FeTi_2O_5$) were treated as ordered components, and the solid solution was assumed to be ideal because not enough experimental data were available to sustain a more complicate model.

4.4.4 Perspectives for new versions of the Fe-Ti oxide thermo-oxybarometers

The experimental data set on the three Fe-Ti oxide solid solutions presented here is intended to support new versions of both the titanomagnetite-ilmenite$_{ss}$ thermo-oxybarometer and the ilmenite$_{ss}$-pseudobrookite$_{ss}$ oxybarometer.

Further, a new version of the Fe-Ti oxide thermo-oxybarometer model will also include compositional data on coexisting synthetic Tmt and Ilm$_{ss}$ in Mg-, Mn- and Al-bearing systems. At $T \geq 1100\,^{\circ}C$ and 1 bar pressure, data for Mg-Al bearing compositions is provided in the present thesis (chapter 6). In the temperature and pressure range of $750-900\,^{\circ}C$ and $100-400\,MPa$ samples, and at relatively high oxygen fugacities (slightly below NNO to NNO+3) data for the system Fe-Ti$\pm$Mg$\pm$Mn$\pm$Al-O is - or soon will be - available by Scaillet & Evans (1999) and Evans *et al.* (in press).

These data will help to improve solid solutions models for chemically complex titanomagnetites and rhombohedral oxides.

Within this study, experimental data on Tmt non-stoichiometry (chapter 5) are derived, which shall also contribute to the development of new thermo-oxybarometer formulations.

The present data on coexisting ilmenite$_{ss}$ and pseudobrookite$_{ss}$ in the Fe-Ti-O system yield the basis for a first experimental calibration of the corresponding oxybarometer.

5 High-T non-stoichiometry in magnetite-ulvöspinel solid solution

5.1 Introduction

It has been known for long that spinel-type minerals can be non-stoichiometric at high temperatures. For example, this was shown by Viertel & Seifert (1979, 1980) for spinel $MgAl_2O_4$. Non-stoichiometry of the spinel-type mineral titanomagnetite at high temperature has been examined in numerous studies (e.g. Taylor, 1964; Simons & Woermann, 1978; Dieckmann, 1982; Lattard, 1987; Senderov *et al.*, 1993; Lattard, 1995; Aggarwal & Dieckmann, 2002). However, the existing data base is contradictory (see section 1.2) and a comprehensive quantification in dependence of temperature and Tmt composition is still missing.

The composition of titanomagnetite can vary along the stoichiometric magnetite-ulvöspinel solid solution join, i.e. at cation/oxygen value p.f.u. of 3/4 (see chapter 1, section 1.2.3). It may deviate from stoichiometry towards a higher cation sum (if cation interstitials are present) or a lower cation sum (in case of cation vacancies, (section 1.2; Aggarwal & Dieckmann, 2002; Senderov *et al.*, 1993). Both compositional variations must affect the physical properties of titanomagnetite, e.g. its magnetic behaviour.

As reported in section 1.1, the composition of titanomagnetite can be estimated from its Curie temperature (T_C), as T_C decreases more or less linearly with increasing X_{Usp}. However, at given cationic ratio of Tmt variations in non-stoichiometry also influence T_C and thus may spoil X_{Usp} estimates (Hauptman, 1974; Rahman & Parry, 1978; Moskowitz, 1987; Wanamaker & Moskowitz, 1994; Engelmann *et al.*, in preparation).

Non-stoichiometry also effects thermo-oxybarometry. It has been suggested in chapter 4 that Tmt non-stoichiometry is one major cause for the failure of the existing formulations of the Tmt-Ilm_{ss} oxide thermo-oxybarometer at low oxygen fugacity and high temperature. However, up to now and due to the limited data base, Tmt non-stoichiometry has not been included in the thermo-oxybarometer formulations.

In order to evaluate the effect of Tmt non-stoichiometry on Fe-Ti oxide thermo-oxybarometry and on magnetometry there is need for consistent non-stoichiometry data covering a broad range in temperature and Tmt composition. This thesis provides a re-investigation, focussing on detecting and quantifying Tmt non-stoichiometry in the system Fe-Ti-O as a function of X_{Usp} in the temperature range between 1100 °C and 1300 °C.

Several experimental and analytical approaches will be evaluated in respect of their suitability to examine Tmt non-stoichiometry. The combination of these methods aims resolve and understand the contradictions encountered in previous literature (section 1.2). The final goal is to quantify the concentration of cation vacancies and so to enable to include this data set in the solid solution model for titanomagnetite that will be incorporated in a new formulation of the Tmt-Ilm_{ss} thermo-oxybarometer.

5.2 Strategy

To investigate Tmt non-stoichiometry as a function of T and X_{Usp}, subsolidus *synthesis experiments* and *re-equilibration experiments* were carried out between 1100 °C and 1300 °C to produce Tmt with maximum cation vacancy concentration (δ_{max}), i.e. titanomagnetite in coexistence with $ilmenite_{ss}$. For comparison, Tmt coexisting with Wus or with metallic iron have been synthesised. Tmt(+Wus) is expected to be stoichiometric or even to have slight cation excess (δ_{min}). Single-phase Tmt with intermediate δ has also been produced.

Subsequent *annealing* (at 950 °C) of selected high-T (i.e. synthesis and re-equilibration) Tmt+Ilm_{ss} samples under oxygen-conserving conditions causes vacancy relaxation in originally non-stoichiometric high-T Tmt (Lattard, 1995) (see details in section 5.3). This is accompanied by changes in phase compositions and proportions, which can be used to estimate the original vacancy concentration in Tmt in the high-T sample. The relative amounts of coexisting phases were determined by image analysis or Rietveld analysis for high-T run products and belonging annealed samples (see section 5.3). Annealing experiments are named after the preceding high-T experiment with a capital D affixed (e.g. annealing experiment 6F63x8D was carried out using synthesis run product 6F63x8).

Further, to obtain information on high-T Tmt non-stoichiometry, Tmt lattice parameters (a_0) were determined for selected samples (T=950 – 1300 °C; Tmt+Ilm_{ss}, Tmt, Tmt+Wus) (see section 5.4). It has been shown in literature (e.g. Hauptman, 1974; Senderov *et al.*, 1993) that at given Ti/(Ti+Fe), a variation in non-stoichiometry results in a change in lattice parameter.

For selected samples $Fe^{3+}/\Sigma Fe$ (f) was determined by electron energy loss spectroscopy (EELS) (see section 5.5). Combined with the Ti/(Ti+Fe) (x) ratio determined by EMP, the vacancy concentration can be calculated (equation 5.1) for Tmt with the general formula $\left(Fe^{3+}_{f(1-x)}Fe^{2+}_{(1-f)(1-x)}Ti^{4+}_{x}\right)_{(3-\delta)}\square_{\delta}O_4$ ($\square$: vacancy).

$$\delta = 3 - \frac{8}{f(1-x)+2(1+x)} \tag{5.1}$$

δ is the number of vacancies per formula unit and can be easily translated into cation per cent (cat%=100*δ/3).

5.3 Annealing under oxygen-conserving conditions

5.3.1 Principles and methods

High-temperature (1100 °C to 1300 °C) synthesis or re-equilibration Tmt(+Ilm_{ss}) samples, containing potentially non-stoichiometric Tmt (Fig. 5.1a) were annealed at oxygen-conserving conditions in an evacuated silica glass ampoule (i.e. at fixed bulk composition) at 950 °C for sufficient time (i.e. 1-3 weeks). The purpose was to cause vacancy relaxation and produce a stoichiometric Tmt(+Ilm_{ss}) from an originally non-stoichiometric high temperature Tmt (in equilibrium with Ilm_{ss}).

Annealing at a temperature below synthesis temperature involves a rotation of the Tmt-Ilm_{ss} tie-line towards a flatter slope. As the oxygen content of the sample is fixed during annealing, the sample bulk composition is the pivotal point of the tie-line rotation (illustrated in the Fe-Ti-O triangle, Fig. 5.1). A decrease in Tmt vacancy concentration (i.e. δ) must be accompanied by an increase of the modal Ilm_{ss} proportion. As shown by Lattard (1995) Ilm_{ss} forms lamellae and rims in or around the Tmt crystals. Therefore, the observation of Ilm_{ss} exsolution features in an annealed sample is a visible evidence for high temperature non-stoichiometry of Tmt. The shift of phase compositions and phase proportions upon annealing can be used to infer the original *high temperature* Tmt non-stoichiometry.

According to the existent literature (e.g. Dieckmann, 1982; Aggarwal & Dieckmann, 2002), vacancy concentration in Tmt coexisting with $ilmenite_{ss}$ decreases with decreasing temperature. Based on the data by Dieckmann (1982, interpolation between 900 and 1000 °C) and by extrapolating that of Aggarwal & Dieckmann (2002, 1100 to 1300 °C) towards lower temperature, we estimate the vacancy concentration of Tmt in coexistence with Ilm_{ss} at 950 °C to be negligible ($\delta_{max} \ll 1$, Fig. 5.2).

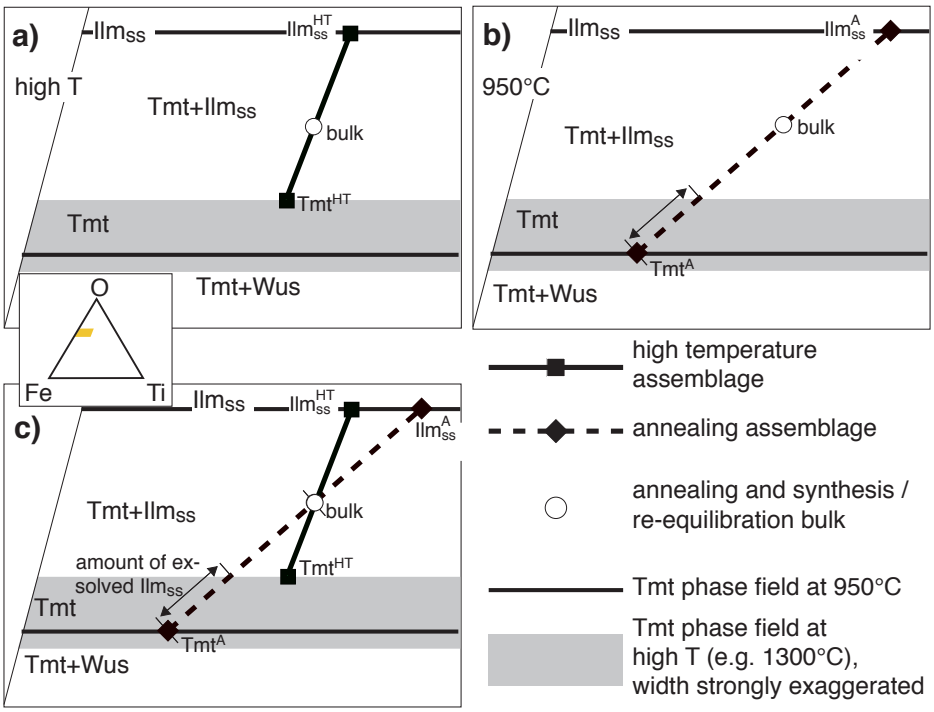

Fig. 5.1 Phase compositions and modal proportions of a high temperature $Tmt+Ilm_{ss}$ assemblage (a) and of the same sample annealed at 950 °C (b), schematically illustrated in the Fe-Ti-O triangle. a) High temperature assemblage with stoichiometric Ilm_{ss} (Ilm_{ss}^{HT}) and coexisting non-stoichiometric Tmt (Tmt^{HT}). b) Assemblage after annealing at 950 °C: stoichiometric Ilm_{ss} (Ilm_{ss}^{A}) and coexisting stoichiometric Tmt (Tmt^{A}). c) Bulk composition (empty circle) remains fixed. Upon annealing, the tie-line rotates around the bulk composition. Vacancy relaxation results in an increase of Ilm_{ss} modal proportion (arrow).

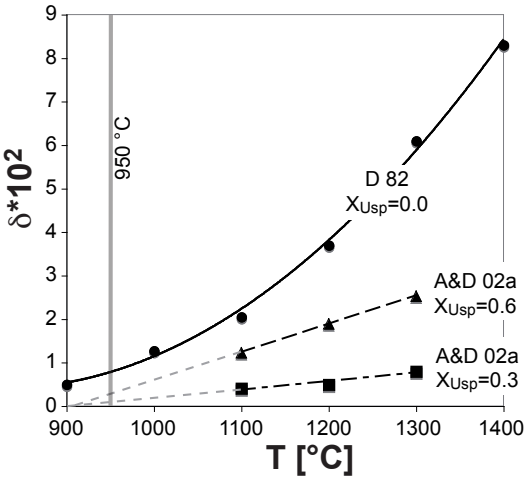

Fig. 5.2 Cation vacancy concentration in Tmt coexisting with Ilm_{ss} expressed as δ_{max}, versus T according to Dieckmann (1982) (D82) for pure magnetite (circles) and Aggarwal & Dieckmann (2002) (A&D02a) for Tmt with X_{Usp}=0.3 (squares) and 0.6 (triangles). Black curves are a second order fit to the data by Dieckmann (1982) (solid curve) and linear fits to the data by Aggarwal & Dieckmann (2002) (dashed lines). Grey dashed lines represent linear extrapolations of the linear fits. The vertical grey bar marks 950°C, the annealing temperature.

As the vacancy concentration decreases with decreasing temperature, annealing at T<950°C should produce a Tmt which is even closer to stoichiometry than 950°C Tmt. Nevertheless, we selected 950°C as annealing temperature because

- kinetics decrease with decreasing T and vacancy relaxation would probably become too sluggish at T<950°C, and
- Tmt and Ilm_{ss} solid solutions display miscibility gaps below about 600°C and 800°C, respectively (section 1.2). Annealing at T<800°C thus results in exsolution of the phases.

Based on the annealing experiments, δ has been quantitatively estimated by

- method A, which is based on the increase of modal Ilm_{ss} abundance during annealing, and
- method B, which evaluates the shift of phase compositions during annealing.

Method A A rough quantitative estimation of non-stoichiometry can be obtained by evaluating the phase proportions observed in annealed versus high-T samples.

Assuming annealed phases and high-T Ilm_{ss} to be stoichiometric, the increase in Ilm_{ss} content during annealing (i.e. the modal proportion of exsolved Ilm_{ss}: $M_{Ilm_{ss}^{ex}}$, see Fig. 5.3) is proportional to δ of high-T Tmt and can be calculated according to equations 5.2 to 5.6.

$$\frac{\mathrm{M}_{Ilm_{ss}^{ex}}}{\Sigma \mathrm{M}} = \frac{\mathrm{M}_{Ilm_{ss}^{ex}}}{1} = \frac{\Delta \mathrm{O}_{Tmt}}{\Delta \mathrm{O}_{Ilm_{ss}-Tmt}} \tag{5.2}$$

$\Delta \mathrm{O}_{Tmt}$ is the difference in oxygen content between non-stoichiometric and stoichiometric Tmt, and $\Delta \mathrm{O}_{Ilm_{ss}-Tmt}$ is the difference in oxygen content between stoichiometric Ilm_{ss} and Tmt. Taking the oxygen contents p.f.u.,

$$\Delta \mathrm{O}_{Ilm_{ss}-Tmt} = \frac{3}{5} - \frac{4}{7} \tag{5.3}$$

and

$$\Delta \mathrm{O}_{Tmt} = \frac{4}{7-\delta} - \frac{4}{7} = \frac{4}{7} * \frac{\delta}{7-\delta} \tag{5.4}$$

Insertion of equations 5.3 and 5.4 to equation 5.2 yields

$$\mathrm{M}_{Ilm_{ss}^{ex}} = 20 * \frac{\delta}{7-\delta} \tag{5.5}$$

which can be converted to

$$\delta = \frac{7 * \mathrm{M}_{Ilm_{ss}^{ex}}}{20 + \mathrm{M}_{Ilm_{ss}^{ex}}} \tag{5.6}$$

Modal phase proportions in both annealed (M_{Tmt^A} and $\mathrm{M}_{Ilm_{ss}^{A}}$) and high-T samples ($M_{Tmt^{HT}}$ and $\mathrm{M}_{Ilm_{ss}^{HT}}$) have been determined by image analysis yielding vol%. Vol% was converted into mol% assuming a linear correlation between composition and density along the solid solution series (see appendix A.4). For samples that were used for lattice parameter determination (see section 5.4) modal phase proportions could also be retrieved from Rietveld analysis (wt%, converted into mol%). Based on these data, the amount of Ilm_{ss} exsolution features ($\mathrm{M}_{Ilm_{ss}^{ex}}$) can be estimated according to equations 5.7 and 5.8 (cf. Fig. 5.3).

$$\frac{M_{Ilm_{ss}^{HT}}}{M_{Tmt^{HT}}} = \frac{M_{Ilm_{ss}^{A}} - M_{Ilm_{ss}^{ex}}}{M_{Tmt^{A}}} \tag{5.7}$$

$$M_{Ilm_{ss}^{ex}} = M_{Ilm_{ss}^{A}} - M_{Tmt^{A}} * \frac{M_{Ilm_{ss}^{HT}}}{M_{Tmt^{HT}}} \tag{5.8}$$

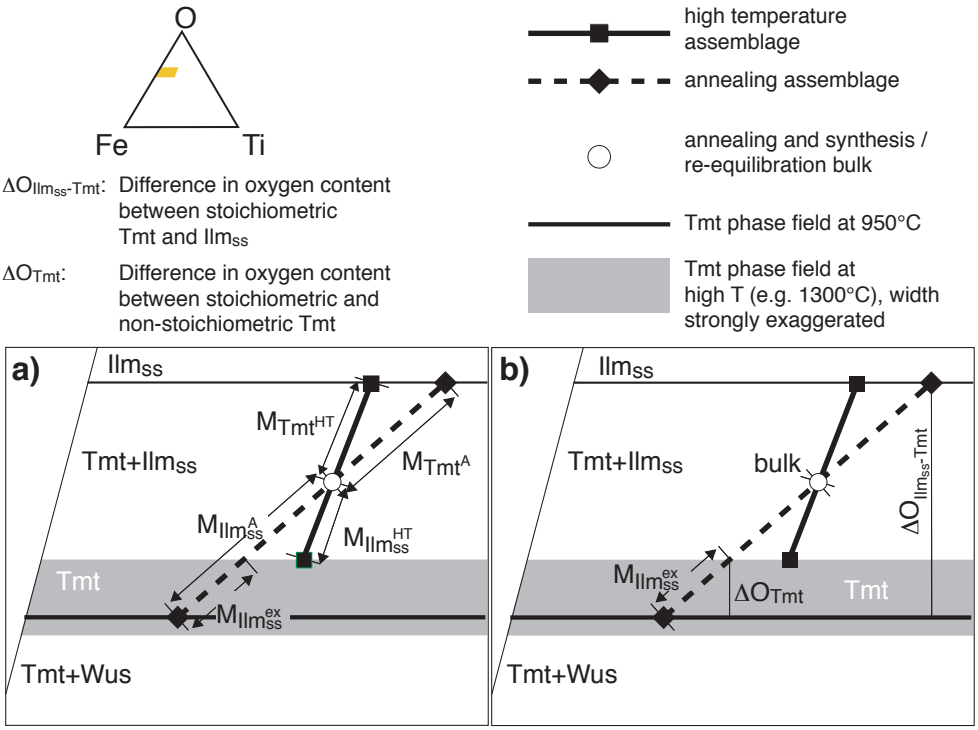

Fig. 5.3 a) Tie-lines of annealing assemblage (dashed line) and belonging high-T assemblage (solid line), and modal phase proportions before and after annealing ($M_{Tmt^{HT}}$, $M_{Tmt^{A}}$, $M_{Ilm_{ss}^{HT}}$, $M_{Ilm_{ss}^{A}}$). The sample bulk (circle) is fixed and is the pivotal point of tie-line rotation. b) The amount of exsolved Ilm_{ss} ($M_{Ilm_{ss}^{ex}}$) is proportional to the change of Tmt oxygen content during annealing (ΔO_{Tmt}).

Method B The above described estimation of non-stoichiometry in synthesis Tmt (method A) is exclusively based on modal phase abundances. It is therefore also subjected to the large uncertainties of these methods (section 5.3.2). An improvement can be attained by considering the phase compositions (cationic ratio Ti/(Ti+Fe) from EMP analysis) and evaluating the rotation of the conode, which is caused by the temperature change.

(I) As annealed phases are assumed to be stoichiometric, their oxygen contents are known and the position of the tie-line $Tmt^A - Ilm^A_{ss}$ can be easily derived from EMP data (Fig. 5.4a). The composition of Ilm^{HT}_{ss} is also assumed to be stoichiometric.

(II) The sample bulk is a point on the $Tmt^A - Ilm^A_{ss}$ tie-line and can be located by two methods.

- Intersecting the line for the Ti/(Ti+Fe) ratio of sample bulk (TTF_{bulk}) with the tie-line between annealed phases (Fig. 5.4a).
- Dividing the $Tmt^A - Ilm^A_{ss}$ tie-line according to the modal proportions of the phases (M_{Tmt^A}, $M_{Ilm^A_{ss}}$). The modal phase proportions can be obtained from image analysis or from Rietveld analysis.

(III) Sample bulk and Ilm^{HT}_{ss} point determine the $Tmt^{HT} - Ilm^{HT}_{ss}$ tie-line (Fig. 5.4b).

(IV) The composition of Tmt^{HT} lies at the intersection of the $Tmt^{HT} - Ilm^{HT}_{ss}$ tie-line with $TTF_{Tmt^{HT}}$ (Ti/(Ti+Fe) of synthesis Tmt from EMP, Fig. 5.4b).

When the composition of Tmt^{HT} (including oxygen) is known, Tmt non-stoichiometry (δ) can be calculated.

For calculation of the tie-lines, phases and intersecting points, the triangle Fe-Ti-O was described in a cartesian coordinate system (Fig. 5.5). Points are described by x-y coordinates, (tie-)lines by linear equations of the form y=mx+b, where m is the gradient and b is the y axis intercept. Following the steps described above, the coordinates for Tmt^{HT} have been calculated. The cartesian y coordinate can be translated into δ according to equation 5.9 (cf. Fig. 5.5).

$$\delta = 7 - \frac{2 * \sqrt{3}}{y} * 100 \tag{5.9}$$

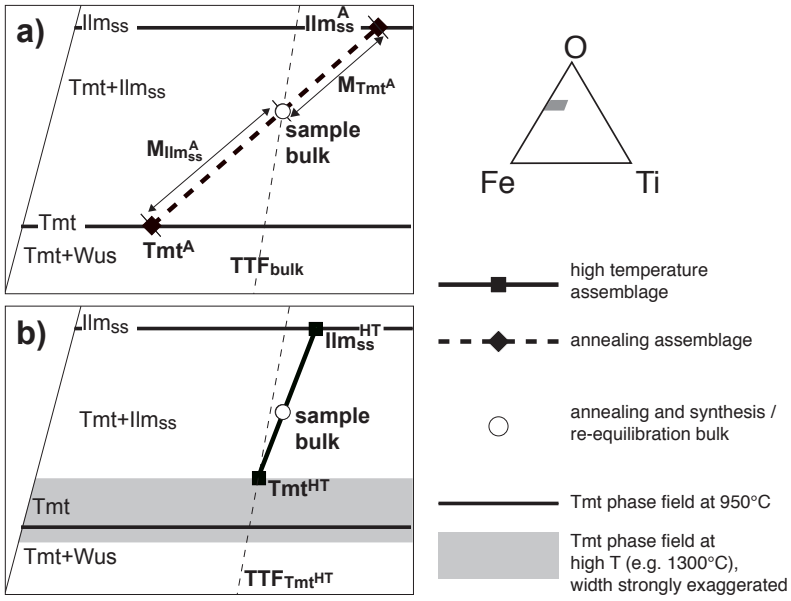

Fig. 5.4 Calculation of coordinates of high-T Tmt. a) Based on modal phase proportions of the annealing sample (M_{Tmt^A}, $M_{Ilm_{ss}^A}$) or sample bulk cationic ratio (TTF_{bulk}), and phase compositions (Tmt^A, Ilm_{ss}^A), the coordinates of sample bulk (circle) including oxygen can be determined. b) Sample bulk and synthesis Ilm_{ss} composition (Ilm_{ss}^{HT}) are known. Tmt^{HT} is the crossing point between a straight line through Ilm_{ss}^{HT} and bulk, and the cationic ratio of synthesis Tmt ($TTF_{Tmt^{HT}}$).

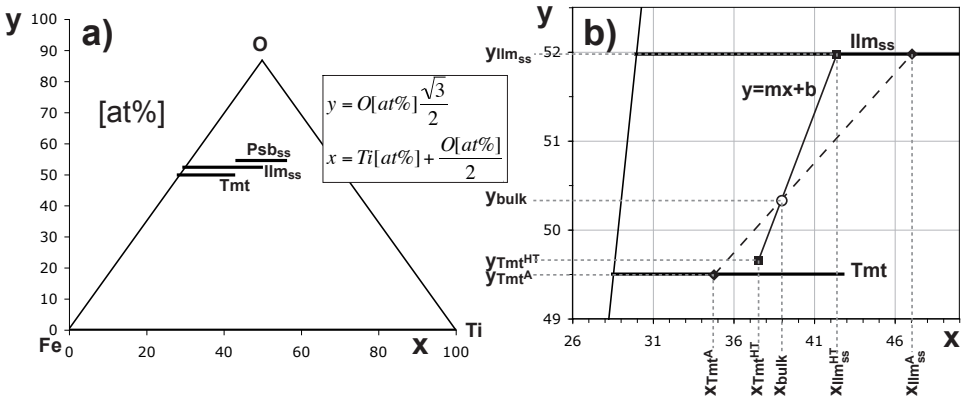

Fig. 5.5 a) Calculation of the triangle Fe-Ti-O in a cartesian x-y coordinate system. b) Section of the triangle Fe-Ti-O and belonging x-y coordinates. Phase compositions can be described by means of x-y coordinates (e.g. y_{bulk}, x_{bulk}), tie-lines by equations of the form y=mx+b (annealing tie-line: dashed, high-T tie-line: solid).

5.3.2 Uncertainties of the methods

Uncertainties for the determination of modal phase abundances The error bars on δ calculated from method A of the annealing method (e.g. Fig. 5.13) result from error propagation of the uncertainties on the modal phase abundances.

The uncertainty on modal phase abundances in vol%, determined by image analysis has to be given as about $\pm 3-6$ vol%. This results from statistically slightly different modal abundances in different sample regions, and consequently in the different BSE pictures that were used for image analysis. Further, variations in brightness within one picture, edge effects etc. have to be considered. In annealed samples, the fine exsolution features could often hardly be resolved by image analysis.

Rietveld analysis yields phase proportions in wt%. The uncertainty is comparable to image analysis, at about $\pm 3-6$ wt%. Additionally to the uncertainty arising from the Rietveld refinement (about ± 1 vol%), statistically slightly different modal abundances in different sample regions have to be considered. Further, textural effects within the powder examined by X-ray diffraction can influence the result.

Both vol% and wt% have to be converted into mol%. The uncertainty on mol% is calculated by error propagation to about $\pm 3-6$ mol%

The modal proportions derived from image analysis and Rietveld analysis are generally in agreement. However, in many cases the modal proportion of Tmt derived with the image analysis is higher than the proportion derived by Rietveld analysis (Fig. 5.6). The reason for this is unclear. It may potentially be related to textural effects in the powdered X-ray sample, which may influence the Rietveld results.

Uncertainties and error bars for method B The calculation of δ according to method B is based on the evaluation of the shift of phase compositions (from EMP) and modal phase abundances during annealing. An important step within the calculation is to determine the sample bulk composition, which is conserved during annealing. The sample bulk can be derived

B 1) from the modal phase abundances derived from image analysis or Rietveld analysis, or

B 2) from the Ti/(Ti+Fe) of starting mixture.

Consequently, the uncertainties of Rietveld and image analysis and those related to homogeneity and composition of the starting mixture have to be considered.

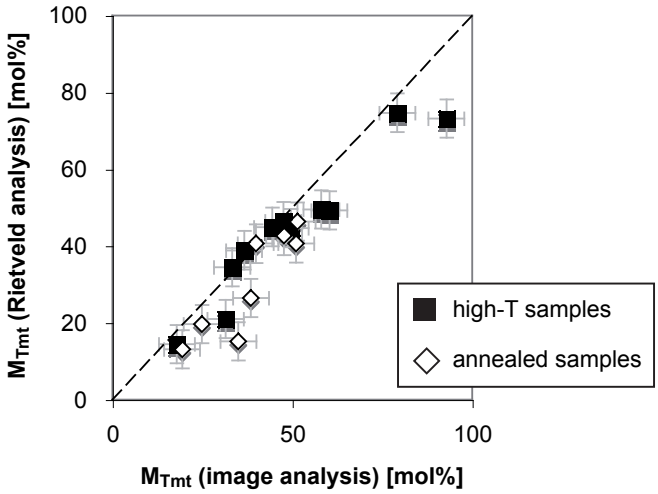

Fig. 5.6 Molar proportions derived from Rietveld analysis versus image analysis, for Tmt in high-T samples (black squares) and annealed samples (empty diamonds). Dashed line represents Rietveld=image analysis.

For the Ti/(Ti+Fe) ratio of the starting mixture, the uncertainty arises from the purity of the reagents and the uncertainty of weighing. The latter is considered to be <0.0001 on Ti/(Ti+Fe). The overall uncertainty on Ti/(Ti+Fe) is assumed to be <0.005.

The coordinates determined for bulk composition by modal phase abundances (B1: Rietveld or image analysis) versus starting mixture composition (B2), and the derived δ (by equation 5.9) are in most cases in very good agreement (Fig. 5.7). δ derived from Rietveld analysis tend to be slightly lower, but within uncertainties are in agreement with results from image analysis and the Ti/(Ti+Fe) of the starting mixture.

Uncertainties on δ derived with method B were estimated for each sample by calculating δ from Ti/(Ti+Fe)$\pm$0.005 (i.e. Ti/(Ti+Fe)+0.005 and Ti/(Ti+Fe)-0.005, 0.005 is taken as the microprobe uncertainty; compare Fig. 5.8) and combining negative and positive deviations for the different phases in order to give maximum error bars. A calculation of the uncertainty by error propagation has not been carried out, as the calculation of δ according to method B comprises too many single steps, resulting in an extremely complicated formula for the uncertainty on δ.

During calculation of δ according to the steps described for method B in section 5.3.1, EMP analysis has turned out to be the most critical point. Small errors in the

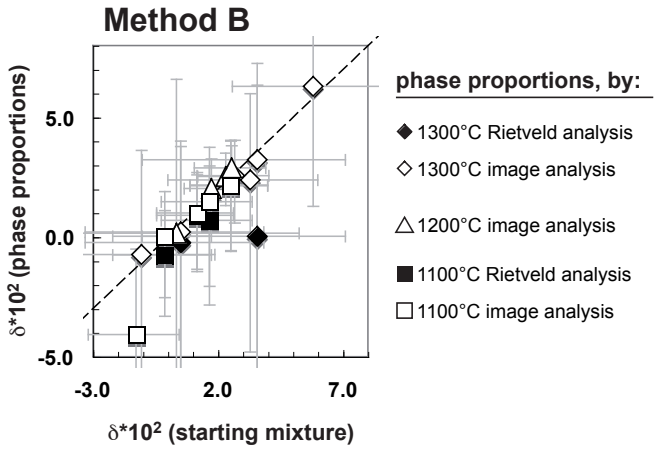

Fig. 5.7 δ values derived from method B using molar proportions from image analysis (empty symbols) or Rietveld analysis (filled symbols) (both method B1), versus δ calculated from Ti/(Ti+Fe) ratio of starting material (method B2). Dashed line represents $\delta_{(startingmixture)} = \delta_{(phaseproportions)}$. Data according to table 5.4.

microprobe analyses, and consequently in the cartesian x coordinates determined for the phases, can produce large errors for δ (Fig. 5.8).

In a sample with high Tmt proportion, the pivotal point of tie-line rotation during annealing is close to Tmt. Annealing involves only a minor shift of Tmt composition, but can produce a significant increase of Ti/(Ti+Fe) of Ilm_{ss}. The lines through bulk and Ilm_{ss}^{HT} for slightly different Ti/(Ti+Fe) (mean$\pm\Delta$) remain closely bundled. In contrast, when the high-T sample has a high modal proportion of Ilm_{ss}, the pivotal point (i.e. sample bulk) is close to Ilm_{ss}^{HT}. Annealing involves a relatively strong shift of Tmt composition towards lower Ti/(Ti+Fe), but only a slight shift of Ilm_{ss} composition. The gradient of the line through sample bulk and Ilm_{ss}^{HT} changes strongly at only small variations in Ti/(Ti+Fe) of Ilm_{ss}^{HT} (according to the EMP uncertainties, Ti/(Ti+Fe)$\pm$0.005). Large differences in the resulting δ are the consequence. This can result in error bars of strongly different sizes for different samples.

5.3.3 Actual and alleged pitfalls

Oxidation during annealing run Concerning the annealing method, a critic might object that the increase in the Ilm_{ss} proportion observed upon annealing could also be explained by oxidation of the sample, for example as a result of a leaky ampoule or of insufficient evacuation of the ampoule before annealing (see chapter 2 for

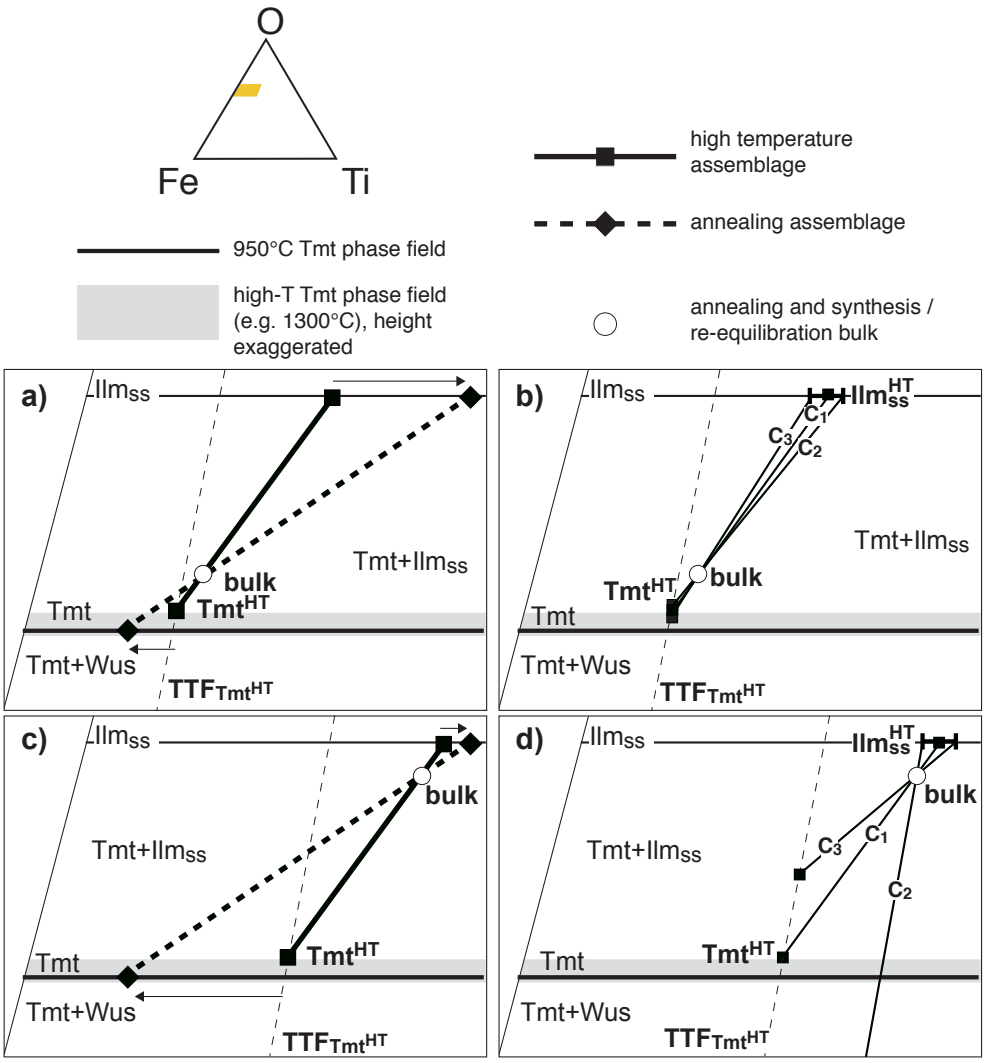

Fig. 5.8 Effect of sample bulk on phase shifts during annealing and on uncertainties on δ, illustrated in the triangle Fe-Ti-O. a) Bulk composition close to Tmt results in a strong shift of Ilm_{ss} composition and minor shift of Tmt composition (arrows). b) Lines through bulk and Ilm_{ss}^{HT} with minimum Ti/(Ti+Fe) ratio (mean-0.005: C3), maximum Ti/(Ti+Fe) ratio (mean+0.005: C2) and mean Ti/(Ti+Fe) ratio (mean$\pm$0: C1) are closely bundled. The coordinates for Tmt^{HT} are derived by intersecting C1, C2, C3 with the Ti/(Ti+Fe) determined for synthesis Tmt ($TTF_{Tmt^{HT}}$). c) Bulk composition close to Ilm_{ss} results in a small shift of Ilm_{ss} composition and a stronger shift of Tmt composition. d) Lines through bulk and Ilm_{ss}^{HT} with minimum (C3), maximum (C2) and mean (C1) Ti/(Ti+Fe) ratio spread strongly.

experimental details). In fact, oxidation would also produce an increase of Ilm_{ss} proportion. In contrast to vacancy relaxation however, oxidation causes a shift of **both** Tmt and Ilm_{ss} towards increased Fe-content.

The formation of Fe° during annealing has been observed for some samples that have been originally synthesised at low fO_2. It is a clear evidence that no strong oxidation could have occurred. Further, Lattard & Partzsch (2001) have shown that sealing in silica glass ampoules ensures closed-system conditions. As the gas volume within an ampoule is small, the amount of enclosed oxygen is negligible compared to the sample oxygen content, even in case of a weak vacuum. A significant oxidation is improbable in a leakproof ampoule. Exchange with the surrounding atmosphere as a result of leakage results in strong oxidation, producing Ilm_{ss}+Psb_{ss} (or even more oxidised assemblages) instead of Tmt+Ilm_{ss}. Therefore, as long as the Tmt+Ilm_{ss} assemblage is maintained during annealing, leakage of the ampoule can be excluded.

While oxidation can be excluded as principle cause for the annealing exsolutions, we observed that application of the annealing method on samples with oxy-exsolution features yields an unusually high calculated δ (Fig. 5.9, see section 5.3.4 for presentation and discussion of results). In high-T samples that display oxy-exsolution features (chapter 3) the oxygen content near the sample surface and along cracks is higher than in the central sample region. Consequently, the bulk oxygen content of any annealed fragment is usually higher than assumed from EMP analysis or image analysis on central sample regions. Samples that display oxy-exsolution features have not been considered in the presented results.

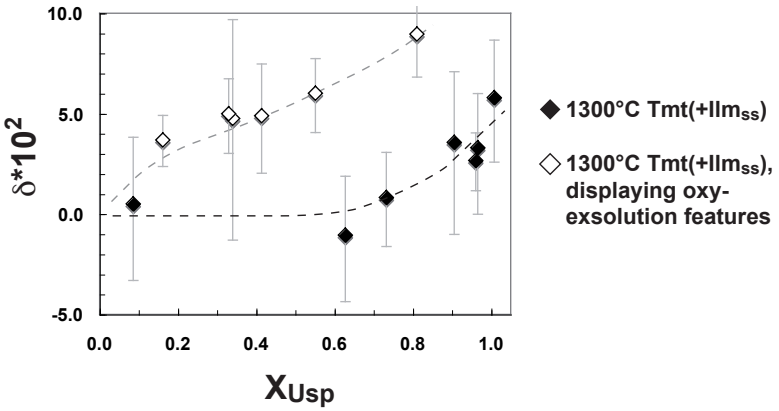

Fig. 5.9 δ as a function of Tmt composition (X_{Usp}) at 1300 °C for samples originally displaying oxy-exsolution features (empty symbols) compared to samples without oxy-exsolution features (filled symbols). δ derived by method B from bulk of starting material. Error bars according to section 5.3.2.

Table 5.1 δ calculated for 1300 °C samples without oxy-exsolution features (upper part of the table) compared to δ calculated for 1300 °C samples with oxy-exsolution features (lower part of the table).

synthesis run no	Tmt at 1300 °C			$\delta*10^2$ (method B)		
	Ti/(Ti+Fe) [at%]		X_{Usp}	TTF	Rietveld	image
	mean	(σ)		starting mixture	analysis	analysis
	1300 °C run products *without* oxy-exsolution					
6F92a	2.86	(06)	0.09	0.5	-0.2	0.2
6F72x2.4	20.92	(11)	0.63	-1.1		-0.7
6F72x4.4	24.42	(13)	0.73	0.8		
6F57x18	30.20	(13)	0.91	3.6	0.0	3.2
6F63x34	32.01	(04)	0.96	2.7		2.6
6F57x34	32.20	(13)	0.97	3.3		2.4
6IT60x49	33.60	(14)	1.01	5.8		6.3
	1300 °C run products *with* oxy-exsolution					
6F92x0.15	5.38	(05)	0.16	3.7		
6F76x0.5	11.32	(19)	0.34	4.8		4.8
6F80x0.5	11.00	(16)	0.33	5.0		4.9
6F80x0.75	13.80	(25)	0.41	4.9		4.9
6F72x1.5	18.36	(13)	0.55	6.0	4.1	6.2
6F63x8	27.01	(22)	0.81	9.0	6.7	8.2

Elevated Ti and O content due to monomineralic rims As described in chapter 3, many Tmt+Ilm_{ss} samples display monomineralic Ilm_{ss} rims. These rims reflect a shift of the local bulk composition towards higher Ti *and* O content. Balancing this shift, the central sample region is slightly poorer in Ti and O. The local bulk composition varies *along the oxy-isobar* that reflects synthesis conditions.

A monomineralic rim might cause a slight variation in the bulk Ti/(Ti+Fe) and oxygen content of different sample fragments, due to a high or low proportion of the monomineralic rim within the selected fragment. A sufficiently large sample fragment should have a bulk composition which reflects the *overall* bulk composition.

Fig. 5.10 shows that the same increase in oxygen content has smaller effect on the alleged δ, when the oxygen content increases along the oxy-isobar (i.e. due to monomineralic rims) compared to an increase at constant Ti/(Ti+Fe) (i.e. by oxidation, e.g. oxy-exsolution).

The effect of concentric variations in bulk composition contributes to the uncertainties on modal proportions and bulk composition of the annealed fragment as described above. We have not observed any systematic shift of the δ value with presence or increasing proportions of monomineralic rims.

Occurrence of Fe° The evaluation of the annealing experiments according to methods A and B is restricted to Tmt+Ilm_{ss} assemblages in the samples both before and after annealing. However, at very high X_{Usp}, a ternary paragenesis Tmt+Ilm_{ss}+Fe° (Fe° present as small blebs) can form from Tmt+Ilm_{ss} during annealing.

With decreasing temperature, the stability field for the assemblage Tmt+Ilm_{ss}+Fe° shifts towards increasing Fe-content of both Tmt and Ilm_{ss} (Simons & Woermann, 1978, Fig. 5.11). While the bulk composition of a sample synthesised at high T and low fO_2 plots within the Tmt+Ilm_{ss} two-phase field at synthesis conditions, it may fall into the three phase field Tmt+Ilm_{ss}+Fe° at annealing temperature (950 °C). This results in the formation of a ternary assemblage Tmt+Ilm_{ss}+Fe° during annealing of a high-T Tmt+Ilm_{ss} sample.

Chemical inhomogeneity of annealed Ilm_{ss}: Grains versus lamellae The Ilm_{ss} lamellae and rims observed in annealed samples (section 5.3.4) in many cases have been too small to be analysed (thickness usually $1-5\,\mu m$). When the lamellae seemed to be big enough, EMP analyses often indicated slightly higher Fe-content (i.e. lower Ti/(Ti+Fe)) than for Ilm_{ss} grains (Table 5.2). This might not necessarily represent a true compositional difference, but - due to the small size of the exsolu-

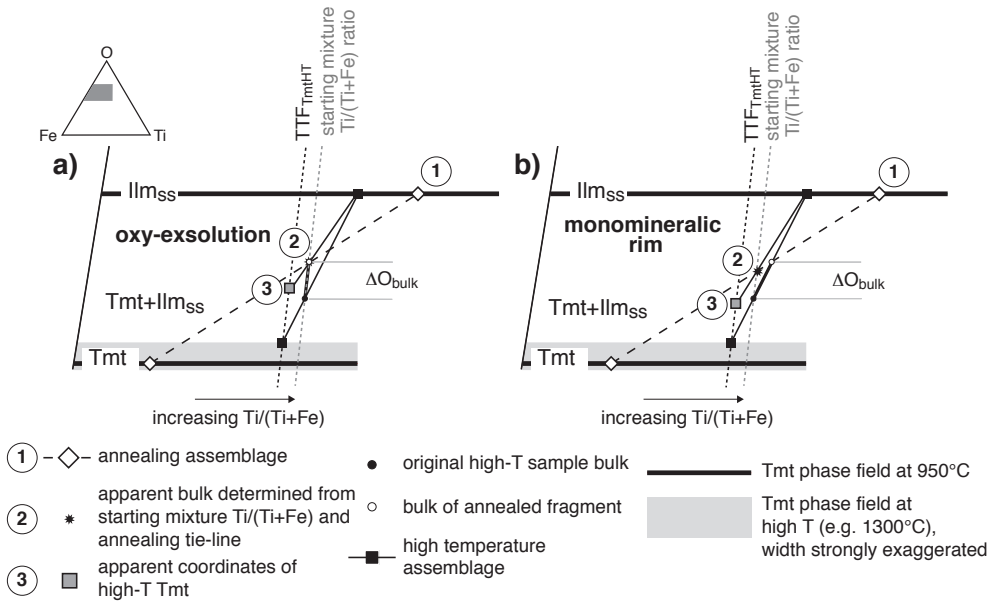

Fig. 5.10 Overestimation of δ as a result of a) oxidation of the sample, and b) shift of fragment Ti/(Ti+Fe) due to monomineralic rims. The difference in oxygen content (ΔO_{bulk}) is the same in both cases. The position of the annealing tie-line is known (1). Intersecting with the line for Ti/(Ti+Fe) of the starting mixture yields the apparent bulk (2). The apparent high-T tie-line and high-T Tmt coordinates (3) are determined. The black dashed line labelled TTF_{TmtHT} marks the Ti/(Ti+Fe) ratio of high-T Tmt.

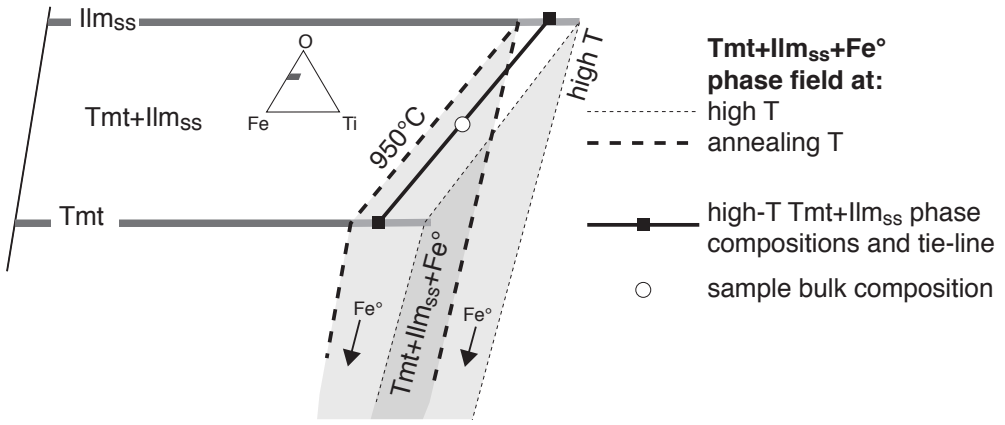

Fig. 5.11 Shift of ternary Tmt+Ilm$_{ss}$+Fe° phase field (black dashed lines, thin: 1300 °C, thick: 950 °C) towards decreased Ti-content with decreasing temperature, schematically illustrated in part of the triangle Fe-Ti-O. Bulk composition (circle) of a binary high-T synthesis sample (black squares, thick solid line), plots within the ternary Tmt+Ilm$_{ss}$+Fe° phase field at annealing T.

tion features - can result from mixed EMP analyses with the surrounding Fe-richer Tmt host. Therefore, we generally selected Ilm_{ss} grain compositions for further calculations.

Table 5.2 Comparison of EMP analyses of Ilm_{ss} grains versus EMP analyses on Ilm_{ss} lamellae and rims

annealing sample	Ilm_{ss} grains n	Ti/(Ti+Fe) [at%] mean	(σ)	Ilm_{ss} lamellae and rims n	Ti/(Ti+Fe) [at%] mean	(σ)	Δ Ti/(Ti+Fe)[1]
			1300 °C				
6F72x2.4D	10	44.19	(16)	3	43.84	(09)	0.35
6F72x4.4D	10	49.90	(18)	3	46.81	(13)	3.09
6F57x18D	10	48.16	(23)	5	48.01	(31)	0.15
6IT60x49D	10	49.78	(19)	3	49.30	(16)	0.48
			1200 °C				
5F63x2.8aD	10	41.61	(31)	4	41.04	(67)	0.57
5F63x33.5D	10	49.41	(21)	3	48.72	(50)	0.69

Ti/(Ti+Fe)(grains)-Ti/(Ti+Fe)(lamellae and rims)

Stoichiometry or non-stoichiometry at 950°C Annealing at 950 °C of a high-T Tmt+Ilm_{ss} assemblage involves a decrease of the vacancy concentration from the original high-T concentration to the equilibrium value at 950 °C. At 950 °C Tmt in equilibrium with Ilm_{ss} is expected to be close to stoichiometry (Dieckmann, 1982; Aggarwal & Dieckmann, 2002). For the sake of simplicity, we have neglected very small vacancy concentrations (< 0.3 cat%) that might potentially be present at 950 °C (Fig. 5.2).

5.3.4 Presentation and discussion of the results

Textures Most of the annealed samples synthesised before at 1200 °C and 1300 °C display Ilm_{ss} exsolution lamellae and rims (usually $1-5\,\mu m$ in thickness; Fig. 5.12). Annealing of samples synthesised before at 1100 °C did not produce Ilm_{ss} exsolution features. Concerning grain size and distribution the textures of the annealed samples are strongly influenced by the original high-T textures.

Ilm_{ss} lamellae are mostly orientated along sets of (111) planes, showing a trellis-like texture. Some lamellae are drop-shaped, and thicken towards the grain boundary, where Ilm_{ss} forms an irregular rim, sometimes resembling a pearl necklace.

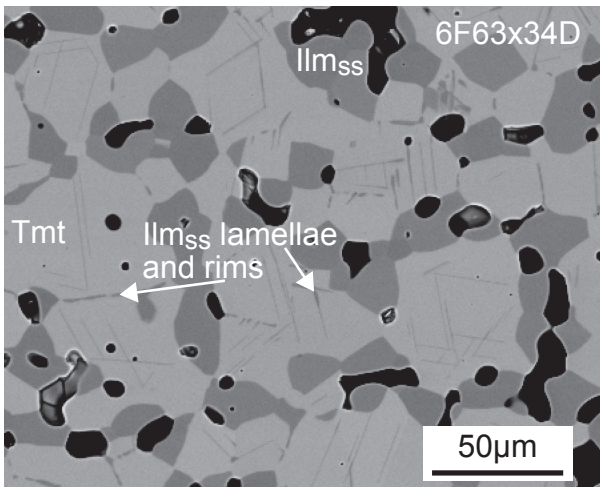

Fig. 5.12 BSE picture of a polished cross section of an annealed Tmt+Ilm$_{ss}$ sample. Ilm$_{ss}$ (medium grey) is present as independent crystals, but also as fine exsolution lamellae (arrows) within Tmt crystals (light grey) and as rims around them.

Annealing under oxygen-conserving conditions produces exsolution features of Ilm$_{ss}$ in Tmt, but no exsolution features of an oxidised phase (i.e. Psb$_{ss}$) in Ilm$_{ss}$. The Ilm$_{ss}$ exsolution features affect the whole sample. In contrast, quench-related oxy-exsolution is restricted to the sample surface and cracks, and usually produces both exsolution of Ilm$_{ss}$ in Tmt *and* of Psb$_{ss}$ in Ilm$_{ss}$.

δ values derived from the annealing method Tmt in most samples investigated with the annealing method are Ti-rich (X_{Usp}>0.6). At these high Ti-contents a trend of increasing δ with increasing X_{Usp} and temperature has been observed. The maximum vacancy concentration is estimated to about 2 cat% at 1300 °C, and about 1 cat% at 1200 °C. For 1100 °C, results indicate stoichiometry or only slight non-stoichiometry. At X_{Usp}<0.6, there are only few data points. These data indicate stoichiometry at all investigated temperatures (i.e. $1100-1300$ °C), however with only few data points a reliable and detailed interpretation is difficult.

Comparison of δ values retrieved with methods A and B Both methods indicate increasing non-stoichiometry with increasing X_{Usp} for Ti-rich compositions.

It has been stated above that image analysis and Rietveld analysis yield modal phase proportions, which may strongly deviate (Table 5.3). The corresponding δ

values derived by method A, which is only based on modal proportions, strongly differ when image analysis or Rietveld analysis were employed (Fig. 5.13, Table 5.4).

In contrast, the δ values derived according to method B with image analysis, Rietveld analysis or the cationic ratio of the starting mixture, are usually in good agreement (Fig. 5.14, Table 5.4). δ values derived from Rietveld analysis are often distinctly smaller than those from the other approaches (image analysis, starting mixture), but the values agree within the uncertainties. Method B is not based on modal proportions alone, but also relies on phase compositions (i.e. cationic ratio Ti/(Ti+Fe)), which can be exactly determined by EMP.

In many cases the values from the two methods are in general agreement, but sometimes method A yields much higher (e.g. samples 6IT60x49, 3IT60IW) or lower (e.g. sample 3F80x0.4) δ values than method B (Table 5.4). Therefore we favour method B.

For this reason, regarding the absolute values of δ, the values according to method B absolutely have to be preferred.

Table 5.3 Modal proportions M in [mol%] from image and Rietveld analysis.

synthesis run no.	high-T Tmt Ti/(Ti+Fe) [at%]	M from image analysis				M from Rietveld analysis			
		high-T		950°C		high-T		950°C	
		Tmt	Ilm_{ss}	Tmt	Ilm_{ss}	Tmt	Ilm_{ss}	Tmt	Ilm_{ss}
synthesis temperature: 1300°C									
6F92a	2.86	49.5	50.5	51.5	48.5	44.7	55.3	46.4	53.6
6F72x2.4	20.92	57.8	42.2	60.3	39.7				
6F57x18	30.20	17.9	82.1	19.4	80.6	14.4	85.6	13.1	86.9
6F63x34	32.01	58.1	41.9	60.2	39.8	45.9	50.5		
6F57x34	32.16	26.0	74.0	22.7	77.3				
6IT60x49	33.60	60.8	39.2	36.2	63.8				
synthesis temperature: 1200°C									
F72(f)5	24.85	92.9	7.1	85.3	14.7	73.2	26.8		
F69(g)5	28.22	79.2	20.8	88.6	11.4	74.7	25.3		
synthesis temperature: 1100°C									
3F80x0.4	10.43	36.6	63.4	51.1	48.9	38.9	61.1	40.7	59.3
3F69Qe	20.14	37.4	62.6	39.0	61.0				
3F63x16.5	28.52	47.5	52.5	39.9	60.1	46.5	53.5	40.6	59.4
3F63x30	29.81	53.8	46.2	47.7	52.3			42.7	57.3
3IT60IW	32.46	44.4	55.6	35.0	65.0	45.0	55.0	15.2	84.8

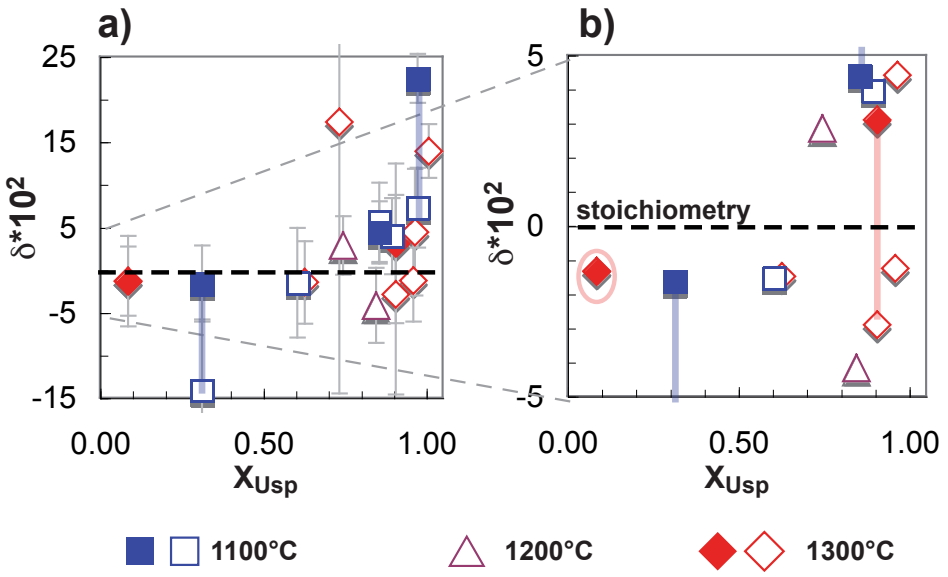

Fig. 5.13 a) δ in high temperature synthesis Tmt (1100°C: blue squares, 1200°C: violet triangles, 1300°C: red rhombs) in coexistence with Ilm_{ss} as a function of X_{Usp}, calculated according to method A described in section 5.3.1. b) Enlargement of the area between $\delta * 10^2$=-5 and 5. The increase of Ilm_{ss} proportion is derived from image analysis (empty symbols) and Rietveld analysis (filled symbols). Results concerning the same sample are connected by bars or surrounded by an ellipse. Horizontal dashed lines represent stoichiometry. The error bars are based on an uncertainty on modal phase abundances of about 5% and have been omitted in picture (b).

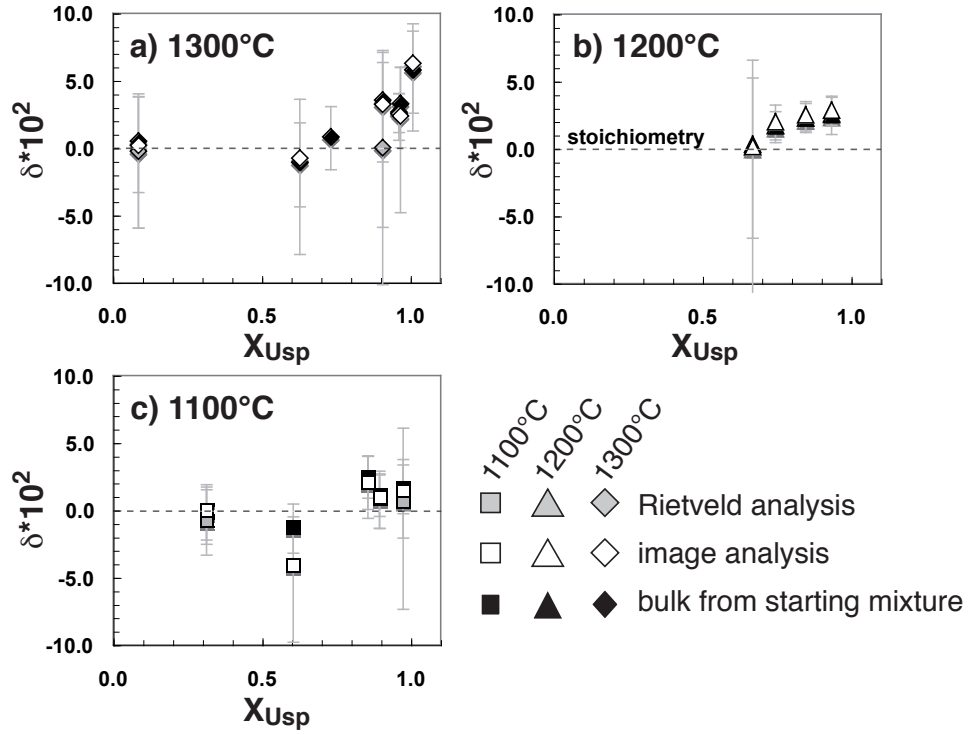

Fig. 5.14 δ of high-T Tmt in Tmt+Ilm$_{ss}$ assemblages, calculated according to method B and plotted against Tmt composition (X_{Usp}). a) 1300 °C (diamonds), b) 1200 °C (triangles), and c) 1100 °C (squares). Positive δ point to cation vacancies, negative δ point to cation excess. Dashed horizontal line represents stoichiometric Tmt composition.

Table 5.4 δ from annealing method A and B.

synthesis run no	X_{Usp}	δ from method A				δ from method B								
		image analysis		Rietveld		from TTF (B1)			image analysis (B1)			Rietveld (B2)		
		$(\delta \pm \Delta\delta) * 10^2$		$(\delta \pm \Delta\delta) * 10^2$		$\delta * 10^2$	max	min	$\delta * 10^2$	max	min	$\delta * 10^2$	max	min
						1300°C								
6F92a	0.09	-1.4	±5.3	-1.3	±4.1	0.5	3.8	-3.3	0.2	3.8	-6.0	-0.2	4.1	-5.9
6F72x2.4	0.63	-1.5	±4.9			-1.1	1.8	-4.4	-0.7	3.7	-7.9			
6F72x4.4	0.73					0.8	3.0	-1.7						
6F57x18	0.91	-2.9	±11.7	3.1	±9.3	3.6	7.1	-1.0	3.2	7.2	-5.9	0.0	6.3	-10.2
6F63x34	0.96	-1.3	±4.8			2.7	4.1	1.2	2.6	4.1	0.6			
6F57x34	0.97	4.4	±7.4			3.3	6.0	0.0	2.4	6.0	-4.8			
6IT60x49	1.01	13.9	±3.2			5.8	8.7	2.6	6.3	9.2	1.0			
						1200°C								
5F63x2.8a	0.67					0.3	5.2	-6.7	0.2	6.6	-20.6			
F72(f)5	0.75	2.8	± 3.4			1.7	2.7	0.6	2.0	3.2	0.5			
F69(g)5	0.85	-4.2	±4.4			2.3	3.3	1.2	2.5	3.5	1.3			
5F63x33.5	0.93					2.5	3.9	1.0	2.9	3.8	1.8			
						1100°C								
3F80x0.4	0.31	-14.1	±8.3	-1.6	±4.5	-0.1	1.8	-2.2	0.0	1.9	-2.6	-0.7	1.6	-3.3
3F69Qe	0.60	-1.5	±6.4			-1.3	0.4	-3.2	-4.1	-0.5	-9.8			
3F63x16.5	0.86	5.6	±4.7	4.4	±3.6	2.5	4.0	0.9	2.3	4.2	-0.4	2.2	4.1	0.1
3F63x30	0.89	4.0	±4.5			1.2	2.7	-0.4	1.0	2.7	-1.4	0.9	2.9	-1.4
3IT60IW	0.97	7.3	± 4.7	22.4	±2.9	1.7	3.4	-0.2	1.5	3.8	-2.0	0.7	6.1	-7.3

5.4 Estimation of Tmt non-stoichiometry from cell dimensions

5.4.1 Principles

Lattice parameters have been derived by Rietveld refinement of X-ray powder patterns of quenched Tmt+Ilm$_{ss}$, Tmt and Tmt+Wus samples, acquired at room temperature. A difference in cell dimensions at constant cationic ratio Ti/(Ti+Fe) and T most probably reflects different cat/O ratios in titanomagnetites. Cation distribution between the octahedral and tetrahedral sites may also affect Tmt lattice parameter (a_0). Equilibrium high-T cation distribution cannot be quenched to room temperature (O'Neill & Navrotsky, 1984). Consequently, the cation distribution prevailing in the quenched samples does not reflect the cation distribution at synthesis (or annealing) conditions. Nevertheless, for samples of identical synthesis temperature and quench rate (i.e. temperature history), of identical X-ray measurement temperature *and* Ti/(Ti+Fe) ratio, we expect the same cation distribution and consequently the same lattice parameter, unless there is a difference in non-stoichiometry.

5.4.2 Results

To evaluate Tmt non-stoichiometry on the basis of lattice parameters, results for Tmt of different temperature series ($1100-1300\,^{\circ}$C) and in different parageneses (Tmt, Tmt+Ilm$_{ss}$, Tmt+Wus) (see Table 5.5) were compared to those for Tmt(+Ilm$_{ss}$) annealed at $950\,^{\circ}$C (Table 5.6, Fig. 5.15). The latter was assumed to be stoichiometric. A second order polynomial curve (equation 5.10, R^2=0.99977) was fitted to the $950\,^{\circ}$C data points.

$$a_0(950^{\circ}\mathrm{C}) = 5.3118 * 10^{-2} * X_{Usp}^2 + 9.7977 * 10^{-2} * X_{Usp} + 8.3962 \qquad (5.10)$$

.

The difference Δa_0 (equation 5.11) between the $950\,^{\circ}$C fit (as reference curve) and measured lattice parameter a_0 at given X_{Usp} is a measure for relative non-stoichiometry. A positive Δa_0 (i.e. deviations towards smaller lattice parameters compared to the reference curve) has been interpreted as pointing to cation deficiency (cation vacancies), a negative Δa_0 as pointing to cation excess (cation interstitials).

$$\Delta a_0 = a_0(950^{\circ}\mathrm{C}) - a_0(T) \qquad (5.11)$$

The uncertainty on lattice parameter a_0 was estimated from the σ value given by the Rietveld refinement software and repeated measurements and refinements on selected samples to be ± 0.003Å.

Table 5.5 Lattice parameter a_0 for high-T (1100 – 1300 °C) Tmt in coexistence with Ilm_{ss} or Wus, or single-phase Tmt.

sample	ΔNNO	assemblage	Ti/(Ti+Fe) [at%]		X_{Usp}	a_0	R value[1]
			mean	(σ)		Å	%
			1300 °C				
6F97x1.6	0.7	Tmt	2.82	(13)	8.5	8.404	11.4
6F97x0.15	2.8	Tmt	2.91	(05)	8.7	8.402	11.5
6F92x1.6	0.7	Tmt	7.60	(24)	23.4	8.423	10.9
6F87x1.6	0.7	Tmt	12.92	(52)	38.7	8.445	11.2
F87(f)6	-0.4	Tmt	13.33	(73)	40.0	8.448	11.6
6F92a	3.4	Tmt+Ilm_{ss}	2.86	(06)	8.6	8.401	10.8
F76(d)6	2.3	Tmt+Ilm_{ss}	7.61	(13)	22.8	8.418	11.5
6F76x1.6	0.7	Tmt+Ilm_{ss}	18.66	(11)	56.0	8.466	10.7
F72(f)6	-0.4	Tmt+Ilm_{ss}	25.32	(18)	76.0	8.497	12.5
6F67x8	-0.7	Tmt+Ilm_{ss}	26.88	(12)	80.6	8.503	12.1
6F63x8	-0.7	Tmt+Ilm_{ss}	27.01	(22)	81.0	8.499	12.3
6F57x18	-1.6	Tmt+Ilm_{ss}	30.19	(09)	90.6	8.513	11.4
6F63x34a	-2.4	Tmt+Ilm_{ss}	31.89	(19)	95.7	8.523	12.2
6F63x34	-2.4	Tmt+Ilm_{ss}	32.09	(10)	96.3	8.525	11.2
6F57x66	-3.5	Tmt+Ilm_{ss}	34.74	(26)	104.2	8.532	12.2
6F87x18	-1.6	Tmt+Wus	12.87	(50)	38.6	8.447	10.8
6F80x34	-2.4	Tmt+Wus	21.09	(15)	63.3	8.486	11.0
6F80x66	-3.5	Tmt+Wus	26.62	(24)	79.9	8.513	11.5
			1200 °C				
5F63x2.8	-0.1	Tmt+Ilm_{ss}	22.01	(11)	66.0	8.484	11.2
F72(f)5	-0.7	Tmt+Ilm_{ss}	24.85	(21)	74.6	8.497	10.2
F69(g)5	-1.5	Tmt+Ilm_{ss}	28.22	(17)	84.7	8.515	11.4
5F63x33.5	-2.6	Tmt+Ilm_{ss}	31.12	(12)	93.4	8.522	10.9
5F54.5Fex83.5	-4.6	Tmt+Ilm_{ss}	34.47	(23)	103.4	8.534	11.8
			1100 °C				
3F80x0.4	1.5	Tmt+Ilm_{ss}	10.43	(21)	31.3	8.433	11.4
3F76Qe	0.0	Tmt+Ilm_{ss}	20.22	(19)	60.7	8.476	11.6
F63(f)3	-0.7	Tmt+Ilm_{ss}	23.26	(19)	69.8	8.493	13.2
F69(x)3	-0.9	Tmt+Ilm_{ss}	24.69	(21)	74.1	8.498	10.9
F72(x)3	-0.9	Tmt+Ilm_{ss}	24.87	(18)	74.6	8.499	12.0
3F63x16.5	-2.0	Tmt+Ilm_{ss}	28.52	(18)	85.6	8.515	11.8
3F65x30	-2.6	Tmt+Ilm_{ss}	30.07	(18)	90.2	8.522	12.9
3IT60IW	-4.4	Tmt+Ilm_{ss}	32.46	(16)	97.4	8.534	11.5
3F80IW	-4.4	Tmt+Wus	25.94	(16)	77.8	8.516	12.0

1) residuum value from GSAS® software (Larsen & von Dreele, 2000).

Table 5.6 Lattice parameter a_0 for Tmt+Ilm$_{ss}$ samples annealed at 950 °C.

sample	assemblage	T [°C]	Ti/(Ti+Fe) [at%]		X_{Usp}	a_0	R[1]
			mean	(σ)	%	Å	%
6F92aD	Tmt+Ilm$_{ss}$	950	2.15	(20)	6.5	8.403	9.3
6F72x1.5D	Tmt+Ilm$_{ss}$	950	12.83	(12)	38.5	8.441	11.8
6F63x8D	Tmt+Ilm$_{ss}$	950	19.09	(21)	57.3	8.471	12.9
6F57x18D	Tmt+Ilm$_{ss}$	950	26.08	(56)	78.2	8.505	12.4
6F57x18D	Tmt+Ilm$_{ss}$	950	26.08	(56)	78.2	8.505	12.4
3F80x0.4D	Tmt+Ilm$_{ss}$	950	9.66	(09)	29.0	8.429	11.6
3F63x16.5D	Tmt+Ilm$_{ss}$	950	26.71	(17)	80.1	8.509	11.1
3F63x30D	Tmt+Ilm$_{ss}$	950	29.05	(10)	87.2	8.523	11.4
3IT60IWD	Tmt+Ilm$_{ss}$	950	31.56	(16)	93.0	8.532	12.6

1) residuum value from GSAS® software (Larsen & von Dreele, 2000).

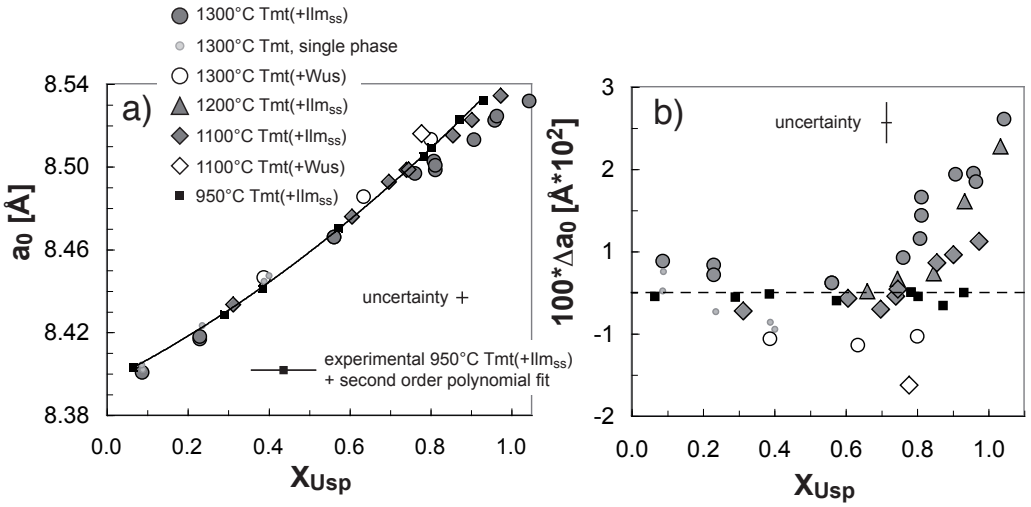

Fig. 5.15 a) Tmt lattice parameter (a_0 [Å]) plotted against X_{Usp} for Tmt synthesised or annealed at different temperatures (symbols). Small black squares represent annealed samples, the black line a second order polynomial fit to the annealing data. b) Difference Δa_0 [Å] between measured a_0 and fit to the 950 °C data versus X_{Usp}. 1200 °C data has been omitted in picture (a).

For Tmt(+Ilm_{ss}) data, Δa_0 increases with increasing temperature and X_{Usp} at $X_{Usp} \geqslant 0.7$. At X_{Usp}<0.7 virtually no difference can be observed in lattice parameter a_0 for different temperature series at a given cationic ratio. Lattice parameters of Tmt coexisting with Ilm_{ss}, at 1300 °C might be slightly smaller than a_0 of Tmt(+Ilm_{ss}) annealed at 950 °C (corresponding to slightly positive Δa_0). However, the observed deviations are within the uncertainties.

The lattice parameters of Tmt in paragenesis with wüstite are larger for all synthesis T (i.e. 1100 and 1300 °C) compared to the 950 °C reference curve (i.e. negative Δa_0). For the only 1100 °C Tmt(+Wus) sample examined, the determined Δa_0 value is even smaller (i.e. Δa_0 more negative) than those for 1300 °C Tmt(+Wus).

The decrease of Δa_0 observed for all data at X_{Usp}<0.6 is due to the fit to 950 °C data, which for low X_{Usp} is only based on few data points.

5.4.3 Summary and interpretation

Comparison of determined cell dimensions to literature data Senderov *et al.* (1993) have determined Tmt lattice parameters of quenched Tmt, Tmt+Ilm_{ss} and Tmt+Wus samples, synthesised at 1300 °C. Our 1300 °C data is in very good agreement with the data of Senderov *et al.* (1993). The lattice parameters for Tmt+Wus according to Senderov *et al.* (1993) are slightly higher than ours (lower Δa_0 in Fig. 5.16), but they are in agreement within the uncertainties given for our data (± 0.003).

Our data are also in general agreement with the data by Wechsler *et al.* (1984). Wechsler *et al.* (1984) have determined lattice parameters of Tmt synthesised at 930 °C, 1200 °C and 1300 °C by X-ray diffraction at room temperature. 930 °C samples have been produced in evacuated silica glass tubes. 1350 °C samples with X_{Usp}=0.25, 0.50 and 0.75 display small amounts of wüstite, the sample synthesised at 1200 °C contains small amounts of Ilm_{ss}.

The samples synthesised by Wechsler *et al.* (1984) at 1200 °C and 1350 °C are in reasonable agreement with our data for Tmt(+Ilm_{ss}) and Tmt(+Wus), respectively. The lattice parameters for 930 °C single-phase Tmt of Wechsler *et al.* (1984) are slightly higher than those for 950 °C Tmt(+Ilm_{ss}) from the present study, resulting in slightly lower Δa_0 (Fig. 5.17). Probably, the single-phase Tmt by Wechsler *et al.* (1984), have a slightly higher cation/oxygen ratio than the Tmt(+Ilm_{ss}) samples. This can be explained by either slight cation excess in the single-phase Tmt by Wechsler *et al.* (1984), or small vacancy concentrations in our 950 °C samples. The deviation could also be explained when the Wechsler *et al.* (1984) data would be slightly richer in titanium than assumed. However, there is no evidence for this. At

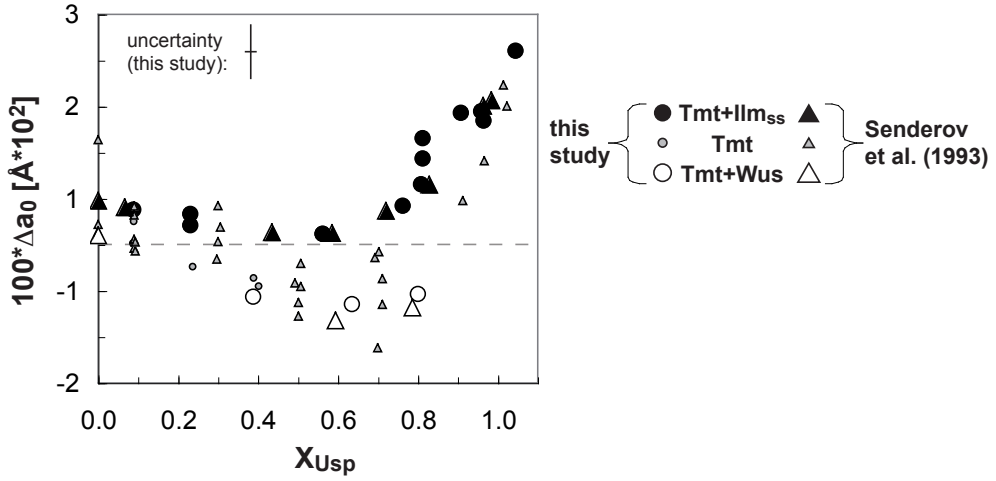

Fig. 5.16 Comparison of lattice parameters determined within the present study (circles), compared to the values according to Senderov *et al.* (1993, triangles). Plotted is Δa_0 (equation 5.11) versus X_{Usp}.

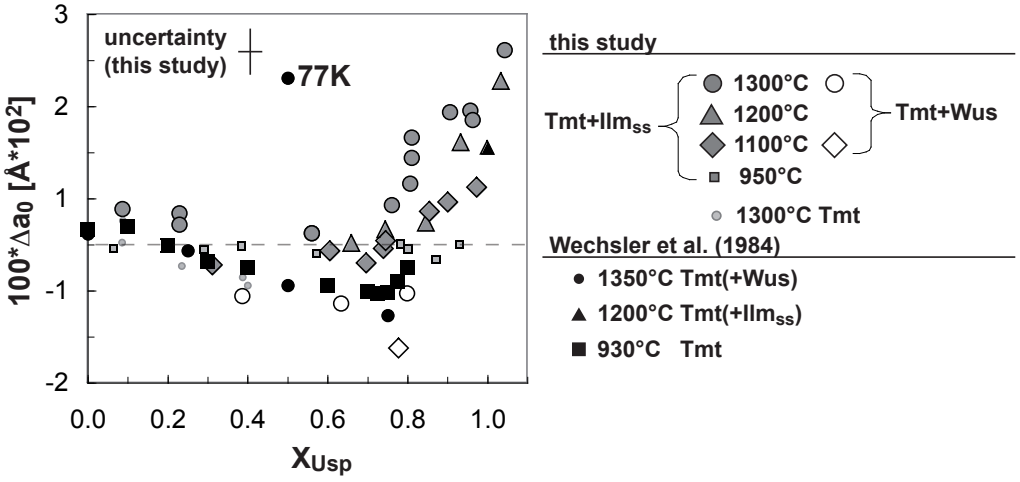

Fig. 5.17 Comparison of lattice parameters determined within the present study (grey and empty symbols), compared to the values according to Wechsler *et al.* (1984, black symbols). Plotted is Δa_0 (equation 5.11) versus X_{Usp}.

last, the uncertainties on the data points and possible systematic deviations between the laboratories have to be considered.

For one data point, Wechsler *et al.* (1984) determined the lattice parameter at

77 K. a_0 is significantly lower than for room temperature data at identical X_{Usp}. This most probably shows the influence of cation distribution on lattice parameters.

Non-stoichiometry from cell dimensions In accordance with the study by Senderov *et al.* (1993), the lattice parameters observed within this study for Tmt in coexistence with Ilm_{ss} at X_{Usp}<0.7 and T$\geq$ 1100 °C are in agreement with or only slightly different to the 950 °C data. At X_{Usp}>0.7, Δa_0 increases with increasing T and fO_2. Assuming 950 °C Tmt(+Ilm_{ss}) to be stoichiometric, this suggests stoichiometry or small vacancy concentrations for Tmt(+Ilm_{ss}) for all temperatures at X_{Usp}<0.7 and increasing cation vacancy concentration with temperature and X_{Usp} towards Ti-rich compositions. The negative Δa_0 for Tmt(+Wus) may point to cation excess. Compared to the 1300 °C Tmt(+Wus), the single data point available for Tmt(+Wus) at 1100 °C could indicate increasing concentration of cation interstitials with decreasing temperature ($a_0(1100) > a_0(1300)$ at $X_{Usp}\approx$0.8), which would be in contradiction to Aggarwal & Dieckmann (2002).

By interpreting the observed Δa_0 versus X_{Usp} for different temperatures, it has to be considered that for different X_{Usp} the same Δa_0 might correspond to *different* δ. The distribution of ferric and ferrous iron between octahedral and tetrahedral sites changes during quenching by transfer of electrons between the iron cations. In contrast, the distribution of Ti and cation vacancies (both are essentially considered to be on the octahedral sites) probably cannot change during the rapid quenching process. Consequently, it is conceivable that at low X_{Usp} (i.e. high Fe-content, vacancy formation probably by substitution $3Fe^{2+} \leftrightarrow 2Fe^{3+} + \square$), the cation distribution might easily adapt to the decreased temperature in order to minimize the effect of cation vacancies on cell dimension. At high X_{Usp} however, only small amounts of Fe^{3+} are left and thus the capability of the cation distribution to balance the effect of cation vacancies might be limited. This might possibly result in higher Δa_0 for given δ at high X_{Usp}.

For the derivation of an empiric, quantitative correlation between a_0 and δ, both δ (e.g. from annealing method or EELS) and a_0 have to be known for sufficient data points. Up to now, this is not possible. An expansion of the data set would be required (determination of non-stoichiometry for Tmt of known a_0 by alternative methods).

5.5 Estimation of Tmt non-stoichiometry (δ) by a combination of EELS and EMP analyses

5.5.1 Principles and measurement

δ can be calculated from $Fe^{3+}/\Sigma Fe$ and Ti/(Ti+Fe) of titanomagnetite (described in section 5.2, see formula 5.12 and equation 5.13).

$$\left(Fe^{3+}_{f(1-x)}Fe^{2+}_{(1-f)(1-x)}Ti^{4+}_{x}\right)_{(3-\delta)}\square_{\delta}O_4 \tag{5.12}$$

$$\delta = 3 - \frac{8}{f(1-x)+2(1+x)} \tag{5.13}$$

Ti/(Ti+Fe) of Tmt is known for all samples from EMP analysis. For selected samples, $Fe^{3+}/\Sigma Fe$ was determined by electron energy-loss spectroscopy (EELS) at a TEM. The EELS measurements were carried out at the Technische Universität Darmstadt in cooperation with Peter van Aken.

Electron energy-loss spectroscopy (EELS) evaluates the energy-loss of a highly focussed electron beam that has passed through the investigated sample. The energy-loss is due to inelastic scattering of electrons. Electron energy-loss spectra carry information on chemical composition, the chemical bond, coordination and *valence state* (van Aken *et al.*, 1998; van Aken, 2002).

The Fe $L_{2,3}$-edges of minerals are characterised by two white-line features and exhibit electron energy-loss near-edge structure (ELNES), characteristic of the Fe valence state. For divalent iron, the Fe L_3-edge is dominated by a sharp peak (white line) at about 707.8 eV, followed by a broader maximum at about 710.5 eV with smaller intensity. The Fe L_3-ELNES spectra of trivalent iron consist of a white line with an absolute maximum at about 709.5 eV and a preceding maximum of smaller intensity at about 708.0 eV. The ratio of the white line intensities for ferric and ferrous iron can be used to estimate $Fe^{3+}/\Sigma Fe$ (van Aken *et al.*, 1998; van Aken & Liebscher, 2002).

EELS measurements have been carried out on a Philips CM12 transmission electron microscope (operating at 120 kV), using a Gatan DigiPEELS 766 parallel electron spectrometer. The TEM is equipped with a LaB_6 cathode with an energy spread defined as full width at half maximum height of the zero-loss peak of about 0.7eV.

On each investigated sample, three to four EEL spectra were recorded. Spectra were corrected for dark current and channel-to-channel gain variation of the detector. The background intensity, extrapolated from the pre-edge region by an inverse power law relationship, was subtracted. To describe the spectral features, Gaussian functions have been fitted to the acquired spectra.

$Fe^{3+}/\Sigma Fe$ was determined by comparing the acquired spectra to standard spectra of samples of known $Fe^{3+}/\Sigma Fe$ and by applying the intensity ratio $I(L_3)/I(L_2)$ to a universal curve (integral intensity ratio versus $Fe^{3+}/\Sigma Fe$, van Aken *et al.*, 1998). The uncertainty on $Fe^{3+}/\Sigma Fe$ is about ± 0.04.

5.5.2 Sample selection and preparation

Samples with various X_{Usp} and different expected δ (i.e. with Tmt in different assemblages: Tmt, Tmt+Ilm_{ss}, Tmt+Wus, Tmt+Fe°) have been examined by EELS analysis at the transmission electron microscope. Because the results of the annealing experiments and lattice parameter determination suggested higher vacancy concentrations in Tmt with $X_{Usp} \geq 0.7$, we have focussed EELS examination on Ti-rich compositions (at $X_{Usp} > 0.7$). TEM samples have been prepared by

- crushing sample fragments between glass plates, or
- ion thinning of cuts of thin sections, or
- cutting a thin foil with the FIB technique (see chapter 2).

The FIB technique provides the best samples, as one specific grain can be selected for analysis, and its position within the sample pellet is known. Further, the FIB foils are of constant thickness (<100nm), which is adequate for EELS analysis.

5.5.3 Pitfalls

We observed significant differences between measured $Fe^{3+}/\Sigma Fe$ ratios (and consequently calculated δ) for different analysis points within sample 6F80x66 that has been prepared by crushing a sample pellet fragment between glass plates (Table 5.7). Such differences in measured $Fe^{3+}/\Sigma Fe$ have also been observed for two analysed fragments of sample 6F57x18D.

Different $Fe^{3+}/\Sigma Fe$ values may point to different non-stoichiometry or to an inhomogeneity in Ti/(Ti+Fe). Assuming constant non-stoichiometry (i.e. δ), higher $Fe^{3+}/\Sigma Fe$ corresponds to lower Ti/(Ti+Fe) and vice versa.

Sample 6F80x66 displays a monomineralic Tmt rim around a central Tmt+Wus assemblage. Tmt in the rim might potentially be richer in Ti compared to Tmt in the central Tmt+Wus region. As Tmt in the rim is considered to be single-phase, it may also display higher oxygen/cation ratios (i.e. higher δ) compared to the central Tmt(+Wus) (compare chapter 1, section 1.2).

Table 5.7 $Fe^{3+}/\Sigma Fe$ determined by EELS analysis on four crushed fragments (1-4) and one analysis point on a FIB foil (5), on sample 6F80x66 (X_{Usp}=0.80, according to EMP). δ calculated according to equation 5.13 from Ti/(Ti+Fe) and $Fe^{3+}/\Sigma Fe$.

no	$Fe^{3+}/\Sigma Fe$ %	$\Delta Fe^{3+}/\Sigma Fe^{(a)}$ %	$\delta * 10^2$	$\Delta\delta * 10^{2(b)}$	
1	13	4	-4.4	3.6	
2	19	4	0.6	3.4	
3	20	4	1.4	3.4	
4	30	4	9.4	3.2	
5	18	3	-0.2	3.5	FIB foil

a) uncertainty on $Fe^{3+}/\Sigma Fe$
b) uncertainty on $\delta * 10^2$, calculated by error propagation

Assuming Tmt stoichiometry, X_{Usp}=0.80 (measured by EMP in central Tmt+Wus) region correlates to $Fe^{3+}/\Sigma Fe$ of about 18%. This is in agreement with the results on fragments 2 and 3 (Table 5.7).

Sample fragment 1 however, yields $Fe^{3+}/\Sigma Fe$=13 %. *Assuming Tmt stoichiometry*, this corresponds to X_{Usp} about 0.86. Fragment 1 might originate from the monomineralic sample rim and be Ti-richer than Tmt in the central sample region. Alternatively, the low $Fe^{3+}/\Sigma Fe$ ratio of 13 % in sample fragment 1 could also be explained by Tmt with about 1.5 % cation interstitials (based on X_{Usp}=0.80, according to EMP analysis).

The high $Fe^{3+}/\Sigma Fe$ of 30 % determined for fragment 4 could potentially correspond to a stoichiometric Tmt with low X_{Usp} of about 0.65. EMP analysis does not provide any evidence for Tmt with X_{Usp}=0.65 in sample 6F80x66. Further, a $Fe^{3+}/\Sigma Fe$ ratio of 30 % can be due to Tmt with X_{Usp}=0.80 and about 3 % cation vacancies, or to a Ti-rich and *non-stoichiometric* Tmt rim, e.g. X_{Usp}=0.86 and >4 % cation vacancies.

To summarise, EELS analysis on crushed sample fragments yielded different $Fe^{3+}/\Sigma Fe$ within one samples but for different fragments. The cause for these differenced could not be conclusively determined, as the original position of the fragments within the samples is unknown.

For this reason, FIB foils (exact selection of the analysed crystal) or at least ion thinned samples (selection of the analysed sample *region*) have to be preferred over crushed sample fragments. On the FIB foils, three to four electron energy-loss spectra have been acquired on each foil and indicate a homogenous composition of the grains.

5.5.4 Results

Comparison of electron energy-loss spectra Spectra of Tmt with identical Ti/(Ti+Fe) but in different assemblages (Tmt+Ilm_{ss} versus Tmt+Wus, and Tmt+Ilm_{ss} versus Tmt+Fe°) show significant differences in intensities at the absolute maxima for ferrous and ferric iron (Fig. 5.18). The spectra for Tmt coexisting with Ilm_{ss} show lower intensities at the Fe^{2+} maximum and slightly higher intensities at the Fe^{3+} maximum compared to the spectra for Tmt(+Wus) and Tmt(+Fe°). This indicates higher $Fe^{3+}/\Sigma Fe$ ratio for Tmt(+Ilm_{ss}), which at identical Ti/(Ti+Fe) corresponds to higher δ.

The difference between Tmt(+Ilm_{ss}) and Tmt(+Wus) or Tmt(+Fe°) can be clearly observed in the spectra, but calculated $Fe^{3+}/\Sigma Fe$ ratios differ by only about 1 % absolute. Absolute values for $Fe^{3+}/\Sigma Fe$ thus agree within the uncertainties (about ± 4 %).

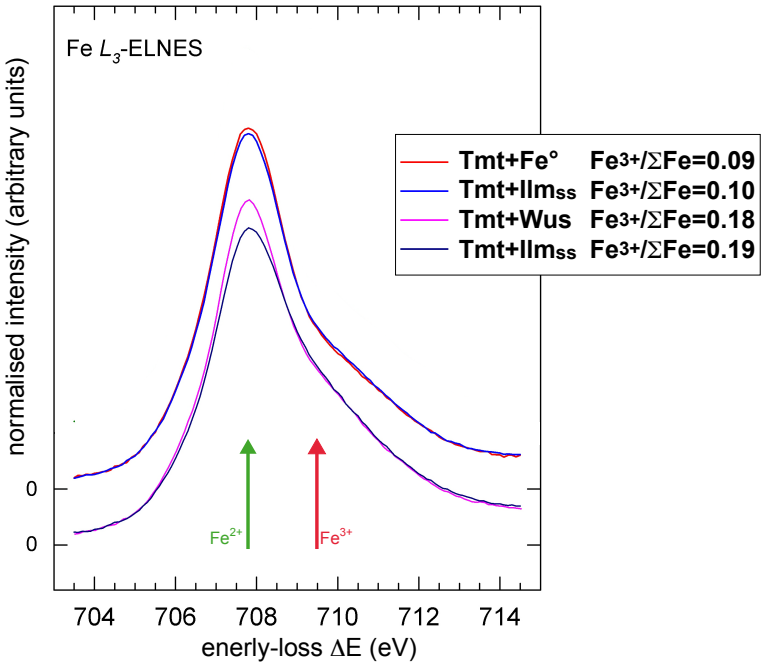

Fig. 5.18 Fe L_3 ELNES-spectra from two pairs of samples with comparable Ti/(Ti+Fe) (upper pair: X_{Usp}=0.91, lower pair: X_{Usp}=0.80-0.81) but Tmt in different assemblages (Tmt+Ilm_{ss}: blue; Tmt+Wus: pink, Tmt+Fe°: red). Arrows indicate positions of absolute maxima of Fe^{3+} (red arrow) and Fe^{2+} (green arrow).

δ calculated from $Fe^{3+}/\Sigma Fe$ and Ti/(Ti+Fe) Fig. 5.19 shows δ values derived from $Fe^{3+}/\Sigma Fe$ ratios (see Table 5.8). The uncertainty bars on δ arise from error propagation of uncertainties on $Fe^{3+}/\Sigma Fe$ (± 0.04, i.e. 4%), and Ti/(Ti+Fe) (± 0.005, i.e. 0.5%; from EMP analysis).

Tmt in coexistence with Ilm_{ss} show clearly higher δ than those in coexistence with Wus or metallic iron, pointing to vacancy concentrations of about 1 to 2 cat% at 1300 °C for Tmt(+Ilm_{ss}). However, the values agree within the uncertainties calculated for δ. The δ values for Tmt in coexistence with Wus or Fe° suggest stoichiometric compositions, but are also in agreement with slight cation excess, i.e. cation interstitials (especially Tmt+Wus 6F80x66, $\delta*10^2$=-0.2).

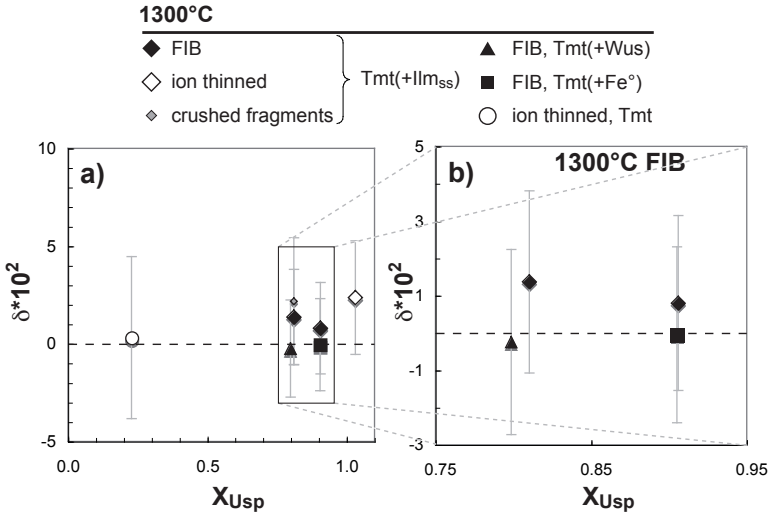

Fig. 5.19 a) δ from EELS versus X_{Usp}, b) close-up on samples prepared with the FIB technique. Dashed horizontal lines represent Tmt stoichiometry.

Table 5.8 $Fe^{3+}/\Sigma Fe$ and resulting δ for Tmt in different assemblages, synthesised at 1300 °C.

sample	assemblage	sample preparation	Tmt Ti/(Ti+Fe) [at%] mean	(σ)	X_{Usp}	$\frac{Fe^{3+}}{\Sigma Fe}$	$\frac{\Delta Fe^{3+}}{\Sigma Fe}$	$\delta * 10^2$	$\Delta\delta * 10^{2\,(a)}$
				Tmt+Wus					
6F80x66	Tmt+Wus	FIB	26.62	(24)	0.80	0.18	0.04	-0.2	3.5
				Tmt+Fe°					
6F80x81	Tmt+Fe°	FIB	30.17	(25)	0.91	0.09	0.04	0.0	3.3
				single-phase Tmt					
6F92x1.6	Tmt	ion thinned	7.60	(24)	0.23	0.56	0.04	0.3	4.2
				$Tmt+Ilm_{ss}$					
6F63x8	$Tmt+Ilm_{ss}$	crushed	27.01	(22)	0.81	0.20	0.04	2.2	3.4
6F63x8	$Tmt+Ilm_{ss}$	FIB	27.01	(22)	0.81	0.19	0.04	1.4	3.4
6F57x18	$Tmt+Ilm_{ss}$	FIB	30.20	(20)	0.91	0.10	0.04	0.8	3.3
6F57x66	$Tmt+Ilm_{ss}$	ion thinned	34.39	(17)	1.03	0.00	0.04	2.4	3.1

a) uncertainty on $\delta * 10^2$, calculated by error propagation

5.6 Discussion

5.6.1 Summary of annealing method results, lattice parameter data and EELS data from the present study

For $X_{Usp} \geqslant 0.7$, the different approaches applied within this study concordantly indicate an increasing amount of non-stoichiometry (cation vacancies) with increasing X_{Usp} and temperature for Tmt coexisting with Ilm_{ss}.

Based on our investigations, Tmt(+Ilm_{ss}) is stoichiometric within uncertainties at X_{Usp}<0.7 for all examined temperatures (Fig. 5.20). However, small concentrations of cation vacancies cannot be excluded (compare sections 5.3.3 and 5.4.2).

From lattice parameter data it follows that Tmt in equilibrium with wüstite at 1300 °C probably has cation excess (Fig. 5.20). The results from EEL spectroscopy support only small concentrations of cation interstitials.

Fig. 5.20 schematically shows the trend for non-stoichiometry vs. X_{Usp} for 1100 °C and 1300 °C, summarised from the annealing method, lattice parameter determination and EELS. The 1200 °C data have been omitted but describe a trend intermediate between the 1100 °C and 1300 °C data. At 1200 °C and 1300 °C a maximum vacancy concentration of 1 resp. 2 cat% is expected near Usp endmember.

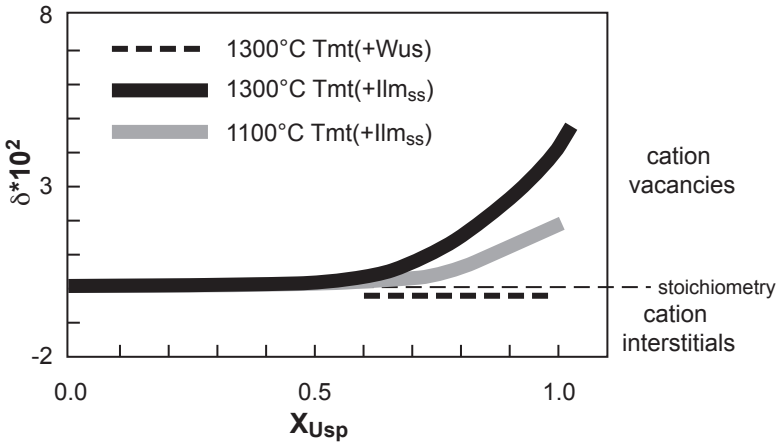

Fig. 5.20 δ versus X_{Usp} for 1100 °C (grey) and 1300 °C (black), for Tmt in coexistence with Ilm_{ss} (thick solid lines) and 1300 °C Tmt(+Wus) (black dashed line). The thin black dashed line indicates the composition of stoichiometric Tmt.

5.6.2 Comparison with literature

Comparison to Senderov *et al.* (1993) The results by Senderov *et al.* (1993) from EMP oxygen analysis could partly be reproduced by alternative methods (annealing method, EELS) within the present study: For 1300 °C both studies suggest nearly stoichiometric Tmt compositions at low X_{Usp}, and up to about 2 % cation vacancies near ulvöspinel endmember (Fig. 5.21). However, based on the data by Senderov *et al.* (1993) no clear δ-X_{Usp} trend can be derived for intermediate Tmt compositions, as there are no δ values for Tmt in coexistence with ilmenite$_{ss}$ for $0.06<X_{Usp}<0.72$. Further, the single-phase Tmt data by Senderov *et al.* (1993) are inconsistent with their Tmt(+Ilm$_{ss}$) data, and as they suggest significant vacancy concentration also at intermediate X_{Usp} contradict our data.

Aggarwal & Dieckmann (2002) have argued that the large uncertainties of oxygen measurement with electron microprobe are the reason for the contradictions between Senderov *et al.* (1993) and Aggarwal & Dieckmann (2002) (chapter 1, section 1.2). However this has to be doubted, as there is basic agreement between our data - which is *not* based on EMP oxygen analysis - and that of Senderov *et al.* (1993). Nevertheless, the large uncertainties of EMP oxygen analysis might cause the inconsistencies within the work of Senderov *et al.* (1993).

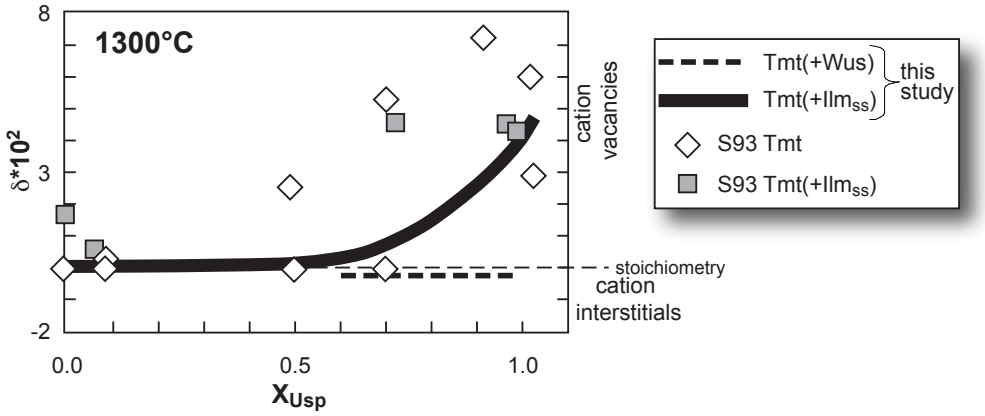

Fig. 5.21 Comparison of this study's data (summarised by dashed and solid lines) to the data of Senderov *et al.* (1993) (symbols, S93) in a plot of δ versus X_{Usp} for quenched products of runs at 1300 °C.

Comparison to Aggarwal & Dieckmann (2002) Comparing our data to the work of Aggarwal & Dieckmann (2002), we have to be aware that Aggarwal & Dieckmann (2002) have carried out thermogravimetric *in-situ* examinations, whereas

within this study, we exclusively investigated *quenched* samples. We observe severe discrepancies, concerning both trend and absolute values. In contradiction to our results, Aggarwal & Dieckmann (2002) report slightly *decreasing* non-stoichiometry with increasing X_{Usp} (Fig. 5.22). At 1100 °C and X_{Usp}=0.3 and 0.6, Aggarwal & Dieckmann (2002) give about $\delta * 10^2$=1.2, whereas at 1100 °C and X_{Usp}<0.7, the data points available from the present study do not provide any clear evidence for significant non-stoichiometry. Nevertheless, there is good agreement for single data points, e.g. 1300 °C, X_{Usp}=0.75.

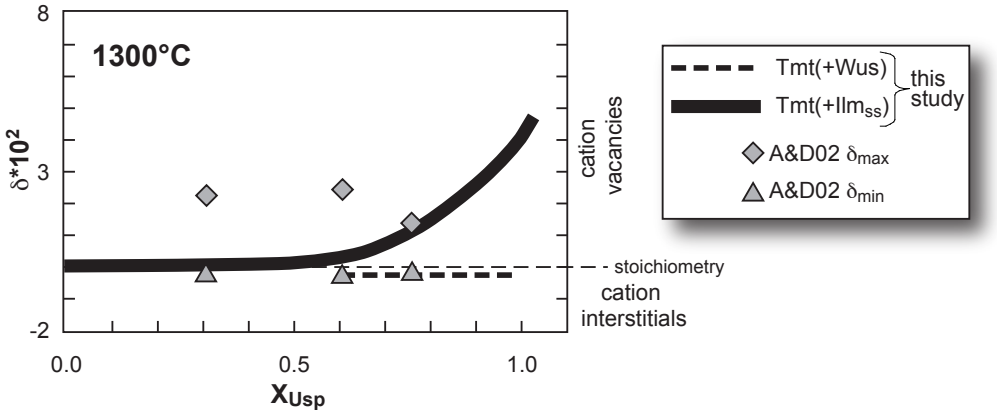

Fig. 5.22 Comparison of this study's data at 1300 °C (summarised by dashed and solid lines) to the data of Aggarwal & Dieckmann (2002) (symbols, A&D02) in a plot of δ versus X_{Usp}.

Concerning titanomagnetite in coexistence with wüstite, Aggarwal & Dieckmann (2002) report only negligible cation excess ($\delta * 10^2 = -0.02$ at X_{Usp}=0.75, 1300 °C), which is in agreement with the amount of non-stoichiometry we suggest from EEL spectroscopy ($\delta * 10^2 = -0.20 \pm 2.4$ at X_{Usp}=0.80, 1300 °C).

Aggarwal & Dieckmann (2002) state that on crossing the upper fO_2 stability limit of Tmt, they record a large mass change due to the oxidation of Tmt to Ilm_{ss}. However, the authors do not report a check for phase purity (for example by X-ray diffraction) in situ or after the experiment. At 1300 °C and X_{Usp}=0.33 and X_{Usp}=0.67 the phase boundary according to Aggarwal & Dieckmann (2002) is shifted towards higher fO_2 compared to our data (chapter 4). Therefore, alleged single-phase Tmt according to Aggarwal & Dieckmann (2002) might actually consist of Tmt plus small amounts of Ilm_{ss}. As the oxygen content of Ilm_{ss} is significantly higher than that of Tmt, neglecting Ilm_{ss} should result in an overestimation of Tmt non-stoichiometry.

While Aggarwal & Dieckmann (2002) have applied *in-situ* measurements to quantify Tmt non-stoichiometry, the examinations of the present study (and also the investigation of Senderov *et al.* (1993)) are carried out on *quenched* samples. The concentration of cation interstitials or cation vacancies might potentially change during the quenching procedure, i.e. high-T cation vacancy concentration might not be quenchable.

In fact, the high-T *cation distribution* of Tmt cannot be quenched to room temperature (e.g. O'Neill & Navrotsky, 1984). However, whereas the change of cation distribution during quenching is basically the transfer of electrons between ferric and ferrous iron (section 1.2) at *constant* Ti/(Ti+Fe) and cation/oxygen ratios of the Tmt, a change in non-stoichiometry involves a change in *Tmt composition* (i.e. oxygen content).

Cation vacant Tmt might become unstable during quenching in favour of the paragenesis stoichiometric Tmt+Ilm_{ss}. This should result in the formation of Ilm_{ss} exsolution features over the complete sample due to an increase of the amount of Ilm_{ss}. However, this has not been observed.

Theoretically it could also be assumed that upon quenching non-stoichiometric Tmt transforms into stoichiometric Tmt at constant Ti/(Ti+Fe) by releasing oxygen ($(Fe_{(1-x)}Ti_x)_{(3-\delta)}O_4 \rightarrow (Fe_{(1-x)}Ti_x)_3O_4 + yO$). However, from our knowledge of phase relations in the system Fe-Ti-O we would rather expect the formation of stoichiometric Tmt + $ilmenite_{ss}$ (see above).

5.7 Conclusion

According to the results of the present study Tmt can incorporate up to 2 cat% vacancies at high T (i.e. 1300 °C) and Ti-rich compositions. At temperatures relevant for nature (<1100 °C), Tmt can be assumed to be stoichiometric.

Tmt non-stoichiometry in the simple system Fe-Ti-O was assumed to be responsible for the deviation between experimental Tmt compositions according to this study, and Tmt compositions estimated from thermo-oxybarometer models at low fO_2 and high T (chapter 4). In fact, significant cation vacancy concentrations could be verified within the present chapter. Thus, based on our results we recommend to incorporate Tmt non-stoichiometry into new versions of the Tmt-Ilm_{ss} thermo-oxybarometer.

However, the data set provided within this study is focussed on high Ti contents and is contradictory to literature data. The fact that we work on quenched samples while other authors (e.g. Aggarwal & Dieckmann, 2002) have worked in situ, limits the comparability between the results. Yet we do not see how this could ex-

plain the observed discrepancies. Nevertheless, an in-situ investigation (e.g. in-situ thermogravimetry) using our samples and involving careful (X-ray and SEM) investigations after and as far as possible during the experiment could help to understand and desirably to finally resolve the remaining contradictions.

To complete the knowledge on Tmt non-stoichiometry a more detailed investigation at X_{Usp}<0.7 and the application of further methods would be worthwhile. Lattice parameter determination with synchrotron radiation can potentially provide information on Tmt cation site occupancy. Cation site occupancy and $Fe^{3+}/\Sigma Fe$ ratio can also be investigated by Mössbauer spectroscopy. Further EELS examinations on our samples covering a broader range in temperature and composition are expected to be enlightening (i.e. EELS on Tmt(+Ilm_{ss}) and Tmt(+Wus) FIB samples with identical X_{Usp}). Another approach is the simultaneous determination of $Fe^{3+}/\Sigma Fe$ and Ti/(Ti+Fe) by the electron microprobe. However, all these spectroscopic methods might be spoiled by electron hopping, especially for Fe-rich Tmts.

Oxygen analysis with the electron microprobe remains a promising method to investigate Tmt non-stoichiometry. The absolute value of the oxygen concentration of Tmt, or the difference in oxygen content between two selected samples can be determined.

With respect to thermo-oxybarometry, it is of major interest, how the small amounts of Al, Mg, Mn, etc contained in natural Tmt influence non-stoichiometry. The effect of minor elements can be significant (for Cr: Lattard, 1995). The following chapter will consider the effect of minor elements of Fe-Ti oxide phase relations, and - for few selected samples - attempt to investigate the effect on Tmt non-stoichiometry.

6 Influence of minor element contents of Mg and Al on Fe-Ti oxide phase compositions, phase relations and non-stoichiometry

6.1 Introduction: minor element contents in Fe-Ti oxides

Fe-Ti oxides are important accessory minerals in many igneous and metamorphic rocks of the Earth's crust, in the Earth's mantle, as well as in lunar and martian rocks (see chapter 1, section 1.1 and chapter 4). In these natural occurrences, the Fe-Ti oxides usually incorporate small amounts (up to some weight per cent) of magnesium (Mg) and aluminium (Al) and < 1 wt% of minor elements, such as manganese (Mn), chromium (Cr), niobium (Nb), and vanadium (V).

To investigate phase relations and non-stoichiometry of Fe-Ti oxides, we have in a first stage carried out experiments in the simple system Fe-Ti-O (chapters 4 and 5). The simplicity of this three-component system allows a straightforward investigation of the principle properties of the Fe-Ti oxides. However, even the small amounts of minor elements that occur in natural rocks can influence Fe-Ti oxide behaviour. Therefore, additional experiments have been carried out in the systems Fe-Ti-Mg-O, Fe-Ti-Al-O and Fe-Ti-Mg-Al-O to approach natural compositions.

Coexisting Tmt and Ilm_{ss} (both natural and synthetic) from selected publications (Table 6.1) have been examined regarding their MgO and Al_2O_3 contents (Fig. 6.1). The data selection comprises volcanic and intrusive rocks of the Earth, as well as martian meterorites (martian basalts), equilibrated at different temperatures (Table 6.1). The Mg and Al contents observed in the literature data range up to 6 wt% MgO in Ilm_{ss} and 4 wt% MgO in Tmt. The Al_2O_3 content in Ilm_{ss} is usually <0.8 wt%. In Tmt, the Al_2O_3 content usually ranges between 1 and 3.5 wt%. Though equilibration temperatures are generally significantly lower (cf. Table 6.1 and Table 6.2) than the experimental temperatures applied in the present study (see below), the literature data can serve as a basis to select reasonable MgO and Al_2O_3 contents in the synthetic starting mixtures.

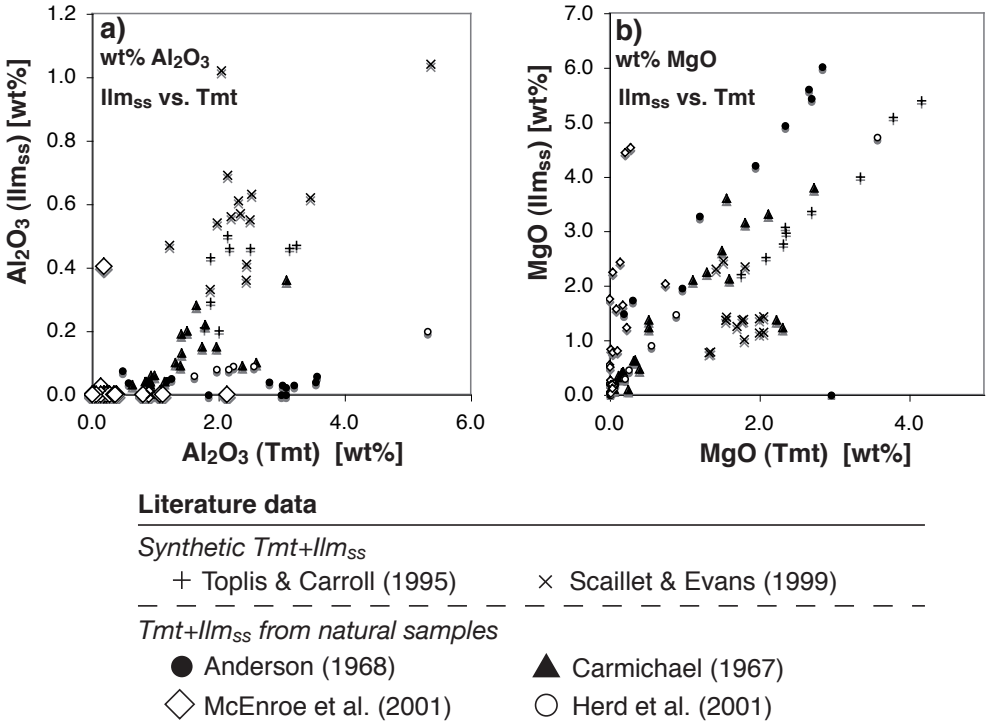

Fig. 6.1 a) Al_2O_3 and b) MgO contents (in weight percent) in Ilm_{ss} versus coexisting Tmt, in natural and synthetic samples from literature (Table 6.1).

Table 6.1 Selected literature on Mg-Al bearing Tmt+Ilm_{ss}.

authors	origin	composition, rock	T[1] [°C]	ΔNNO[1]
Toplis & Carroll (1995)	synthetic	ferrobasalt[2]	1050-1100	-1.6 to +0.3
Scaillet & Evans (1999)	synthetic	dacite[3]	770-870	0.0 to +2.7
Carmichael (1967)	various origins	salic volcanic rocks	800-1000	
Anderson (1968)	Quebec	magnetite deposit	750-850	
Herd *et al.* (2001)	martian meteorites	basalt	700-800	-4.0 to -1.0
McEnroe *et al.* (2001)	Norway	norite	500-550	-2.7 to +5.0

1) experimental or estimated equilibration conditions
2) synthetic glass powder of ferrobasaltic composition
3) from Mt. Pinatubo

6.2 Experimental and analytical approach

To synthesise Mg-Al bearing Fe-Ti oxide assemblages, which resemble natural compositions, TiO_2+Fe_2O_3±Fe°+MgO, TiO_2+Fe_2O_3±Fe°+Al_2O_3 and TiO_2+Fe_2O_3±Fe°+MgO+Al_2O_3 starting mixtures have been prepared and equilibrated following the procedures described in chapter 2. The majority of the mixtures have been prepared with about 2 wt% of minor element oxides, i.e. either 2 wt% MgO *or* Al_2O_3 for the systems Fe-Ti-Al-O and Fe-Ti-Mg-O, and about 1 wt% MgO *plus* 1 wt% Al_2O_3 for the system Fe-Ti-Mg-Al-O. Further, two starting mixtures with higher contents have been prepared (3.1 wt% MgO for system Fe-Ti-Mg-O, 4.3 wt% Al_2O_3 for system Fe-Ti-Al-O).

The experiments have been restricted to temperatures of 1100 °C and above ($1100-1300$ °C), and intermediate to low fO_2 (NNO-5 to NNO+1). The syntheses were essentially intended to produce Tmt+Ilm_{ss} assemblages, but other parageneses (mainly Ilm_{ss}+Psb_{ss} and the ternary paragenesis Tmt+Ilm_{ss}+Psb_{ss}) have also been synthesised. The run products have been characterised by X-ray powder diffraction and the SEM, and analysed with the EMP.

To investigate non-stoichiometry of Mg-Al bearing Tmt, three selected 1300 °C Tmt+Ilm_{ss} samples have been annealed under oxygen conserving conditions at 950 °C in order to induce vacancy relaxation (see chapter 2 and especially chapter 5). The phase proportions of Tmt and Ilm_{ss} in annealed and corresponding high-T synthesis samples have been determined by image analysis.

6.3 Phase relations in the system Fe-Ti-Mg-Al-O

The phase relations in the simple system Fe-Ti-O have been discussed in chapters 1 (section 1.2) and 4. The amounts of Mg and Al added to the starting materials are small (about $1.0-3.1$ wt% MgO, $1.0-4.3$ wt% Al_2O_3 in bulk), and just like for the Fe-Ti-O system, we mainly obtained binary Tmt+Ilm_{ss} and Ilm_{ss}+Psb_{ss} assemblages.

In the simple system Fe-Ti-O, Tmt and Ilm_{ss} can be treated as binary solid solutions between the endmembers magnetite and ulvöspinel, and hematite and ilmenite, respectively. The incorporation of minor amounts of Mg and Al creates supplementary endmembers (e.g. in case of Ilm_{ss}: $MgTiO_3$ and Al_2O_3).

It is well-known that Mg-titanates form continuous solid solution towards ferrous titanates at high T (Johnson *et al.*, 1971, review in Lindsley, 1991), for example between $MgTiO_3$ and $FeTiO_3$. Between $MgTiO_3$ and Fe_2O_3 there is a miscibility gap, but at temperatures relevant for the present study, Fe_2O_3 can incorporate more

than 40 mol% $MgTiO_3$ (Woermann *et al.*, 1969, 1970; Pownceby & Fisher-White, 1999).

In contrast, there are broad miscibility gaps between the Al-bearing endmembers and the Fe-Ti oxide phases (Muan & Gee, 1956; Turnock & Eugster, 1962; Muan *et al.*, 1972), especially between Al_2O_3 and Fe_2O_3, and Al_2O_3 and $FeTiO_3$ (Fig. 6.2). This results in the formation of the ternary paragenesis Tmt+Ilm_{ss}+Psb_{ss}, and the binary assemblage Tmt+Psb_{ss} for sufficiently high bulk Al contents.

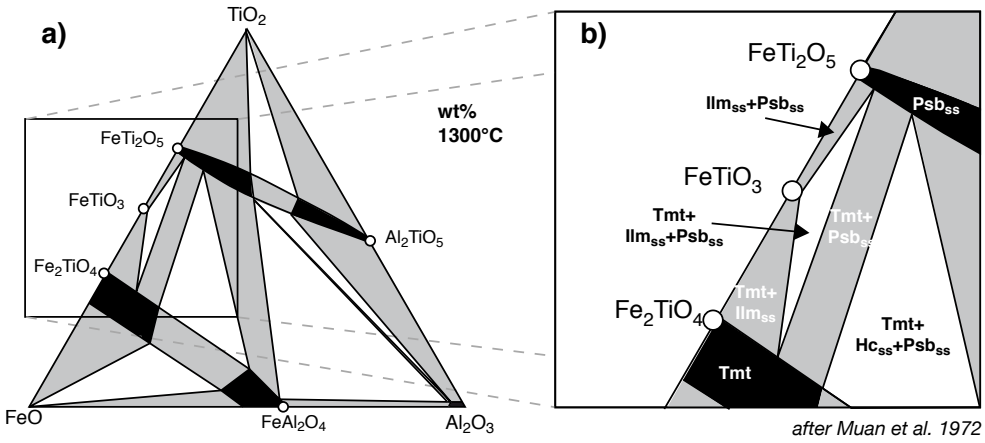

Fig. 6.2 a) Phase relations in the system FeO-Al_2O_3-TiO_2 at 1300 °C in contact with metallic iron according to Muan *et al.* (1972), Fig. 1. Single-phase fields are black, two-phase fields grey, ternary fields white. b) Enlargement of the Al-poor part of the system.

Within this study, a ternary paragenesis Tmt+Ilm_{ss}+Psb_{ss} has been synthesised in the system Fe-Ti-Al-O at 1200 °C and 1300 °C (Fig. 6.3). The phase compositions presented in Fig. 6.3 are projected from the Fe_2O_3 apex onto the FeO-Al_2O_3-TiO_2 plane, whereby FeO and Fe_2O_3 are derived from mineral formula calculation assuming stoichiometry of the phases.

At 1100 °C we have only produced two data points in the system Fe-Ti-Al-O, both yielding Tmt+Ilm_{ss} assemblages. In the system Fe-Ti-Al-Mg-O, only binary assemblages (Tmt+Ilm_{ss}, Ilm_{ss}+Psb_{ss}) have been observed. This can be ascribed to the small amounts of Mg and Al present in the sample bulk.

In the ternary paragenesis Tmt+Ilm_{ss}+Psb_{ss}, the concentration of Al in Ilm_{ss} corresponds to the maximum solubility at synthesis conditions (compare Fig. 6.2). For other parageneses and concerning Mg, maximum solubilities for Mg and Al at synthesis conditions were not reached.

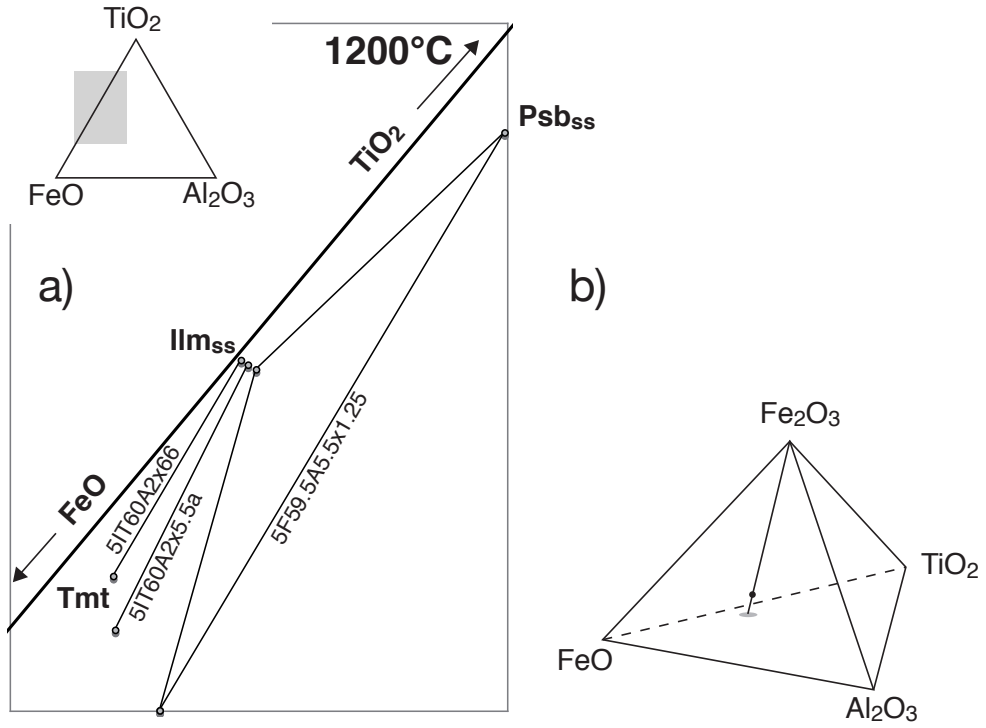

Fig. 6.3 Phase compositions in samples synthesised within this study at 1200°C in the system Fe-Ti-Al-O, projected onto the FeO-Al_2O_3-TiO_2 triangle. a) Enlargement of the triangle near the FeO-TiO_2 join. Small empty circles represent phase compositions, connected by solid tie-lines. Sample names are denoted next to the tie-lines. b) Compositions of the phases (exemplified by black circle) are projected from the Fe_2O_3 apex onto the FeO-Al_2O_3-TiO_2 plane as schematised.

6.4 Phase compositions in the system Fe-Ti-Mg-Al-O

As in the simple system Fe-Ti-O, the distribution of Fe and Ti in coexisting phases in the system Fe-Ti-Mg-Al-O is a function of oxygen fugacity and temperature. In both phases, the Ti content increases with decreasing fO_2. In Tmt, a slight increase of the Ti content with increasing temperature can be observed. The phase compositions of the synthesised phases are listed in appendix A.3.

6.4.1 Mg- and Al-contents of the Fe-Ti oxide phases

Al-content In accordance with the phase relations established by Muan *et al.* (1972, Fig. 6.2), in the run products synthesised in the present study, aluminium partitions preferentially into Tmt, followed by Psb_{ss} and Ilm_{ss}.

In the system Fe-Ti-Al-O at 1200 °C and 1300 °C, Ilm_{ss} in the ternary assemblage Tmt+Ilm_{ss}+Psb_{ss} has a maximum Al_2O_3 content of about $1.0-1.3$ wt% (Fig. 6.4a). This maximum solubility is within the examined conditions (NNO-4 to +1) independent of the oxygen fugacity (Fig. 6.4b). At 1100 °C the highest observed Al_2O_3 content in Ilm_{ss} is about 0.6 wt% (Ilm_{ss} in equilibrium with Tmt). The low Al_2O_3 content of Ilm_{ss} in the synthetic samples comes along with relatively high Al_2O_3 contents in coexisting Tmt (about $8-12$ wt% Al_2O_3), and Psb_{ss} ($3-5$ wt% Al_2O_3).

The Al_2O_3 contents in the phases in the system Fe-Ti-Mg-Al-O are lower, due to lower Al_2O_3 content in the starting material.

Fig. 6.5 shows the distribution of Al (in wt% Al_2O_3) between Tmt and coexisting Ilm_{ss} in Tmt+Ilm_{ss} and also Tmt+Ilm_{ss}+Psb_{ss} assemblages. As stated above, Al partitions preferably in Tmt, a feature which is enhanced with decreasing temperature (increasingly flat trends with decreasing temperature in Fig. 6.5).

Mg-content At the investigated temperatures and oxygen fugacities, Mg partitions preferably in Ilm_{ss} (up to 3.4 wt%), followed by Tmt (up to $2.7-3.1$ wt%) and Psb_{ss} (up to 1.4 wt%) (Fig. 6.6). The MgO content of both Ilm_{ss} and Psb_{ss} is practically independent of temperature. With increasing temperature, the highest observed MgO content in Tmt increases only very slightly.

The experimental data for Tmt+Ilm_{ss} derived in the present study show a roughly linear correlation between MgO [wt%] in Tmt and MgO [wt%] in Ilm_{ss}. The gradient MgO(Tmt)/MgO(Ilm_{ss}) slightly decreases with increasing temperature (Fig. 6.7).

The trends for the different temperature series strongly overlap. At given temperature (e.g. 1300 °C), the distribution of MgO between Tmt and Ilm_{ss} varies, probably as a function of oxygen fugacity. The experimental data suggest that with

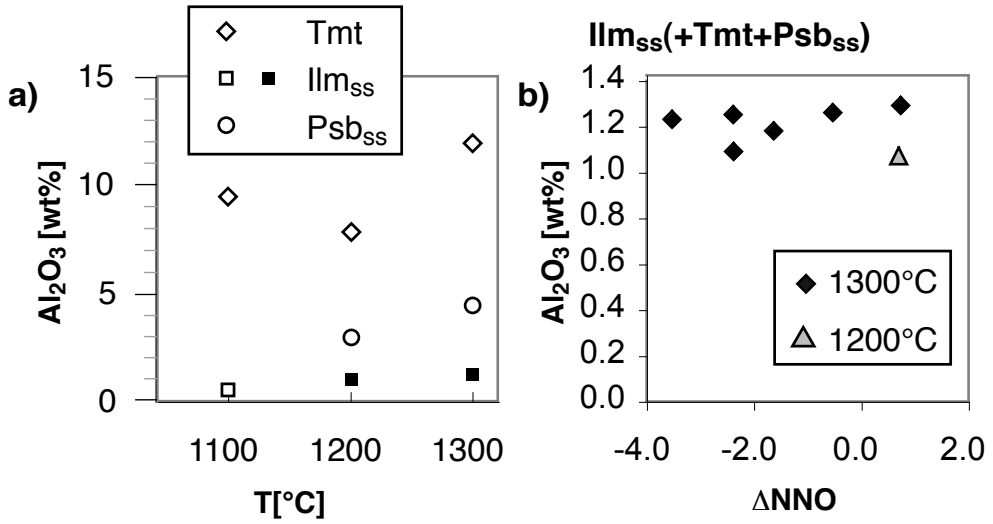

Fig. 6.4 a) Maximum Al_2O_3 solubility (black symbols) and highest observed Al_2O_3 content (empty symbols) versus temperature (1100 – 1300 °C) for Fe-Ti oxide phases Tmt (diamonds), Ilm_{ss} (squares) and Psb_{ss} (circles). b) Maximum Al_2O_3 contents in Ilm_{ss} (in ternary assemblage Ilm_{ss}+Tmt+Psb_{ss}) in system Fe-Ti-Al-O as a function of oxygen fugacity at 1200 °C (grey triangle) and 1300 °C (black rhombs). The reason for the different Al contents at 1300 °C and NNO-2.5 is unknown.

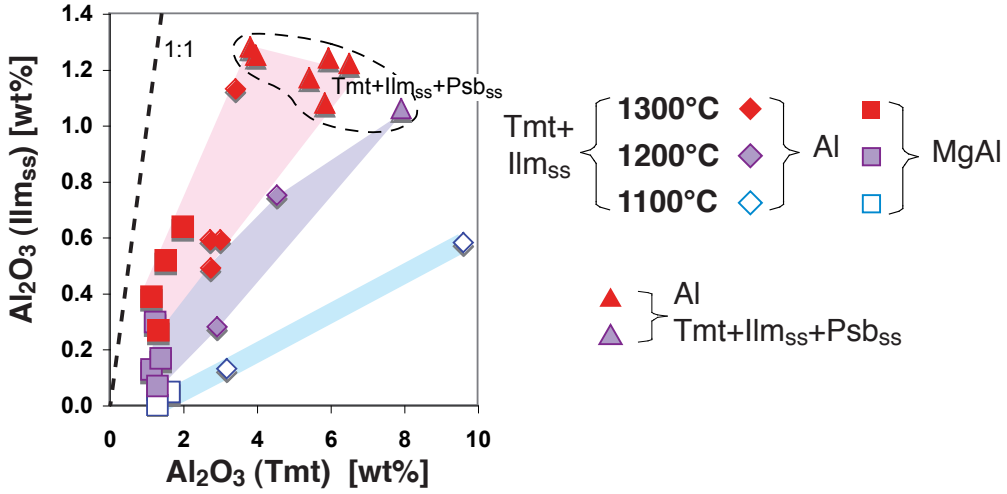

Fig. 6.5 Al_2O_3-contents [wt%] in Ilm_{ss} versus those in coexisting Tmt. Symbols represent experimental data of this thesis for different systems or assemblages, colours indicate different synthesis temperatures. Light coloured regions span this study's experimental data at 1100 °C (light blue), 1200 °C (lilac) and 1300 °C (light pink). Dashed line represents equal Al_2O_3 contents in Tmt and Ilm_{ss}.

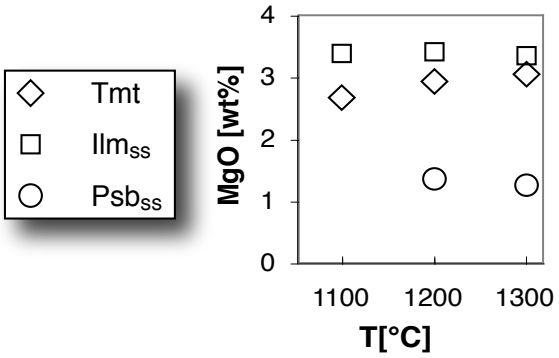

Fig. 6.6 Highest observed MgO content versus temperature (1100 – 1300 °C) for Fe-Ti oxide phases Tmt (diamonds), Ilm_{ss} (squares) and Psb_{ss} (circles). Tmt, Ilm_{ss}: system Fe-Ti-Mg-O; Psb_{ss}: system Fe-Ti-Mg-Al-O (no Psb_{ss} bearing samples synthesised in the system Fe-Ti-Mg-O).

increasing fO_2 the MgO content in Tmt increases while the MgO content in Ilm_{ss} decreases (Fig. 6.7b).

A linear relation between the MgO contents in Tmt and coexisting Ilm_{ss} can also be observed in part of the literature data presented above in Table 6.1 (Herd *et al.*, 2001; Toplis & Carroll, 1995; Anderson, 1968).

The trend of increasing gradient MgO(Tmt)/MgO(Ilm_{ss}) with decreasing temperature is also confirmed in many cases (e.g. McEnroe *et al.*, 2001; Anderson, 1968, see Fig. 6.7). Comparing the gradients observed in the data by Anderson (1968) and Herd *et al.* (2001), we would expect higher equilibration temperatures in the latter. However, the authors give similar equilibration temperatures in both cases (750 – 850 °C and 700 – 800 °C, respectively; see Table 6.1). It has to be stated that Anderson (1968) could only use the version of the Tmt+Ilm_{ss} thermo-oxybarometer by Buddington & Lindsley (1964). Estimates with the QUILF model (Andersen & Lindsley, 1988) and the model by Ghiorso & Sack (1991) give temperatures which are significantly lower than those given in Anderson (1968, Table 6.2), and thus indeed lower than those given for the data of Herd *et al.* (2001). The experimental data by Toplis & Carroll (1995), which reflect synthesis temperatures of 1050 – 1100 °C, is in good agreement with our 1100 °C data. The experimental data by Scaillet & Evans (1999) do not show a pronounced linear correlation between the MgO contents in Tmt and Ilm_{ss}. Although these samples were equilibrated at relatively low T (i.e. 770 – 870 °C), the corresponding data points plot to the right, i.e. on the presumed high-T side of our experimental 1300 °C data. The reason is unclear. A relation to the equilibration oxygen fugacity could not be found.

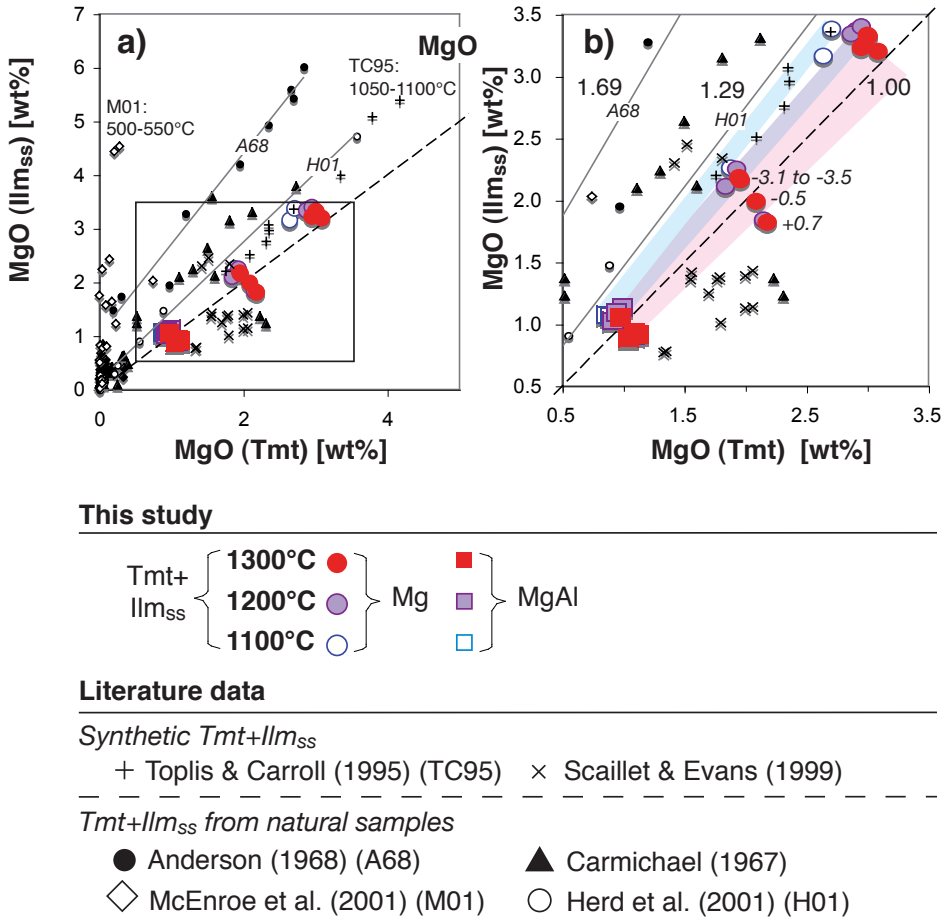

Fig. 6.7 a) MgO-contents [wt%] in Ilm_{ss} versus those in Tmt. Symbols represent literature data (black) and experimental data of this thesis (coloured). Dashed line represents equal MgO contents in both phases. Grey lines are linear fits to the literature data by Anderson (1968, black filled circles) and Herd *et al.* (2001, black empty circles). Equilibration temperatures (see Table 6.1) are annotated for the data by McEnroe *et al.* (2001) and Toplis & Carroll (1995). b) Enlargement of rectangle shown in picture (a). Coloured shaded areas span this study's experimental data at 1100 °C (light blue), 1200 °C (lilac) and 1100 °C (light pink). Italic numbers next to experimental 1300 °C data points indicate oxygen fugacity (expressed as ΔNNO). Numbers next to the grey lines for linear fits represent slopes.

Table 6.2 Selected literature data on Mg-Al bearing Tmt+Ilm_{ss}.

authors	QUILF[1]		Ghiorso & Sack (1991)	
	T [°C]	ΔNNO	T [°C]	ΔNNO
Carmichael (1967) 2[2]	780-920	+0.4 to +2.1	820-1070	+0.2 to +1.9
Carmichael (1967) 3[2]	780-880	-0.3 to +0.7	780-980	-0.7 to +0.5
Carmichael (1967) 4[2]	730-880	-2.1 to -0.9	710-860	-2.6 to -1.1
Anderson (1968), A[3]	550-660	-7.2 to -2.9	560-620	-4.3 to -3.6
Anderson (1968), B[3]	400-470	+1.7 to +5.6	300-340	1.3 to -3.8

1) Andersen & Lindsley (1988)
2) number refers to table number in Anderson (1968), for Fe-Ti oxides in paragenesis with different silicate phases. Table 2: Al_2O_3 and MgO contents <1.2 wt% in both phases. Tables 3 and 4: higher Mg and Al contents.
3) divided into two groups according to phase compositions and T-fO_2 estimates, group B has MgO contents $\leq$ 0.2 wt% in both phases, group A has $0.9-2.8$ wt% MgO in Tmt and $1.9-5.6$ wt% in Ilm_{ss}.

6.4.2 Projection of Mg-Al bearing compositions into the Ilm-Hem and Mag-Usp binaries

The Tmt-Ilm_{ss} thermo-oxybarometer is based on the Fe-Ti distribution between Ilm_{ss} and Tmt. In the simple system Fe-Ti-O, Ilm_{ss} and Tmt are binary solid solutions. The mole fractions of the endmembers, X_{Usp} and X_{Ilm}, can be very easily derived (equations 6.1 and 6.2, [ ]: cations pfu) from the cation concentrations obtained through EMP analysis.

$$X_{\mathrm{Usp}} = 3 * \frac{[\mathrm{Ti}]}{[\mathrm{Ti}] + [\mathrm{Fe}_{tot}]} \tag{6.1}$$

$$X_{\mathrm{Ilm}} = 2 * \frac{[\mathrm{Ti}]}{[\mathrm{Ti}] + [\mathrm{Fe}_{tot}]} \tag{6.2}$$

In multi-component systems, additional endmembers are necessary to describe Tmt and Ilm_{ss} compositions. For the system Fe-Ti-Mg-Al-O, the possible endmember components are given in Table 6.3. A projection into the simple system Fe-Ti-O is necessary to compare the phase compositions with the results in the simple system Fe-Ti-O. The projection to the Fe-Ti oxide binaries is achieved by equations 6.3 and 6.4, yielding projected fractions of endmembers X'_{Usp} and X'_{Ilm}.

$$X'_{Usp} = \frac{X_{Usp}}{X_{Usp} + X_{Mag}} \tag{6.3}$$

$$X'_{Ilm} = \frac{X_{Ilm}}{X_{Ilm} + X_{Hem}} \tag{6.4}$$

Since the 1960ties, several schemes have been proposed to calculate the molefractions of the endmembers and subsequently derive X'_{Usp} and X'_{Ilm} (e.g. Carmichael, 1967; Anderson, 1968; Lindsley & Spencer, 1982; Stormer, 1983). The Fe-Ti oxide thermo-oxybarometer formulations (QUILF Andersen & Lindsley, 1988; Ghiorso & Sack, 1991) also comprise schemes to calculate the molefractions of the endmembers of Ilm_{ss} and Tmt.

For the present study, a projection scheme was chosen in agreement with Bernard Evans (Seattle) and Mark Ghiorso (Seattle). The ratio of $Ti^{4+}/Al^{3+}/Fe^{3+}$ per formula unit determines the ratio of titanates, aluminates and ferrites. Further the ratio Fe^{2+}/Mg^{2+} is assumed to be the same in all three groups. With this background, the molefractions of all Tmt and Ilm_{ss} endmembers can be calculated (Table 6.3). For

Table 6.3 Spinel endmember components (upper part of the table) and endmember components of the rhombohedral phase (lower part), for Mg- and Al-bearing Tmt and Ilm_{ss}, respectively

component	name	abbr.		X^1
		titanomagnetite		
		Fe^{2+} components		
$Fe_2^{2+}Ti^{4+}O_4$	ulvöspinel	Usp	titanate	$Ti^{4+} * \frac{Fe^{2+}}{Fe^{2+}+Mg^{2+}}$
$Fe^{2+}Fe_2^{3+}O_4$	magnetite	Mag	ferrite	$\frac{Fe^{3+}}{2} * \frac{Fe^{2+}}{Fe^{2+}+Mg^{2+}}$
$Fe^{2+}Al_2^{3+}O_4$	hercynite	Hc	aluminate	$\frac{Al^{3+}}{2} * \frac{Fe^{2+}}{Fe^{2+}+Mg^{2+}}$
		Mg^{2+} components		
$Mg_2^{2+}Ti^{4+}O_4$	qandilite	Qan	titanate	$Ti^{4+} * \frac{Mg^{2+}}{Fe^{2+}+Mg^{2+}}$
$Mg^{2+}Fe_2^{3+}O_4$	magnesioferrite	MgF	ferrite	$\frac{Fe^{3+}}{2} * \frac{Mg^{2+}}{Fe^{2+}+Mg^{2+}}$
$Mg^{2+}Al_2^{3+}O_4$	spinel	Spl	aluminate	$\frac{Al^{3+}}{2} * \frac{Fe^{2+}}{Mg^{2+}+Mg^{2+}}$
		$ilmenite_{ss}$		
$Fe_2^{3+}O_3$	hematite	Hem		$\frac{Fe^{3+}}{2}$
$Fe^{2+}Ti^{4+}O_3$	ilmenite	Ilm		Fe^{2+}
$Mg^{2+}Ti^{4+}O_3$	geikielite	Gk		Mg^{2+}
$Al_2^{3+}O_3$	corundum	Crn		$\frac{Al^{3+}}{2}$

1) molefraction of endmembers, calculated from cations pfu

the system Fe-Ti±Mg±Al-O, the calculation given in Ghiorso & Sack (1991) yields identical values for the endmember components. X'_{Usp} and X'_{Ilm} can subsequently be derived.

The spinel endmembers, i.e. ferrous and magnesian ferrites, titanates and aluminates, can be illustrated in a triangular prism (Table 6.3, Fig. 6.8). X'_{Usp} can be derived from cations pfu according to equation 6.5. For a more detailed description of Tmt projection see appendix A.5.

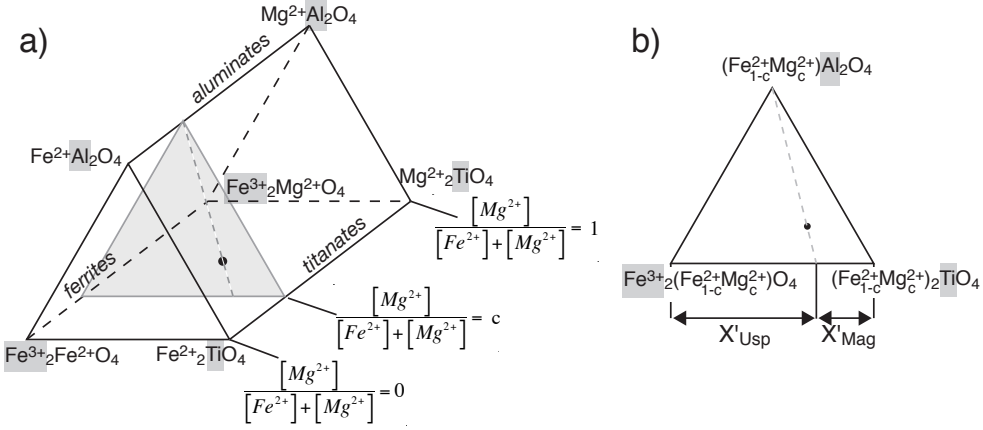

Fig. 6.8 a) Endmember components of Mg- and Al-bearing Tmt solid solution in a triangular prism. The black circle indicates the composition of Mg-Al bearing Tmt. The ratio of Fe^{2+} and Mg^{2+} components of titanates, aluminates and ferrites is assumed to be identical. b) Focus on the shaded triangle in picture (a). Tmt composition is projected to the titanate-ferrite join from the aluminate apex.

$$X'_{Usp} = \frac{X_{Usp}}{X_{Usp} + X_{Mag}} = \frac{[Ti^{4+}]}{[Ti^{4+}] + \frac{[Fe^{3+}]}{2}} \tag{6.5}$$

The projection of the Ilm_{ss} compositions can be illustrated in a tetrahedron with the four Ilm_{ss} endmember components at its apices (Fig. 6.9). The composition of a Mg-Al-bearing Ilm_{ss} is projected onto the plane $Fe_2O_3 - FeTiO_3 - MgTiO_3$ from the opposite Al_2O_3 apex and subsequently onto the $Fe_2O_3 - FeTiO_3$ binary from the $MgTiO_3$ apex. The order of projection from Al_2O_3 or $MgTiO_3$ is arbitrary. X'_{Ilm} can be derived according to equation 6.6 from the cation numbers pfu.

$$X'_{Ilm} = \frac{X_{Ilm}}{X_{Ilm} + X_{Hem}} = \frac{[Fe^{2+}]}{[Fe^{2+}] + \frac{[Fe^{3+}]}{2}} \tag{6.6}$$

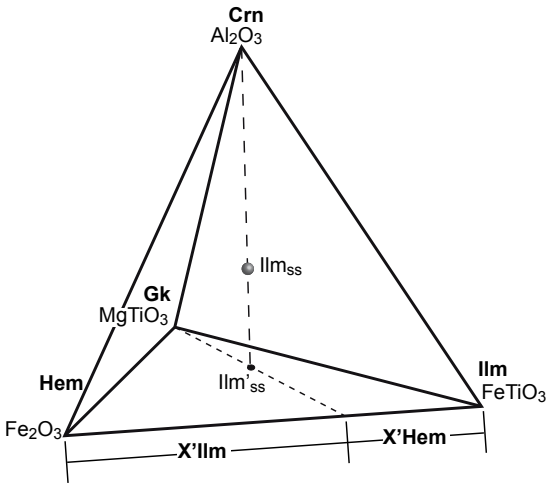

Fig. 6.9 Schematic illustration of the projection of Ilm_{ss} composition onto the Hem-Ilm binary in the tetrahedron $Al_2O_3 - Fe_2O_3 - FeTiO_3 - MgTiO_3$. The dashed lines represent projection lines of the Mg-Al bearing Ilm_{ss} composition (sphere) onto a face of the tetrahedron (circle, Ilm'_{ss}) and finally on the Fe-Ti binary.

6.4.3 Comparison of the projection schemes

The projection schemes available in literature (Carmichael, 1967; Anderson, 1968; Stormer, 1983), the calculation schemes within the thermo-oxybarometric formulations, and the calculation scheme presented within the present study, yield broadly different values for X'_{Usp} and X'_{Ilm}. This has already been shown by Stormer (1983, Tab. 1) and is exemplified for two samples from the present study (Table 6.4). X'_{Usp} and X'_{Ilm} have been calculated with equations 6.5 and 6.6, and with the Stormer (1983) and QUILF projections (Andersen & Lindsley, 1988; Andersen *et al.*, 1993, see also Fig. 6.15).

X'_{Ilm} derived with the Stormer (1983) projection and the projection according to equation 6.6 for the experimental Ilm_{ss} data provided within this study are in good agreement or only slightly deviate (Fig. 6.10b). For Tmt, the observed deviations are larger. Especially for the system Fe-Ti-Al-O, the Stormer (1983) projection yields significantly higher X'_{Usp} than equation 6.5. These deviations can be explained by comparing equations 6.5 and 6.6 to the equations provided by Stormer (1983, equation 6.7 for Tmt, equation 6.8 for Ilm_{ss}).

$$X'_{Usp} = \frac{[Ti] * \frac{[Fe^{2+}]}{[M^{2+}]}}{0.5\,[Fe^{3+}] * \frac{[Fe^{3+}]}{[M^{3+}]} + [Ti] * \frac{[Fe^{2+}]}{[M^{2+}]}} \tag{6.7}$$

Table 6.4 Comparison of projections, exemplarily for two Al±Mg bearing samples from the present study.

	6IT70M1A1x6a		6F59.5A5.5x34a	
EMP [wt%]	Tmt	Ilm_{ss}	Tmt	Ilm_{ss}
$Fe_{tot}O$	68.45	51.81	62.14	47.19
TiO_2	27.38	44.91	32.04	51.59
Al_2O_3	1.13	0.39	5.97	1.24
MgO	1.04	0.89	0.00	0.01
Total	98.09	98.05	100.23	100.08
	X'_{Usp}	X'_{Ilm}	X'_{Usp}	X'_{Ilm}
this study	0.785	0.856	0.996	0.991
Stormer (1983)	0.663	0.859	1.000	0.991
QUILF[1]	0.784	0.857	0.996	0.991
	NTi	1-Xhem	NTi	1-Xhem
QUILF[2]	0.765	0.862	0.870	0.991

1) Values for geothermometry as given in QUILF
2) NTi and 1-Xhem, which are used for QUILF calculation

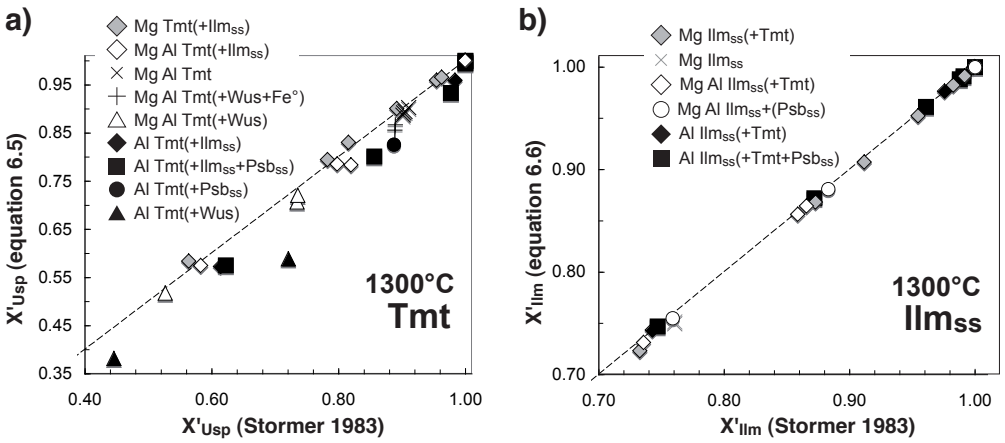

Fig. 6.10 Comparison between a) X'_{Usp} and b) X'_{Ilm}, derived with equations 6.5, 6.6, versus Stormer (1983) projection, both applied to the experimental data provided in this chapter (appendix A.3, Table A.18). Systems Fe-Ti-Mg-O (Mg, grey symbols), Fe-Ti-Al-O (Al, black symbols) and Fe-Ti-Mg-Al-O (Mg Al, empty symbols) at 1300 °C. Dashed lines represent X(Stormer)=X(equations 6.5, 6.6).

$$X'_{Ilm} = \frac{\sqrt{[Fe^{2+}] * [Ti]}}{0.5\,[Fe^{3+}] + \sqrt{[Fe^{2+}] * [Ti]}} \tag{6.8}$$

The Stormer (1983) equation for Tmt deviates from equation 6.5 by the factors Fe^{2+}/M^{2+} and Fe^{3+}/M^{3+}, which in the simple system Fe-Ti-O are 1 (and equation 6.7 can be simplified to equation 6.5). For the present purpose, only Mg^{2+} and Al^{3+} have to be considered and equation 6.7 can be modified to equation 6.9.

$$X'_{Usp} = \frac{[Ti] * \frac{[Fe^{2+}]}{[Fe^{2+}]+[Mg^{2+}]}}{0.5\,[Fe^{3+}] * \frac{[Fe^{3+}]}{[Fe^{3+}]+[Al^{3+}]} + [Ti] * \frac{[Fe^{2+}]}{[Fe^{2+}]+[Mg^{2+}]}} \tag{6.9}$$

For Mg bearing compositions, X'_{Usp}(Stormer)<X'_{Usp}(equation 6.5). In contrast, in the system Fe-Ti-Al-O, X'_{Usp}(Stormer) becomes larger than X'_{Usp}(equation 6.5). When both Al and Mg are present, the relative amounts of both cations determine the deviation of X'_{Usp}(Stormer) from X'_{Usp}(equation 6.5). The relatively high Al contents of Tmt in some samples explain the significant deviations between the re-calculation schemes (Fig. 6.10a).

For the system Fe-Ti-Al-Mg-O, the Stormer (1983) equation for ilmenite$_{ss}$ can be transformed to equation 6.10.

$$X'_{Ilm} = \frac{[Fe^{2+}] * \sqrt{\frac{[Fe^{2+}]}{[Fe^{2+}]+[Mg^{2+}]}}}{0.5\,[Fe^{3+}] + [Fe^{2+}] * \sqrt{\frac{[Fe^{2+}]}{[Fe^{2+}]+[Mg^{2+}]}}} \tag{6.10}$$

In Mg-free systems (Fe-Ti-O, Fe-Ti-Al-O), $Fe^{2+}/(Fe^{2+}+Mg^{2+})$=1 and equation 6.10 equals equation 6.6. In Mg-bearing systems within this study the amounts of Mg^{2+} are usually small and thus $Fe^{2+}/(Fe^{2+}+Mg^{2+})$ is close to - but smaller than - one. Therefore, at low Mg^{2+} contents, there are only slight deviations between the calculation schemes.

6.4.4 Comparison of X'_{Usp} and X'_{Ilm} derived with equations 6.5 and 6.6, with the data from the simple system Fe-Ti-O and with the existing thermodynamic thermo-oxybarometer models

For the majority of samples in the system Fe-Ti±Mg±Al-O there is reasonable agreement between X'_{Usp} and X'_{Ilm} (derived with equations 6.5 and 6.6), and X_{Usp},

X_{Ilm} derived from our experimental data in the system Fe-Ti-O. For a given oxygen fugacity, X'_{Usp} is in agreement with X_{Usp} within ± 0.03, X'_{Ilm} and X_{Ilm} agree within ± 0.02 (Fig. 6.11). In most cases, X'_{Usp} and X'_{Ilm} for Mg-Al bearing systems are slightly higher compared to those in the simple system. This deviation is especially pronounced for one data point at 1100 °C and NNO$\approx$ +0.5.

Comparing data in the Fe-Ti$\pm$Mg$\pm$Al-O system and those in the simple system Fe-Ti-O, we have to be aware of the strong influence of the projection scheme. For example, for the system Fe-Ti-Al-O, the use of the Stormer (1983) projection scheme would lead to higher X'_{Usp} and thus enhance the deviation between the data in the Mg-Al bearing systems and the system Fe-Ti-O.

At low fO_2 (<NNO-3) and high T, Fe-Mg data deviate towards lower X'_{Usp} and X'_{Ilm}. As an artefact of the calculations, equations 6.5 and 6.6 cannot yield $X'_{Usp}>1$ and $X'_{Ilm}>1$. The calculation of X_{Usp} and X_{Ilm} for simple system Fe-Ti-O data however (equations 6.2, 6.1), can very well give values greater than 1 (which are probably related to non-stoichiometry, see chapters 1, 4).

In a Roozeboom diagram (X'_{Ilm} vs. X'_{Usp}) a comparison of the projected Mg-Al bearing data with the isotherms derived from the simple system Fe-Ti-O data shows good agreement for most data points (Fig. 6.12). At $X'_{Usp}>0.8$, 1300 °C data in the system Fe-Ti-Mg-O shows an offset compared to the Fe-Ti-O isotherm (towards increased X'_{Ilm} or decreased X'_{Usp}). This may also be true for 1200 °C and 1100 °C, however at these temperatures we have not enough data points at high X_{Usp} to draw a safe conclusion.

Summarised, the Mg-Al bearing data is in reasonable agreement with isotherms derived for the simple system Fe-Ti-O in both Roozeboom diagrams and diagrams of ΔNNO vs. phase composition. Consequently, our experimental data in the Fe-Ti-Mg-Al-O system also deviate significantly from the isotherms predicted by the thermo-oxybarometer models of Ghiorso & Sack (1991) and Andersen & Lindsley (1988, QUILF). In a diagram ΔNNO versus X'_{Usp} (or X_{Usp}) our Tmt data points for the system Fe-Ti-O plot at higher X_{Usp} than the model of Ghiorso & Sack (1991). At 1300 °C they also plot at higher X_{Usp} than the QUILF model. For Mg-Al bearing Tmt projected with equations 6.5 and 6.6, the deviation to the models is even larger (see above).

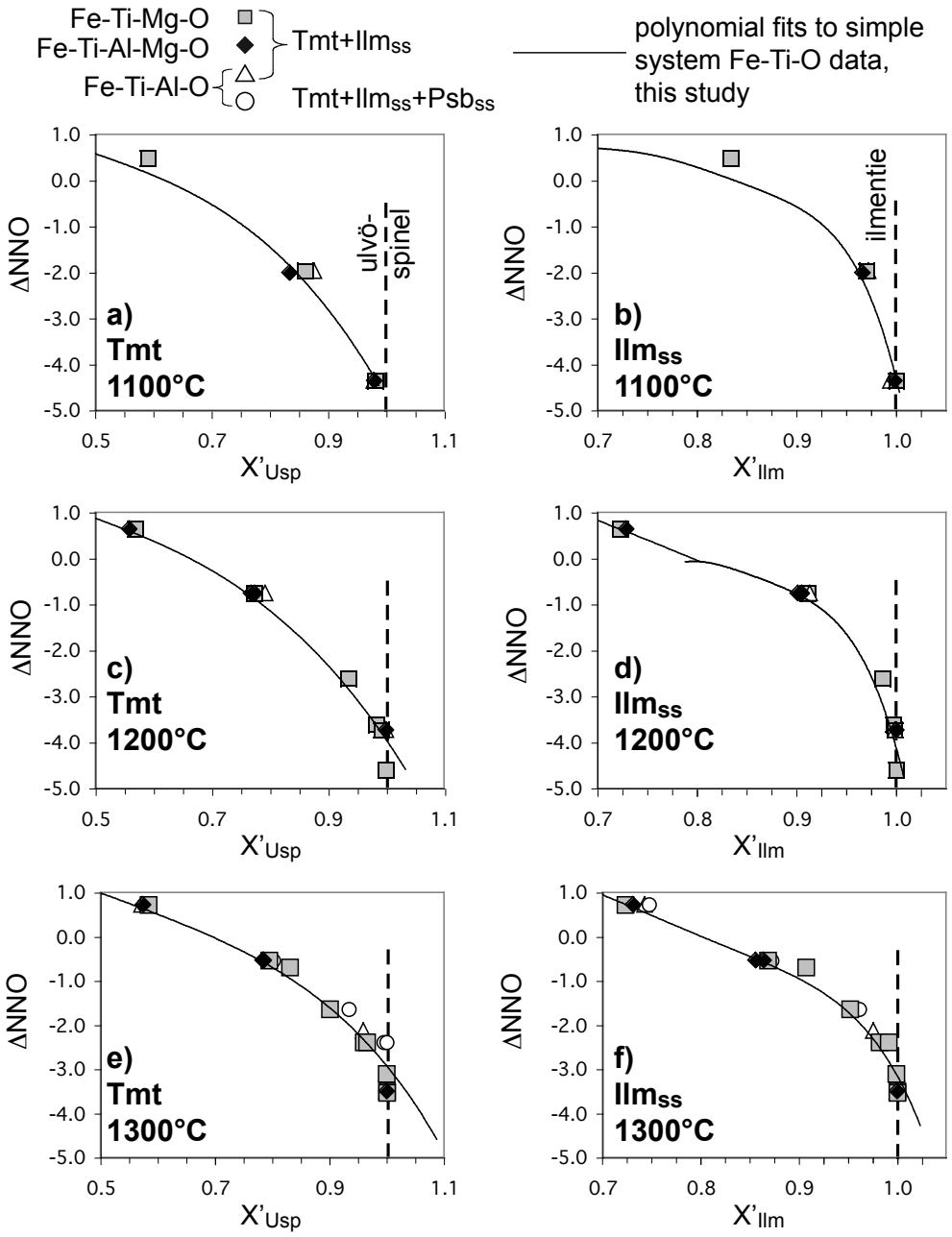

Fig. 6.11 Compositional variations of coexisting Tmt (diagrams on the left) and Ilm_{ss} (right) as a function of oxygen fugacity (in term of ΔNNO) at a), b) 1100 °C, c), d) 1200 °C, and e), f) 1300 °C in the systems Fe-Ti-Mg-O (grey filled symbols), Fe-Ti-Al-Mg-O (black filled symbols), and Fe-Ti-Al-O (empty symbols). X'_{Usp} and X'_{Ilm} were derived by equations 6.5 and 6.6. Solid black lines represent polynomial fits to this study's experimental Fe-Ti-O data. Vertical dashed lines indicate ulvöspinel and ilmenite endmember compositions.

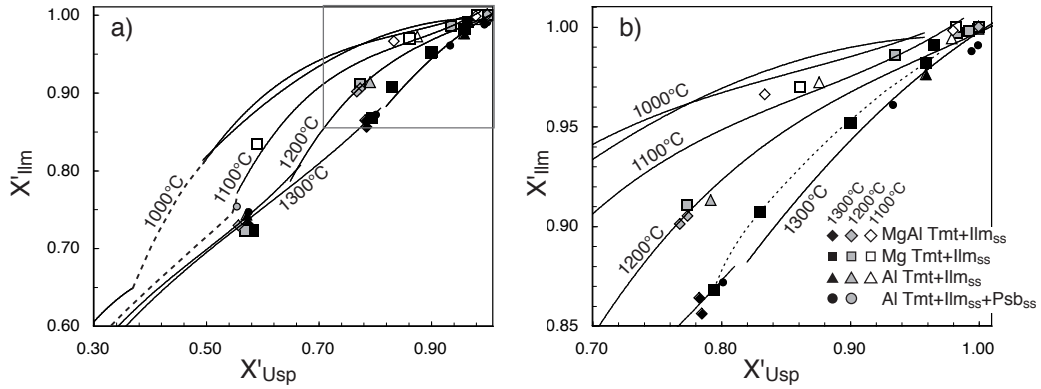

Fig. 6.12 Roozeboom plot of X'_{Ilm} versus X'_{Usp}. a) Solid lines represent isotherms derived from the simple system Fe-Ti-O data (3rd order fits, 2nd and 3rd order fits for 1000 °C at high X_{Usp}). Dashed lines are graphical interpolations between the fit curves. Symbols represent the Mg-Al data for different systems and parageneses, and temperatures (black filled symbols: 1300 °C, grey filled symbols: 1200 °C, empty symbols: 1100 °C). X'_{Usp} and X'_{Ilm} have been derived according to equations 6.5 and 6.6. b) Enlargement for high X'_{Usp} and X'_{Ilm} (rectangle in picture (a)). Dotted line connects 1300 °C Fe-Ti-Mg-O data at $X'_{Usp} \geq 0.8$.

6.5 Non-stoichiometry in Mg-Al bearing Tmt - results from annealing experiments

According to the experimental procedure described in chapter 2, three Mg±Al bearing samples have been annealed under oxygen conserving conditions at 950 °C. These samples were first equilibrated at 1300 °C and NNO-0.5 and consisted of Tmt+Ilm_{ss} assemblages (Table 6.5).

Table 6.5 Annealed Mg-Al bearing Tmt+Ilm_{ss} assemblages.

sample	6IT60M2x6aD	6IT70M1A1x6aD	6IT60M1A1x6aD
system	Fe-Ti-Mg-O	Fe-Ti-Al-Mg-O	Fe-Ti-Al-Mg-O
ΔNNO (synthesis)	-0.5	-0.5	-0.5
assemblage	Tmt+Ilm_{ss}	Tmt+Ilm_{ss}	Tmt+Ilm_{ss}
bulk Ti/(Ti+Fe) [at%]	40	30	40
X'_{Usp} (synthesis)	0.794	0.785	0.783

After annealing, the samples display frequent Ilm_{ss} lamellae in Tmt, but also Tmt lamellae and rims in or around Ilm_{ss} (Fig. 6.13). However, the Tmt exsolution features are less common than Ilm_{ss} exsolution features. Image analysis reveals that the modal proportion of $ilmenite_{ss}$ significantly increases during annealing, which points to significant amounts of cation vacancies in the original high-T Mg±Al bearing Tmt (cf. Table 6.7).

The formation of Tmt exsolution lamellae in Ilm_{ss} may be related to the significant decrease of the Al content of Ilm_{ss} during annealing. The Al content of Tmt increases (Table 6.6) during annealing. It may be suggested that Tmt forms at the place where Al is released from Ilm_{ss} upon annealing.

Table 6.6 MgO contents (upper part of the table) and Al_2O_3 contents (lower part) in wt% in high-T (left) and annealed (right) Tmt and coexisting Ilm_{ss}

	MgO content [wt%]			
	high-T		annealed	
sample	Tmt^{HT}	Ilm_{ss}^{HT}	Tmt^{A}	Ilm_{ss}^{A}
6IT60M2x6aD	2.08	2.00	1.47	2.19
6IT70M1A1x6aD	1.04	0.89	0.92	1.31
6IT60M1A1x6aD	1.09	0.94	0.76	1.06
	Al_2O_3 content [wt%]			
6IT60M2x6aD	-	-	-	-
6IT70M1A1x6aD	1.13	0.39	1.22	0.00
6IT60M1A1x6aD	1.97	0.64	3.17	0.10

The vacancy concentration (δ) in the high-T (1300 °C) Tmts was estimated from the change of modal proportions upon annealing (see Table 6.7), according to method A (chapter 5). The results point to slightly higher vacancy concentrations than in the simple system Fe-Ti-O. Especially the high temperature Tmt with the highest Al content shows high δ ($\delta * 10^2 = 7.8$, i.e. 2.6 cat%, at moderate X'$_{Usp}$). This suggests that Al in Tmt promotes the formation of cation vacancies in Tmt.

Table 6.7 δ of high-T Tmt, calculated according to method A, and modal proportions of Tmt and Ilm$_{ss}$ in high-T and annealed samples.

sample	high-T Tmt $\delta * 10^2$		modal proportions M [vol%] high-T run product		annealed sample	
	mean	Δ^1	Tmt^{HT}	Ilm_{ss}^{HT}	Tmt^{A}	Ilm_{ss}^{A}
6IT60M2x6aD	4.1	9.5	31.9	68.1	28.4	71.6
6IT70M1A1x6aD	4.3	3.2	79.3	20.7	71.7	28.3
6IT60M1A1x6aD	7.8	11.9	24.5	75.5	19.3	80.7

1) uncertainty on $\delta * 10^2$, calculated by error propagation

To calculate δ from the shift of phase compositions during annealing according to method B (chapter 5), the calculation has to be carried out in a three- or four dimensional system (due the increased number of components). However, whereas two non-parallel lines have always an intersecting point in two dimensions, they may be skew in three (or more) dimensions and no intersecting point can be determined. This was the case for the annealed Mg(+Al) bearing samples, probably due to the underestimation of MgO content by electron microprobe (chapter 2). Consequently, method B (chapter 5) could not be used for Mg-Al bearing annealed samples.

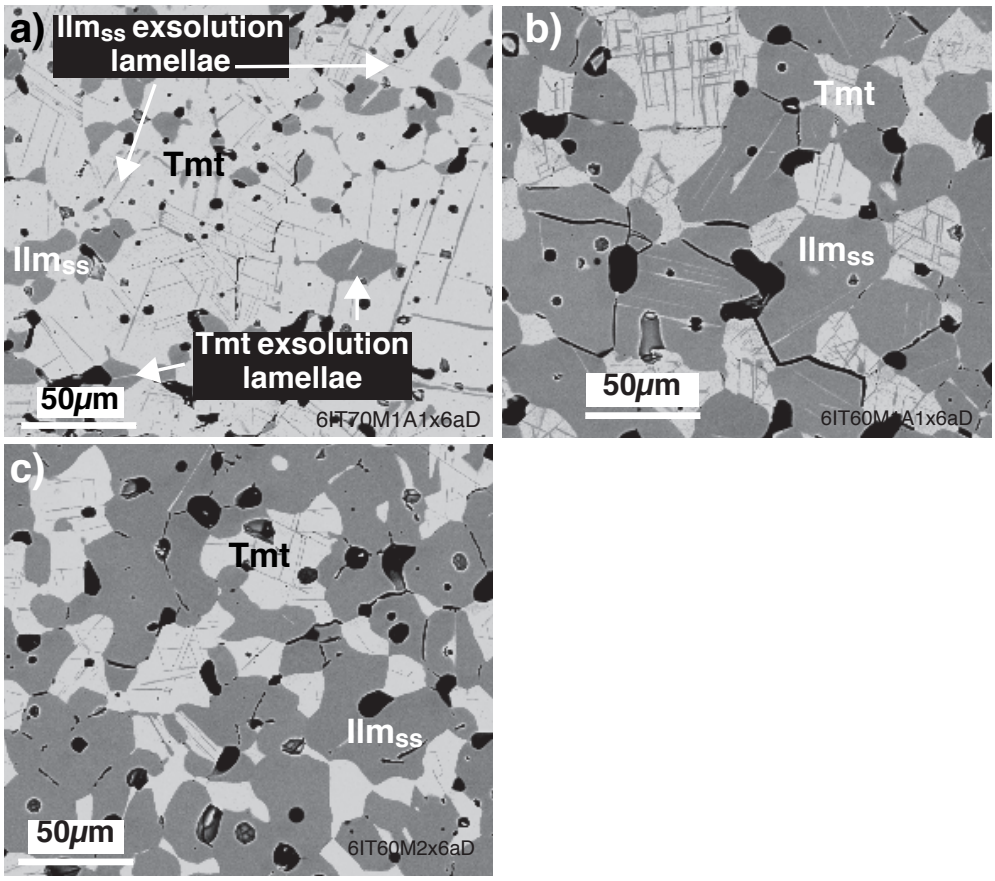

Fig. 6.13 BSE pictures of annealed samples a) 6IT70M1A1x6aD, b) 6IT60M1A1x6aD, and c) 6IT60M2x6aD, displaying frequent Ilm_{ss} lamellae in Tmt and also few Tmt lamellae in Ilm_{ss}.

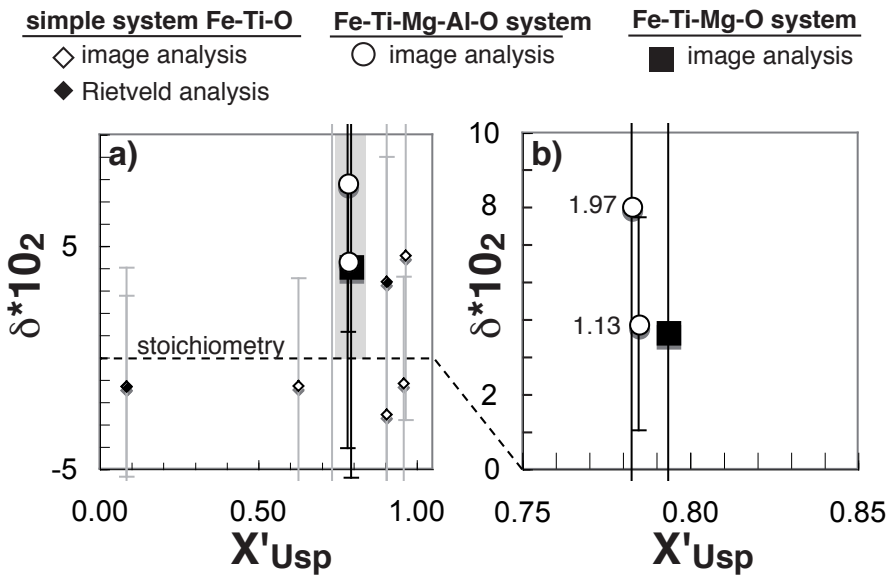

Fig. 6.14 a) δ in 1300°C synthesis Tmt as a function of X'_{Usp} as calculated from the increase of Ilm_{ss} proportion during annealing (Table 6.7, calculated after method A, chapter 5). For the simple system (small circles) the increase of Ilm_{ss} proportion is derived from image analysis (empty rhombs) or Rietveld analysis (filled rhombs). Large symbols represent data points from systems Fe-Ti-Mg-O (black square) and Fe-Ti-Mg-Al-O (empty circles), both derived from image analysis. b) Enlargement of the shaded area in picture (a). Numbers next to data points give the Al_2O_3 content in wt%.

6.6 Discussion and conclusion

Test of a provisional version of the Tmt-Ilm$_{ss}$ thermo-oxybarometer Fig. 6.15 provides a comparison of the Toplis & Carroll (1995) data projected with different schemes (QUILF, Stormer, 1983, equations 6.5 and 6.6) to the isotherms derived from the experimental Fe-Ti-O data (chapter 4). The latter are in reasonable agreement with this study's experimental Mg-Al data.

Equilibration temperature and oxygen fugacity of Tmt+Ilm$_{ss}$ assemblages can be graphically estimated from X'$_{Usp}$ and X'$_{Ilm}$ based on Fig. 6.15 and Fig. 6.16. At first, the temperature is estimated from the isotherm spacing in the Roozeboom diagram (Fig. 6.15). The oxygen fugacity is subsequently estimated using the isotherms in the ΔNNO vs. X'$_{Usp}$ or X'$_{Ilm}$ diagrams (Fig. 6.16).

Applied to the data by Toplis & Carroll (1995), the QUILF projection yields temperature estimates which are clearly too low compared to the experimental temperatures (Fig. 6.15). In contrast, the Stormer (1983) projection scheme gives higher X'$_{Usp}$ and in most cases slightly overestimated temperatures. For the projection according to equations 6.5, 6.6, estimated and experimental temperatures are usually in good agreement ($\Delta T < 50\,^{\circ}C$, Table 6.8). Estimated and experimental fO_2 agree within ≤ 0.5 log units (for most samples even ≤ 0.2). fO_2 estimated based on X'$_{Usp}$ and X'$_{Ilm}$ (Fig. 6.16a or b) are in agreement within <0.2 log units.

Compared to the estimates derived with the models by Andersen & Lindsley (1988) and Ghiorso & Sack (1991), our graphical estimation brings a significant improvement, especially concerning the temperature estimates (Fig. 6.17). While the thermodynamic models - in particular the QUILF model - yielded temperatures which were up to 150 °C too low, temperatures read off from Fig. 6.15 agree with the experimental T within $\leq 50\,^{\circ}C$.

The most significant improvement of the T-fO_2 estimates was achieved for the data points at NNO$\leq$ -1.5. While both thermodynamic models yielded much too low temperatures (up to 150 °C) and also too low oxygen fugacity (up to 0.5 log units), experimental conditions, and T and fO_2 estimated graphically within this study are in very good agreement. For the data points at NNO-1 to -0.5 the temperature estimates are only slightly improved compared to the model by Ghiorso & Sack (1991). The poorest agreement is found for two data points at NNO+0.2 and -1.0 for both T and fO_2 (Fig. 6.17).

Consideration of non-stoichiometry In chapter 5 we have stressed that non-stoichiometry of Tmt should be considered for the thermo-oxybarometer modelling, though Tmt is probably stoichiometric at naturally relevant temperatures. Investigations on selected Mg-Al bearing Tmt+Ilm$_{ss}$ samples indicate > 2 cat% vacancies in

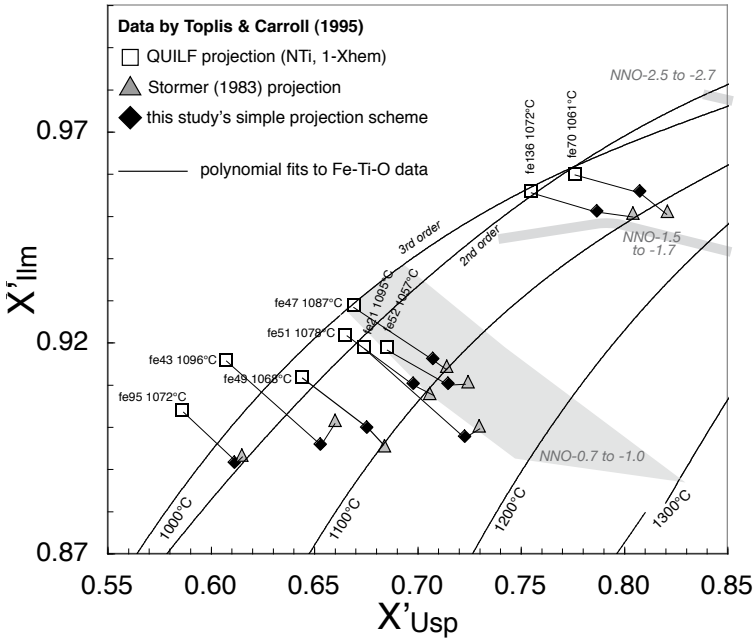

Fig. 6.15 Roozeboom plot of X'_{Ilm} versus X'_{Usp}. Symbols represent experimental data by Toplis & Carroll (1995), projected with the QUILF software package (empty squares), the Stormer (1983) projection (grey triangles), and according to equations 6.5, 6.6 (black diamonds). Projected compositions of the same sample are connected by thin lines. Labels next to the data points comprise sample number and experimental temperature. The curves represent the isotherms derived from experimental Fe-Ti-O data (this study). Note that the 1000 °C data can be fitted by a 2nd or a 3rd order polynomial. The shaded regions are based on the experimental data in the system Fe-Ti-O and connect compositions of identical or similar ΔNNO between the different temperature series.

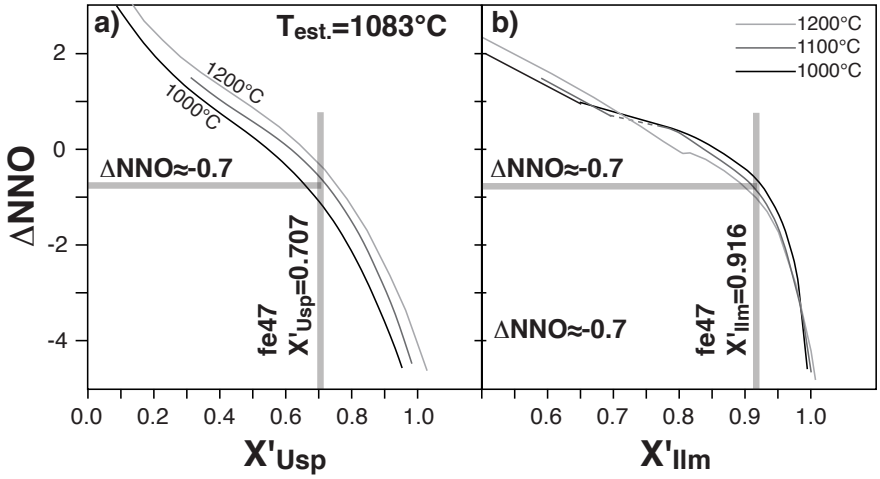

Fig. 6.16 Graphical estimation of oxygen fugacity (expressed as ΔNNO) on the basis of ΔNNO vs. a) X'_{Usp} or b) X'_{Ilm} diagrams. Solid lines are experimental isotherms at 1000 °C (black), 1100 °C (dark grey) and 1200 °C (medium grey). Grey vertical bars mark X'_{Usp} and X'_{Ilm} of an exemplary sample by Toplis & Carroll (1995, sample fe 47). Horizontal bars mark estimated oxygen fugacities.

Table 6.8 Data by Toplis & Carroll (1995): X'_{Usp} and X'_{Ilm} derived with equations 6.5 and 6.6, and comparison of experimental and estimated temperature and oxygen fugacity.

sample name	X'_{Usp} equation 6.5	X'_{Ilm} equation 6.6	equilibration conditions				
			experimental, TC95[1]		estimated[2]		
			T[°C]	ΔNNO	T[°C][3]	T[°C][4]	ΔNNO
fe 95	0.611	0.892	1072	0.2	1020	993	-0.3
fe 43	0.653	0.896	1096	-0.8	1060	1048	-0.4
fe 21	0.723	0.898	1095	-1.0	1147	-[5]	-0.6
fe 47	0.707	0.916	1087	-0.8	1083	1077	-0.7
fe 51	0.698	0.910	1078	-0.7	1087	1082	-0.7
fe 49	0.675	0.900	1068	-0.7	1081	1075	-0.5
fe 52	0.715	0.910	1057	-0.8	1110	-[5]	-0.6
fe 136	0.787	0.951	1072	-1.5	1067	1067	-1.5
fe 70	0.808	0.956	1061	-1.8	1067	1075	-1.7

1) TC95: Toplis & Carroll (1995)
2) estimated according to Fig. 6.15 and Fig. 6.16.
3) based on 3rd order fit for experimental 1000 °C isotherm
4) based on 2nd order fit for experimental 1000 °C isotherm
5) T estimate according to spacing between 1100 °C and 1200 °C isotherms, fit to 1000 °C data not considered

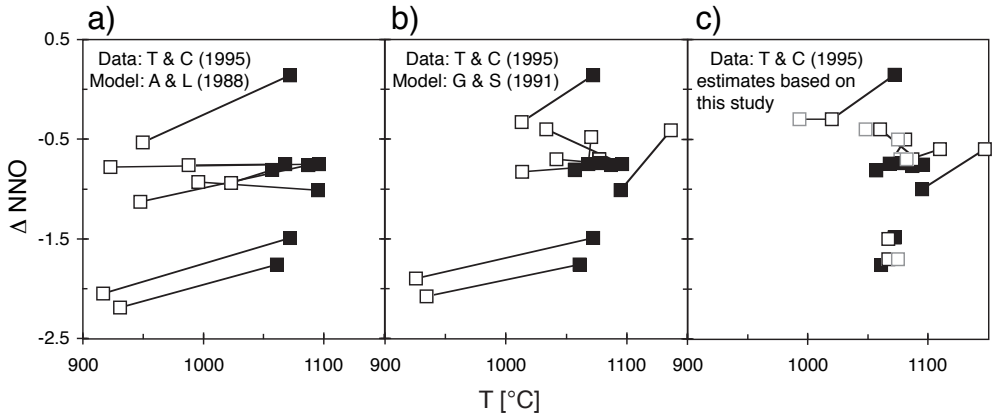

Fig. 6.17 Comparison of experimental (filled symbols) and calculated values (open symbols) of temperature and oxygen fugacity (expressed as ΔNNO) for Tmt-Ilm_{ss} parageneses synthesised by Toplis & Carroll (1995). a) Values calculated from the QUILF model, b) values calculated from the model by Ghiorso & Sack (1991), and c) values estimated from Fig. 6.15 (3rd order fits of isotherms: black open squares, 2nd order fit of 1000 °C isotherm: grey open squares) and Fig. 6.16.

Tmt at intermediate X'_{Usp}. This suggests that the presence of Mg and particularly Al might result in higher vacancy concentrations than in the simple system Fe-Ti-O. Therefore, for solid solution models that involve additional elements like Mg and Al, it becomes even more important to account for Tmt non-stoichiometry.

7 Outlook

Within the frame of this study, a large data set on equilibrium Fe-Ti distribution between Fe-Ti oxide minerals has been provided, mainly in the system Fe-Ti-O, but also in the systems Fe-Ti-Mg-O, Fe-Ti-Al-O and Fe-Ti-Mg-Al-O, at 1 bar pressure, $1000-1300\,^{\circ}$C, and a large range of oxygen fugacities (NNO-5 to NNO+5). Together with data by Evans *et al.* (in press) for $800-900\,^{\circ}$C, our results provide the basis for a re-calibration of the Tmt+Ilm_{ss} thermo-oxybarometer by Mark S. Ghiorso (Seattle).

The experimental data provided here represent an extensive enlargement of the pre-existing dataset towards high temperatures and over a larger range of oxygen fugacities. For the system Fe-Ti-O, new experimental isotherms have been determined, which for both titanomagnetite (Tmt) and ilmenite-hematite solid solution (Ilm_{ss}) deviate from those retrieved from the thermo-oxybarometer models of Andersen & Lindsley (1988) and Ghiorso & Sack (1991).

In Roozeboom or ΔNNO-composition diagrams, the experimental isotherms display pronounced discontinuities at X_{Ilm} values marking the transition from the $R\bar{3}$ to the $R\bar{3}c$ structure in the ilmenite-hematite solid solution (Harrison *et al.*, 2000). As the thermo-oxybarometer models of Andersen & Lindsley (1988) and Ghiorso & Sack (1991) do not adequately account for this transition, experimental and model isotherms strongly deviate.

Tmt compositions are generally Ti-richer than predicted from the models. At high fO_2 this is probably related to errors in the standard state properties used for the Tmt endmember. At low fO_2 and high T, the discrepancies between the compositions of synthetic Tmt and those calculated with the models are especially pronounced, and probably reflect the non-stoichiometry of these titanomagnetites.

Compositions of Mg-Al bearing Tmt+Ilm_{ss} have been projected to the Hem-Ilm and Mag-Usp binaries. The data for Mg-Al bearing phases are in reasonable agreement with the isotherms in the system Fe-Ti-O.

On the basis of the new experimental isotherms, we have established a preliminary, graphical version of the Fe-Ti oxide thermo-oxybarometer. We have tested this preliminary version with the data of Toplis & Carroll (1995), i.e. by using the compositions of their synthetic Mg and Al-bearing Tmt and Ilm_{ss} equilibrated at known T-fO_2 conditions. Our T-fO_2 estimates agree with experimental values

within $< 50\,^{\circ}$C and <0.5 log units. This represents a significant improvement compared to the estimates with the previous thermo-oxybarometer models (ΔT up to 170 °C, $\Delta f O_2$ up to 0.7 log units), especially regarding temperature.

Our new data set for Mg-Al bearing Tmt+Ilm_{ss} assemblages is restricted to intermediate and low oxygen fugacities, and at 1100 °C only few data points are available. For a more accurate description of the experimental isotherms more experimental data at high oxygen fugacities (>NNO+1) and low temperatures (1000 and 1100 °C) should prove useful.

As stated above, for Tmt the major discrepancy between the existent thermo-oxybarometer models and our experimental data is observed at low fO_2 and high T and is probably related to Tmt non-stoichiometry. We have investigated Tmt non-stoichiometry in the simple system Fe-Ti-O and for three selected samples in the systems Fe-Ti-Mg-O and Fe-Ti-Mg-Al-O at 1100 °C to 1300 °C. The investigations were focussed on Ti-rich Tmt (X_{Usp}>0.7), although some data were also obtained for X_{Usp}<0.7. The results show that Tmt is close to stoichiometry at T$\leq$ 1100 °C over the complete solid solution series. At T$\geq$ 1200 °C and X_{Usp}>0.7 Tmt non-stoichiometry increases with increasing T and X_{Usp} to about 2 cat% at 1300 °C, and 1 cat% at 1200 °C, both for compositions near the ulvöspinel endmember. For the system Fe-Ti-Mg$\pm$Al-O, our results suggest that the presence of Al in Tmt might favour the formation of cation vacancies.

The results on Tmt non-stoichiometry obtained in the present study show discrepancies to some literature data. In particular, whereas we found no clear indication for non-stoichiometry at X_{Usp}<0.7, Aggarwal & Dieckmann (2002) reported significant vacancy concentration (about 0.7 cat% at 1300 °C) at $X_{Usp}\leq$ 0.6, and Senderov *et al.* (1993) also suggested significant non-stoichiometry at X_{Usp}<0.7. Careful EMP oxygen analyses and thermogravimetric measurements with long equilibration times may help to resolve the existing contradictions. Such examinations in the system Fe-Ti-Mg-Al-O should also cover Ti-poor Tmts, as only relatively few data points are up to now available for X_{Usp}<0.7.

As magmatic crystallisation temperatures for Tmt in terrestrial basic rocks rarely exceed 1100 °C, significant vacancy concentrations are not expected in basaltic Tmt. Yet, the non-stoichiometry in the synthetic high-temperature Tmt used to calibrate the solid solution model has to be accounted for.

In the course of this study, the textures of the synthetic Fe-Ti oxides have been examined carefully and evaluated with respect of their meaning for the attainment of equilibrium, the processes taking place during synthesis, and their kinetics. The

synthetic run products essentially consist of polycrystalline, equigranular aggregates with idiomorphic, homogeneous and evenly distributed grains, which suggests that they reflect or at least are close to an equilibrium state.

Many of the synthetic run products produced from binary starting mixtures (Fe_2O_3+TiO_2 or Fe°+TiO_2 mixtures) display concentric features. Single-phase Tmt samples display concentric compositional zoning. In binary run products concentric variations in the modal proportions are common, in particular monomineralic rims at the sample surface. If the starting material contained metallic iron, the run products show a decrease of Ti/(Ti+Fe) towards the pellet surface. If the starting mixture contained Fe_2O_3, the run products have increasing Ti/(Ti+Fe) towards the pellet surface. Samples synthesised from *ternary* Fe_2O_3+Fe°+TiO_2 mixtures in gas mixing or solid-state buffer experiments do not show a pronounced rim formation.

The different behaviour of Fe_2O_3+TiO_2 and Fe°+TiO_2 mixtures is probably related to their different original oxygen contents, which lead to different redox processes during the synthesis of the Fe-Ti oxide assemblages (oxidation of the Fe°+TiO_2 starting mixtures but reduction of the Fe_2O_3+TiO_2 mixtures). The formation of the concentric features involves significant element migration of both Fe and Ti. However, we could not fully resolve the mechanisms responsible for the formation of concentric textures and inhomogeneities, especially regarding Fe_2O_3+TiO_2 mixtures. Time-dependent experiments may shed more light on these mechanisms.

The textural investigations also revealed that the Fe-Ti oxide samples are very sensitive to oxidation. Exposure of a reduced assemblage to a high oxygen fugacity at high temperature during only few seconds produces oxy-exsolution features, which may extend several tens of micrometers into the pellet. Although oxy-exsolution affects the phase compositions only near the surface of the pellet, it changes the bulk oxygen content of the sample. Because Fe-Ti oxide phases are so sensitive to oxidation, quenching as well as any measurement at elevated temperature must be performed in controlled atmosphere.

Bibliography

Aggarwal S, Dieckmann R (2002) Point defects and cation tracer diffusion in $(Ti_xFe_{1-x})_{3-\delta}O_4$. I. Non-stoichiometry and point defects. *Physics and Chemistry of Minerals* 29: 695–706

van Aken PA (2002) Elektronen-Energieverlust-Spektroskopie in den Geomaterialwissenschaften: Prinzip, Methodik und Anwendung. In: Rosendahl W, Hoppe A (eds.) *Angewandte Geowissenschaften in Darmstadt*, vol. 15 of *Schriftenreihe der Deutschen Geologischen Gesellschaft*, 245–266, Deutsche Geologische Gesellschaft, Hannover

van Aken PA, Liebscher B (2002) Quantification of ferrous/ferric ratios in minerals: new evaluation schemes of Fe L_{23} electron energy-loss near-edge spectra. *Physics and Chemistry of Minerals* 29: 188–200

van Aken PA, Liebscher B, Styrsa VJ (1998) Quantitative determination of iron oxidation states in minerals using Fe $L_{2,3}$-edge electron energy-loss near-edge structure spectroscopy. *Physics and Chemistry of Minerals* 25: 323–327

Akimoto S (1954) Thermo-magnetic study of ferromagnetic minerals contained in igneous rocks. *Journal of Geomagnetism and Geoelectricity* 6: 1–14

Akimoto S (1962) Magnetic properties of $FeO - Fe_2O_3 - TiO_2$ system as a basis of rock magnetism. *Journal of the Physical Scociety of Japan* 17: 706–710

Akimoto S, Katsura T, Yoshida M (1958) Magnetic properties of $TiFe_2O_4 - Fe_3O_4$ system and their change with oxidation. *Journal of Geomagnetism and Geoelectricity* 9: 165–178

Allan JEM, Coey JMD, Sanders IS, Schwertmann U, Friedrich G, Wiechowski A (1989) An occurrence of a fully-oxidized natural titanomaghemite in basalt. *Mineralogical Magazine* 53: 299–304

Andersen DJ, Lindsley DH (1988) Internally consistent solution models for Fe-Mg-Mn-Ti oxides: Fe-Ti oxides. *American Mineralogist* 73: 714–726

Andersen DJ, Bishop FC, Lindsley DH (1991) Internally consistent solution models for Fe-Mg-Mn-Ti oxides: Fe-Mg-Ti oxides and olivine. *American Mineralogist* 76: 427–444

Andersen DJ, Lindsley DH, Davidson PM (1993) QUILF: A Pascal program to assess equilibria among Fe-Mg-Mn-Ti oxides, pyroxene, olivine, and quartz. *Computers and Geosciences* 19: 1333–1350

Anderson AT (1968) Oxidation of the LaBlache Lake titaniferous magnetite deposit, Quebec. *Journal of Geology* 76: 528–547

Anovitz LM, Treimann AH, Essene EJ, Hemingway BS (1985) The heat-capacity of ilmenite and phase equilibria in the system Fe-Ti-O. *Geochimica et Cosmochimica Acta* 49: 2027–2040

Aragón R, McCallister RH (1982) Phase and point defect equilibria in the titanomagnetite solid solutions. *Physics and Chemistry of Minerals* 8: 112–120

Banerjee SK (1991) Magnetic properties of Fe-Ti oxides. In: Lindsley DH (ed.) *Oxide Minerals: Petrologic and Magnetic Significance*, vol. 25 of *Reviews in Mineralogy*, 107–128, Mineralogical Society of America, Washington, DC

Banerjee SK, O'Reilly W, Gibb TC, Greenwood NN (1967) The behaviour of ferrous ions in iron-titanium spinels. *Journal of the Physics and Chemistry of Solids* 28: 1323–1335

Berman RG (1988) Internally-consistent thermodynamic data for minerals in the system Na_2O-K_2O-CaO-MgO-FeO-Fe_2O_3-Al_2O_3-SiO_2-TiO_2-H_2O-CO_2. *Journal of Petrology* 29: 445–522

Berman RG, Brown TH (1985) Heat capacities of minerals in the system Na_2O-K_2O-CaO-MgO-FeO-Fe_2O_3-Al_2O_3-SiO_2-TiO_2-H_2O-CO_2: representation, estimation, and high-temperature extrapolation. *Contributions to Mineralogy and Petrology* 89: 168–183

Bleil U (1971) Cation distribution in titanomagnetites. *Zeitschrift für Geophysik* 37: 305–319

Bleil U (1976) An experimental study of the titanomagnetite solid solution series. *Pure and Applied Geophysics* 114: 165–175

Buddington AF, Lindsley DH (1964) Iron-titanium oxide minerals and synthetic equivalents. *Journal of Petrology* 5: 310–357

Carmichael ISE (1967) The iron-titanium oxide minerals of salic volcanic rocks and their associated ferromagnesian silicates. *Contributions to Mineralogy and Petrology* 14: 36–64

Chevallier R, Bolfa J, Mathieu S (1955) Titanomagnétites et ilménites ferromagnétiques (I) Étude optique, radiocristallographique, chimique. *Bulletin de la Société Française de Minéralogie et de Cristallographie* 128: 307–346

Collyer S, Grimes NW, Vaughan DJ, Longworth G (1988) Studies of the crystal structure and crystal chemistry of titanomaghemite. *American Mineralogist* 73: 153–160

Darken LS, Gurry RW (1945) The system iron-oxygen. I. The wüstite field and related equilibria. *Journal of the American Chemical Society* 67: 1398–1412

Davidson PM, Lindsley DH (1989) Thermodynamic analysis of pyroxene-olivine-quartz equilibria in the system CaO-MgO-FeO-SiO_2. *American Mineralogist* 74: 18–30

Deer WA, Howie RA, Zussman J (1992) *An Introduction to the Rock-Forming Minerals*. Addison Wesley Longman Limited, Essex, England, 2nd edn.

Deines P, Nafziger RH, Ulmer GC, Woermann E (1974) Temperature-oxygen fugacity tables for selected gas mixtures in the system C-H-O at one atmosphere total pressure. *Bulletin of the Earth and Mineral Sciences Experiment Station* 88: 129pp

Devine JD, Rutherford MJ, Norton GE, Young SR (2003) Magma storage region processes inferred from geochemistry of Fe-Ti oxides in andesitic magma, Soufrière Hills Volcano, Montserrat. *Journal of Petrology* 44: 1375–1400

Dieckmann R (1982) Defects and cation diffusion in magnetite (IV): nonstoichiometry and point defect structure of magnetite ($Fe_{3-\delta}O_4$). *Berichte der Bunsengesellschaft für Physikalische Chemie* 86: 112–118

Dunlop DJ, Özdemir Ö (1997) *Rock Magnetism - Fundamentals and Frontiers*. Cambridge University Press

El Goresy A, Woermann E (1977) Opaque minerals as sensitive oxygen barometers and geothermometers in lunar basalts. In: Fraser DG (ed.) *Thermodynamics in Geology*, 249–277, Reidel, Dordrecht

El Goresy A, Ramdohr P, Medenbach O, Bernhardt HJ (1974) Taurus-Littrow TiO_2-rich basalts: opaque mineralogy and geochemistry. *Proceedings of the 5th Lunar Science Conference, Geochimica et Cosmochimica Acta, Supplements* 5: 627–652

Ender A, Hofmann R, Stapper L, Dhupia G, Woermann E (1980) Die Stabilität von Pseudobrookitmischkristallen. *Fortschritte der Mineralogie* 58: 26–28

Engelmann R, Lattard D, Kontny A, Sauerzapf U (in preparation) Magnetic susceptibilities and Curie temperatures of synthetic titanomagnetites in the Fe-Ti-O system. Reassessment of some methodological and crystal chemical effects.

Eugster HP (1957) Heterogeneous reactions involving oxidation and reduction at high pressures and temperatures. *Journal of Chemical Physics* 26: 1760–1761

Eugster HP, Wones DR (1962) Stability relations of the ferruginous biotite, annite. *Journal of Petrology* 3: 82–125

Evans BW, Scaillet B (1997) The redox state of Pinatubo dacite and the ilmenite-hematite solvus. *American Mineralogist* 82: 625–629

Evans BW, Scaillet B, Kuehner SM (in press) Experimental determination of coexisting iron-titanium oxides in the systems FeTiAlO, FeTiAlMgO, FeTiAlMnO, and FeTiAlMgMnO at 800 and 900 °C, 1 to 4 kbar, and relatively high oxygen fugacity. *Contributions to Mineralogy and Petrology*

Fleet ME (1981) The structure of magnetite. *Acta Crystallographica* B37: 917–920

Fleet ME (1982) The structure of magnetite: Defect structure II. *Acta Crystallographica* B38: 1718–1723

Forster RH, Hall EO (1965) A neutron and X-ray diffraction study of ulvöspinel, Fe_2TiO_4. *Acta Crystallographica* 18: 857–862

Frost BR (1991) Introduction to oxygen fugacity and its petrologic importance. In: Lindsley DH (ed.) *Oxide Minerals: Petrologic and Magnetic Significance*, vol. 25 of *Reviews in Mineralogy*, 1–9, Mineralogical Society of America, Washington, DC

Frost BR, Lindsley DH (1991) Occurrence of iron-titanium oxides in igneous rocks. In: Lindsley DH (ed.) *Oxide Minerals: Petrologic and Magnetic Significance*, vol. 25 of *Reviews in Mineralogy*, 433–462, Mineralogical Society of America, Washington, DC

Frost BR, Lindsley DH (1992) Equilibria among Fe-Ti oxides, pyroxenes, olivine, and quartz: Part II. Application. *American Mineralogist* 77: 1004–1020

Ghiorso MS (1990) Thermodynamic properties of hematite-ilmenite-geikielite solid solutions. *Contributions to Mineralogy and Petrology* 104: 645–667

Ghiorso MS, Sack RO (1991) Fe-Ti oxide geothermometry: thermodynamic formulation and the estimation of intensive variables in silicic magmas. *Contributions to Mineralogy and Petrology* 108: 485–510

Gorter EW (1957) Chemistry and magnetic properties of some ferrimagnetic oxides like those occurring in nature. *Advances in Physics* 63: 336–361

Grey IE, Merritt RR (1981) Stability in the pseudobrookite solid solution $Fe_yTi_{3-y}O_5$. *Journal of Solid State Chemistry* 37: 284–293

Grey IE, Ward J (1973) An X-ray and Mössbauer study of the $FeTi_2O_5$-Ti_3O_5 system. *Journal of Solid State Chemistry* 7: 300–307

Grey IE, Li C, Reid AF (1974) A thermodynamic study of iron in reduced rutile. *Journal of Solid State Chemistry* 11: 120–127

Haggerty SE (1991a) Oxide textures - a mini atlas. In: Lindsley DH (ed.) *Oxide Minerals: Petrologic and Magnetic Significance*, vol. 25 of *Reviews in Mineralogy*, 129–137, Mineralogical Society of America, Washington, DC

Haggerty SE (1991b) Oxide mineralogy of the upper mantle. In: Lindsley DH (ed.) *Oxide Minerals: Petrologic and Magnetic Significance*, vol. 25 of *Reviews in Mineralogy*, 355–416, Mineralogical Society of America, Washington, DC

Haggerty SE, Lindsley DH (1969) Stability of the pseudobrookite (Fe_2TiO_5)-ferropseudobrookite ($FeTi_2O_5$) series. *Carnegie Institution of Washington Yearbook* 68: 247–249

Hammond PL, Tompkins LA, Haggerty SE, Taylor SE, Spencer KJ, Lindsley DH (1982) Revised data for coexisting magnetite and ilmenite near 1000 °C, NNO and FMQ buffers. *GSA Meeting Abstracts with Program* 14: 506

Harlov DE (1992) Comparative oxygen barometry in granulites, Bamble Sector, SE Norway. *Journal of Geology* 100: 447–464

Harlov DE (2000) Titaniferous magnetite-ilmenite thermometry and titaniferous magnetite-ilmenite-orthopyroxene-quartz oxygen barometry in granulite facies gneisses, Bamble Sector, SE Norway: implications for the role of high-grade CO_2-rich fluids during granulite genesis. *Contributions to Mineralogy and Petrology* 139: 180–197

Harrison RJ, Putnis A (1996) Magnetic properties of the magnetite-spinel solid solution: Curie temperatures, magnetic susceptibilities, and cation ordering. *American Mineralogist* 81: 375–384

Harrison RJ, Redfern SAT (2001) Short- and long-range ordering in the ilmenite-hematite solid solution. *Physics and Chemistry of Minerals* 28: 399–412

Harrison RJ, Becker U, Redfern SAT (2000) Thermodynamics of the $R\bar{3}$ to $R\bar{3}c$ phase transition in the ilmenite-hematite solid solution. *American Mineralogist* 85: 1694–1705

Hauptman Z (1974) High temperature oxidation, range of non-stoichiometry and Curie point variation of cation deficient titanomagnetite $Fe_{2.4}Ti_{0.6}O_{4+\gamma}$. *Geophysical Journal of the Royal Astronomical Society* 29–47

Herd CDK, Papike JJ, Brearley AJ (2001) Oxygen fugacity of martian basalts from electron microprobe oxygen and TEM-EELS analyses of Fe-Ti oxides. *American Mineralogist* 86: 1015–1024

Herd CDK, Borg LE, Jones JH, Papike JJ (2002) Oxygen fugacity and geochemical variations in the martian basalts: implications for martian basalt petrogenesis and the oxidation state of the upper mantle of Mars. *Geochimica et Cosmochimica Acta* 66: 2025–2036

Huebner JS (1971) Buffering techniques for hydrostatic systems at elevated pressures. In: Ulmer GC (ed.) *Research Techniques for High Pressure and High Temperature*, 123–177, Springer, New York, Heidelberg, Berlin

Huebner JS (1975) Oxygen fugacity values of furnace gas mixtures. *American Mineralogist* 60: 815–823

Hunt CP, Moskowitz BM, Banerjee SK (1995) Magnetic properties of rocks and minerals. In: *Rock Physics and Phase Relations. A Handbook of Physical Constants.*, vol. 3 of *AGU References Shelf*, 189–204, American Geophysical Union

Ishikawa Y (1958) An order-disorder transformation phenomenon in the $FeTiO_3 - Fe_2O_3$ solid solution series. *Journal of the Physical Scociety of Japan* 13: 828–837

Ishikawa Y, Syono Y, Akimoto S (1964) Neutron diffraction study of $Fe_3O_4 - Fe_2TiO_4$ series. *Annual Progress Report of the Rock Magnetism Group Japan* 14–20

Jensen SD, Shive PN (1973) Cation distribution in sintered titanomagnetites. *Journal of Geophysical Research* 78: 8474–8480

Johnson RE, Woermann E, Muan A (1971) Equilibrium studies in the system MgO-"FeO"-TiO_2. *American Journal of Science* 271: 278–292

Klein C, Hurlbut CS (1993) *Manual of Mineralogy*. John Wiley & Sons, Inc.

Kontny A, Vahle C, de Wall H (2003) Characteristic magnetic behavior of subaerial and submarine lava units from the Hawaiian Scientific Drilling Project (HSDP-2). *G3 Geochemistry, Geophysics, Geosystems* 4

Kress VC, Carmichael ISE (1988) Stoichiometry of the iron oxidation reaction in silicate melt. *American Mineralogist* 73: 1267–1274

Larsen AC, von Dreele RB (2000) Generalized structure analysis system. Tech. Rep. No. LA-UR-86-748, Los Alamos National Laboratory

Lattard D (1987) Subsolidus phase relations in the system Zr-Fe-Ti-O in equilibrium with metallic iron. Implications for lunar petrology. *Contributions to Mineralogy and Petrology* 97: 264–278

Lattard D (1995) Experimental evidence for the exsolution of ilmenite from titaniferous spinel. *American Mineralogist* 80: 968–981

Lattard D, Partzsch GM (2001) Magmatic crystallization experiments at 1 bar in systems closed to oxygen: a new/old experimental approach. *European Journal of Mineralogy* 13: 467–478

Lattard D, Sauerzapf U, Käsemann M (2005) New calibration data for the Fe-Ti oxide thermo-oxybarometers from experiments in the Fe-Ti-O system at 1 bar, $1000 - 1300\,^{\circ}C$ and a large range of oxygen fugacities. *Contributions to Mineralogy and Petrology* 149: 735–754

Lindsley DH (1962) Investigations in the system FeO-Fe_2O_3-TiO_2. *Carnegie Institution of Washington Yearbook* 61: 100–106

Lindsley DH (1963) Fe-Ti oxides in rocks as thermometers and oxygen barometers. *Carnegie Institution of Washington Yearbook* 62: 60–66

Lindsley DH (1976) The crystal chemistry and structure of oxide minerals as exemplified by the Fe-Ti oxides. In: Lindsley DH (ed.) *Oxide Minerals*, vol. 3 of *Reviews in Mineralogy*, 1–60, Mineralogical Society of America, Washington, DC

Lindsley DH (1981) Some experiments pertaining to the magnetite-ulvöspinel miscibility gap. *American Mineralogist* 66: 759–762

Lindsley DH (1991) Experimental studies of oxide minerals. In: Lindsley DH (ed.) *Oxide Minerals: Petrologic and Magnetic Significance*, vol. 25 of *Reviews in Mineralogy*, 69–106, Mineralogical Society of America, Washington, DC

Lindsley DH, Frost BR (1992) Equilibria among Fe-Ti oxides, pyroxenes, olivine, and quartz: Part I. Theory. *American Mineralogist* 77: 987–1003

Lindsley DH, Podpora C (1983) Experimental calibration of the equilibrium $Fe_2SiO_4 + 2FeTiO_3 = 2Fe_2TiO_4 + SiO_2$. *Geological Society of America Abstracts with Programs* 15: 628

Lindsley DH, Spencer KJ (1982) Fe-Ti oxide geothermometry: reducing analyses of coexisting Ti-magnetite (Mt) and ilmenite (Ilm). *Eos, Transactions, American Geophysical Union* 63: 471

McEnroe SA, Robinson P, Panish PT (2001) Aeromagnetic anomalies, magnetic petrology, and rock magnetism of hemo-ilmenite- and magnetite-rich cumulate rocks from the Sokndal Region, South Rogaland, Norway. *American Mineralogist* 86: 1447–1468

Merritt RR, Turnbull AG (1974) A solid-state cell study of oxygen activities in the Fe-Ti-O system. *Journal of Solid State Chemistry* 10: 252–259

Moskowitz BM (1987) Towards resolving the inconsistencies in characteristic physical properties of synthetic titanomaghemites. *Physics of the Earth and Planetary Interiors* 46: 173–183

Muan A, Gee CL (1956) Phase equilibrium studies in the system iron oxide-Al_2O_3 in air and at 1 atm O_2 pressure. *Journal of the American Ceramic Society* 39: 207–214

Muan A, Hauck J, Löfall T (1972) Equilibrium studies with a bearing on lunar rocks. *Proceedings of the Third Lunar Science Conference, Geochimica et Cosmochimica Acta, Supplements 3* 134: 185–196

Néel L (1948) Propriétés magnétiques des ferrites; ferrimagnétisme et antiferromagnétisme. *Annales de Physique* 3: 137–198

Néel L (1955) Some theoretical aspects of rock magnetism. *Advances in Physics* 46: 191–243

Nishitani T, Kono M (1983) Curie temperature and lattice constant of oxidized titanomagnetite. *Geophysical Journal of the Royal Astronomical Society* 74: 585–600

O'Donovan JB, O'Reilly W (1978) Cation distribution in synthetic titanomaghemites. *Physics of the Earth and Planetary Interiors* 16: 200–208

O'Donovan JB, O'Reilly W (1980) The temperature dependent cation distribution in titanomagnetites. *Physics and Chemistry of Minerals* 5: 235–243

O'Neill HSC (1987) Quartz-fayalite-iron and quartz-fayalite-magnetite equilibria and the free energy of formation of fayalite (Fe_2SiO_4) and magnetite (Fe_3O_4). *American Mineralogist* 72: 67–75

O'Neill HSC (1988) Systems $Fe-O$ and $Cu-O$: thermodynamic data for the equilibria $Fe-$"FeO", $Fe-Fe_3O_4$, "FeO"$-Fe_3O_4$, $Fe_3O_4-Fe_2O_3$, $Cu-Cu_2O$, and Cu_2O-CuO from emf measurements. *American Mineralogist* 73: 470–486

O'Neill HSC, Navrotsky A (1983) Simple spinels: Crystallographic parameters, cation radii, lattice energies and cation distribution. *American Mineralogist* 68: 181–194

O'Neill HSC, Navrotsky A (1984) Cation distribution and thermodynamic properties of binary spinel solid solutions. *American Mineralogist* 69: 733–753

O'Neill HSC, Pownceby MI (1993a) Thermodynamic data from redox reactions at high temperatures. I. An experimental and theoretical assessment of the electrochemical method using stabilized zirconia electrolytes, with revised values for the $Fe-$"FeO", $Co-CoO$, $Ni-NiO$ and $Cu-Cu_2O$ oxygen buffers, and new data for the $W-WO_2$ buffer. *Contributions to Mineralogy and Petrology* 114: 296–314

O'Neill HSC, Pownceby MI (1993b) Thermodynamic data from redox reactions at high temperatures. II. The MnO-Mn_3O_4 oxygen buffer, and implications for the thermodynamid properties of MnO and Mn_3O_4. *Contributions to Mineralogy and Petrology* 114: 315–320

O'Reilly W (1984) *Rock and Mineral Magnetism*. Blackie

O'Reilly W, Banerjee SK (1965) Cation distribution in titanomagnetites $(1-x)Fe_3O_4 - xFe_2TiO_4$. *Physics Letters* 17: 237–238

O'Reilly W, Banerjee SK (1967) The mechanisms of oxidation in titanomagnetites: a magnetic study. *Mineralogical Magazine* 36: 29–37

Ozima M, Larson EE (1970) Low- and high-temperature oxidation of titanomagnetite in relation to irreversible changes in the magnetic properties of submarine basalts. *Journal of Geophysical Research* 75: 1003–1017

Pickney LR, Lindsley DH (1976) Effects of magnesium on iron-titanium oxides. *GSA Meeting Abstracts with Program* 8: 1051

Pouchou JL, Pichoir F (1985) 'PAP' ϕ (ρZ) procedure for improved quantitative microanalysis. *Microbeam Analysis* 1985: 104–106

Powell R, Powell M (1977) Geothermometry and oygen barometry using coexisting iron-titanium oxides: a reappraisal. *Mineralogical Magazine* 41: 257–263

Pownceby MI, Fisher-White MJ (1999) Phase equilibria in the systems $Fe_2O_3 - MgO - TiO_2$ and $FeO - MgO - TiO_2$ between 1173 and 1473 K, and $Fe^{2+} - Mg$ mixing properties of ilmenite, ferrous-pseudobrookite and ulvöspinel solid solutions. *Contributions to Mineralogy and Petrology* 135: 198–211

Price GD (1980) Exsolution microstructures in titanomagnetites and their magnetic significance. *Physics of the Earth and Planetary Interiors* 23: 2–12

Price GD (1981) Subsolidus phase relations in the titanomagnetite solid solution series. *American Mineralogist* 66: 751–758

Price GD (1982) Exsolution in titanomagnetites as an indicator of cooling rates. *Mineralogical Magazine* 46: 19–25

Rahman AA, Parry LG (1978) Titanomagnetites prepared at different oxidation conditions: hysteresis properties. *Physics of the Earth and Planetary Interiors* 16: 232–239

Ramdohr P (1955) *Die Erzmineralien und ihre Verwachsungen*. Akademie-Verlag, Berlin

Readman PW, O'Reilly W (1970) The synthesis and inversion of non-stoichiometric titanomagnetites. *Physics of the Earth and Planetary Interiors* 4: 121–128

Readman PW, O'Reilly W (1971) Oxidation processes in titanomagnetites. *Zeitschrift für Geophysik* 37: 329–338

Readman PW, O'Reilly W (1972) Magnetic properties of oxidized (cation deficient) titanomagnetites (Fe,Ti,□)$_3$O$_4$. *Journal of Geomagnetism and Geoelectricity* 24: 69–90

Rumble DI (1970) Thermodynamic analysis of phase equilibria in the system Fe_2TiO_4-Fe_3O_4-TiO_2. *Carnegie Institution of Washington Yearbook* 69: 198–207

Sack RO, Ghiorso MS (1989) Importance of considerations of mixing properties in establishing an internally consistent thermodynamic database: thermochemistry of minerals in the system Mg_2SiO_4-Fe_2SiO_4-SiO_2. *Contributions to Mineralogy and Petrology* 102: 41–68

Sack RO, Ghiorso MS (1991a) Chromian spinels as petrogenetic indicators: Thermodynamics and petrological application. *American Mineralogist* 76: 827–847

Sack RO, Ghiorso MS (1991b) An internally consistent model for the thermodynamic properties of Fe-Mg-tianomagnetite-aluminate spinels. *Contributions to Mineralogy and Petrology* 106: 474–505

Sanver M, O'Reilly W (1970) Identification of naturally occurring non-stoichiometric titanomagnetites. *Physics of the Earth and Planetary Interiors* 2: 166–174

Sauerzapf U, Engelmann R, Wirth R, Lattard D (2005) Nanoscale titanomagnetite exsolutions in quenched synthetic wüstite: insights from transmission electron microscopy (TEM) and magnetic susceptibility measurements. *Beihefte zum European Journal of Mineralogy* 17: 116

Scaillet B, Evans BW (1999) The 15 June 1991 eruption of Mount Pinatubo. I. Phase equilibria and pre-eruption P-T-fO_2-fH_2O conditions of the dacite magma. *Journal of Petrology* 40: 381–411

Schmidbauer E (1987) ^{57}Fe Mössbauer spectroscopy and magnetization of cation deficient Fe_2TiO_4 and $FeCr_2O_4$. Part II: magnetization data. *Physics and Chemistry of Minerals* 15: 201–207

Schneiderhöhn H, Ramdohr P (1931) *Lehrbuch der Erzmikroskopie*. Bornträger, Berlin

Senderov E, Dogan AU, Navrotsky A (1993) Nonstoichiometry of magnetite-ulvöspinel solid solutions quenched from 1300 °C. *American Mineralogist* 78: 565–573

Simons B, Woermann E (1978) Iron-titanium oxides in equilibrium with metallic iron. *Contributions to Mineralogy and Petrology* 66: 81–89

Spencer KJ, Lindsley DH (1981) A solution model for coexisting iron-titanium oxides. *American Mineralogist* 66: 1189–1201

Stephenson A (1969) The temperature dependent cation distribution in titanomagnetites. *Geophysical Journal of the Royal Astronomical Society* 18: 199–210

Stormer JCJ (1983) The effects of recalculation on estimates of temperature and oxygen fugacity from analyses of multicomponent iron-titanium oxides. *American Mineralogist* 68: 286–294

Taylor RW (1964) Phase equilibria in the systems $FeO - Fe_2O_3 - TiO_2$ at 1300 °C. *American Mineralogist* 49: 1016–1031

Toplis MJ, Carroll MR (1995) An experimental study of the influence of oxygen fugacity on Fe-Ti oxide stability, phase relations, and mineral-melt equilibria in ferro-basaltic systems. *Journal of Petrology* 36: 1137–1170

Trestman-Matts A, Dorris SE, Kumarakrishnan S, Mason TO (1983) Thermoelectric determination of cation distributions in $Fe_3O_4 - Fe_2TiO_4$. *Journal of the American Ceramic Society* 66: 829–834

Turnock AC, Eugster HP (1962) Fe-Al oxides: phase relationships below 1000 °C. *Journal of Petrology* 3: 533–565

Verwey EJW (1939) Electronic conduction of magnetite (Fe_3O_4) and its transition point at low temperatures. *Nature* 364: 327

Viertel HU, Seifert F (1979) Physical properties of defect spinels in the system $MgAl_2O_4 - Al_2O_3$. *Neues Jahrbuch für Geologie und Paläontologie, Abhandlungen* 134: 167–182

Viertel HU, Seifert F (1980) Thermal stability of defect spinels in the system $MgAl_2O_4 - Al_2O_3$. *Neues Jahrbuch für Geologie und Paläontologie, Abhandlungen* 140: 89–101

Vincent EA, Wright JB, Chevallier R, Mathieu S (1957) Heating experiments on some natural titaniferous magnetites. *Mineralogical Magazine* 31: 624–655

Wanamaker BJ, Moskowitz BM (1994) Effect of nonstoichiometry on the magnetic and electrical properties of synthetic single crystal $Fe_{2.4}Ti_{0.6}O_4$. *Geophysical Research Letters* 21: 983–986

Waychunas GA (1991) Crystal chemistry of oxides and oxyhydroxides. In: Lindsley DH (ed.) *Oxide Minerals: Petrologic and Magnetic Significance*, vol. 25 of *Reviews in Mineralogy*, 11–68, Mineralogical Society of America, Washington, DC

Webster AH, Bright NFH (1961) The system iron-titanium-oxygen at 1200 °C and oxygen partial pressures between 1 atm. and 2×10^{14} atm. *Journal of the American Ceramic Society* 44: 110–116

Wechsler BA, Lindsley DH, Prewitt CT (1981) Crystal structure and cation distribution in titanomagnetites. *Geological Society of America Abstracts with Programs* 13: 577

Wechsler BA, Lindsley DH, Prewitt CT (1984) Crystal structure and cation distribution in titanomagnetites ($Fe_{3-x}Ti_xO_4$). *American Mineralogist* 69: 754–770

Woermann E, Brezny B, Muan A (1969) Phase equilibria in the system MgO-iron oxide-TiO_2 in air. *American Journal of Science* 267A: 463–479

Woermann E, Hirschberg A, Lamprecht A (1970) Das System Hematit-Ilmenit-Geikielith unter hohen Temperaturen und hohen Drucken. *Fortschritte der Mineralogie* 47: 79–80

Wu CC, Mason TO (1981) Thermopower measurement of cation distribution in magnetite. *Journal of the American Ceramic Society* 64: 520–522

Xirouchakis D, Draper DS, Schwandt CS, Lanzirotti A (2002) Crystallization conditions of Los Angeles, a basaltic Martian meteorite. *Geochimica et Cosmochimica Acta* 66: 1867–1880

Zuo JM, Spence JCH, Petuskey W (1990) Charge ordering in magnetite at low temperatures. *Physical Review B* 42: 8451–8464

A Appendix

A.1 Table of abbreviations

Table A.1: Table of abbreviations

symbol / abbreviation	explanation
	physical values and measures
T	temperature
P	pressure
fO_2	oxygen fugacity
a_0	lattice dimension of a cubic unit cell
e.m.f.	electromotive force
M	modal proportion of a phase in a sample
$M_{Ilm_{ss}^{ex}}$	modal proportion of Ilm_{ss} exsolved from Tmt in annealed sample
	mineral names and compositional parameters
Fe^0	metallic iron
Wus	wüstite
Tmt	titanomagnetite, see Table 1.1 in chapter 1
Mag	magnetite
Usp	ulvöspinel
Hc	hercynite, $FeAl_2O_4$
Ilm_{ss}	$ilmenite_{ss}$, see Table 1.1 in chapter 1
Hem	hematite
Ilm	ilmenite
Psb_{ss}	$pseudobrookite_{ss}$, see Table 1.1 in chapter 1
Psb	pseudobrookite Fe_2TiO_5
Rt	rutile
Ti^0	metallic titanium
X	composition
X_{Usp}	molefraction of ulvöspinel endmember in titanomagnetite
X_{Mag}	molefraction of magnetite endmember in titanomagnetite
X_{Ilm}	molefraction of ilmenite endmember in $ilmenite_{ss}$
X_{Hem}	molefraction of hematite endmember in $ilmenite_{ss}$
Ilm_{ss}^{A}	$ilmenite_{ss}$ in annealed sample

A Appendix

Table A.1: Table of abbreviations

symbol / abbreviation	**explanation**
Ilm_{ss}^{HT}	$ilmenite_{ss}$ in high-T sample
Tmt^{A}	Tmt in annealed sample
Tmt^{HT}	Tmt in high-T sample
	instruments and methods
EELS	electron energy-loss spectroscopy
EMP	electron microprobe
SEM	scanning electron microscope
	solid-state oxygen buffer equilibria
NNO	nickel-nickeloxide (O'Neill & Pownceby, 1993a)
WM	wüstite-magnetite (O'Neill, 1988)
FMQ	fayalite-magnetite-quartz (O'Neill, 1987)
IW	iron-wüstite (O'Neill, 1988)
CCO	Co-CoO (O'Neill & Pownceby, 1993a)
Man/H	MnO-Mn_3O_4 (O'Neill & Pownceby, 1993b)
IQF	iron-quartz-fayalite
MH	magnetite-hematite
ΔNNO	logfO_2(experimental)-logfO_2(NNO)
ΔFMQ	logfO_2(experimental)-logfO_2(FMQ)
	experimenters
AU	Angela Ullrich, student assistant
HH	Heike Höltzen, laboratory assistant
MB	Mark Bornefeld, student assistant
MF	Meike Fleischhammer, diploma thesis
MK	Martin Käsemann, diploma thesis
RE	Ralf Engelmann, Ph.D. student
RL	Ramona Langner, student assistant
SP	Sandra Panienka, student assistant
US	Ursula Sauerzapf, author
VG	Verena Gastner, student assistant

A.2 Starting mixtures

In the following tables the starting materials are listed. They are summarised in different groups based on the reagents used, and are arranged in order of increasing Ti/(Ti+Fe). For nomenclature see Fig. A.1.

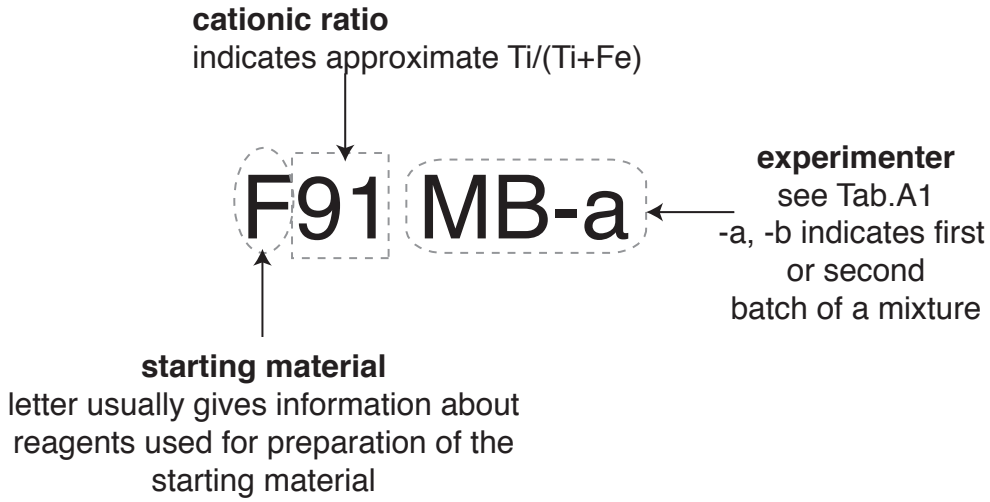

Fig. A.1 Nomenclature of starting materials

Table A.2: Oxide starting mixtures in the system Fe-Ti-O

name	[wt%]			Ti/(Ti+Fe)
	Fe_2O_3	TiO_2	Fe°	[at%]
ternary $Fe_2O_3 - Fe^\circ - TiO_2$ mixtures				
F92Q HH-a	85.5	8.2	6.2	8.0
P76 MK-a	65.4	24.5	10.1	23.5
F76Q HH-a	64.7	25.1	10.2	24.0
F72Q HH-a	59.4	29.4	11.3	28.0
F69Q HH-a	55.4	32.6	12.0	31.0
P63 MK-a	49.0	38.9	12.1	37.0
IT60 AU-a	43.2	42.5	14.3	40.0
F57K67 US	44.6	44.9	10.5	43.0
IP41 AU-a	28.0	61.6	10.4	59.0
F39 MF-a[1]	25.3	63.8	10.9	50.9

continued on next page

Table A.2: Oxide starting mixtures in the system Fe-Ti-O

name	[wt%]			Ti/(Ti+Fe)
	Fe_2O_3	TiO_2	Fe°	[at%]
binary $Fe_2O_3 - TiO_2$ mixtures				
F97 HH-a	97.0	3.0		3.0
F92 HH-a	92.0	8.0		8.0
F90 MB-a	90.0	10.0		10.0
F90 AU-a	90.0	10.0		10.0
F87 HH-a	87.0	13.0		13.0
F87 MK-a	86.8	13.2		13.2
F87 MK-b	86.7	13.3		13.3
F83 MB-a	83.0	17.0		17.0
F82 MB-a	82.0	18.0		18.0
F80 HH-a	80.0	20.0		20.0
F76 MK-a	76.5	23.5		23.5
F72 MK-a	72.4	27.6		27.6
F72 MK-b	72.0	28.0		28.0
F69 MK-a	69.0	31.0		31.0
F68 MB-a	68.0	32.0		32.0
F67 MB-a	67.0	33.0		33.0
F63 MK-a	63.0	37.0		37.0
F60 AU-a	60.0	40.0		40.0
F57 VG-a	57.0	43.0		43.0
F57 MK-a	56.7	43.3		43.3
F54.5 RE-a	54.5	45.5		45.5
F50 HH-a	50.0	50.0		50.0
F47 MK-a	47.2	52.8		52.7
F42 MK-a	42.5	57.5		57.5
binary $Fe^\circ - TiO_2$ mixtures				
F65 RE-a		43.5	56.5	35.0
F470 RESP-a		61.7	38.3	53.0
F44 RE-a		64.5	35.5	56.0

1) formerly named 1.56Ti

Table A.3 Starting mixtures in the systems Fe-Ti-Al-O, Fe-Ti-Mg-O and Fe-Ti-Al-Mg-O

name	[wt%]					[at%]					Ti/(Ti+Fe)	M/O%[1]
	Fe_2O_3	TiO_2	Fe°	MgO	Al_2O_3	Fe	Ti	Mg	Al	O	[at%]	
						system Fe-Ti-Al-O						
F90A10 AU-a	84.6	9.4			6.0	32.1	3.6		3.6	60.7	10.0	64.7
F70A2 IG-a	68.6	29.4			2.0	25.6	11.0		1.2	62.2	30.0	60.8
IT60A2 IG-a	47.0	40.9	10.0		2.1	23.3	15.6		1.2	59.8	40.0	67.1
F59.5A5.5 US-a	56.9	38.8			4.3	20.7	14.1		2.4	62.8	40.6	59.2
						system Fe-Ti-Mg-O						
F70M2 IG-a	68.6	29.4		2.0		25.6	11.0	1.5		61.9	30.0	61.5
IT60M2 IG-a	47.0	40.9	10.0	2.1		23.3	15.6	1.6		59.5	40.0	68.0
F57.4M10 AU-a	55.6	41.2		3.1		20.2	15.0	2.2		62.5	42.6	59.9
						system Fe-Ti-Al-Mg-O						
F90M1A1 RL-a	88.2	9.8		1.0	1.0	34.2	3.8	0.8	0.6	60.6	10.0	65.0
F85M1A1 RL-a	83.3	14.7		1.0	1.0	32.0	5.6	0.8	0.6	61.0	15.0	64.0
IT70M1A1 IG-a	55.2	30.9	11.8	1.1	1.0	28.2	12.1	0.8	0.6	58.3	30.0	71.5
IT60M1A1 IG-a	47.0	40.9	10.0	1.0	1.0	23.3	15.6	0.8	0.6	59.7	40.0	67.5
IP46M1A1 IG-a	35.7	54.7	7.6	1.0	1.0	17.1	20.1	0.8	0.6	61.5	54.0	62.7

1) M/O %: cation / oxygen ratio in percent

A.3 Tables of experimental conditions and analysis results

Nomenclature The sample names contain information on the starting material, equilibration temperature and oxygen fugacity (Fig. A.2). In most cases, the temperature is indicated by the number at the beginning of the samples name, or sometimes as a number at the end. Details of the starting material composition can be derived from tables A.2 and A.3. A capital D at the end of the sample name indicates an annealing experiment. A capital R indicates a re-equilibration experiment.

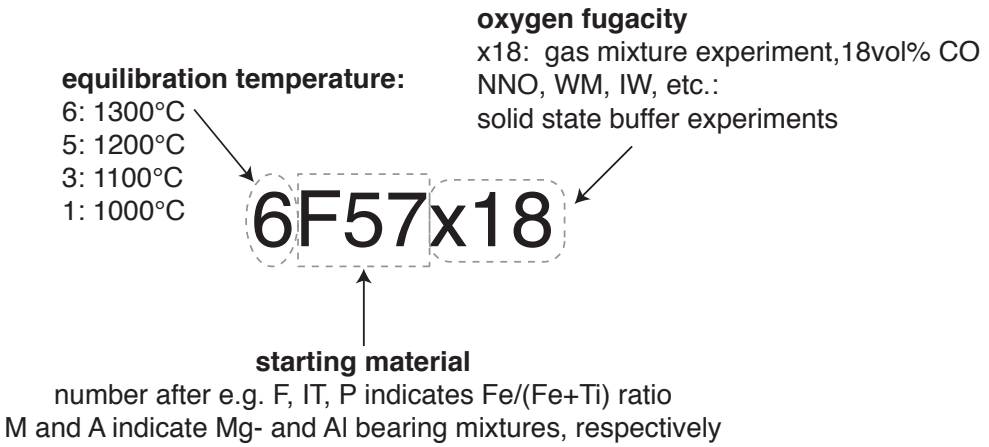

Fig. A.2 Nomenclature of synthesis and re-equilibration samples

Additional information The tables contain the most important information on run conditions and analysis results. More detailed and additional information, e.g. EMP single analyses, results of X-ray diffraction and BSE pictures, are available from the author.

Additional to the information contained in the following tables, this thesis comprises a number of tables within chapters 1.2 to 6 that present analytical results and experimental details. These are listed in Table A.4.

Table A.4 Tables of results and experimental details in chapters 1.2 to 6.

chapter	table no.	contents
2	2.1	composition of single-phase Tmt compared to Ti/(Ti+Fe) of starting mixture
	2.2	composition of Ilm_{ss} in single-phase sample 6IT60M2x1.5a
3	3.1	compositions of Ilm_{ss} and Psb_{ss} in sample rim vs. sample core
	3.2	phase compositions in sample 5F72x1.25 and compared to other samples equilibrated at 1200 °C and NNO+0.7
	3.3	phase compositions in central sample regions for samples with and without oxy-exsolutions
	3.4	selected analyses of Fe-Al spinel grains
4	4.1	re-equilibration experiments: Comparison of phase compositions to synthesis experiments
	4.2	re-equilibration experiments and preceding synthesis runs: experimental conditions
	4.3	phase compositions in products of synthesis runs and subsequent re-equilibration runs
5	5.1	δ calculated for samples with and without oxy-exsolution
	5.2	EMP analyses of Ilm_{ss} grains vs. Ilm_{ss} lamellae
	5.3	modal proportions from image analysis and Rietveld analysis
	5.4	δ from annealing method A and B
	5.5	lattice parameter a_0 at $1100-1300$ °C
	5.6	lattice parameter a_0 at 950 °C
	5.7	$Fe^{3+}/\Sigma Fe$ determined by EELS on different fragments of sample 6F80x66
	5.8	$Fe^{3+}/\Sigma Fe$ and resulting δ
6	6.4	comparison of projection for two Mg-Al bearing samples of the present study
	6.5	annealed Mg-Al bearing Tmt+Ilm_{ss} samples
	6.6	MgO and Al_2O_3 contents in high-T and annealed samples
	6.7	δ of high-T Mg-Al bearing Tmt, calculated according to method A
	6.8	data by Toplis & Carroll (1995): experimental and estimated T and ΔNNO

Table A.5: Experimental conditions of 1000 °C synthesis and re-equilibration runs, system Fe-Ti-O

run no	date[1]	by[2]	ref.[3]	bulk Ti/(Ti+Fe) [at%]	T [°C]	t [h]	buffer/ CO [vol%]	oxygen fugacity[4]			quenching
								-log fO_2	ΔFMQ[4]	ΔNNO[4]	
1F87x0.25		HH[2]	L05	13.0	999	264	0.25	8.8	2.3	1.5	?[5]
1F80x0.25		HH	L05	20.0	999	264	0.25	8.8	2.3	1.5	?
F72(X)1		MK[2]	L05	28.0	1000	120	0.50	9.3	1.8	1.0	?
1F80x0.5		HH	L05	20.0	1001	192	0.50	9.3	1.8	1.0	?
1F72x1	26.03.03	US[2]	L05	28.0	1001	285	1.00	10.0	1.1	0.3	EQ[5]
1F69x1	26.03.03	US	L05	31.0	1001	285	1.00	10.0	1.1	0.3	EQ
1F92Qc		HH	L05	8.0	999	240	Man/H[4]	6.8	4.3	3.6	AQ[5]
1F72Qe		HH	L05	28.0	999	192	NNO[4]	10.3	0.8	0.0	AQ
F72(e)1		MK	L05	28.0	1000	120	NNO	10.3	0.8	0.0	AQ
F63(g)1		MK	L05	37.0	1000	120	Co/CoO[4]	11.8	-0.7	-1.5	AQ
1P63WM	26.08.03	US	L05	37.0	1000	357	WM[4]	12.8	-1.7	-2.5	AQ
1IT60WM	26.08.04	US	L05	40.0	1000	357	WM	12.8	-1.7	-2.5	AQ
1P63IW	24.07.03	US	L05	37.0	1001	331	IW[4]	14.9	-3.8	-4.6	AQ
1F57K67IW	24.07.03	US	L05	43.0	1001	331	IW	14.9	-3.8	-4.6	AQ
1F57x0.25		HH	L05	43.3	999	264	0.25	8.8	2.3	1.5	?
1F57x0.5		HH	L05	43.3	1001	192	0.50	9.3	1.8	1.0	?
1F47x1	26.03.03	US	L05	52.7	1001	285	1.00	10.0	1.1	0.3	EQ
1IP41WM	26.08.03	US	L05	59.0	1000	357	WM	12.8	-1.7	-2.5	AQ
1F39IW	24.07.03	US	L05	60.9	1001	331	IW	14.9	-3.8	-4.6	AQ

1) first day of experiment (i.e. synthesis or re-equilibration run).
2) experimenters: see Table A.1.
3) reference: L05: Lattard *et al.* (2005).
4) from e.m.f. measurements, or for solid-state buffer experiments according to literature (Table A.1).
5) quenching procedures: ?) not documented or uncertain, EQ) external quench, AQ) quenching of ampoules, DQ) drop quench.

Table A.6: Phase compositions of synthesis and re-equilibration run products at 1000 °C, system Fe-Ti-O, derived by EMP analysis

run no	ΔNNO	assemblage	Tmt				Ilm_{ss}				Psb_{ss}		
			n	Ti/(Ti+Fe) [at%] mean	(σ)	X_{Usp}	n	Ti/(Ti+Fe) [at%] mean	(σ)	X_{Ilm}	n	Ti/(Ti+Fe) [at%] mean	(σ)
1F87x0.25	1.5	Tmt+Ilm_{ss}	10	8.81	(10)	0.26	10	28.65	(14)	0.57			
1F80x0.25	1.5	Tmt+Ilm_{ss}	10	8.36	(14)	0.25	10	28.00	(26)	0.56			
F72(X)1	1.0	Tmt+Ilm_{ss}	10	12.36	(27)	0.37	8	32.43	(41)	0.65			
1F80x0.5	1.0	Tmt+Ilm_{ss}	10	12.22	(13)	0.37	10	32.38	(16)	0.65			
1F72x1	0.3	Tmt+Ilm_{ss}	10	16.57	(18)	0.50	10	40.43	(26)	0.81			
1F69x1	0.3	Tmt+Ilm_{ss}	10	16.49	(11)	0.49	10	40.22	(17)	0.80			
1F92Qc	3.6	Tmt+Ilm_{ss}	5	1.59	(09)	0.05	10	12.72	(53)	0.25			
1F72Qe	0.0	Tmt+Ilm_{ss}	13	17.98	(26)	0.54	9	42.77	(21)	0.86			
F72(e)1	0.0	Tmt+Ilm_{ss}	10	17.89	(22)	0.54	10	42.57	(14)	0.85			
F63(g)1	-1.5	Tmt+Ilm_{ss}	10	24.66	(24)	0.74	11	47.20	(77)	0.94			
1P63WM	-2.5	Tmt+Ilm_{ss}	10	28.09	(10)	0.84	10	48.93	(12)	0.98			
1IT60WM	-2.5	Tmt+Ilm_{ss}	10	27.99	(12)	0.84	10	48.90	(15)	0.98			
1P63IW	-4.6	Tmt+Ilm_{ss}	9	31.89	(13)	0.96	10	49.79	(21)	1.00			
1F57K67IW	-4.6	Tmt+Ilm_{ss}	10	31.92	(08)	0.96	10	49.78	(16)	1.00			
1F57x0.25	1.5	Ilm_{ss}+Psb_{ss}					10	32.82	(25)	0.66	10	50.77	(68)
1F57x0.5	1.0	Ilm_{ss}+Psb_{ss}					10	38.62	(21)	0.77	10	53.37	(62)
1F47x1	0.3	Ilm_{ss}+Psb_{ss}					10	45.60	(21)	0.91	10	57.54	(25)
												rutile	
1IP41WM	-2.5	Ilm_{ss}+Rt					10	50.40	(23)	1.01	10	99.50	(10)
1F39IW	-4.6	Ilm_{ss}+Rt					10	50.99	(29)	1.02	10	99.48	(10)

Table A.7: Experimental conditions of 1100 °C synthesis and re-equilibration runs, system Fe-Ti-O. For footnotes see Table A.5

run no	date[1]	by[2]	ref.[3]	bulk Ti/(Ti+Fe) [at%]	T [°C]	t [h]	buffer/ CO [vol%]	oxygen fugacity[4]			quenching
								-log fO_2	ΔFMQ[4]	ΔNNO[4]	
3F80IW	26.02.04	US	-	20.0	1100	332	IW[4]	13.3	-3.6	-4.4	AQ[5]
3F80x0.4	09.02.01	HH	L05	20.0	1099	116	0.40	7.5	2.2	1.5	?[5]
3F76x0.9	27.02.01	HH	L05	23.5	1100	144	0.90	8.2	1.4	0.7	?
3F72x1.25	26.03.03	US	L05	28.0	1101	144	1.25	8.4	1.2	0.5	?
3F69x1.25	26.03.03	US	L05	31.0	1101	144	1.25	8.4	1.2	0.5	?
F57 (X) 3	13.04.00	MK	L05	43.3	1100	93	5.50	9.8	-0.1	-0.8	?
F72 (X) 3	17.03.00	MK	L05	28.0	1104	72	5.50	9.8	-0.1	-0.9	?
F69 (X) 3	17.03.00	MK	L05	31.0	1104	72	5.50	9.8	-0.1	-0.9	?
3F69x16.5	05.05.03	US	L05	31.0	1100	135	16.51	10.9	-1.2	-2.0	DQ[5]
3F63x16.5	05.05.03	US	L05	37.0	1100	135	16.51	10.9	-1.2	-2.0	DQ
3F65x30	07.07.03	RE/US[2]	L05	35.0	1100	96	30.00	11.5	-1.8	-2.6	DQ
3F63x30	07.07.03	RE/US	L05	37.0	1100	96	30.00	11.5	-1.8	-2.6	DQ
3F76Qe	25.05.01	HH	L05	24.0	1098	120	NNO[4]	8.9	0.8	0.0	AQ
3F72QNNORa	10.02.05	US	L05	28.0	1100	143	NNO	8.9	0.8	0.0	AQ
3F69Qe	25.05.01	HH	L05	31.0	1098	120	NNO	8.9	0.8	0.0	AQ
F69 (e) 3	28.04.00	MK	L05	31.0	1100	93	NNO	8.9	0.7	0.0	AQ
F63 (f) 3	28.04.00	MK	L05	37.0	1100	93	FMQ[4]	9.7	0.0	-0.7	AQ
F63 (g) 3	28.04.00	MK	L05	37.0	1100	93	Co/CoO[4]	10.4	-0.8	-1.5	AQ
3F69QWMR	17.09.03	US	L05	31.0	1100	217	WM[4]	10.9	-1.3	-2.0	AQ
3IT60WMa	02.10.03	US	L05	40.0	1101	138	WM	10.9	-1.3	-2.0	AQ
3F57WMRc	10.02.05	US	L05	43.3	1100	143	WM	10.9	-1.3	-2.0	AQ
3IT60IW	15.08.03	US	L05	40.0	1100	153	IW	13.3	-3.6	-4.4	AQ
3F57K67IWa	02.10.03	US	-	43.0	1101	138	IW	13.3	-3.6	-4.4	AQ
3F57IWR	17.09.03	US	L05	43.3	1100	217	IW	13.3	-3.6	-4.4	AQ
3F97a	23.03.01	HH	L05	3.0	1099	260	0.00	3.7	6.0	5.3	?
3P76x0	07.05.03	US	L05	23.5	1100	165	0.00	3.3	6.4	5.7	DQ

Table A.7: Experimental conditions of 1100 °C synthesis and re-equilibration runs, system Fe-Ti-O. For footnotes see Table A.5

run no	date[1]	by[2]	ref.[3]	bulk Ti/(Ti+Fe) [at%]	T [°C]	t [h]	buffer/ CO [vol%]	oxygen fugacity[4]			quenching
								-log fO_2	ΔFMQ[4]	ΔNNO[4]	
3F72x0	07.05.03	US	L05	28.0	1100	165	0.00	3.3	6.4	5.7	DQ
3F69x0	07.05.03	US	L05	31.0	1100	165	0.00	3.3	6.4	5.7	DQ
3F57x0.4	09.02.01	HH	L05	43.3	1099	116	0.40	7.5	2.2	1.5	?
3F57x0.9	27.02.01	HH	L05	43.3	1100	144	0.90	8.2	1.4	0.7	?
3F50x1.25	26.03.03	US	L05	50.0	1101	144	1.25	8.4	1.2	0.5	?
F47 (X) 3	13.04.00	MK	L05	52.7	1100	93	5.50	9.8	-0.1	-0.8	?
3F47x16.5	05.05.03	US	L05	52.7	1100	135	16.51	10.9	-1.2	-2.0	DQ
3F47x30	07.07.03	RE/US	L05	52.7	1100	96	30.00	11.5	-1.8	-2.6	DQ
3F44x30	07.07.03	RE/US	L05	56.0	1100	96	30.00	11.5	-1.8	-2.6	DQ
F42 (g) 3	28.04.00	MK	L05	57.5	1100	93	Co/CoO	10.4	-0.8	-1.5	AQ
3IP41IW	15.08.03	US	L05	59.0	1100	153	IW	13.3	-3.6	-4.4	AQ

Table A.8: Phase compositions of synthesis and re-equilibration run products at 1100 °C, system Fe-Ti-O, derived by EMP analysis

run no	ΔNNO	assemblage	Tmt				Ilm_{ss}				Psb_{ss}		
			n	Ti/(Ti+Fe) [at%] mean	(σ)	X_{Usp}	n	Ti/(Ti+Fe) [at%] mean	(σ)	X_{Ilm}	n	Ti/(Ti+Fe) [at%] mean	(σ)
3F80IW	-4.4	Tmt+Wus	10	25.97	(16)	0.78							
3F80x0.4	1.5	Tmt+Ilm_{ss}	13	10.43	(21)	0.31	14	29.58	(31)	0.59			
3F76x0.9	0.7	Tmt+Ilm_{ss}	11	15.95	(25)	0.48	9	34.84	(40)	0.70			
3F72x1.25	0.5	Tmt+Ilm_{ss}	10	18.56	(15)	0.56	10	38.41	(16)	0.77			
3F69x1.25	0.5	Tmt+Ilm_{ss}	10	18.52	(10)	0.56	10	38.23	(25)	0.76			
F57 (X) 3	-0.8	Tmt+Ilm_{ss}	10	24.73	(24)	0.74	10	46.22	(28)	0.92			
F72 (X) 3	-0.9	Tmt+Ilm_{ss}	10	24.87	(18)	0.75	10	46.02	(30)	0.92			
F69 (X) 3	-0.9	Tmt+Ilm_{ss}	10	24.69	(21)	0.74	10	45.89	(25)	0.92			
3F69x16.5	-2.0	Tmt+Ilm_{ss}	10	28.35	(15)	0.85	9	48.06	(19)	0.96			
3F63x16.5	-2.0	Tmt+Ilm_{ss}	10	28.52	(18)	0.86	10	48.07	(15)	0.96			
3F65x30	-2.6	Tmt+Ilm_{ss}	10	30.07	(18)	0.90	10	48.76	(29)	0.98			
3F63x30	-2.6	Tmt+Ilm_{ss}	10	29.81	(26)	0.89	10	48.75	(34)	0.98			
3F76Qe	0.0	Tmt+Ilm_{ss}	10	20.22	(19)	0.61	10	41.76	(17)	0.84			
3F72QNNORa	0.0	Tmt+Ilm_{ss}	10	20.54	(19)	0.62	10	42.00	(20)	0.84			
3F69Qe	0.0	Tmt+Ilm_{ss}	10	20.14	(15)	0.60	10	41.76	(15)	0.84			
F69 (e) 3	0.0	Tmt+Ilm_{ss}	10	19.99	(21)	0.60	10	41.85	(40)	0.84			
F63 (f) 3	-0.7	Tmt+Ilm_{ss}	10	23.26	(19)	0.70	10	45.24	(26)	0.90			
F63 (g) 3	-1.5	Tmt+Ilm_{ss}	10	26.36	(25)	0.79	10	47.40	(19)	0.95			
3F69QWMR	-2.0	Tmt+Ilm_{ss}	10	27.97	(13)	0.84	10	48.06	(14)	0.96			
3IT60WMa	-2.0	Tmt+Ilm_{ss}	10	27.81	(18)	0.83	10	48.08	(16)	0.96			
3F57WMRc	-2.0	Tmt+Ilm_{ss}	10	28.29	(12)	0.85	10	48.37	(09)	0.97			
3IT60IW	-4.4	Tmt+Ilm_{ss}	10	32.46	(16)	0.97	10	49.78	(10)	1.00			
3F57K67IWa	-4.4	Tmt+Ilm_{ss}	10	32.55	(13)	0.98	10	50.03	(23)	1.00			
3F57IWR	-4.4	Tmt+Ilm_{ss}	10	32.94	(18)	0.99	10	50.16	(20)	1.00			
3F97a	5.3	Ilm_{ss}					13	3.02	(10)	0.06			
3P76x0	5.7	Ilm_{ss}+Psb_{ss}					10	12.31	(08)	0.25	10	35.84	(39)
3F72x0	5.7	Ilm_{ss}+Psb_{ss}					10	12.39	(11)	0.25	10	35.83	(49)

Table A.8: Phase compositions of synthesis and re-equilibration run products at 1100 °C, system Fe-Ti-O, derived by EMP analysis

run no	ΔNNO	assemblage	Tmt				Ilm_{ss}				Psb_{ss}		
			n	Ti/(Ti+Fe) [at%] mean	(σ)	X_{Usp}	n	Ti/(Ti+Fe) [at%] mean	(σ)	X_{Ilm}	n	Ti/(Ti+Fe) [at%] mean	(σ)
3F69x0	5.7	Ilm_{ss}+Psb_{ss}					10	12.59	(17)	0.25	10	35.93	(42)
3F57x0.4	1.5	Ilm_{ss}+Psb_{ss}					11	32.97	(27)	0.66	10	51.40	(30)
3F57x0.9	0.7	Ilm_{ss}+Psb_{ss}					9	38.05	(28)	0.76	11	55.11	(18)
3F50x1.25	0.5	Ilm_{ss}+Psb_{ss}					10	43.69	(16)	0.87	10	57.54	(17)
F47 (X) 3	-0.8	Ilm_{ss}+Psb_{ss}+Rt[6]					10	48.74	(63)	0.97	10	63.23	(32)
												rutile	
3F47x16.5	-2.0	Ilm_{ss}+Rt					10	49.88	(17)	1.00	10	98.94	(13)
3F47x30	-2.6	Ilm_{ss}+Rt					10	50.41	(38)	1.01	10	99.44	(11)
3F44x30	-2.6	Ilm_{ss}+Rt					10	50.16	(17)	1.00	10	99.21	(15)
F42 (g) 3	-1.5	Ilm_{ss}+Rt					10	49.61	(17)	0.99	10	99.22	(12)
3IP41IW	-4.4	Ilm_{ss}+Rt					10	51.10	(17)	1.02	10	99.45	(08)

6) F47(X)3, Rt: Ti/(Ti+Fe)=99.04 at%

Table A.9: Experimental conditions of 1200 °C synthesis and re-equilibration runs, system Fe-Ti-O. For footnotes see Table A.5.

run no	date[1]	by[2]	ref.[3]	bulk Ti/(Ti+Fe) [at%]	T [°C]	t [h]	buffer/ CO [vol%]	oxygen fugacity[4]			quenching
								-log fO_2	ΔFMQ[4]	ΔNNO[4]	
5F92x0.5	26.01.01	HH	L05	8.0	1202	76	0.50	6.2	2.2	1.6	EQ[5]
5F92x0.25[7]	26.02.01	HH	-	8.0	1201	99	0.25	5.4	3.0	2.3	EQ[5]
F87 (f) 5	27.12.99	MK	L05	13.3	1194	48	5.41	8.5	0.0	-0.7	DQ?[5]
F87 (g) 5	29.12.99	MK	L05	13.3	1194	48	12.50	9.3	-0.8	-1.4	DQ?
F72 (g) 5	29.12.99	MK	L05	27.6	1194	48	12.50	9.3	-0.8	-1.4	DQ?
5F97a	19.12.00	HH	L05	3.0	1201	99	0.00	3.5	4.9	4.2	?[5]
5F87x0.25	26.02.01	HH	L05	13.0	1201	99	0.25	5.4	3.0	2.3	EQ
5F87x0.5	26.01.01	HH	L05	13.3	1202	76	0.50	6.2	2.2	1.6	EQ?
5F76x0.5	26.01.01	HH	L05	23.5	1202	76	0.50	6.2	2.2	1.6	EQ?
5F72x0.5	26.01.01	HH	L05	28.0	1202	76	0.50	6.2	2.2	1.6	EQ?
5F76x0.65	18.01.01	HH	L05	23.5	1201	93	0.65	6.4	2.0	1.3	EQ
5F72x0.65	18.01.01	HH	L05	28.0	1201	93	0.65	6.4	2.0	1.3	EQ
5F72x1.25	30.04.03	US	L05	28.0	1200	68	1.25	7.0	1.4	0.7	DQ?
5F69x1.25	30.04.03	US	L05	31.0	1200	68	1.25	7.0	1.4	0.7	DQ?
5F69Qx2.8	04.07.03	RE/US	L05	31.0	1200	1200	2.81	7.8	0.6	-0.1	EQ
5F69Qx2.8a	01.08.03	US	L05	31.0	1200	>24	2.81	7.8	0.6	-0.1	DQ
5F69x2.8a	01.08.03	US	L05	31.0	1200	>24	2.81	7.8	0.6	-0.1	DQ
5F65x2.8a[8]	01.08.03	US	-	31.0	1200	>24	2.81	7.8	0.6	-0.1	DQ
5F63x2.8	04.07.03	RE/US	L05	37.0	1200	1200	2.81	7.8	0.6	-0.1	EQ
5F63x2.8a	01.08.03	US	L05	37.0	1200	>24	2.81	7.8	0.6	-0.1	DQ
F72 (f) 5	27.12.99	MK	L05	27.6	1194	48	5.41	8.5	0.0	-0.7	DQ?
F69 (g) 5	20.03.00	MK	L05	31.0	1200	48	12.50	9.3	-0.8	-1.5	?
5F63x33.5	02.05.03	US	L05	37.0	1201	52	33.50	10.3	-1.9	-2.6	DQ?
5F57x33.5	02.05.03	US	L05	43.3	1201	52	33.50	10.3	-1.9	-2.6	DQ?
5F60x61.5	13.05.03	AU[2]	L05	40.0	1200	48	61.50	11.3	-2.9	-3.6	DQ?
5F54.5x61.5	13.05.03	AU	L05	45.5	1200	48	61.50	11.3	-2.9	-3.6	DQ?

Table A.9: Experimental conditions of 1200 °C synthesis and re-equilibration runs, system Fe-Ti-O. For footnotes see Table A.5.

run no	date[1]	by[2]	ref.[3]	bulk Ti/(Ti+Fe) [at%]	T [°C]	t [h]	buffer/ CO [vol%]	oxygen fugacity[4]			quenching
								-log fO_2	ΔFMQ[4]	ΔNNO[4]	
5F60x83.5	29.04.03	AU	L05	40.0	1200	27	83.50	12.3	-3.9	-4.6	DQ?
5F54.5x83.5	29.04.03	AU	L05	45.5	1200	27	83.50	12.3	-3.9	-4.6	DQ?
5F92a	19.12.00	HH	L05	8.0	1201	99	0.00	3.5	4.9	4.2	?
5F90a	25.03.02	MB[2]	L05	10.0	1201	53	0.00	3.5	4.9	4.2	DQ?
F87(a)5	06.12.99	MK	L05	13.2	1194	44	0.00	3.5	5.0	4.3	EQ
5F76a	09.01.01	HH	L05	23.5	1201	68	0.00	3.5	4.9	4.2	?
5F72a	09.01.01	HH	L05	28.0	1201	68	0.00	3.5	4.9	4.2	?
5F57x0.25	26.02.01	HH	L05	43.3	1201	99	0.25	5.4	3.0	2.3	?
5F57x0.5	26.01.01	HH	L05	43.3	1202	76	0.50	6.2	2.2	1.6	EQ?
5F57x0.65	18.01.01	HH	L05	43.3	1201	93	0.65	6.4	2.0	1.3	EQ
5F50x0.65	18.01.01	HH	L05	50.0	1201	93	0.65	6.4	2.0	1.3	EQ
5F50x1.25	30.04.03	US	L05	50.0	1200	68	1.25	7.0	1.4	0.7	DQ?
5F47x2.8	04.07.03	RE/US	L05	52.7	1200	1200	2.81	7.8	0.6	-0.1	EQ
5F47x2.8a	01.08.03	US	L05	52.7	1200	>24	2.81	7.8	0.6	-0.1	DQ
F47 (f) 5	26.03.00	MK	L05	52.7	1200	48	4.50	8.2	0.2	-0.5	DQ?
F42 (g) 5	23.03.00	MK	L05	57.5	1200	69	12.50	9.3	-0.8	-1.5	?
5F42x33.5	02.05.03	US	L05	57.5	1201	52	33.50	10.3	-1.9	-2.6	DQ?
5F42x61.5	13.05.03	AU	L05	57.5	1200	48	61.50	11.3	-2.9	-3.6	DQ?
5F42x83.5	29.04.03	AU	L05	57.5	1200	27	83.50	12.3	-3.9	-4.6	DQ?
5F44x2.8	04.07.03	RE/US	-	56.0	1200	1200	2.81	7.8	0.6	-0.1	EQ

7) exclusively used to document Ilm_{ss} oxy-exsolution features in Tmt (chapter 3).
8) exclusively used to document Fe-rich rims (chapter 3). No two-phase sample region.

Table A.10: Phase compositions of synthesis and re-equilibration run products at 1200 °C, system Fe-Ti-O, derived by EMP analysis

run no	ΔNNO	assemblage	Tmt				Ilm_{ss}				Psb_{ss}		
			n	Ti/(Ti+Fe) [at%] mean	(σ)	X_{Usp}	n	Ti/(Ti+Fe) [at%] mean	(σ)	X_{Ilm}	n	Ti/(Ti+Fe) [at%] mean	(σ)
5F92x0.5	1.6	Tmt	42	7.84	(11)	0.24							
5F92x0.25[7]	2.3	Tmt	8	7.50	(17)	0.23							
F87 (f) 5	-0.7	Tmt	16	13.40	(186)	0.40							
F87 (g) 5	-1.4	Tmt	14	13.86	(175)	0.42							
F72 (g) 5	-1.4	Tmt	15	27.72	(39)	0.83							
5F97a	4.2	Tmt+Ilm_{ss}	10	0.66	(03)	0.02	9	6.86	(21)	0.14			
5F87x0.25	2.3	Tmt+Ilm_{ss}	10	7.51	(14)	0.23	10	24.92	(14)	0.50			
5F87x0.5	1.6	Tmt+Ilm_{ss}	12	11.70	(09)	0.35	11	30.06	(18)	0.60			
5F76x0.5	1.6	Tmt+Ilm_{ss}	10	11.83	(11)	0.35	10	30.14	(18)	0.60			
5F72x0.5	1.6	Tmt+Ilm_{ss}	11	11.66	(17)	0.35	10	30.12	(26)	0.60			
5F76x0.65	1.3	Tmt+Ilm_{ss}	11	13.40	(11)	0.40	12	31.79	(13)	0.64			
5F72x0.65	1.3	Tmt+Ilm_{ss}	14	13.75	(16)	0.41	13	32.16	(16)	0.64			
5F72x1.25	0.7	Tmt+Ilm_{ss}	10	18.03	(15)	0.54	10	36.34	(16)	0.73			
5F69x1.25	0.7	Tmt+Ilm_{ss}	10	18.22	(10)	0.55	10	36.57	(20)	0.73			
5F69Qx2.8	-0.1	Tmt+Ilm_{ss}	10	22.12	(13)	0.66	10	40.08	(12)	0.80			
5F69Qx2.8a	-0.1	Tmt+Ilm_{ss}	10	22.10	(15)	0.66	10	40.03	(16)	0.80			
5F69x2.8a	-0.1	Tmt+Ilm_{ss}	10	21.66	(11)	0.65	11	39.42	(18)	0.79			
5F65x2.8a[8]	-0.1	Tmt, Ilm_{ss}	-	-	-	-	-	-	-	-			
5F63x2.8	-0.1	Tmt+Ilm_{ss}	10	22.01	(11)	0.66	10	40.20	(22)	0.80			
5F63x2.8a	-0.1	Tmt+Ilm_{ss}	10	22.27	(14)	0.67	10	40.21	(19)	0.80			
F72 (f) 5	-0.7	Tmt+Ilm_{ss}	11	24.85	(21)	0.75	14	44.55	(32)	0.89			
F69 (g) 5	-1.5	Tmt+Ilm_{ss}	10	28.22	(17)	0.85	10	47.05	(32)	0.94			
5F63x33.5	-2.6	Tmt+Ilm_{ss}	10	31.12	(12)	0.93	10	49.02	(26)	0.98			
5F57x33.5	-2.6	Tmt+Ilm_{ss}	9	31.21	(13)	0.94	10	48.91	(12)	0.98			
5F60x61.5	-3.6	Tmt+Ilm_{ss}	10	32.64	(15)	0.98	10	49.55	(19)	0.99			
5F54.5x61.5	-3.6	Tmt+Ilm_{ss}	10	32.52	(14)	0.98	10	49.50	(17)	0.99			
5F60x83.5	-4.6	Tmt+Ilm_{ss}	10	34.15	(09)	1.02	10	50.40	(21)	1.01			

Table A.10: Phase compositions of synthesis and re-equilibration run products at 1200 °C, system Fe-Ti-O, derived by EMP analysis

run no	ΔNNO	assemblage	Tmt				Ilm_{ss}				Psb_{ss}		
			n	Ti/(Ti+Fe) [at%] mean	(σ)	X_{Usp}	n	Ti/(Ti+Fe) [at%] mean	(σ)	X_{Ilm}	n	Ti/(Ti+Fe) [at%] mean	(σ)
5F54.5x83.5	-4.6	Tmt+Ilm_{ss}	10	34.46	(23)	1.03	10	50.20	(18)	1.00			
5F92a	4.2	Ilm_{ss}					64	7.85	(10)	0.16			
5F90a	4.2	Ilm_{ss}					43	8.99	(84)	0.18			
F87(a)5	4.3	Ilm_{ss}					10	13.11	(94)	0.26			
5F76a	4.2	Ilm_{ss}+Psb_{ss}					12	14.06	(20)	0.28	12	36.66	(38)
5F72a	4.2	Ilm_{ss}+Psb_{ss}					11	14.17	(19)	0.28	10	37.20	(13)
5F57x0.25	2.3	Ilm_{ss}+Psb_{ss}					10	28.39	(29)	0.57	10	47.33	(24)
5F57x0.5	1.6	Ilm_{ss}+Psb_{ss}					10	32.86	(42)	0.66	10	51.04	(22)
5F57x0.65	1.3	Ilm_{ss}+Psb_{ss}					10	34.81	(24)	0.70	10	52.55	(21)
5F50x0.65	1.3	Ilm_{ss}+Psb_{ss}					12	34.84	(16)	0.70	12	52.61	(18)
5F50x1.25	0.7	Ilm_{ss}+Psb_{ss}					10	39.10	(18)	0.78	10	56.42	(11)
5F47x2.8	-0.1	Ilm_{ss}+Psb_{ss}					10	43.49	(11)	0.87	10	58.96	(22)
5F47x2.8a	-0.1	Ilm_{ss}+Psb_{ss}					10	43.21	(13)	0.86	10	58.40	(11)
F47 (f) 5	-0.5	Ilm_{ss}+Psb_{ss}					10	46.82	(32)	0.94	10	60.92	(24)
F42 (g) 5	-1.5	Ilm_{ss}+Psb_{ss}					10	49.07	(20)	0.98	10	63.90	(34)
5F42x33.5	-2.6	Ilm_{ss}+Psb_{ss}					10	49.92	(13)	1.00	10	65.77	(14)
5F42x61.5	-3.6	Ilm_{ss}+Psb_{ss}					10	50.82	(30)	1.02	10	67.51	(21)
5F42x83.5	-4.6	Ilm_{ss}+Psb_{ss}					10	51.64	(17)	1.03	10	69.49	(07)
5F44x2.8	-0.1	Psb_{ss}+Rt[9]									10	61.82	(17)

7) exclusively used to document Ilm_{ss} oxy-exsolution features in Tmt (chapter 3).
8) exclusively used to document Fe-rich rims (chapter 3). No two-phase sample region.
9) 5F44x2.8, Rt: Ti/(Ti+Fe)=99.14 at%

Table A.11: Experimental conditions of 1300 °C synthesis and re-equilibration runs, system Fe-Ti-O. For footnotes see Table A.5.

run no	date[1]	by[2]	ref.[3]	bulk Ti/(Ti+Fe) [at%]	T [°C]	t [h]	buffer/ CO [vol%]	oxygen fugacity[4]			quenching
								-log fO_2	ΔFMQ[4]	ΔNNO[4]	
6F80x81	03.03.04	RE	-	20.0	1300	25	81.00	10.9	-3.6	-4.2	
6F87x18	26.01.04	RE	-	13.0	1299	24	18.00	8.3	-1.0	-1.6	
6F80x34	10.01.04	RE	-	20.0	1300	20	34.00	9.1	-1.8	-2.4	
6F83x66	09.01.04	RE	-	17.0	1300	25	66.00	10.2	-2.9	-3.5	
6F80x66	09.01.04	RE	-	20.0	1300	25	66.00	10.2	-2.9	-3.5	
6F100x0	13.04.04	RE	-	0.0	1300	25	0.00	3.4	3.9	3.3	
6F97x0.15	05.02.01	HH	L05	3.0	1303	24	0.15	3.9	3.4	2.8	EQ[5]
6F97x1.6	30.01.01	HH	L05	3.0	1303	23	1.58	6.0	1.3	0.7	EQ
6F92x1.6	30.01.01	HH	L05	8.0	1303	23	1.58	6.0	1.3	0.7	EQ
6F87x1.6	30.01.01	HH	L05	13.3	1303	23	1.58	6.0	1.3	0.7	EQ
6F100x2.4	04.03.04	RE	-	0.0	1300	45	2.40	6.4	0.9	0.3	
6F97x2.4	04.03.04	RE	-	3.0	1300	45	2.40	6.4	0.9	0.3	
6F92x2.4	04.03.04	RE	-	8.0	1300	45	2.40	6.4	0.9	0.3	
6F87x2.4	04.03.04	RE	-	13.0	1300	45	2.40	6.4	0.9	0.3	
6F80x2.4	04.03.04	RE	-	20.0	1300	45	2.40	6.4	0.9	0.3	
F87 (f) 6	07.01.00	MK	L05	13.2	1300	>22	5.76	7.1	0.2	-0.4	DQ?[5]
6F92x12	13.10.04	RE	-	8.0	1300	23	12.00	7.9	-0.6	-1.3	
6F83ax18	26.01.04	RE	L05	17.0	1299	24	18.00	8.3	-1.0	-1.6	
6F80x18	26.01.04	RE	L05	20.0	1299	24	18.00	8.3	-1.0	-1.6	
6F76x34	10.01.04	RE	L05	23.5	1300	20	34.00	9.1	-1.8	-2.4	
6F72x49	29.02.04	RE	-	28.0	1300	24	49.00	9.7	-2.4	-3.0	
6F69x81	03.03.04	RE	-	31.0	1300	25	81.00	10.9	-3.6	-4.2	
6F68x81	03.03.04	RE	-	32.0	1300	25	81.00	10.9	-3.6	-4.2	
6F67x81	03.03.04	RE	-	33.0	1300	25	81.00	10.9	-3.6	-4.2	
6F97x0	13.04.04	RE	-	3.0	1300	25	0.00	3.4	3.9	3.3	
6F92x0	13.04.04	RE	-	8.0	1300	25	0.00	3.4	3.9	3.3	
6F90x0	05.01.04	US	-	10.0	1300	43	0.00	3.3	4.0	3.4	EQ

Table A.11: Experimental conditions of 1300 °C synthesis and re-equilibration runs, system Fe-Ti-O. For footnotes see Table A.5.

run no	date[1]	by[2]	ref.[3]	bulk Ti/(Ti+Fe) [at%]	T [°C]	t [h]	buffer/ CO [vol%]	oxygen fugacity[4]			quenching
								-log fO_2	ΔFMQ[4]	ΔNNO[4]	
6F92a	18.02.01	HH	L05	8.0	1302	22	0.00	3.3	4.0	3.4	?[5]
6F92x0.15	05.02.01	HH	L05	8.0	1303	24	0.15	3.9	3.4	2.8	EQ
6F87x0.15	05.02.01	HH	L05	13.3	1303	24	0.15	3.9	3.4	2.8	EQ
F76 (d) 6	19.02.00	MK	L05	23.5	1300	42	0.25	4.4	2.9	2.3	EQ
6F80x0.5	17.01.01	HH	L05	20.0	1301	25	0.50	4.8	2.5	1.9	EQ
6F76x0.5	16.01.01	HH	L05	23.5	1301	42	0.50	4.8	2.5	1.9	DQ
6F80x0.75	17.01.01	HH	L05	20.0	1301	40	0.75	5.2	2.1	1.4	DQ
6F76x0.75	17.01.01	HH	L05	23.5	1301	40	0.75	5.2	2.1	1.4	DQ
6F72x1.5	08.02.01	HH	L05	28.0	1302	24	1.50	5.9	1.4	0.8	EQ
6F69x1.5	08.02.01	HH	L05	31.0	1302	24	1.50	5.9	1.4	0.8	EQ
6F69x1.5a	12.10.04	RE	-	31.0	1300	24	1.50	6.0	1.3	0.7	
6F76x1.6	31.01.01	HH	L05	23.5	1303	23	1.58	6.0	1.3	0.7	EQ
6F72x1.6	31.01.01	HH	L05	28.0	1303	23	1.58	6.0	1.3	0.7	EQ
6F69x1.6	31.01.01	HH	L05	31.0	1303	23	1.58	6.0	1.3	0.7	EQ
6F72x2.4	05.12.03	RE	L05	28.0	1299	25	2.40	6.4	0.9	0.3	
6F67x2.4	05.12.03	RE	L05	33.0	1299	25	2.40	6.4	0.9	0.3	
6F76x3.4	01.12.04	RE	-	24.0	1299	47	3.35	6.7	0.6	0.0	
6F72x3.4	02.12.04	RE	L05	28.0	1299	47	3.35	6.7	0.6	0.0	
6F69x3.4	04.12.04	RE	L05	31.0	1299	47	3.35	6.7	0.6	0.0	
6F67x3.4	03.12.04	RE	-	33.0	1299	47	3.35	6.7	0.6	0.0	
6F60x3.4	05.12.04	RE	-	40.0	1299	47	3.35	6.7	0.6	0.0	
6F72x4.4	11.12.03	RE	L05	28.0	1300	20	4.40	7.0	0.3	-0.3	
6IT60x4.4	11.12.03	RE	L05	40.0	1300	20	4.40	7.0	0.3	-0.3	
F72 (f) 6	07.01.00	MK	L05	27.6	1300	>24	5.76	7.1	0.2	-0.4	DQ
6F67x7[10]	26.11.02	US	-	33.0	1299	50	7.00	7.2	0.1	-0.5	EQ
6F72x8R	10.01.05	US	L05	28.0	1300	26	8.00	7.5	-0.2	-0.8	DQ
6F69x8R	10.01.05	US	L05	31.0	1300	26	8.00	7.5	-0.2	-0.8	DQ

Table A.11: Experimental conditions of 1300 °C synthesis and re-equilibration runs, system Fe-Ti-O. For footnotes see Table A.5.

run no	date[1]	by[2]	ref.[3]	bulk Ti/(Ti+Fe) [at%]	T [°C]	t [h]	buffer/ CO [vol%]	oxygen fugacity[4]			quenching
								-log fO_2	ΔFMQ[4]	ΔNNO[4]	
6F67x8	10.03.03	US/AU	L05	33.0	1300	44	8.00	7.4	-0.1	-0.7	EQ
6F63x8	10.03.03	US/AU	L05	37.0	1300	44	8.00	7.4	-0.1	-0.7	EQ
6F63x8R	10.01.05	US	L05	37.0	1300	26	8.00	7.5	-0.2	-0.8	DQ
6F57x18R	10.04.03	US	L05	43.3	1301	24	18.00	8.3	-1.0	-1.6	DQ
6F57x18	10.04.03	US	L05	43.3	1301	24	18.00	8.3	-1.0	-1.6	DQ
6F63x34	07.04.03	US	L05	37.0	1300	>28	34.00	9.1	-1.8	-2.4	DQ
6F57x34	07.04.03	US	L05	43.3	1300	>28	34.00	9.1	-1.8	-2.4	DQ
6F63x34a	09.04.03	US	L05	37.0	1301	22	34.00	9.1	-1.8	-2.4	DQ
6F57x34a	09.04.03	US	L05	43.3	1301	22	34.00	9.1	-1.8	-2.4	DQ
6IT60x49	29.02.04	RE	-	40.0	1300	24	49.00	9.7	-2.4	-3.0	
6F63x66	15.04.03	US	L05	37.0	1299	18	66.00	10.2	-2.9	-3.5	DQ?
6F57x66	15.04.03	US	L05	43.3	1299	18	66.00	10.2	-2.9	-3.5	DQ?
6F57x66R	15.04.03	US	L05	43.3	1299	18	66.00	10.2	-2.9	-3.5	DQ?
6IT60x81	03.03.04	RE	-	40.0	1300	25	81.00	10.9	-3.6	-4.2	
6IT60x85	14.07.04	RE	-	40.0	1300	30	85.00	11.1	-3.8	-4.4	
6F83a	21.02.02	MB	L05	17.0	1303	46	0.00	3.3	4.0	3.4	DQ?
6F82a	28.01.02	MB	L05	18.0	1300	51	0.00	3.3	4.0	3.4	EQ
6F72a	18.02.01	HH	L05	28.0	1302	22	0.00	3.3	4.0	3.4	
6F63a	18.02.01	HH	L05	37.0	1302	22	0.00	3.3	4.0	3.4	
6F72x0.15	06.02.01	HH	L05	28.0	1303	24	0.15	3.9	3.4	2.8	DQ?
F57 (d) 6	22.03.00	MK	L05	43.3	1300	24	0.25	4.4	2.9	2.3	EQ
6F57x0.5	16.01.01	HH	L05	43.3	1301	42	0.50	4.8	2.5	1.9	
6F57x0.75	17.01.01	HH	L05	43.3	1301	40	0.75	5.2	2.1	1.4	DQ
6F50x0.75	17.01.01	HH	L05	50.0	1301	40	0.75	5.2	2.1	1.4	DQ
6F50x1.5	08.02.01	HH	L05	50.0	1302	24	1.50	5.9	1.4	0.8	EQ
6F47x1.5	08.02.01	HH	L05	52.7	1302	24	1.50	5.9	1.4	0.8	EQ
6F50x2.4	05.12.03	RE	L05	50.0	1299	25	2.40	6.4	0.9	0.3	

Table A.11: Experimental conditions of 1300 °C synthesis and re-equilibration runs, system Fe-Ti-O. For footnotes see Table A.5.

run no	date[1]	by[2]	ref.[3]	bulk Ti/(Ti+Fe) [at%]	T [°C]	t [h]	buffer/ CO [vol%]	oxygen fugacity[4]			quenching
								-log fO_2	ΔFMQ[4]	ΔNNO[4]	
6F47x2.4	05.12.03	RE	L05	53.0	1299	25	2.40	6.4	0.9	0.3	
6F50x4.4	11.12.03	RE	L05	50.0	1300	20	4.40	7.0	0.3	-0.3	
6F42x4.4	11.12.03	RE	L05	58.0	1300	20	4.40	7.0	0.3	-0.3	
F47 (f) 6	21.03.00	MK	L05	52.7	1300	24	5.76	7.1	0.2	-0.4	
6F47x7	27.11.02	US	L05	52.7	1300	60	7.00	7.2	0.1	-0.6	DQ
6F47x8	10.03.03	US/AU	L05	52.7	1300	44	8.00	7.4	-0.1	-0.7	EQ
F47 (g) 6	20.03.00	MK	L05	52.7	1300	25	10.28	7.6	-0.3	-0.9	
F42 (g) 6	20.03.00	MK	L05	57.5	1300	25	10.28	7.6	-0.3	-0.9	
6F42x18	10.04.03	US	L05	57.5	1301	24	18.00	8.3	-1.0	-1.6	DQ
6F42x34	07.04.03	US	L05	57.5	1300	>28	34.00	9.1	-1.8	-2.4	DQ
6F42x34a	09.04.03	US	L05	57.5	1301	22	34.00	9.1	-1.8	-2.4	DQ
6F42x49	29.02.04	RE	-	58.0	1300	24	49.00	9.7	-2.4	-3.0	
6F42x66	15.04.03	US	L05	57.5	1299	18	66.00	10.2	-2.9	-3.5	DQ?
6F42x81	03.03.04	RE	-	58.0	1300	25	81.00	10.9	-3.6	-4.2	
6F42x85	14.07.04	RE	-	58.0	1300	30	85.00	11.1	-3.8	-4.4	

10) exclusively used for documentation and analysis of oxy-exsolution textures (chapter 3).

Table A.12: Phase compositions of synthesis and re-equilibration run products at 1300 °C, system Fe-Ti-O, derived by EMP analysis

run no	ΔNNO	assemblage	Tmt				Ilm_{ss}				Psb_{ss}		
			n	Ti/(Ti+Fe) [at%] mean	(σ)	X_{Usp}	n	Ti/(Ti+Fe) [at%] mean	(σ)	X_{Ilm}	n	Ti/(Ti+Fe) [at%] mean	(σ)
6F80x81	-4.2	Tmt+Fe°	10	30.17	(25)	0.91							
6F87x18	-1.6	Tmt+Wus	10	12.78	(50)	0.38							
6F80x34	-2.4	Tmt+Wus	10	21.09	(15)	0.63							
6F83x66	-3.5	Tmt+Wus	10	26.79	(12)	0.80							
6F80x66	-3.5	Tmt+Wus	10	26.62	(24)	0.80							
6F100x0	3.3	Tmt	10	0.01	(02)	0.00							
6F97x0.15	2.8	Tmt	10	2.91	(05)	0.09							
6F97x1.6	0.7	Tmt	10	2.82	(13)	0.08							
6F92x1.6	0.7	Tmt	10	7.60	(24)	0.23							
6F87x1.6	0.7	Tmt	10	12.92	(52)	0.39							
6F100x2.4	0.3	Tmt	10	0.00	(00)	0.00							
6F97x2.4	0.3	Tmt	10	2.78	(05)	0.08							
6F92x2.4	0.3	Tmt	10	7.52	(23)	0.23							
6F87x2.4	0.3	Tmt	10	13.04	(20)	0.39							
6F80x2.4	0.3	Tmt	10	20.22	(14)	0.61							
F87 (f) 6	-0.4	Tmt	12	13.33	(73)	0.40							
6F92x12	-1.3	Tmt	10	7.87	(10)	0.24							
6F83ax18	-1.6	Tmt	10	16.75	(21)	0.50							
6F80x18	-1.6	Tmt	10	20.04	(18)	0.60							
6F76x34	-2.4	Tmt	10	23.70	(71)	0.71							
6F72x49	-3.0	Tmt	10	28.43	(29)	0.85							
6F69x81	-4.2	Tmt	10	30.94	(20)	0.93							
6F68x81	-4.2	Tmt	10	31.95	(11)	0.96							
6F67x81	-4.2	Tmt	10	32.95	(11)	0.99							
6F97x0	3.3	Tmt+Ilm_{ss}	10	2.65	(05)	0.08	2	15.15	18.00	0.30			
6F92x0	3.3	Tmt+Ilm_{ss}	10	2.80	(10)	0.08	10	15.22	23.00	0.30			
6F90x0	3.4	Tmt+Ilm_{ss}	10	2.78	(06)	0.08	10	15.35	(07)	0.31			

Table A.12: Phase compositions of synthesis and re-equilibration run products at 1300 °C, system Fe-Ti-O, derived by EMP analysis

run no	ΔNNO	assemblage	Tmt				Ilm_{ss}				Psb_{ss}		
			n	Ti/(Ti+Fe) [at%] mean	(σ)	X_{Usp}	n	Ti/(Ti+Fe) [at%] mean	(σ)	X_{Ilm}	n	Ti/(Ti+Fe) [at%] mean	(σ)
6F92a	3.4	Tmt+Ilm_{ss}	10	2.86	(06)	0.09	12	15.19	(12)	0.30			
6F92x0.15	2.8	Tmt+Ilm_{ss}	10	5.38	(05)	0.16	10	20.96	(08)	0.42			
6F87x0.15	2.8	Tmt+Ilm_{ss}	10	5.38	(09)	0.16	10	20.96	(24)	0.42			
F76 (d) 6	2.3	Tmt+Ilm_{ss}	10	7.61	(13)	0.23	10	24.98	(37)	0.50			
6F80x0.5	1.9	Tmt+Ilm_{ss}	14	11.00	(16)	0.33	10	28.49	(18)	0.57			
6F76x0.5	1.9	Tmt+Ilm_{ss}	10	11.32	(19)	0.34	11	29.35	(20)	0.59			
6F80x0.75	1.4	Tmt+Ilm_{ss}	12	13.80	(25)	0.41	10	31.49	(24)	0.63			
6F76x0.75	1.4	Tmt+Ilm_{ss}	12	13.81	(11)	0.41	12	31.77	(14)	0.64			
6F72x1.5	0.8	Tmt+Ilm_{ss}	11	18.36	(13)	0.55	11	36.20	(21)	0.72			
6F69x1.5	0.8	Tmt+Ilm_{ss}	11	18.36	(14)	0.55	14	36.18	(19)	0.72			
6F69x1.5a	0.7	Tmt+Ilm_{ss}	5	18.55	(09)	0.56	5	36.29	(21)	0.73			
6F76x1.6	0.7	Tmt+Ilm_{ss}	10	18.53	(09)	0.56	10	36.28	(28)	0.73			
6F72x1.6	0.7	Tmt+Ilm_{ss}	10	18.55	(11)	0.56	10	36.21	(17)	0.72			
6F69x1.6	0.7	Tmt+Ilm_{ss}	10	18.60	(25)	0.56	10	36.24	(16)	0.72			
6F72x2.4	0.3	Tmt+Ilm_{ss}	10	20.92	(11)	0.63	10	38.19	(14)	0.76			
6F67x2.4	0.3	Tmt+Ilm_{ss}	10	20.91	(15)	0.63	10	38.31	(13)	0.77			
6F76x3.4	0.0	Tmt+Ilm_{ss}	10	22.73	(17)	0.68	10	40.32	(17)	0.81			
6F72x3.4	0.0	Tmt+Ilm_{ss}	10	22.82	(13)	0.68	10	39.99	(15)	0.80			
6F69x3.4	0.0	Tmt+Ilm_{ss}	10	22.84	(12)	0.69	10	39.96	(17)	0.80			
6F67x3.4	0.0	Tmt+Ilm_{ss}	10	23.00	(17)	0.69	10	40.43	(16)	0.81			
6F60x3.4	0.0	Tmt+Ilm_{ss}	10	23.02	(13)	0.69	10	40.24	(17)	0.80			
6F72x4.4	-0.3	Tmt+Ilm_{ss}	10	24.42	(13)	0.73	10	41.21	(21)	0.82			
6IT60x4.4	-0.3	Tmt+Ilm_{ss}	10	24.46	(14)	0.73	10	41.52	(14)	0.83			
F72 (f) 6	-0.4	Tmt+Ilm_{ss}	10	25.32	(18)	0.76	10	42.61	(16)	0.85			
6F67x7[10]	-0.5	Tmt+Ilm_{ss}	3	25.11	(27)	0.75	3	42.74	(21)	0.85			
6F72x8R	-0.8	Tmt+Ilm_{ss}	10	27.34	(17)	0.82	10	44.19	(16)	0.88			
6F69x8R	-0.8	Tmt+Ilm_{ss}	10	27.36	(12)	0.82	10	44.11	(15)	0.88			

Table A.12: Phase compositions of synthesis and re-equilibration run products at 1300 °C, system Fe-Ti-O, derived by EMP analysis

run no	ΔNNO	assemblage	Tmt				Ilm_{ss}				Psb_{ss}			
			n	Ti/(Ti+Fe) [at%] mean	(σ)	X_{Usp}	n	Ti/(Ti+Fe) [at%] mean	(σ)	X_{Ilm}	n	Ti/(Ti+Fe) [at%] mean	(σ)	
6F67x8	-0.7	Tmt+Ilm_{ss}	10	26.88	(12)	0.81	10	43.48	(17)	0.87				
6F63x8	-0.7	Tmt+Ilm_{ss}	10	27.01	(22)	0.81	10	43.75	(21)	0.88				
6F63x8R	-0.8	Tmt+Ilm_{ss}	10	27.57	(11)	0.83	10	44.26	(18)	0.89				
6F57x18R	-1.6	Tmt+Ilm_{ss}	10	30.41	(13)	0.91	10	47.58	(20)	0.95				
6F57x18	-1.6	Tmt+Ilm_{ss}	10	30.20	(13)	0.91	10	47.45	(25)	0.95				
6F63x34	-2.4	Tmt+Ilm_{ss}	10	32.09	(10)	0.96	10	48.77	(13)	0.98				
6F57x34	-2.4	Tmt+Ilm_{ss}	10	32.16	(09)	0.96	10	48.95	(16)	0.98				
6F63x34a	-2.4	Tmt+Ilm_{ss}	10	31.89	(19)	0.96	10	48.81	(20)	0.98				
6F57x34a	-2.4	Tmt+Ilm_{ss}	10	31.89	(18)	0.96	10	48.89	(17)	0.98				
6IT60x49	-3.0	Tmt+Ilm_{ss}	10	33.60	(14)	1.01	10	50.24	(29)	1.00				
6F63x66	-3.5	Tmt+Ilm_{ss}	11	34.31	(16)	1.03	8	50.17	(24)	1.00				
6F57x66	-3.5	Tmt+Ilm_{ss}	10	34.39	(17)	1.03	10	50.40	(19)	1.01				
6F57x66R	-3.5	Tmt+Ilm_{ss}	10	34.52	(26)	1.04	10	50.65	(17)	1.01				
6IT60x81	-4.2	Tmt+Ilm_{ss}	10	35.45	(13)	1.06	10	51.19	(24)	1.02				
6IT60x85	-4.4	Tmt+Ilm_{ss}	10	36.25	(21)	1.09	10	51.08	17.00	1.02				
6F83a	3.4	Ilm_{ss}					52	16.59	(12)	0.33				
6F82a	3.4	Ilm_{ss}					30	17.64	(22)	0.35				
6F72a	3.4	Ilm_{ss}+Psb_{ss}					12	20.50	(15)	0.41	11	41.26	(26)	
6F63a	3.4	Ilm_{ss}+Psb_{ss}					12	20.92	(14)	0.42	9	41.39	(15)	
6F72x0.15	2.8	Ilm_{ss}+Psb_{ss}					10	26.12	(17)	0.52	16	45.13	(29)	
F57 (d) 6	2.3	Ilm_{ss}+Psb_{ss}					10	27.12	(24)	0.54	10	46.20	(24)	
6F57x0.5	1.9	Ilm_{ss}+Psb_{ss}					12	31.40	(13)	0.63	13	49.59	(17)	
6F57x0.75	1.4	Ilm_{ss}+Psb_{ss}					10	34.49	(09)	0.69	10	52.20	(20)	
6F50x0.75	1.4	Ilm_{ss}+Psb_{ss}					10	34.76	(12)	0.70	10	52.44	(20)	
6F50x1.5	0.8	Ilm_{ss}+Psb_{ss}					10	38.35	(18)	0.77	10	55.47	(24)	
6F47x1.5	0.8	Ilm_{ss}+Psb_{ss}					10	38.54	(12)	0.77	10	55.70	(15)	
6F50x2.4	0.3	Ilm_{ss}+Psb_{ss}					10	40.58	(16)	0.81	10	57.18	(11)	

Table A.12: Phase compositions of synthesis and re-equilibration run products at 1300 °C, system Fe-Ti-O, derived by EMP analysis

run no	ΔNNO	assemblage	Tmt				Ilm_{ss}				Psb_{ss}		
			n	Ti/(Ti+Fe) [at%] mean	(σ)	X_{Usp}	n	Ti/(Ti+Fe) [at%] mean	(σ)	X_{Ilm}	n	Ti/(Ti+Fe) [at%] mean	(σ)
6F47x2.4	0.3	Ilm_{ss}+Psb_{ss}					10	40.44	(18)	0.81	10	57.28	(13)
6F50x4.4	-0.3	Ilm_{ss}+Psb_{ss}					10	43.35	(28)	0.87	10	59.76	(15)
6F42x4.4	-0.3	Ilm_{ss}+Psb_{ss}					10	43.41	(21)	0.87	10	59.80	(14)
F47 (f) 6	-0.4	Ilm_{ss}+Psb_{ss}					10	44.54	(23)	0.89	10	60.64	(23)
6F47x7	-0.6	Ilm_{ss}+Psb_{ss}					10	45.71	(14)	0.91	10	61.63	(21)
6F47x8	-0.7	Ilm_{ss}+Psb_{ss}					10	46.02	(15)	0.92	9	61.81	(17)
F47 (g) 6	-0.9	Ilm_{ss}+Psb_{ss}					11	47.29	(17)	0.95	13	62.51	(18)
F42 (g) 6	-0.9	Ilm_{ss}+Psb_{ss}					10	47.31	(30)	0.95	10	62.55	(22)
6F42x18	-1.6	Ilm_{ss}+Psb_{ss}					10	48.96	(19)	0.98	10	64.21	(19)
6F42x34	-2.4	Ilm_{ss}+Psb_{ss}					10	50.25	(20)	1.01	10	65.87	(14)
6F42x34a	-2.4	Ilm_{ss}+Psb_{ss}					10	50.14	(17)	1.00	10	65.64	(25)
6F42x49	-3.0	Ilm_{ss}+Psb_{ss}					10	51.29	(19)	1.03	10	67.25	(25)
6F42x66	-3.5	Ilm_{ss}+Psb_{ss}					10	51.80	(29)	1.04	10	68.23	(13)
6F42x81	-4.2	Ilm_{ss}+Psb_{ss}					10	52.60	(37)	1.05	10	69.53	(26)
6F42x85	-4.4	Ilm_{ss}+Psb_{ss}					10	53.30	17.00	1.07	10	70.38	(18)

10) exclusively used for documentation and analysis of oxy-exsolution textures (chapter 3).

Table A.13: Experimental conditions of 1100 °C synthesis runs with Mg-Al bearing starting mixtures. For footnotes see Table A.5.

run no	date[1]	by[2]	ref.[3]	bulk Ti/(Ti+Fe) [at%]	T [°C]	t [h]	buffer/ CO [vol%]	oxygen fugacity[4]			quenching
								-log fO_2	ΔFMQ[4]	ΔNNO[4]	
3F59.5A5.5x16.5	05.05.03	US[2]	-	40.6	1100	135	16.51	-10.9	-1.2	-2.0	DQ[5]
3IT60A2IW	26.02.04	US	-	40.0	1100	332	IW[4]	-13.3	-3.6	-4.4	AQ[5]
3F57.4M10x1.25	26.03.03	US	-	42.6	1101	144	1.25	-8.4	1.2	0.5	?[5]
3F57.4M10x16.5	05.05.03	US	-	42.6	1100	135	16.51	-10.9	-1.2	-2.0	DQ
3IT60M2IW	26.02.04	US	-	40.0	1100	332	IW	-13.3	-3.6	-4.4	AQ
3IT60M1A1WM	09.02.04	US	-	40.0	1100	330	WM[3]	-10.9	-1.3	-2.0	AQ
3IT60M1A1IW	09.02.04	US	-	40.0	1100	330	IW	-13.3	-3.6	-4.4	AQ

Table A.14: Phase compositions of Mg-Al bearing synthesis run products at 1100 °C, derived by EMP analysis.

run no	ass.[11]	Tmt				Ilm_{ss}				Psb_{ss}				
			[wt%]				[wt%]				[wt%]			
		n	Al_2O_3	MgO	X'_{Usp}[12]	n	Al[13]	Mg[13]	X'_{Ilm}	n	TiO_2	$Fe_{tot}O$	Al[13]	Mg[13]
3F59.5A5.5x16.5	TI	10	9.61	0.00	0.88	10	0.58	0.00	0.97					
3IT60A2IW	TI	10	3.19	0.00	0.98	9	0.13	0.00	0.99					
3F57.4M10x1.25	TI	10	0.00	2.63	0.59	10	0.00	3.17	0.83					
3F57.4M10x16.5	TI	11	0.00	2.70	0.86	10	0.00	3.39	0.97					
3IT60M2IW	TI	10	0.00	1.87	0.98	10	0.00	2.27	1.00					
3IT60M1A1WM	TI	15	1.61	0.86	0.83	15	0.05	1.08	0.97					
3IT60M1A1IW	TI	15	1.29	0.89	0.98	14	0.00	1.07	1.00					

11) assemblage: TI: Tmt+Ilm_{ss}; IP: Ilm_{ss}+Psb_{ss}; TIP: Tmt+Ilm_{ss}+Psb_{ss}, WT: Wus+Tmt, FT: Fe°+Tmt, FWT: Fe°+Wus+Tmt, I: Ilm_{ss}
12) X'_{Usp} and X'_{Ilm} derived according to equations 6.5, 6.6, chapter 6.
13) Al: Al_2O_3 Mg: MgO

Table A.15: Experimental conditions of 1200 °C synthesis runs with Mg-Al bearing starting mixtures. For footnotes see Table A.5.

run no	date[1]	by[2]	ref.[3]	bulk Ti/(Ti+Fe) [at%]	T [°C]	t [h]	buffer/ CO [vol%]	oxygen fugacity[4]			quenching
								-log fO_2	ΔFMQ[4]	ΔNNO[4]	
5IT60A2x5.5a	24.11.03	US[2]	-	40.0	1200	>75	5.50	-8.5	-0.1	-0.8	DQ[5]
5IT60A2x66	18.12.03	US	-	40.0	1200	71	66.00	-11.5	-3.1	-3.7	DQ
5F59.5A5.5x1.25	30.04.03	US	-	40.6	1200	68	1.25	-7.0	1.4	0.7	?[5]
5F59.5A5.5x33.5[14]	02.03.03	US	-	40.6	1201	52	33.5	-10.3	-1.9	-2.6	?
5F59.5A5.5x61.5[14]	13.05.03	AU	-	40.6	1200	47.5	61.5	-11.3	-2.9	-3.6	?
5F59.5A5.5x83.5[14]	29.04.03	AU	-	40.6	1200	27	83.5	-12.3	-3.9	-4.6	?
5F70M2x1.25a	24.11.03	US	-	30.0	1200	>100	1.25	-7.1	1.3	0.6	DQ
5IT60M2x5.5a	24.11.03	US	-	40.0	1200	>75	5.50	-8.5	-0.1	-0.8	?
5F57.4M10x33.5	22.04.03	US	-	42.6	1201	52	33.50	-10.3	-1.9	-2.6	DQ
5F57.4M10x61.5	13.05.03	AU[2]	-	42.6	1200	48	61.50	-11.3	-2.9	-3.6	DQ
5IT60M2x66	18.12.03	US	-	40.0	1200	71	66.00	-11.5	-3.1	-3.7	DQ
5F57.4M10x83.5	29.04.03	AU	-	42.6	1200	27	83.50	-12.3	-3.9	-4.6	DQ
5IT70M1A1x1.25a	24.11.03	US	-	30.0	1200	>100	1.25	-7.1	1.3	0.6	?
5IT70M1A1x5.5a	24.11.03	US	-	30.0	1200	>75	5.50	-8.5	-0.1	-0.8	DQ
5IT60M1A1x5.5a	24.11.03	US	-	40.0	1200	>75	5.50	-8.5	-0.1	-0.8	DQ
5IT60M1A1x66	18.12.03	US	-	40.0	1200	71	66.00	-11.5	-3.1	-3.7	DQ
5IT60M1A1x1.25a	24.11.03	US	-	40.0	1200	>100	1.25	-7.1	1.3	0.6	?
5IP46M1A1x1.25a	24.11.03	US	-	54.0	1200	>100	1.25	-7.1	1.3	0.0	?
5IP46M1A1x5.5a	24.11.03	US	-	54.0	1200	>75	5.50	-8.5	-0.1	-0.8	DQ
5IP46M1A1x66	18.12.03	US	-	54.0	1200	71	66.00	-11.5	-3.1	-3.7	DQ

14) Run products contain Fe-Al spinel. Exclusively used to document texture and inhomogeneity (chapter 3).

Table A.16: Phase compositions of Mg-Al bearing synthesis run products at 1200 °C, derived by EMP analysis. For footnotes see Table A.14.

run no	ass.[11]	Tmt				Ilm_{ss}				Psb_{ss}				
			[wt%]				[wt%]				[wt%]			
		n	Al_2O_3	MgO	X'_{Usp}[12]	n	Al[13]	Mg[13]	X'_{Ilm}	n	TiO_2	$Fe_{tot}O$	Al[13]	Mg[13]
5IT60A2x5.5a	TI	10	4.55	0.00	0.79	10	0.75	0.00	0.91					
5IT60A2x66	TI	10	2.92	0.00	1.00	10	0.28	0.00	1.00					
5F59.5A5.5x1.25	TIP	6	7.93	0.01	0.55	10	1.06	0.00	0.75	5	54.89	38.46	3.05	0.00
5F70M2x1.25a	TI	10	0.00	2.14	0.57	10	0.00	1.85	0.72					
5IT60M2x5.5a	TI	10	0.00	1.83	0.77	10	0.00	2.12	0.91					
5F57.4M10x33.5	TI	10	0.00	2.90	0.94	10	0.00	3.38	0.99					
5F57.4M10x61.5	TI	10	0.00	2.86	0.98	10	0.00	3.35	1.00					
5IT60M2x66	TI	10	0.00	1.92	0.99	15	0.00	2.26	1.00					
5F57.4M10x83.5	TI	10	0.00	2.94	1.00	10	0.00	3.41	1.00					
5IT70M1A1x1.25a	TI	10	1.22	1.09	0.56	10	0.30	0.91	0.73					
5IT70M1A1x5.5a	TI	10	1.12	0.99	0.77	10	0.13	1.14	0.91					
5IT60M1A1x5.5a	TI	10	1.37	0.91	0.77	10	0.17	1.03	0.90					
5IT60M1A1x66	TI	5	1.29	0.94	1.00	10	0.07	1.10	1.00					
5IT60M1A1x1.25a	IP					10	0.50	0.95	0.74	10	56.76	37.07	1.74	1.40
5IP46M1A1x1.25a	IP					10	0.33	0.69	0.76	10	57.36	38.16	0.87	1.04
5IP46M1A1x5.5a	IP					10	0.33	0.93	0.94	10	62.87	32.89	1.66	1.07
5IP46M1A1x66	IP					10	0.46	0.98	1.00	15	69.04	26.78	2.80	1.12

Table A.17: Experimental conditions of 1300 °C synthesis runs with Mg-Al bearing starting mixtures. For footnotes see Table A.5.

run no	date[1]	by[2]	ref.[3]	bulk Ti/(Ti+Fe) [at%]	T [°C]	t [h]	buffer/ CO [vol%]	oxygen fugacity[4]			quenching
								-log fO_2	ΔFMQ[4]	ΔNNO[4]	
6F90A10x28	27.09.04	VG[2]	-	10.0	1300	48	28.00	8.8	-1.5	-2.1	DQ[5]
6F90A10x55	16.09.04	VG	-	10.0	1300	46	55.00	9.8	-2.5	-3.1	DQ
6F70A2x1.5	27.02.04	US	-	30.0	1300	53	1.50	6.0	1.3	0.7	EQ[5]
6F60A2x28	27.09.04	VG	-	40.0	1300	48	28.00	8.8	-1.5	-2.1	DQ
6F60A2x55	16.09.04	VG	-	40.0	1300	46	55.00	9.8	-2.5	-3.1	DQ
6IT60A2x66	09.02.04	US	-	40.0	1300	53	66.00	10.2	-2.9	-3.5	EQ
6IT60A2x1.5a	18.12.03	US	-	40.0	1300	53	1.50	6.0	1.3	0.7	DQ
6IT60A2x6a	27.11.03	US	-	40.0	1299	<61	6.00	7.2	0.1	-0.5	?[5]
6F59.5A5.5x18	10.04.03	US	-	40.6	1301	24	18.00	8.3	-1.0	-1.6	DQ
6F59.5A5.5x34	07.04.03	US	-	40.6	1300	>28	34.00	9.1	-1.8	-2.4	DQ
6F59.5A5.5x34a	09.04.03	US	-	40.6	1301	22	34.00	9.1	-1.8	-2.4	DQ
6F59.5A5.5x66	15.04.03	US	-	40.6	1299	18	66.00	10.2	-2.9	-3.5	DQ
6F59.5A5.5x8	10.03.03	US/AU	-	40.6	1300	44	8.00	7.4	-0.1	-0.7	EQ
6IT60M2x1.5a	18.12.03	US	-	40.0	1300	53	1.50	6.0	1.3	0.7	DQ
6F70M2x1.5	27.02.04	US	-	30.0	1300	53	1.50	6.0	1.3	0.7	EQ
6IT60M2x6a	27.11.03	US	-	40.0	1299	<61	6.00	7.2	0.1	-0.5	?
6F57.4M10x8	10.03.03	US / AU	-	42.6	1300	44	8.00	7.4	-0.1	-0.7	EQ
6F57.4M10x18	10.04.03	US	-	42.6	1301	24	18.00	8.3	-1.0	-1.6	DQ
6F57.4M10x34	07.04.03	US	-	42.6	1300	>28	34.00	9.1	-1.8	-2.4	DQ
6F57.4M10x34a	09.04.03	US	-	42.6	1301	22	34.00	9.1	-1.8	-2.4	DQ
6IT60M2x55	16.09.04	VG	-	40.0	1300	46	55.00	9.8	-2.5	-3.1	DQ
6IT60M2x66	09.02.04	US	-	40.0	1300	53	66.00	10.2	-2.9	-3.5	EQ
6F57.4M10x66	15.04.03	US	-	42.6	1299	18	66.00	10.2	-2.9	-3.5	DQ
6F90M1A1x28	27.09.04	VG	-	10.0	1300	48	28.00	8.8	-1.5	-2.1	DQ
6F90M1A1x55	16.09.04	VG	-	10.0	1300	46	55.00	9.8	-2.5	-3.1	DQ

Table A.17: Experimental conditions of 1300 °C synthesis runs with Mg-Al bearing starting mixtures. For footnotes see Table A.5.

run no	date[1]	by[2]	ref.[3]	bulk Ti/(Ti+Fe) [at%]	T [°C]	t [h]	buffer/ CO [vol%]	oxygen fugacity[4]			quenching
								-log fO_2	ΔFMQ[4]	ΔNNO[4]	
6F85M1A1x55	16.09.04	VG	-	15.0	1300	46	55.00	9.8	-2.5	-3.1	DQ
6F90M1A1x79	23.09.04	VG	-	10.0	1300	>28	79.50	10.8	-3.5	-4.1	DQ
6F85M1A1x79	23.09.04	VG	-	15.0	1300	>28	79.50	10.8	-3.5	-4.1	DQ
6IT70M1A1x55	16.09.04	VG	-	40.0	1300	46	55.00	9.8	-2.5	-3.1	DQ
6IT70M1A1x28	27.09.04	VG	-	30.0	1300	48	28.00	8.8	-1.5	-2.1	DQ
6IT70M1A1x66	09.02.04	US	-	30.0	1300	53	66.00	10.2	-2.9	-3.5	EQ
6IT70M1A1x79	23.09.04	VG	-	30.0	1300	>28	79.50	10.8	-3.5	-4.1	DQ
6IT70M1A1x1.5	27.02.04	US	-	30.0	1300	53	1.50	6.0	1.3	0.7	EQ
6IT70M1A1x6a	27.11.03	US	-	30.0	1299	<61	6.00	7.2	0.1	-0.5	?
6IT60M1A1x6a	27.11.03	US	-	40.0	1299	<61	6.00	7.2	0.1	-0.5	?
6IT60M1A1x66	09.02.04	US	-	40.0	1300	53	66.00	10.2	-2.9	-3.5	EQ
6IT60M1A1x1.5a	18.12.03	US	-	40.0	1300	53	1.50	6.0	1.3	0.7	DQ
6IP46M1A1x1.5a	18.12.03	US	-	54.0	1300	53	1.50	6.0	1.3	0.7	DQ
6IP46M1A1x6a	27.11.03	US	-	54.0	1299	<61	6.00	7.2	0.1	-0.5	?
6IP46M1A1x55	16.09.04	VG	-	54.0	1300	46	55.00	9.8	-2.5	-3.1	DQ
6IP46M1A1x66	09.02.04	US	-	54.0	1300	53	66.00	10.2	-2.9	-3.5	EQ
6IP46M1A1x79	23.09.04	VG	-	54.0	1300	>28	79.50	10.8	-3.5	-4.1	DQ

Table A.18: Phase compositions of Mg-Al bearing synthesis run products at 1300 °C, derived by EMP analysis. For footnotes see Table A.14.

run no	ass.[11]	Tmt				Ilm_{ss}				Psb_{ss}				
			[wt%]				[wt%]				[wt%]			
		n	Al_2O_3	MgO	X'_{Usp}[12]	n	Al^{13}	Mg^{13}	X'_{Ilm}	n	TiO_2	$Fe_{tot}O$	Al^{13}	Mg^{13}
6F90A10x28	WT	10	7.43	0.01	0.38									
6F90A10x55	WT	10	11.94	0.04	0.59									
6F70A2x1.5	TI	10	3.42	0.00	0.57	10	1.13	0.00	0.74					
6F60A2x28	TI	10	3.01	0.00	0.96	10	0.59	0.00	0.98					
6F60A2x55	TI	10	2.75	0.00	1.00	10	0.49	0.00	1.00					
6IT60A2x66	TI	10	2.74	0.01	1.00	10	0.59	0.00	1.00					
6IT60A2x1.5a	TIP	10	3.82	0.01	0.58	10	1.28	0.00	0.75	10	54.31	39.46	2.89	0.00
6IT60A2x6a	TIP	10	3.98	0.01	0.80	10	1.25	0.01	0.87	10	60.02	34.97	2.95	0.00
6F59.5A5.5x18	TIP	3	5.43	0.00	0.93	3	1.17	0.00	0.96	3	63.62	31.42	3.76	0.00
6F59.5A5.5x34	TIP	10	5.85	0.00	0.99	10	1.08	0.00	0.99	10	65.26	29.91	4.07	0.00
6F59.5A5.5x34a	TIP	10	5.95	0.01	1.00	10	1.24	0.01	0.99	10	65.72	29.77	4.26	0.00
6F59.5A5.5x66	TIP	10	6.51	0.00	1.00	5	1.22	0.00	1.00	5	67.28	27.76	4.61	0.00
6F59.5A5.5x8	TP	15	4.79	0.00	0.83					15	61.16	34.15	3.33	0.00
6IT60M2x1.5a	Ilm_{ss}					10	0.00	2.00	0.75					
6F70M2x1.5	TI	10	0.03	2.17	0.58	10	0.01	1.83	0.72					
6IT60M2x6a	TI	10	0.02	2.08	0.79	10	0.00	2.00	0.87					
6F57.4M10x8	TI	10	0.00	3.08	0.83	10	0.00	3.21	0.91					
6F57.4M10x18	TI	16	0.00	2.94	0.90	15	0.00	3.24	0.95					
6F57.4M10x34	TI	10	0.00	3.00	0.96	10	0.00	3.33	0.98					
6F57.4M10x34a	TI	10	0.02	2.97	0.97	10	0.00	3.26	0.99					
6IT60M2x55	TI	10	0.00	1.95	1.00	10	0.00	2.17	1.00					
6IT60M2x66	TI	10	0.00	1.94	1.00	10	0.00	2.19	1.00					
6F57.4M10x66	TI	10	0.00	2.99	1.00	10	0.00	3.34	1.00					
6F90M1A1x28	WT	10	1.69	1.02	0.52									
6F90M1A1x55	WT	10	2.52	1.07	0.71									

Table A.18: Phase compositions of Mg-Al bearing synthesis run products at 1300 °C, derived by EMP analysis. For footnotes see Table A.14.

run no	ass.[11]	Tmt				Ilm_{ss}				Psb_{ss}				
			[wt%]				[wt%]				[wt%]			
		n	Al_2O_3	MgO	X'_{Usp}[12]	n	Al[13]	Mg[13]	X'_{Ilm}	n	TiO_2	$Fe_{tot}O$	Al[13]	Mg[13]
6F85M1A1x55	WT	10	1.56	1.05	0.72									
6F90M1A1x79	FWT[11]	5	1.86	1.79	0.87									
6F85M1A1x79	FWT	5	2.99	2.49	0.86									
6IT70M1A1x55	Tmt	10	1.21	1.01	0.89									
6IT70M1A1x28	Tmt	10	0.83	1.01	0.89									
6IT70M1A1x66	Tmt	15	0.86	1.01	0.89									
6IT70M1A1x79	Tmt	10	0.65	0.99	0.90									
6IT70M1A1x1.5	TI	10	1.51	1.12	0.57	10	0.52	0.92	0.73					
6IT70M1A1x6a	TI	10	1.13	1.04	0.79	10	0.39	0.89	0.86					
6IT60M1A1x6a	TI	10	1.97	1.09	0.78	10	0.64	0.94	0.86					
6IT60M1A1x66	TI	10	1.31	0.97	1.00	10	0.27	1.06	1.00					
6IT60M1A1x1.5a	IP					10	0.90	0.94	0.75	10	55.93	37.66	1.89	1.29
6IP46M1A1x1.5a	IP					10	0.52	0.74	0.76	10	56.46	38.25	1.05	1.02
6IP46M1A1x6a	IP					10	0.53	0.82	0.88	10	61.85	33.60	1.21	1.12
6IP46M1A1x55	IP					10	0.48	0.96	1.00	15	68.04	27.68	1.97	1.10
6IP46M1A1x66	IP					10	0.66	0.97	1.00	10	68.60	27.30	2.33	1.10
6IP46M1A1x79	IP					10	0.66	0.97	1.00	10	70.47	25.58	2.55	1.13

Table A.19: Experimental conditions and phase compositions (EMP analysis) of samples annealed at 950 °C, system Fe-Ti±Mg±Al-O.

annealing run no	bulk Ti/(Ti+Fe) [at%]	T [°C]	run duration [*d*]	assemblage	Tmt n	Tmt Ti/(Ti+Fe) [at%] mean	Tmt Ti/(Ti+Fe) [at%] (σ)	Tmt X'_{Usp}	Ilm_{ss} n	Ilm_{ss} Ti/(Ti+Fe) [at%] mean	Ilm_{ss} Ti/(Ti+Fe) [at%] (σ)	Ilm_{ss} X'_{Ilm}
samples **without** oxy-exsolutions annealed at 950 °C after 1300 °C synthesis												
6F92aD	8.0	950	12.0	Tmt+Ilm_{ss}	10	2.15	(24)	0.06	10	15.92	(08)	0.32
6F72x2.4D	28.0	951	32.7	Tmt+Ilm_{ss}	10	17.85	(11)	0.54	10	43.84	(16)	0.88
6F72x4.4D	28.0	951	32.7	Tmt+Ilm_{ss}	10	22.33	(11)	0.67	10	46.90	(18)	0.94
6F57x18D	43.3	948	14.0	Tmt+Ilm_{ss}	4	25.80	(10)	0.77	10	48.16	(23)	0.96
6F63x34D	37.0	950	7.0	Tmt+Ilm_{ss}	5	30.37	(12)	0.91	5	49.55	(16)	0.99
6F57x34D	43.3	950	21.0	Tmt+Ilm_{ss}	5	29.37	(17)	0.88	5	49.44	(17)	0.99
6IT60x49D	40.0	951	32.7	Tmt+Ilm_{ss}	9	30.90	(14)	0.93	10	49.79	(19)	1.00
6F63x66D	37.0	950	7.6	Tmt+Ilm_{ss}+Fe°	5	32.59	(15)	0.98	5	49.99	(26)	1.00
6F57x66D	43.3	950	21.0	Tmt+Ilm_{ss}+Fe°	5	32.38	(10)	0.97	5	50.04	(15)	1.00
6IT60M2x6aD	40.0	950	21.0	Tmt+Ilm_{ss}	10			0.61	10			0.91
6IT70M1A1x6aD	30.0	950	21.0	Tmt+Ilm_{ss}	10			0.71	10			0.95
6IT60M1A1x6aD	40.0	950	21.0	Tmt+Ilm_{ss}	10			0.57	10			0.91
samples **with** oxy-exsolutions annealed at 950 °C after 1300 °C synthesis												
6F92x0.15D	8.0	948	14.0	Tmt+Ilm_{ss}	10	4.02	(38)	0.12	5	19.87	(90)	0.40
6F76x0.5D	23.5	951	32.7	Tmt+Ilm_{ss}	10	8.80	(09)	0.26	10	29.29	(19)	0.59
6F80x0.5D	20.0	950	13.9	Tmt+Ilm_{ss}	5	8.59	(06)	0.26	7	28.25	(16)	0.57
6F80x0.75D	20.0	951	32.7	Tmt+Ilm_{ss}	10	10.90	(12)	0.33	10	31.74	(20)	0.63
6F72x1.5D	28.0	948	14.0	Tmt+Ilm_{ss}	10	12.83	(12)	0.38	10	37.47	(28)	0.75
6F63x8D	37.0	948	14.0	Tmt+Ilm_{ss}	5	18.97	(14)	0.57	10	44.87	(15)	0.90
samples annealed at 950 °C after 1200 °C synthesis												
5F63x2.8aD	37.0	950	21.0	Tmt+Ilm_{ss}	10	15.61	(16)	0.47	10	41.61	(31)	0.83

Table A.19: Experimental conditions and phase compositions (EMP analysis) of samples annealed at 950°C, system Fe-Ti±Mg±Al-O.

annealing run no	bulk Ti/(Ti+Fe) [at%]	T [°C]	run duration [d]	assemblage	Tmt n	Tmt Ti/(Ti+Fe) [at%] mean	Tmt Ti/(Ti+Fe) [at%] (σ)	Tmt X'_{Usp}	Ilm_{ss} n	Ilm_{ss} Ti/(Ti+Fe) [at%] mean	Ilm_{ss} Ti/(Ti+Fe) [at%] (σ)	Ilm_{ss} X'_{Ilm}
F72(f)5D	27.6	950	21.0	Tmt+Ilm_{ss}	10	23.27	(13)	0.70	10	47.35	(34)	0.95
F69(g)5D	31.0	950	21.0	Tmt+Ilm_{ss}	10	26.73	(12)	0.80	10	48.02	(22)	0.96
5F63x33.5D	37.0	950	7.1	Tmt+Ilm_{ss}	10	29.57	(19)	0.89	10	49.41	(21)	0.99
5F54.5Fex83.5D	45.5	950	21.0	Tmt+Ilm_{ss}+Fe°	10	32.20	(18)	0.97	10	49.55	(20)	0.99
samples annealed at 950°C after 1100°C synthesis												
3F80x0.4D	20.0	950	12.0	Tmt+Ilm_{ss}	10	9.66	(09)	0.29	10	30.42	(14)	0.61
3F69QeD	31.0	950	12.0	Tmt+Ilm_{ss}	10	18.31	(18)	0.55	10	44.45	(20)	0.89
3F63x16.5D	37.0	950	7.0	Tmt+Ilm_{ss}	10	26.71	(17)	0.80	10	48.51	(21)	0.97
3F63x30D	37.0	950	13.9	Tmt+Ilm_{ss}	10	29.05	(14)	0.87	10	48.98	(12)	0.98
3IT60IWD	40.0	948	14.0	Tmt+Ilm_{ss}	10	31.56	(16)	0.95	10	49.89	(12)	1.00

A.4 Conversion of wt% and vol% into mol%

For the system Fe-Ti-O, wt% (from Rietveld analysis) and vol% (from image analysis) have been translated into mol% by equations A.1 and A.2.

$$\text{mol\%(phase A)} = \frac{\frac{\text{vol\%(phase A)}}{\text{molar volume (phase A)}}}{\frac{\text{vol\%(phase A)}}{\text{molar volume (phase A)}} + \frac{\text{vol\%(phase B)}}{\text{molar volume (phase B)}}} \tag{A.1}$$

$$\text{mol\%(phase A)} = \frac{\frac{\text{wt\%(phase A)}}{\text{molar weight (phase A)}}}{\frac{\text{wt\%(phase A)}}{\text{molar weight (phase A)}} + \frac{\text{wt\%(phase B)}}{\text{molar weight (phase B)}}} \tag{A.2}$$

The molar volume is calculated according to equation A.3.

$$\frac{\text{molar weight}}{\text{density}} \tag{A.3}$$

The molar weight is calculated from the Ti/(Ti+Fe) ratio (according to EMP analysis) and assuming stoichiometry of the phases, based on the atomic weights given in Table A.20.

Table A.20 Fe-Ti oxide solid solution series

element	atomic weight [g/mol]
O	15.9994
Fe	55.8470
Ti	47.9000

The density along Tmt and Ilm_{ss} solid solution is interpolated from the endmember densities given in Deer *et al.* (1992) and the JCPDS-ICDD data base (Fig. A.3).

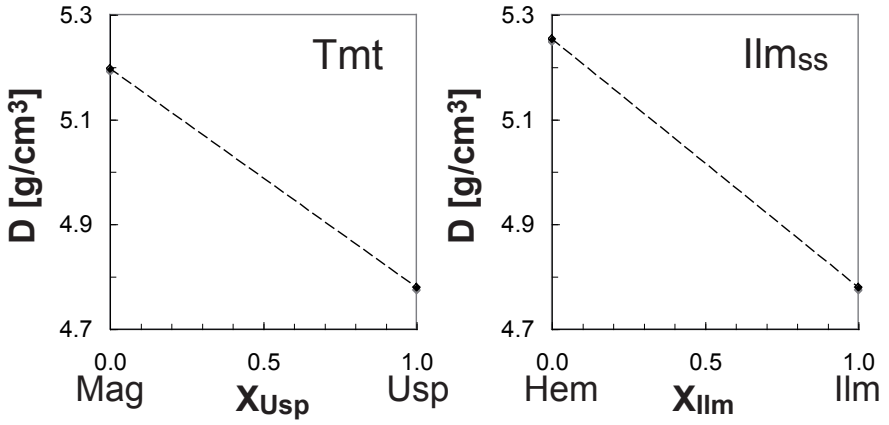

Fig. A.3 Linear interpolation for density along a) Tmt and b) Ilm_{ss} solution between endmember values.

A.5 Tmt projection

To compare Mg-Al bearing Tmt with Tmt in the simple system Fe-Ti-O, the composition of the former has to be projected into the system Mag-Usp binary. There are several calculation schemes in literature (e.g. Stormer, 1983). Within this study, the calculation according to equation 6.5 has been applied (chapter 6).

For calculation of X'_{Usp} according to equation 6.5, the basic assumption is that Fe^{2+} and Mg^{2+} are equally distributed between aluminates, ferrites, and titanates. Accordingly, the molefractions of the endmember components (Table 6.3, chapter 6) in Tmt can be calculated.

For the projection of the molefractions of the endmembers to the magnetite-ulvöspinel binary, we can use one of the following two approaches.

(1) Mg^{2+} titanate (qandilite) is ignored for the calculation of X'_{Usp}.

(2) Fe^{2+} and Mg^{2+} (i.e. molefractions of qandilite and ulvöspinel, X_{Qan} and X_{Usp}) are summarised for the calculation.

As is shown below, both approaches yield the same formula.

Approach 1

$$X'_{Usp} = \frac{X_{Usp}}{X_{Usp} + X_{Mag}} = \frac{\left[Ti^{4+}\right] * \frac{\left[Fe^{2+}\right]}{\left[Fe^{2+}\right]+\left[Mg^{2+}\right]}}{\left[Ti^{4+}\right] * \frac{\left[Fe^{2+}\right]}{\left[Fe^{2+}\right]+\left[Mg^{2+}\right]} + \frac{\left[Fe^{3+}\right]}{2} * \frac{\left[Fe^{2+}\right]}{\left[Fe^{2+}\right]+\left[Mg^{2+}\right]}} \tag{A.4}$$

$$X'_{Usp} = \frac{\left[Ti^{4+}\right]}{\left[Ti^{4+}\right] + \frac{\left[Fe^{3+}\right]}{2}} \tag{A.5}$$

Approach 2

$$X'_{Usp} = \frac{X_{Usp} + X_{Qan}}{X_{Usp} + X_{Qan} + X_{Mag} + X_{MgF}} = \frac{\left[Ti^{4+}\right]}{\left[Ti^{4+}\right] + \frac{\left[Fe^{3+}\right]}{2}} \tag{A.6}$$

Approach 1 can be visualised as a sequence of projections in tetrahedra (Fig. A.4). Approach 2 can be thought of as folding up the top and bottom triangles of a triangular prism (Fig. 6.8, chapter 6).

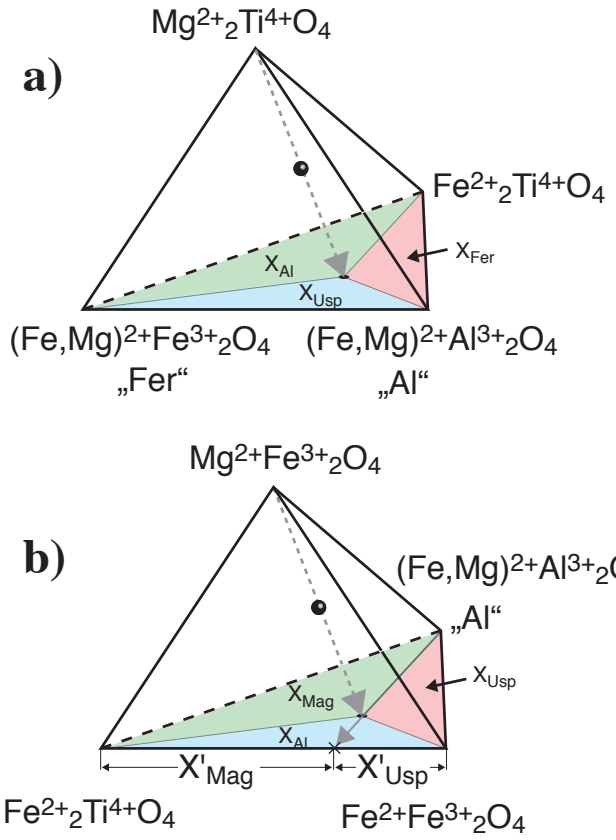

$$X_{Fer} = \frac{Fe^{3+}}{2}$$

$$X_{Al} = \frac{Al^{3+}}{2}$$

$$X_{Usp} = Ti^{4+}\frac{Fe^{2+}}{Fe^{2+} + Mg^{2+}}$$

$$X_{Mag} = \frac{Fe^{3+}}{2}\frac{Fe^{2+}}{Fe^{2+} + Mg^{2+}}$$

$$X_{Al} = \frac{Al^{3+}}{2}$$

$$X_{Usp} = Ti^{4+}\frac{Fe^{2+}}{Fe^{2+} + Mg^{2+}}$$

Fig. A.4 Re-calculation according to approach 1, visualised as subsequent projections in tetrahedra. a) Tetrahedron with the apices ferrite "Fer", aluminate "Al" (both Mg^{2+}+Fe^{2+}), qandilite and ulvöspinel. Projection from qandilite onto the Fer-Al-Usp plane. b) Tetrahedron with the apices ulvöspinel, aluminate "Al" (Mg^{2+}+Fe^{2+}), magnetite and magnesioferrite. Projection from magnesioferrite onto the Usp-Al-Mag plane, and subsequently from "Al" to the Mag-Usp binary.

B Author's publications related to this thesis

B.1 Paper

The following publication covers much of the data and figures presented in chapter 4 of this thesis:

Lattard D, Sauerzapf U, Käsemann M (2005) New calibration data for the Fe-Ti oxide thermo-oxybarometers from experiments in the Fe-Ti-O system at 1 bar, $1000-1300\,^{\circ}$C and a large range of oxygen fugacities. *Contributions to Mineralogy and Petrology* 149: 735-754

B.2 Abstracts and conference participations

Sauerzapf U, Engelmann R, Lattard D, Kontny A, van Aken PA, Ullrich A (2005) High-temperature non-stoichiometry in titanomagnetite - significance for petrology and rock magnetism. *EOS Transactions AGU* 86 (52), Fall Meeting Supplemental, Abstract V31B-0609. AGU Fall meeting 2005; San Francisco, USA

Sauerzapf U, Lattard D, Engelmann R, van Aken PA, Ghiorso MS (2005) Experimental contributions to a revised version of the Fe-Ti oxide thermo-oxybarometer. *Beihefte zum European Journal of Mineralogy* 17: 115. 83th annual meeting of the DMG; Aachen, Germany

Sauerzapf U, Engelmann R, Lattard D, van Aken PA, Kontny A, Ullrich A (2005) Is the Curie temperature of titanomagnetite dependent on its high-temperature non-stoichiometry? New experimental constraints for the Fe-Ti-O system. 10th Scientific Assembly of the International Association of Geomagnetism and Aeronomy; Toulouse, France

Sauerzapf U, Lattard D, Ghiorso MS (2005) Phase relations in the system Fe-Ti$\pm$Mg$\pm$Al-O - new calibration data for the Fe-Ti, two-oxide thermooxybarometer. *Geophysical Research Abstracts* 7, European Geosciences Union General Assembly 2005; Vienna, Austria

Sauerzapf U, Lattard D, Ullrich A, Engelmann R (2004) High-T non-stoichiometry of titanomagnetite re-examined - new experimental data. *Conference Supplement to Conference Supplement to Geochimica et Cosmochimica Acta*: A88 Abstract 1.4.P10. 14th Annual Goldschmidt Conference 2004; Copenhagen, Denmark

Sauerzapf U, Lattard D, Ghiorso MS (2004) New experiments in the system Fe-Ti±Mg±Al-O - a contribution to a re-calibration of the Fe-Ti, two-oxide thermo-oxybarometer. Tenth International Symposium on Experimental Mineralogy, Petrology and Geochemistry; Frankfurt, Germany

Sauerzapf U, Lattard D (2003) Oxy-Exsolution and subsolidus growth textures in synthetic Fe-Ti oxide assemblages. GSA Annual Meeting 2003; Seattle, USA

Acknowledgements

First and foremost, I would like to express my sincere gratitude to my supervisor Prof. Dr. Dominique Lattard. She initiated the project and guided me through the past three years with many stimulating discussions, and helpful advice. Thanks for all the encouragement and motivation - in general and especially when an experiment had failed *again*.

Thanks a lot to Agnes Kontny for many fruitful discussions on Fe-Ti oxides, as well as agreeing to examine this thesis.

I want to thank all co-operating scientists at other institutes and research facilities: Peter van Aken for the opportunity to carry out EELS measurements at the TU Darmstadt, for help during the measurements, and also for enlightening discussions on the analysis results; Bernard Evans (Seattle) for advice in many experimental and analytical questions on Fe-Ti oxides - I have profited a lot from his experience; Mark S. Ghiorso (Seattle) for exchange on the progress towards a new version of the Tmt-Ilm_{ss} thermo-oxybarometer, regarding experiments on our side, and the new modelling on his side; Donald H. Lindsley for sharing his profound knowledge on Fe-Ti oxides and re-analysing some of our run products at Stony Brook.

Special thanks go to the students, staff and researchers at the "experimental mineralogy" group at the Mineralogisches Institut, Heidelberg and all users of the "6th floor labs": Thank you for help and cooperation in the labs or at the computer, for discussions, for friendly words, and for sharing your sweets. Ralf Engelmann contributed to this thesis by providing samples produced within the frame of his own Ph.D. thesis. Thank you Ramona and Verena for help with the experiments and analysis, with tables, figures and calculations. Special thanks go to Angela Ullrich for doing a great job with the lattice parameter determination.

Further, I want to thank **all** members of the Mineralogisches Institut Heidelberg, present and past, who contributed to this thesis by their work, advice or friendship. Ilse Glass helped at the SEM and in the X-Ray diffraction lab; Ilona Fin and Oliver Winand prepared the polished sections for EMP, SEM and TEM work. Thanks to Hans Peter Meyer for maintenance of the EMP and SEM and help during EMP measurements. Thank you Melanie and Joan for being great roommates at several conferences!

I want to thank the DFG for funding through project LA1164/4.

Finally, I would like to thank all my family and friends for support, advice, encouragement, and for just being there. In particular, I want to thank my parents, Richard and Maria Sauerzapf, and my husband Markus Schwarz.

Erklärung

Ich erkläre hiermit, dass ich die vorgelegte Dissertation selbst verfasst und mich keiner anderen als der von mir ausdrücklich bezeichneten Quellen und Hilfen bedient habe.

Ich erkläre hiermit, dass ich an keiner anderen Stelle ein Prüfungsverfahren beantragt bzw. die Dissertation in dieser oder anderer Form bereits anderweitig als Prüfungsarbeit verwendet oder einer anderen Fakultät als Dissertation vorgelegt habe.

Heidelberg, den 30. März 2006